

**WA School of Mines: Minerals, Energy and Chemical Engineering**

**Development of Non-precious Metal Electrocatalysts for  
Electrochemical Energy Conversion and Storage Applications**

**Zhang Xiaoran**

**This thesis is presented for the Degree of  
Doctor of Philosophy  
Of  
Curtin University**

## **Declaration**

To the best of my knowledge and belief this thesis contains no material previously published by any other person except where due acknowledgement has been made.

This thesis contains no material which has been accepted for the award of any other degree or diploma in any university.

## **Abstract**

Oxygen reduction reaction (ORR), oxygen evolution reaction (OER) and hydrogen evolution reaction (HER) are three important and fundamental reactions in the renewable electrochemical device. Electrochemical catalyst is the most important core of these electrochemical devices. One of the critical challenges in the development of highly efficient electrocatalysts with low cost for the commercial viability and large-scale application of the technologies. Among all kinds of alternative electrocatalysts, heteroatoms doped carbon based materials and transition metal single-atom catalysts are considered as substitutions for replacing precious metal electrocatalysts for ORR, OER and HER electrocatalysts due to their wide range of configurations, high catalytic activity, and abundance. However, the challenge is to control configuration of active sites for tuning their performance. Therefore, this project focus on developing new heteroatoms doped carbon based electrocatalysts for ORR, OER and HER via the heteroatom doping engineering through a new precursor modulation method and to understand fundamentally the effect of heteroatom configuration on the electrocatalytic activity.

This project started with the research on N doped carbon materials, which is considered as one of the most effective and popular electrocatalysts due to their competitive performance, excellent durability with low-cost. However, despite the extensive studies, there is still a significant challenge of highly efficient NPM electrocatalysts and the lacking of elucidation of the relationship between precursors and type and amount of doped N species in the derived N doped carbon materials. This issue seriously impedes

the development of highly efficient N doped NPM electrocatalysts for ORR. Furthermore, due to complicated pyrolysis process, there exist various N species in the N-doped NPM catalysts that includes graphitic N ( $N_G$ ), pyridinic N ( $N_P$ ) and pyrrolic N ( $N_{PY}$ ). However, correlation and fundamental relationships between different N species and the electrocatalytic activity are not clear. This stems from the difficulty in the precise control of the type and amount of doped N species in conventional pyrolysis methods. The results indicate that N doped carbon with dominant  $N_P$  and  $N_G$ , *etc.* shows excellent catalytic activity for ORR, with the onset potential ( $E_{onset}$ ) of 1.01 V and half-wave potential ( $E_{1/2}$ ) of 0.86 V vs. RHE, respectively. This is in turn supported by the observation that for catalyst with only the dominant  $N_P$  component but with low content of  $N_G$  displays poor catalytic activity as compared with  $N/C-N_P+N_G$ , which is caused by low spin density in spite of strong charge density. The work demonstrates the effectiveness of precursor modulation strategy in the control of type and configuration of doped N species and sheds light on the intrinsic relationship between the doped N species and ORR performance of carbon based catalysts.

The work is extended to the effect of various heteroatoms co-doping like N, S and/or P on tuning of their active sites configuration. In the case of N and S co-doping, two N and/ or S co-doped carbon nanospheres are synthesised with three typical analogous precursors of 2, 6-Diaminopyridine, 1, 3-Diaminobenzene and 4, 6-Diaminopyrimidine using  $H_2O_2$  and ammonium persulfate as initiators, respectively. The electrocatalytic activity of N, S co-doped catalyst is even better than that of commercial Pt/C. Both the experimental measurement and density functional theory (DFT)



calculation indicate that there is a close link between the location of N in six-membered rings of these precursors and the final formation of N-doping species, which directly induce the electronic structure distribution of doped carbon and thus lead to a significant difference for ORR performance. Meanwhile, few studies focus on their selectivity for different reactions due to the complicated active sites configurations and unclear catalytic mechanism. Based on this, two N, S co-doped graphene based carbon materials with different configuration of N, S dopants are synthesised with 2, 6-Diaminopyridine as nitrogen source, 2,5-Dithiobiurea and Ammonium persulfate as S-containing source, respectively. Interestingly, it is notable that the S-containing precursors are crucial on deciding the formation of final N dopant types in graphene matrix. The results demonstrate that the NSG sample with Ammonium persulfate as S-containing precursors possess the high content of  $N_G$  and S displays superior ORR catalytic activity with the half-wave potential of 0.87V vs. RHE. By contrast, NSG catalyst derived from 2, 5-Dithiobiurea as sulfur source featured with low content of  $N_G$  but high content of  $N_{PY}$  and  $N_P$  that induces catalytic activity for ORR and OER.

Finally, based on the precursor modulation approach, transition metal based single atoms such as cobalt (Co) is successfully introduced to N doped carbon materials, Co-N/C, with similar Co and N concentration but with controlled N species, i.e.,  $N_G$ ,  $N_P$  and  $N_{PY}$ . Herein, new single cobalt atoms embedded in N-doped carbon, Co-N/C, materials through the engineering control of N species by using a precursor modulation strategy are successfully synthesized. The best performed Co-N/C is obtained on the Co-N<sub>4</sub> moieties coordinated with  $N_G$ , Co-N/C+ $N_G$ , displaying superior activity for

ORR with the half-wave potential of 0.815, 0.915, 0.73 V *vs.* RHE in alkaline, acidic, and neutral media, respectively. The Co-N/C catalysts show the order of activity as a function of coordinated N species: Co-N/C+N<sub>G</sub> > Co-N/C+N<sub>P</sub> > Co-N/C+N<sub>PY</sub>.

In the thesis, from the perspective of material synthesis, the correlation between N-containing polymer precursors (especially the Five membered / six membered heterocyclic compounds) and the preference of the formation of different N species (N<sub>G</sub>, N<sub>P</sub> and N<sub>PY</sub>) after pyrolysis are revealed. Meanwhile, combined with theoretical calculation, the synergistic effect between different kinds of N types and various heteroatoms N, S, P *etc.* are studied for ORR, OER and HER, respectively. These work shed light on the optimal active centers as well as providing new concept for designing and control of heteroatoms doped carbon materials based on tuning N-containing precursor platform with high activity and stability for the electrochemical energy conversion and storage areas.

## **Acknowledgements**

I would like to first give my sincere gratitude to my supervisors Prof. San Ping Jiang and Prof. Zongping Shao for giving me inspiration of new ideas, consistent support, and invaluable guidance. It is such an honor for me to be their student, this thesis would not have been completed without their patient guidance. I would like to thank our group members for the friendship and help during my PhD study, especially Dr. Shiyong Zhao, Dr. Xiao Zhang, Dr. Yu Liu, Dr. Xiaomin Xu, Dr. Jianyun Zheng, and Dr. Shuai He for their help on XANES and TEM analysis. I would like to thank Ms. Angelina Rossiter, Mr. Nathan Tarom and Ms. Lana McQueen for their support on lab safety and administrative issues. I would also like to express my heartfelt gratitude to Prof. Zhi Qun Tian and Prof. Pei Kang Shen and their research group members of Guangxi University and Dr. Chen Chen, as well as Prof. Shuangyin Wang from Hunan University for providing me with invaluable advices and excellent support during the difficult COVID-19 period. Special thanks shall go to my family members for the constant encouragement and support throughout the project.

## List of Publications

1. **Xiaoran Zhang**, Xiaomin Xu, Kun Wang, Yilin Huang, Zhi Qun Tian\*, Pei Kang Shen, San Ping Jiang,\* Zongping Shao\*. Boosting electrocatalytic activity of single atom catalysts supported on nitrogen-doped carbon through N coordination environment engineering. *Small*. 2022. DOI: 10.1002/sml.202105329.
2. **Xiaoran Zhang**, Xingyu Wen, Can Pan, Xue Xiang, Chao Hao, Qinghao Meng, Zhi Qun Tian\*, Pei Kang Shen, San Ping Jiang\*. N species tuning strategy in N, S co-doped Graphene Nanosheets for electrocatalytic activity and selectivity of Oxygen redox reactions. *Chem. Eng. J.* doi.org/10.1016/j.cej.2021.133216.
3. **Xiaoran Zhang**, Yunqiu Wang, Kun Wang, Yilin Huang, Dandan Lyu, Feng Yu, Shuangbao Wang, Zhi Qun Tian\*, Pei Kang Shen, San Ping Jiang\*. Active sites engineering via tuning configuration between graphitic-N and thiophenic-S dopants in one-step synthesized graphene nanosheets for efficient water-cycled electrocatalysis. *Chem. Eng. J.* 2021, 416, 129096.
4. **Xiaoran Zhang**, Xiao Zhang, Xue Xiang, Can Pan, Qinghao Meng, Chao Hao, Zhi Qun Tian\*, Pei Kang Shen, San Ping Jiang\*. Nitrogen and Phosphate Co-doped Graphene as Efficient Bifunctional Electrocatalysts by Precursor Modulation Strategy for Oxygen Reduction and Evolution Reactions. *ChemElectroChem*. DOI10.1002/celec.202100599.
5. **Xiaoran Zhang**, Sixian. Yao, Pinsong. Chen, Yunqiu. Wang, Dandan. Lyu, Feng. Yu, Ming. Qing, Zhi Qun Tian\*, Pei Kang Shen. Revealing the dependence of active site configuration of N doped and N, S-co-doped carbon nanospheres on six-membered heterocyclic precursors for oxygen reduction reaction, *J. Catal.* 2020, 389, 677-689.
6. **Xiaoran Zhang**, Xiao Zhang, Shiyong Zhao, Yunqiu Wang, Zhi Qun Tian\*, Pei Kang Shen, San Ping Jiang\*. Precursor modulated active sites of nitrogen doped graphene-based carbon catalysts via one-step pyrolysis method for the enhanced oxygen reduction reaction. *Electrochim. Acta* 2020, 370, 137712.
7. **Xiaoran Zhang**, Yaser Bahari Mollamahale, Dandan Lyu, Lizhe Liang, Feng Yu, Ming Qing, Yonghua Du, Xinyi Zhang, Zhi Qun Tian, Pei Kang Shen. Molecular-

level design of Fe-N-C catalysts derived from Fe-dual pyridine coordination complexes for highly efficient oxygen reduction. *J. Catal.* **2019**, *327*, 245-257.

8. **Xiaoran Zhang**, Yunqiu Wang, Yonghua Du, Mingqing, Zhi Qun Tian\*, Pei Kang Shen\*. Highly active N, S co-doped hierarchical porous carbon nanospheres from green and template-free method for super capacitors and oxygen reduction reaction. *Electrochimi. Acta* **2019**, *318*, 272-280.
9. **Xiaoran Zhang**, Dandan Lyu, Yaser Bahari Mollamahale, Feng Yu, Ming Qing, Shibin Yin, Xinyi Zhang, Zhi Qun Tian\*, Pei Kang Shen. Critical role of iron carbide nanodots on 3D graphene based nonprecious metal catalysts for enhancing oxygen reduction reaction. *Electrochimi. Acta* **2018**, *281*,502-509.

## Table of contents

Abstract .....	3
Acknowledgements .....	7
Table of contents .....	10
Chapter 1: Introduction.....	14
1.1 Background.....	14
1.2 Objectives and outline of the thesis .....	14
Chapter 1: Introduction.....	15
Chapter 2: Literature Review.....	15
Chapter 3: Precursor modulated active sites of nitrogen doped graphene-based carbon catalysts via one-step pyrolysis method for ORR .....	16
Chapter 4: Precursor modulated synergy of N, P co-doped graphene materials via a bottom-up doping strategy for electrocatalytic selectivity for oxygen redox reaction .....	16
Chapter 5: Revealing the dependence of active site configuration of N doped and N, S-co doped carbon nanospheres with six-membered heterocyclic compounds as precursors for enhancing oxygen reduction reaction.....	16
Chapter 6: Precursors Modulated active sites of One-step Synthesized N, S co-doped Graphene Nanosheets for tuning the activity and selectivity for Oxygen redox reactions.....	17
Chapter 7: Active Sites Engineering via Tuning Configuration between Graphitic-N and Thiophenic-S Dopants in one-step Synthesized Graphene Nanosheets for Efficient Water-Cycled Electrocatalysis.....	17
Chapter 8: Boosting electrocatalytic activity for oxygen reduction reaction of single atom catalysts in full pH range through doped N types engineering .....	18
Chapter 9: Conclusions and recommendations for future work.....	18
Chapter 2: Literature Review .....	21
2.1 Introduction .....	21
2.2 Electrode Reactions in Fuel Cells.....	22
2.2.1 Oxygen reduction reaction.....	22
2.3 Development of precious metal based catalyst for ORR, OER and HER.....	26
2.4 Carbon based efficient electrocatalysts.....	28
2.4.1 Heteroatoms doped carbon materials.....	29
2.4.2 Nitrogen-doped carbon materials as electrocatalysts.....	31
2.4.3 Heteroatoms Co-doping doped carbon materials in electrocatalysts .....	35
2.5 Development status and problems to be solved for heteroatom-doped carbon materials. ....	44
2.6 Summary and Perspective .....	45
Reference .....	47
Chapter 3: Precursor modulated active sites of nitrogen doped graphene-based carbon catalysts via one-step pyrolysis method for the enhanced oxygen reduction reaction .....	56

Abstract .....	56
3.1. Introduction .....	57
3.2. Experimental.....	59
3.2.1 <i>Materials and synthesis</i> .....	59
3.2.2 <i>Characterization</i> .....	60
3.2.3 <i>Density functional theory calculation</i> .....	62
3.3 Results and discussion .....	62
3.3.1 <i>Synthesis and characterization of graphene structured N/C</i> .....	62
3.3.2. <i>Distribution of N configurations of N/C</i> .....	65
3.3.3. <i>Electrochemical activity for ORR</i> .....	69
3.3.4. <i>DFT calculation of the origin of catalytic activity</i> .....	72
3.4 Conclusion.....	75
References .....	76
Chapter 4: Precursor modulated active sites of N, P Co-doped graphene-structured based carbon catalysts via One-step pyrolysis method for Enhanced Oxygen Reduction Reaction and Oxygen Evolution Reaction.....	84
Abstract .....	84
4.1 Introduction .....	85
4.2 Experimental.....	88
4.2.1. <i>Materials and synthesis</i> .....	88
4.2.2 <i>Materials characterization</i> .....	90
4.2.3 <i>Electrochemical Measurements</i> .....	91
4.2.4 <i>Density functional theory calculation</i> .....	92
4.3 Results and discussion .....	92
4.3.1 <i>Microstructure and phase of N, P co-doped graphene catalysts</i> .....	92
4.3.2 <i>Element analysis of NP-G catalysts</i> .....	95
4.3.2 <i>Electrochemical activity for ORR and OER</i> .....	100
4.3.4 <i>Density functional theory (DFT) calculations</i> .....	103
4. 4 Conclusion.....	107
Reference.....	108
Chapter 5: Revealing the dependence of active site configuration of N doped and N, S-co-doped carbon nanospheres on six-membered heterocyclic precursors for oxygen reduction reaction.....	117
Abstract .....	117
5.1 Introduction .....	118
5. 2 Experimental.....	121
5. 2.1 <i>Synthesis of N doped and N, S co-doped nanospheres</i> .....	121
5.2.2 <i>Materials characterization</i> .....	122
5.2.3 <i>Electrochemical measurements</i> .....	122

5.2.4 Density functional theory calculation.....	124
5.3 Results and discussion .....	124
5.3.1 Synthesis and characterization of N doped and N, S co-doped carbon nanospheres ....	124
5.3.2 Electrochemical evaluation for ORR .....	131
5.3.3 The origin of catalytic activity difference for ORR.....	136
5.4 Conclusion.....	149
References .....	150
Chapter 6: Active Sites Engineering via Tuning Configuration between Graphitic-N and Thiophenic-S Dopants in one-step Synthesized Graphene Nanosheets for Efficient Water-Cycled Electrocatalysis	159
Abstract .....	159
6.1 Introduction .....	160
6.2 Results and Discussion .....	163
6.2.1 Structure properties .....	163
6.2.2 Electrochemical evaluation .....	171
6.2.3 Discussion on the synergistic effect of N and S with different ratio in graphene matrix for water splitting and oxygen reduction reactions. ....	174
6.3 Conclusion.....	181
References .....	182
Chapter 7: N species tuning strategy in N, S co-doped graphene Nanosheets for electrocatalytic activity and selectivity of oxygen redox reactions .....	188
Abstract .....	188
7.1 Introduction .....	190
7.2 Experimental.....	192
7.2.1 Synthesis of N doped and N, S co-doped graphene nanosheets .....	192
7.2.2 Characterization .....	193
7.2.3 Electrochemical Measurements .....	193
7.2.4 Homemade Zn-Air batteries fabrication and testing .....	194
7.3 Results and discussion .....	194
7.3.1 Structural analysis of NSG nanosheets.....	194
7.3.2 Electrocatalysis for ORR, OER and Zn-air battery. ....	203
7.3.3 Discussion on active sites in N, S co-doped graphene for ORR and OER.....	208
7.4 Conclusion.....	213
References .....	214
Chapter 8: Boosting electrocatalytic activity for oxygen reduction reaction of single atom catalysts in full pH range through doped N types engineering .....	221
Abstract .....	221
8.1 Introduction .....	222
8.2 Experimental.....	226



8.2.1 <i>Synthesis of Co-based SACs nanospheres.</i> .....	226
8.3 Results and Discussion .....	228
8.3.1 <i>Microstructure and phase properties</i> .....	228
8.3.2. <i>Types of N species and coordination environment of catalysts</i> .....	232
8.3.3. <i>Electrochemical activity for ORR</i> .....	238
8.3.4. <i>Application for Zn-Air battery and fuel cells</i> .....	243
8.3.5 <i>Computational calculation</i> .....	245
8.4 Conclusion.....	249
References .....	251
9. Summary .....	262

# **Chapter 1: Introduction**

## **1.1 Background**

ORR, OER and HER are the most crucial reactions in electrochemical conversion and storage systems [1-3]. The most widely used electrocatalysts for ORR, OER and HER are kind of precious electrocatalysts such as Pt/C, IrO<sub>2</sub>, and RuO<sub>2</sub> *etc* [4-6]. However, precious metal based materials are expensive with very limited resources. Therefore, seeking for the efficient metal free or non-precious electrocatalysts is absolutely critical to solve limited resources and cost problems for their large-scale industrial application. Among all kinds of candidates, carbon based electrocatalysts are attractive due to their competitive activity, low cost and abundance [7-10]. In spite of tremendous efforts been made on development of highly active heteroatoms doped carbon based materials, their catalytic activity is still much lower than that of Pt-based precious metal catalysts [11, 12]. Meanwhile, the origin and fundamental catalytic mechanism of doped carbon catalysts are not clear and still controversial in some cases. One of the main reasons is due to the significant variation of types and amount of doped species and the difficulties in the control of the types and configurations of the doped species by conventional pyrolysis methods [12-15]. It is both scientifically and technologically important to fundamentally understand the intrinsic correlation between types and configuration of doped heteroatoms and the formation of active sites and this in turn will facilitate and accelerate the developing highly efficient electrocatalysts for the electrochemical energy conversion and storage devices.

## **1.2 Objectives and outline of the thesis**

The project is focus on the development a new precursor modulation method for the control and manipulation of the types and amount of doped heteroatoms of carbon materials to fundamentally reveal the relationship between the construction of active sites and intrinsic activity of heteroatoms doped carbon materials. A series of heteroatoms doped carbon materials were synthesized based on the precursor modulation method and the activity and selectivity of the as-synthesised carbon based materials were characterized for ORR, HER and OER. Theoretical computational calculation was also carried out to provide additional support for the synergistic effect among various heteroatoms species.

This thesis includes 6 chapters. The first chapter focus on the background and the outline of this thesis. Chapter 2 shows a literature review on heteroatoms doped metal free carbon materials and related topics. The experiment results and discussions are presentd in chapter 3-8. Conclusions and future work are present in Chapter 9.

### **Chapter 1: Introduction**

The first chapter briefly introduces the development process and research status of electrocatalysts for ORR, OER and HER, objectives of the PhD project and outline of chapters of the Thesis.

### **Chapter 2: Literature Review**

A comprehensive review on synthesis, application and characterization of non-precious metal electrocatalyst, especially heteroatoms doped carbon based non-metallic materials for ORR, OER and HER. The critical issue and challenges are discussed.

### **Chapter 3: Precursor modulated active sites of nitrogen doped graphene-based carbon catalysts via one-step pyrolysis method for ORR**

In this Chapter, three nitrogen doped carbon materials with different active sites configurations of N species were successfully synthesized. Three polymer precursors were selected to modulate N types such as pyridine nitrogen ( $N_P$ ), graphitic nitrogen ( $N_G$ ) and pyrrole nitrogen ( $N_{PY}$ ). The results display that  $N_P$  and  $N_G$  as main component induces the best performance for ORR, due to the fact that the combination of  $N_P$  and  $N_G$  could produce a strong electron redistribution on surrounding carbon atoms, which is benefit for ORR catalytic performance. This work proposed a new concept for designing graphene based nitrogen doped carbon materials with effective N configurations as active sites for ORR.

### **Chapter 4: Precursor modulated synergy of N, P co-doped graphene materials via a bottom-up doping strategy for electrocatalytic selectivity for oxygen redox reaction**

In this Chapter, we propose an effective active sites tuning strategy for obtaining N, P co-doped graphene nanosheets (NPG) with certain N species and graphitic P configurations. It is found that the configuration of  $N_P + N_G + P$  prefer to producing enhanced catalytic activity for ORR. Meanwhile,  $N_{PY} + N_G + P$  contributes to promoting OER performance greatly.

### **Chapter 5: Revealing the dependence of active site configuration of N doped and N, S-co doped carbon nanospheres with six-membered heterocyclic compounds as precursors for enhancing oxygen reduction reaction**

In this Chapter, a series of N and/or S co-doped carbon materials were obtained derived

from three typical analogous precursors. The results indicates that the formation of different N-doping types and synergistic effects of N and S dopants in their derived carbon nanospheres, which directly induce the change of electronic structure of doped carbon and thus lead to a significant difference for ORR performance.

### **Chapter 6: Precursors Modulated active sites of One-step Synthesized N, S co-doped Graphene Nanosheets for tuning the activity and selectivity for Oxygen redox reactions.**

In this Chapter, two N, S co-doped catalysts with different N, S dopants species were synthesized with 2, 6-Diaminopyridine as the same N-containing precursor platform. It is found that the NSG catalyst featured with the high content of N<sub>G</sub> and S displays superior catalytic activity for ORR. By contrast, NSG catalyst derived from 2, 5-Dithiobiurea as S-containing precursor featured with relatively low content of N<sub>G</sub> but high content of N<sub>PY</sub> and N<sub>P</sub> that induces bifunctional performance for both ORR and OER (with a metric potential difference of 0.76 V in 0.1 M KOH).

### **Chapter 7: Active Sites Engineering via Tuning Configuration between Graphitic-N and Thiophenic-S Dopants in one-step Synthesized Graphene Nanosheets for Efficient Water-Cycled Electrocatalysis.**

In this Chapter, we propose an effective active sites engineering strategy of N, S co-doped graphene (NSG with certain graphitic N and thiophenic S configurations. It is found that the lower ratio of graphitic N and thiophenic S in N, S co-doped graphene nanosheets induce the enhanced performance for HER, the moderate ratio of graphitic N and thiophenic S contributes to better performance for ORR, in contrast, the higher ratio of graphitic N and thiophenic S benefit for increased performance for OER.

## **Chapter 8: Boosting electrocatalytic activity for oxygen reduction reaction of single atom catalysts in full pH range through doped N types engineering.**

In this Chapter, Co-N/C, with the same cobalt content and nitrogen concentration but different N types, i.e., N<sub>P</sub>, N<sub>G</sub>, N<sub>PY</sub> show completely different performance for ORR. DFT calculation indicates that the different coordinations of N species and Co single atoms bring about different electron distributions on carbon matrix that leads to different catalytic performance for ORR.

## **Chapter 9: Conclusions and recommendations for future work.**

The Chapter focus on the summary and the outlook of the research in the thesis.

## **References**

- [1] A. S. Arico, P. Bruce, B. Scrosati, J. M. Tarascon, W. Van Schalkwijk, Nanostructured materials for advanced energy conversion and storage devices. *Nat. Mater.* 2005, 4 (5), 366-377.
- [2] U. Martinez, S. K. Babu, E. F. Holby, H. T. Chung, X. Yin, P. Zelenay, Progress in the Development of Fe-Based PGM-Free Electrocatalysts for the Oxygen Reduction Reaction, *Adv. Mater.*, 2019, 31(31)1806545 .
- [3] F. Cheng, J. Chen, Metal-air batteries: from oxygen reduction electrochemistry to cathode catalysts. *Chem. Rev.* 2012, 41 (6), 2172-2192.
- [4] L. Chai, L. Zhang, X. Wang, L. Xu, C. Han, T.-T. Li, Y. Hu, J. Qian, S. Huang, Bottom-up synthesis of MOF-derived hollow N-doped carbon materials for enhanced ORR performance, *Carbon*, 2019, 146(7) 248-256.
- [5] X. Zhong, W. Yi, Y. Qu, L. Zhang, H. Bai, Y. Zhu, J. Wan, S. Chen, M. Yang, L. Huang,

M. Gu, H. Pan, B. Xu, Co single-atom anchored on Co<sub>3</sub>O<sub>4</sub> and nitrogen-doped active carbon toward bifunctional catalyst for zinc-air batteries, *Appl. Catal. B*, 2020, 260(8) 267-272.

[6] W. Liu, J. Zhang, Z. Bai, G. Jiang, M. Li, K. Feng, L. Yang, Y. Ding, T. Yu, Z.Chen, ;A. Yu, Controllable Urchin-Like NiCo<sub>2</sub>S<sub>4</sub> Microsphere Synergized with Sulfur-Doped Graphene as Bifunctional Catalyst for Superior Rechargeable Zn-Air Battery. *Adv. Funct. Mater.* 2018, 28 (11).

[7] W. Zhang, H. Sun, Z. Zhu, R. Jiao, P. Mu, W. Liang, A. Li, N-doped hard carbon nanotubes derived from conjugated microporous polymer for electrocatalytic oxygen reduction reaction, *Renew. Energ.*, 2020, (146), 2270-2280.

[8] C. Hu, L. Dai, Multifunctional Carbon-Based Metal-Free Electrocatalysts for Simultaneous Oxygen Reduction, Oxygen Evolution, and Hydrogen Evolution, *Adv. Mater.*, 2017, (29), 1604942

[9] H. Zhang, H.T. Chung, D. A. Cullen, S. Wagner, U. I. Kramm, K.L. More, P. Zelenay, G. Wu, High-performance fuel cell cathodes exclusively containing atomically dispersed iron active sites, *Energy Environ. Sci.*, 2019, (12), 2548-2558.

[10] Q. Hu, G. Li, G. Li, X. Liu, B. Zhu, X. Chai, Q. Zhang, J. Liu, C. He, Trifunctional Electrocatalysis on Dual-Doped Graphene Nanorings-Integrated Boxes for Efficient Water Splitting and Zn-Air Batteries, *Adv. Energy Mater.*, 2019, 9(14) 1803867.

[11] Y. Shao, J.-P. Dodelet, G. Wu, P. Zelenay, PGM-Free Cathode Catalysts for PEM Fuel Cells: A Mini-Review on Stability Challenges, *Adv. Mater.*, 2019, 31(31) 1807615.

[12] N. T. Suen, S. F. Hung, Q. Quan, N. Zhang, Y. J. Xu, H. M. Chen, Electrocatalysis for the oxygen evolution reaction: recent development and future perspectives. *Chem Soc Rev* 2017,

46 (2), 337-365.

[13] X. Ren, Q. Lv, L. Liu, B. Liu, Y. Wang, A. Liu, G. Wu, Current progress of Pt and Pt-based electrocatalysts used for fuel cells, *Sustain Energy Fuels*, 2020, 14 (3) 15-30.

[14] Y. Jiao, Y. Zheng, K. Davey, S. Z. Qiao, Activity origin and catalyst design principles for electrocatalytic hydrogen evolution on heteroatom-doped graphene, *Nat. Energy*, 2016, 12 (4).

[15] Y. Zhang, M. Luo, Y. Yang, Y. Li, S. Guo, Advanced Multifunctional Electrocatalysts for Energy Conversion, *ACS Energy Lett.*, 2019, (4) 1672-1680.



## Chapter 2: Literature Review

### 2.1 Introduction

Excessive use and burning of fossil fuels (such as crude oil, natural gas, *etc.*) are examples of some of the greatest challenges facing humanity in the 21st century [1-3]. It requires urgent needs to seek clean, renewable and carbon-neutral alternatives to fossil fuel energy resources and to develop more energy efficient energy conversion and storage technologies [4-6]. To date, the most widely recognized and efficient electrochemical energy conversion and storage devices mainly include fuel cells, water electrolyzers, lithium-ion batteries, supercapacitors *etc* [7, 8]. Among all these devices, the development of fuel cell has attracted people's wide attention. As shown in Figure 1-1, there are some typical energy conversion system in life and industry.

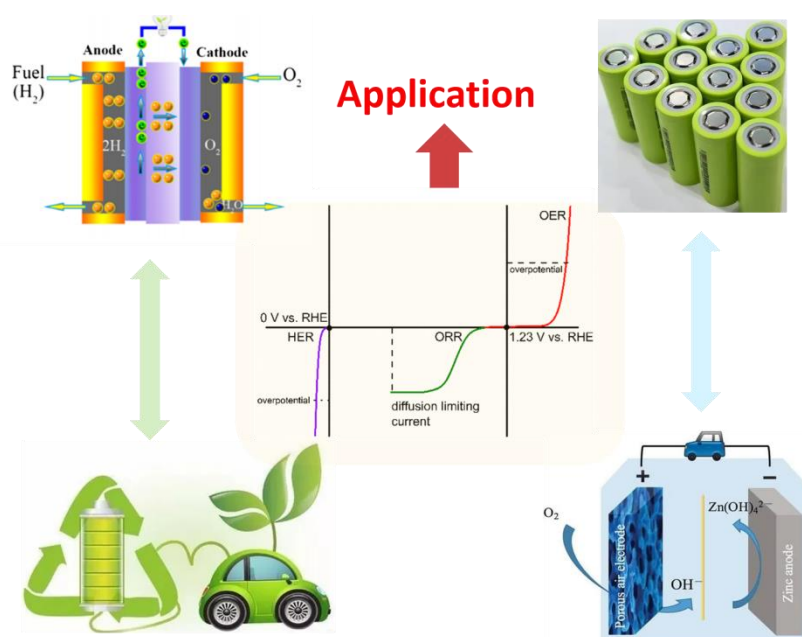


**Figure 1-1.** Various electrochemical devices and technologies in life and industry.

The electrochemical reaction in fuel cell process is clean, completely or rarely produces harmful substances [9], and the energy conversion rate is high, thus, fuel cell is kind of

promising clean energy generation device [10-12].

## 2.2 Electrode Reactions in Fuel Cells

### 2.2.1 Oxygen reduction reaction

The oxygen reduction reaction process in the working process of the fuel cell is very complex, which consists of multi-step elementary reactions and involves the formation of various intermediate oxygen-containing products, mainly including  $O_2^-$ ,  $H_2O_2$  etc [13], as shown in Figure 1-2. This directly leads to low energy conversion efficiency of batteries, and the development of efficient oxygen reduction catalysts requires an in-depth understanding of the oxygen reduction mechanism.

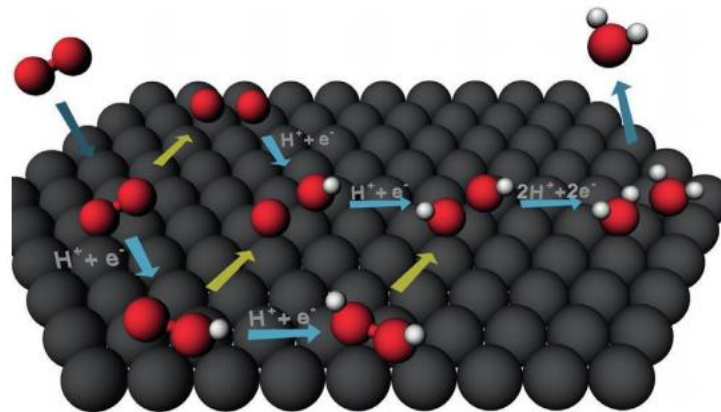
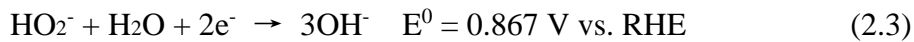
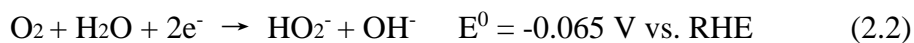
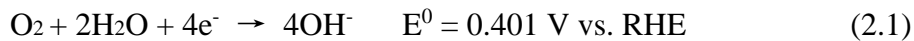
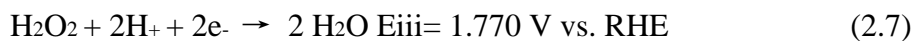
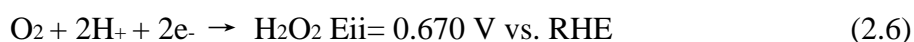
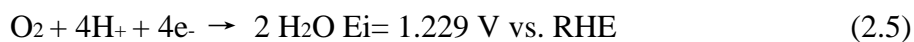


**Figure 1-2.** The illustration of proposed pathways for ORR. The ORR process in alkaline medium consists of four elementary reactions [14]:



In acidic electrolytes, ORR also consists of four elementary reactions [15]:



ORR is kind of multi-step reaction process with a very complex mechanism. The

kinetics of the reaction depends rely on the reaction conditions and intrinsic activity of the electrocatalysts. Even with the same catalysts, the oxygen reduction reaction exhibits marked environmental sensitivity [16]. The 4-electron reaction can directly reduce oxygen to  $\text{HO}^-$  with high energy efficiency. The hydrogen peroxide generated during the 2-electron reaction has strong oxidizing properties, which will corrode the active sites of the catalyst to a certain extent, thereby affecting the performance of the fuel cell [17, 18]. Usually, the number of reaction electrons is also an important indicator to measure the oxygen reduction activity [19]. The closer the number of reaction electrons is to 4, the better catalytic performance. Nevertheless, in the actual reaction process, most of the catalytic processes belong to the mixed reaction of 4-electrons and 2-electrons reactions [20]. Therefore, it is the direction that researchers pursue to study oxygen reduction catalysts that are infinitely close to the 4-electron reaction process.

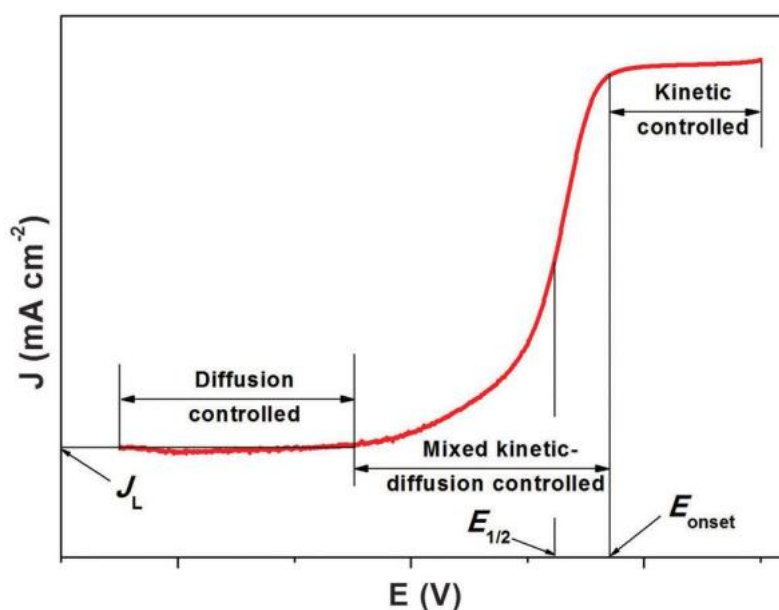


**Figure 1-3.** Typical ORR polarization curve.

A typical oxygen reduction polarization curve is shown in the Figure 1-3. The

polarization curve includes the following three distinct characteristic areas [21]: the appearance of the peak potential in the high potential stage is controlled by the kinetics, which is mainly related to the catalytic activity of the active site of the catalyst material itself; then the mixed kinetic diffusion control the half-wave potential, the stage is mainly related to the density of the active sites of the catalytic material and the conductivity of the material; the final diffusion control stage, which is affected by mass transfer, is mainly related to the conductivity of the material itself and the structure of the catalyst material. It can be seen that there are many factors affecting the oxygen reduction activity of catalyst materials, not only to have efficient catalytic active sites, the physical structure design of catalyst materials is also the key to catalyst research [22, 23]. Oxygen evolution reaction is an important chemical reaction with the opposite pathway to oxygen reduction as mentioned above [24-26].

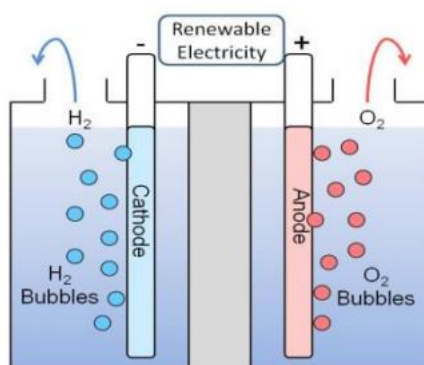


**Figure 1-4.** The illustration of fuel cells device.

As present in Figure 1-4. Among various types of fuel cells, PEMFC has attracted much attention in sustainable energy systems with its 60% energy conversion efficiency, over 80% power generation and thermal energy efficiency, and almost zero pollution [27]. In addition, PEMFC has the advantages of low temperature operation and high power

density, *etc.*, it is a very potential clean energy conversion device, and also has good commercial feasibility [28, 29].

The principle structure of the PEMFC is shown in Figure 1-5. During cell discharge, hydrogen and oxidizing gases flow through designated inlets on the sides of the fuel cell. Hydrogen protonation occurs on the anode side, followed by proton diffusion through the proton exchange membrane towards the cathode side. The electrochemical reactions that occur in the PEMFC are shown in equations (2.9)-(2.11) [30].

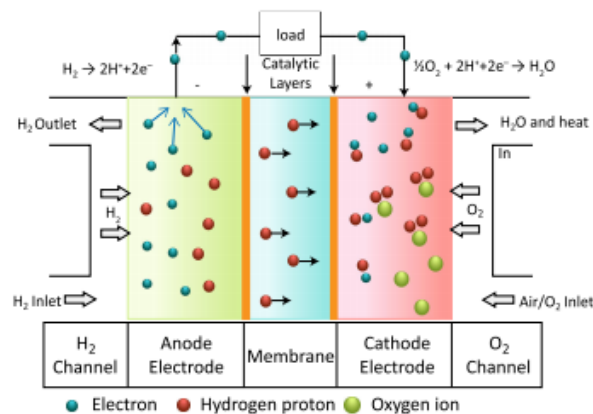
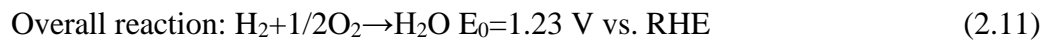
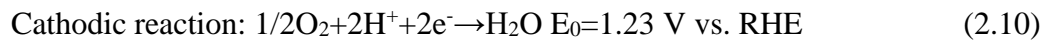
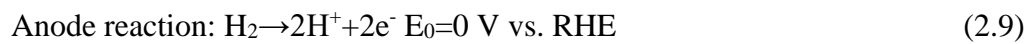


**Figure 1-5.** A schematic diagram of a PEMFC.

Improving the performance and durability of PEMFCs and reducing the production cost are the main problems facing their commercialization [31-33]. However, developing an ideal fuel cell is not an easy task because naturally durable materials are expensive, and low-cost materials often fall short of the battery's durability standards. In order to improve performance while keeping costs low, people tend to follow one or even multiple research lines [34, 35]. This can be summarized as: (1) reduce the loading of

electrocatalysts in both anode and cathode, (2) development of new nano-thin film Pt catalysts (such as 3M s nano-thin film (NSTF) electrodes), (3) reduce the size of electrocatalyst nanoparticles, (4) reduce the dependence on platinum by developing metal alloys (binary and ternary) and platinum-free electrocatalysts, (5) using a new preparation method to improve the dispersibility of electrocatalysts, (6) develop membrane electrode device (MEA) fabrication methods to enable better dispersion and utilization of catalysts, (7) adopt a new technique to increase the mass transport on the FC electrode, and (8) improve the performance of carbonaceous electrocatalyst supports and explore new non-carbonaceous electrocatalyst support materials [36-41].

### **2.3 Development of precious metal based catalyst for ORR, OER and HER.**

To date, the widely used electrocatalysts are mainly precious metal based catalysts for ORR, OER and HER , such as platinum-based catalysts for ORR, IrO<sub>2</sub> catalysts for HER *etc* [42- 44]. Although this kind of precious metal based electrocatalysts exhibits superior catalytic performance, it is notable that they also suffer disadvantages of insufficient reserves, high price and relatively low stability that hampered the industrial application of these renewable energy storage and conversion device [45]. Therefore, seeking for highly efficient electrocatalysts with low price and abundant reserves to substitute for precious metal based catalysts is highly desirable. On the other hand, designing and developing new types of precious metal based electrocatalysts with high efficiency and low precious metal atoms usage is highly demand. Tremendous studied have been conducted on developing new high efficiency noble metal electrocatalysts

from the following points [46]. Increasing the number of exposed platinum atoms on surface of the catalyst while avoiding coating of surface platinum atoms. In addition, by tuning the electronic structure of the Pt site, the binding energy between the oxidation-related species and the Pt atom can be weakened, thereby increasing the rate of the oxygen reduction reaction [47]. So far, researchers have reported many methods to expose more surface platinum atoms and tune their electronic structures. The essence of the catalytic reaction is a surface reaction, so only the platinum atoms on the surface can be used as active sites. On the other hand, while ensuring the exposure of precious metal active sites as much as possible, how to maximize the intrinsic activity of the active sites is another important issue. From the perspective of geometric configuration, the inter-planar spacing of Pt atoms is changed by alloying and core-shelling to promote the adsorption of intermediate products, while the size effect of alloying eliminates material stress or ligand effect and improves the stability of alloy catalysts [48-53]. It is known that the d-band density of states (DOS) is structure-sensitive and varies in different crystal structure planes due to the fact that the Pt atoms in each crystal plane have different coordination numbers that leads to the different the d-band width. At present, there are four main methods to improve the surface structure characteristics of Pt-based catalyst materials [54] as list in Figure 1-7: (i) Control the shape and crystal face of Pt noncrystalline to expose as much as possible. (ii) In-depth study of platinum-based alloy materials, especially with special morphology; (iii) functional modification of the surface of Pt nanoparticles is also a commonly used method. (iv) Reasonable selection of catalyst supports is of great help in improving the catalytic activity and

stability of the material. Kim [55] *et al.* successfully synthesized dendrite Pt supported on Pd nanocrystals, and obtained a Pd-Pt alloy-based catalyst material with large specific surface area and high oxygen reduction activity, which showed higher performance than equivalent Pt. The catalytic activity of the content of commercial Pt/C is 2.5 times. Elezovic [56] *et al.* used tungsten as a carrier and supported Pt nanoparticles on tungsten by borohydride reduction. The Pt/W catalyst material synthesized by this method showed better electrochemical activity compared with Pt/C especially. The above methods are all committed to decreasing the addition of Pt without affecting the catalytic activity and stability, but in the long run, reducing the amount of Pt blindly is only a temporary solution [57]. Focusing on the development of low-cost and abundant non-precious metal catalyst as oxygen reduction catalyst materials is the solution to the root cause.

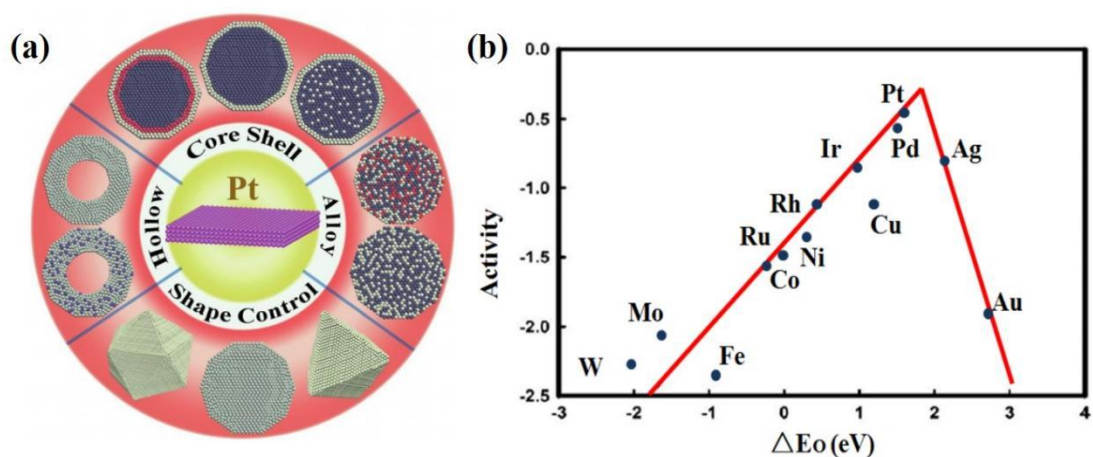


**Figure 1-7.** The important new progress in the development of Pt-based electrocatalysts. Theoretically calculated plotted against  $O^*$  adsorption energy of various kinds of metal for ORR. Reprinted with permission from ref [23]. Copyright 2020 American Chemical Society

## 2.4 Carbon based efficient electrocatalysts.

Carbon is the most ubiquitous element in nature which is closely related to human



production and life. Furthermore, it has various electronic orbital includes  $SP$ ,  $SP_2$ , and  $SP_3$  hybridization *etc*, that could bring about the anisotropy of crystals and other anisotropic nature of the arrangement. On this basis, a variety of new carbon materials have emerged. In fact, no single element can form as many different structures and properties as carbon, such as three-dimensional diamond crystals, two-dimensional graphite sheets, one-dimensional carotene and carbon nanotubes, zero-dimensional fullerene molecules, *etc* [58] as shown in Figure 1-8. Carbon materials are low-cost and they have a wide range of sources in nature, at the same time, carbon materials have variable and adjustable electronic structures, making them widely used in various fields. It is widely used in energy materials due to its good electrochemical properties [59].

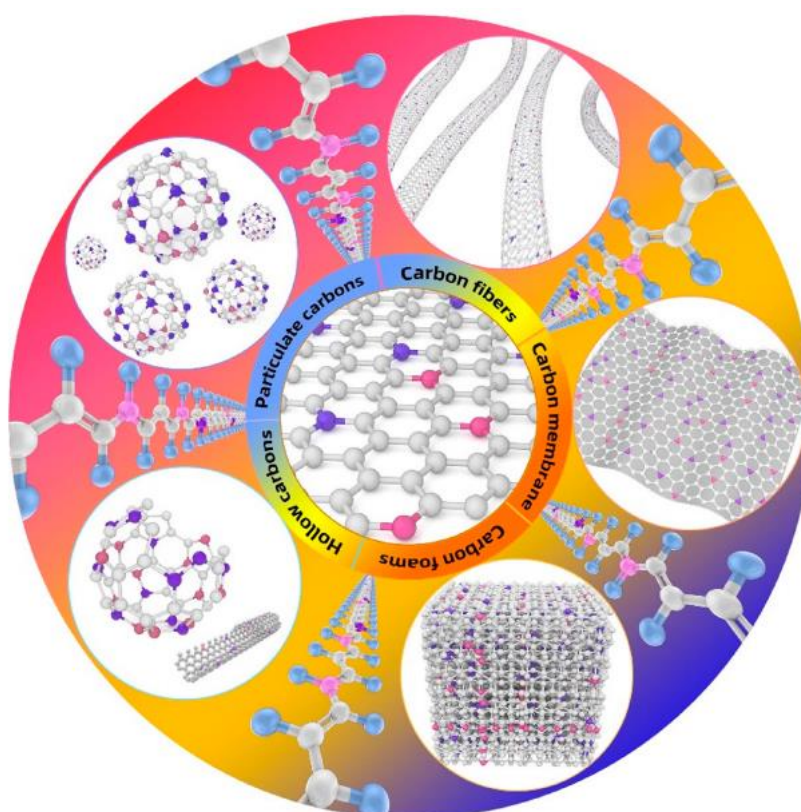


**Figure 1-8.** Recent development of carbon materials with different morphologies.

#### **2.4.1 Heteroatoms doped carbon materials.**

Chemical doping is one of the most widely used methods for tuning electronic structures of carbon matrix [60, 61]. This endows carbon materials with tunable functionalities for electrocatalysis, energy storage and conversion technologies. In recent years, the research of heteroatoms doped carbon materials as highly efficient electrochemical catalysts has attracted researcher's extensive attention.

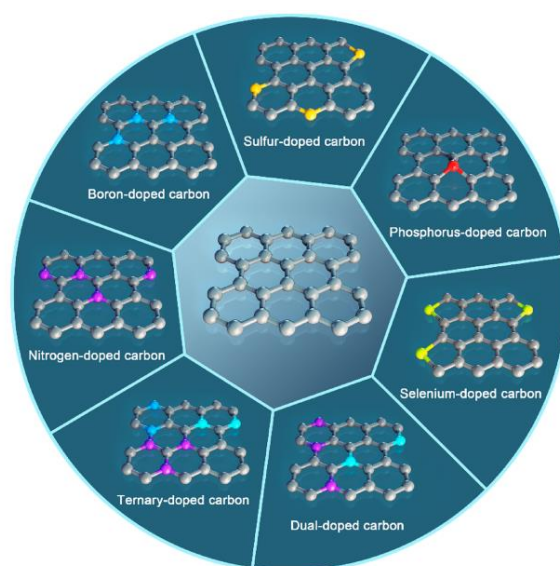


**Figure 1-9.** Schematic diagram of various heteroatom-doped carbon materials.

As shown in Figure 1-9, all these kinds of carbon materials could be selected as the ideal matrix to prepare heteroatoms doped carbon materials [62-63]. To date, the most widely studied heteroatoms includes nitrogen (N), sulfur (S), phosphor (P), boron (B), fluorine (F) *etc* [64]. Due to the fact that the incorporation of heteroatoms on carbon matrix could cause the distribution of electronic and energy band gap of surrounding carbon atoms, which produces significant influence on the conductive form of the carbon matrix, inducing the increase of the number of free carriers. Furthermore, the doping of heteroatoms in carbon matrix causes the formation of defects that combined with doping atoms can cause spin redistribution to generate new and more excellent

electrochemical properties, such as enhanced electrocatalytic activity, stability, and resistance to CO toxicity that can be widely used in electrocatalytic field [65]. Especially for ORR, the positive charge generated by doped atoms inside the carbon matrix will affect the chemical sorption mode of O<sub>2</sub>, and the smooth absorption of electrons from the anode is beneficial to increase the whole process of oxygen reduction reaction, see Figure 1-10 [66]. In general, heteroatoms doping can adjust the electronic properties of carbon matrix via tuning their electronic structures, which makes heteroatoms doped carbon materials widely used in many fields.

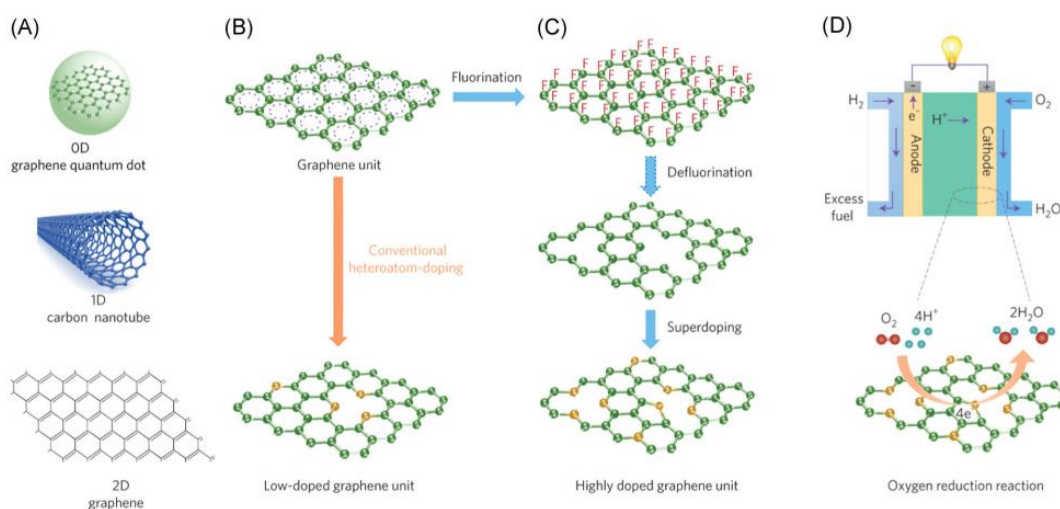


**Figure 1-10.** Superdoping low-dimensional graphene materials. (A) Examples of low-dimensional graphene materials, including a zero-dimensional (0D) graphene quantum dot, a 1D carbon nanotube, and 2D graphene. (B) Conventional heteroatom-doping of the graphitic honeycomb network consisting of conjugated alternating C–C single and C=C double bonds with delocalized electrons (represented by the blue dotted rings; omitted in the subsequent structures for clarity). Carbon atoms are shown in green and dopant atoms in yellow. (C) Superdoping of the conjugated graphitic honeycomb network through fluorination, followed by defluorination in the presence of a heteroatom dopant source. Defluorination and superdoping occur simultaneously. (D) Heteroatom-doped graphene materials as metal-free electrocatalysts for the oxygen reduction reaction at the cathode of a fuel cell (reproduced with permission from ref, 66 copyright 2016 to Macmillan Publication Ltd) (reproduced with permission from ref, 66 copyright 2016 to Macmillan Publication Ltd).

## 2.4.2 Nitrogen-doped carbon materials as electrocatalysts

As the nearest atom to C atom in the periodic table, nitrogen atom act as the most popular doping elements for carbon-based catalysts, which is the main reason why C-N bonds have similar bond lengths to C-C [67]. Almost the same bond length greatly reduces the distortion of the carbon grid caused by the nitrogen-doped carbon substrate, and maintains the original carbon structure as much as possible. On the other hand, N exhibits the higher electron negativity than that of C, and thus a higher electron density is enriched around nitrogen atoms, which provides good conditions for adjusting the electronic structure of carbon atoms by nitrogen atom doping. A series of heteroatom doping (N, B, S, O, P, *etc.*) carbon nanomaterials have been reported and attracted great interest [68, 69]. Among various heteroatom-doped carbon materials, N-based heteroatom-doped catalyst is considered to be the most promising catalyst due to its strong electronegativity and excellent electron accepting ability, resulting in increased oxygen adsorption or/ and subsequent OO bond cleavage [70].

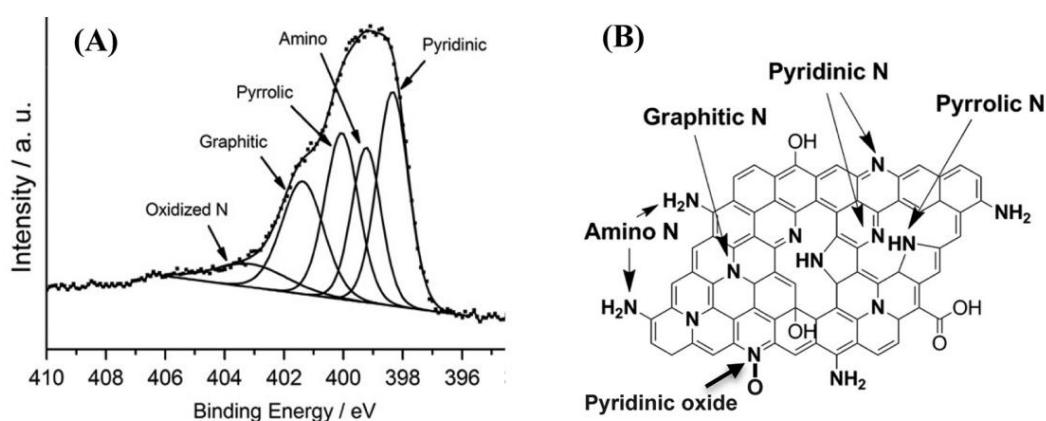


**Figure 1-11.** (A) Typical N 1s XPS spectrum and their specific location of four N types (B). Reproduced with permission from ref 47. Copyright 2013 Elsevier.

Nitrogen-doped carbon materials have become a research hotspot due to their unique

properties. Through XPS analysis, it is found that usually the full spectrum of N 1s includes the following four peaks: Pyrrolic N ( $N_{PY}$ ), Pyridinic N ( $N_P$ ), Graphical N ( $N_G$ ), Oxidized N ( $N_O$ ), and four peaks [71] (as shown in Figure 1-11). Pyridine nitrogen or  $N_P$  refers to located at the edge of carbon matrix. Studies have also shown that the more graphitic nitrogen contained in carbon materials, the better the catalytic activity for ORR [72]. In addition, when the carbon material containing pyridine nitrogen is used as a catalyst support, the lone electron pair of pyridine nitrogen can also effectively "anchor" noble gold. It belongs to nanoparticles (such as Pt NPs) and can change the nucleation process of the catalyst, so that it can be firmly supported on the carbon support with a smaller particle size [73].

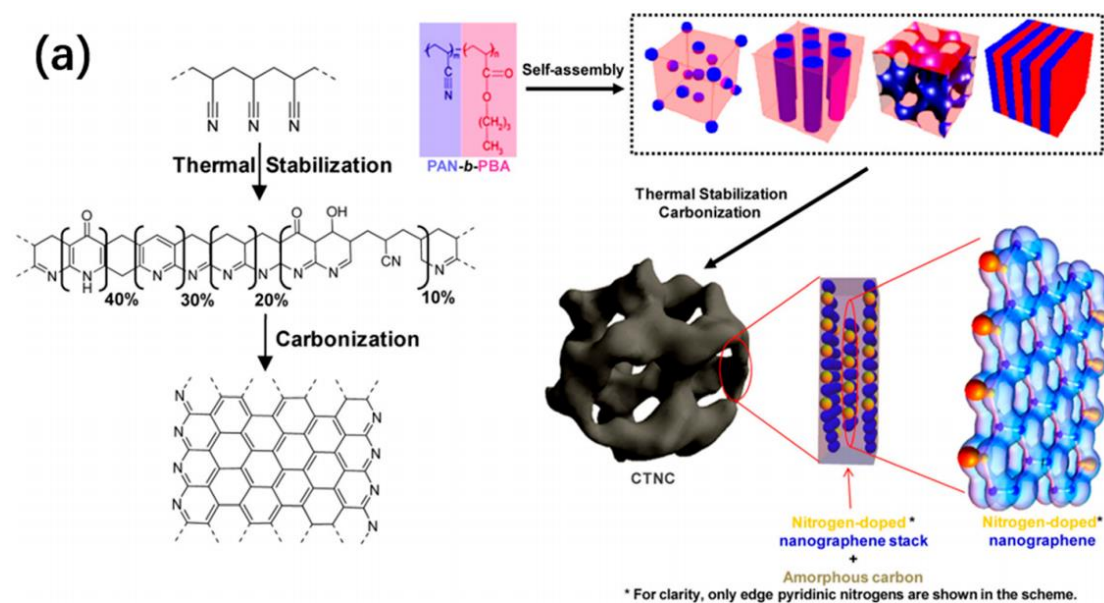


**Figure 1-12.** (a) Schematic diagram of the synthesis process of N-doped carbon electrocatalysts. Reproduced with permission from ref 43. Copyright 2012 American Chemical Society.

The application of N-doped carbon materials in fuel cell electrocatalysis mainly focuses on two aspects: as a support for noble metal catalysts. Shukla [74]; Roy [75] and his team also found that nitrogen doping can effectively promote the catalytic performance

of DMFC in 1996. Therefore, the research on nitrogen-doped carbon materials has attracted extensive attention and made breakthrough progress. The importance of the existing form of N in the material is self-evident as present in Figure 1-12. In a nitrogen-doped catalyst material, the four types of N with different bonding structures generally coexist, but with different contents of each N species. Meanwhile,  $N_P$ ,  $N_{PY}$  and  $N_G$  are now generally believed to affect the catalytic activity of nitrogen-doped carbon material catalysts for ORR greatly. Especially, pyridinic-N is the most popular one among all these N types [76], but some other scholars also believe that graphite-N may be the efficient active sites for electrocatalysis. Therefore, researchers have carried out a series of study based on designing various types of heteroatoms doped carbon catalysts. Such as, Wang *et al.* prepared N-doped porous carbon materials possess superior high-temperature oxidation stability [77]. The experimental results show that the nitrogen-doped porous membrane material can be stored in a butane flame for at least 60 seconds, and the temperature can reach about 1300 °C. Based on this, Antonietti *et al.* have called it the nobility of antioxidant materials in their published review article [78]. At the same time, the theoretical calculation results show that the nitrogen doped carbon material enriches more positive charges near the carbon atom, which makes the binding energy of O higher than that of in nitrogen doped carbon material, which is beneficial to the ORR conduct as present in Figure 1-13.



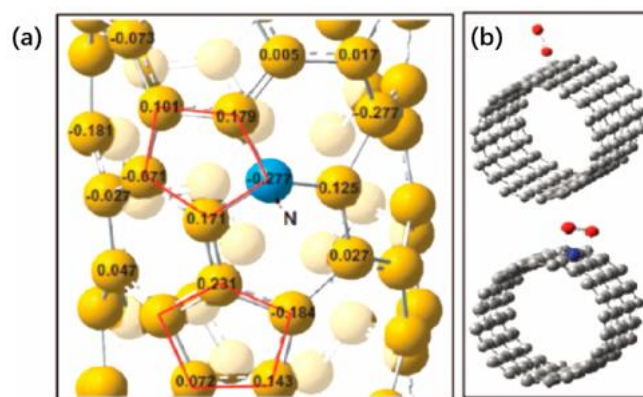


**Figure 1-13.** (a) Charge density distribution of N-doped carbon nanotubes from theoretical calculation. (b) Two typical O<sub>2</sub> adsorption mode from end-on to side-on. Reprinted with permission from ref 35. Copyright 2009, AAAS.

Related research result show that doping nitrogen atoms can endow the carbon substrate with a larger work function, which means that the doped carbon substrate is more likely to accept electrons instead of donating electrons. According to the phenomenon of Mott-Schottky effect that the electrons are inevitably enriched near the nitrogen-doped carbon during the reaction, and this electron interaction is described as the [79]. Therefore, N-doped carbon materials are considered as cheap and readily available materials that can replace traditional noble metal electrocatalysts, and can also become excellent substrate materials.

### 2.4.3 Heteroatoms Co-doping doped carbon materials in electrocatalysts

#### 2.4.3.1 N, S co-doped carbon materials as highly efficiency electrocatalysts

In the periodic table of elements, sulfur is located just below nitrogen. The doping of sulfur atoms into carbon matrix also has certain advantages similar to N doping. Meanwhile, unlike nitrogen atoms with high electronegativity compared to carbon atoms, sulfur atoms have electronegativity similar to that of carbon atoms. However, it is worth noting that the C-S bond length is 25% longer than that of C-C bond length, this unique structure makes the sulfur atom becomes the preferred heteroatom for carbon five-membered rings [80]. Even in other cases, twisted aromatic systems can be

formed to some extent by virtue of the SP<sup>2</sup> structure. In addition, when the content of sulfur atoms in the carbon substrate is too high, the carbon structure is promoted to form ribbons, which means that the sulfur atoms are beneficial to terminate the edge extension to a certain extent. DFT results show that the doped S atoms could open the energy band gap of carbon substrates, and sulfur doping can also induce charge polarization and increase the conductivity of sulfur-doped carbon materials that endows them act as suitable anode materials [81]. For example, Huang *et al.* reported that N, S co-doped carbon materials exhibit high catalytic performance than that of nitrogen-doped carbon materials in sodium-ion batteries, which is mainly due to the fact that N, S co-doping on carbon matrix bring about more rearrangement of electronic structure than that of N doping (Figure 1-14) [82, 83]. The larger inter-layer spacing is more conducive to the shuttle of sodium ions, thus bringing about higher performance of sodium ion batteries. When sulfur atoms are doped at the edge of the carbon substrate, it will cause an increased charge and spin densities, based on which adjacent carbon atoms located at zigzag edges or doped sulfur oxides are considered to be the most efficient catalytically active sites, which also have large spin or charge densities. On the other hand, S atoms exhibits the big atomic radius of is considered to be mismatched with the outermost orbital of C, resulting in uneven spin density distribution and increased catalytic performance [84]. Besides, the polarization of the bond of S-C may greatly enhance the binding ability between catalyst surface and intermediates that further promote the electrocatalytic process.



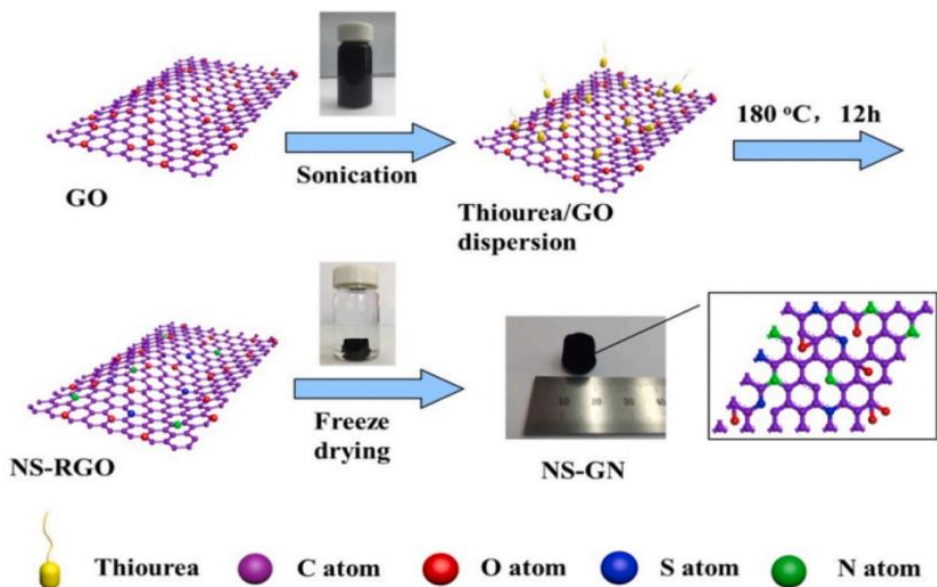


**Figure 1-14.** The flow chart of preparation of N, S-doped CNTs (or rGO).

#### 2.4.3.2 N, P co-doped carbon materials as highly efficiency electrocatalysts

Phosphorus atom, as an element in group V elements of the periodic table, has a similar binding shell electron configuration to nitrogen atom, which has attracted extensive attention of researchers [85-86]. The development of phosphorus-nitrogen co-doped carbon materials has made great progress these years. However, it is worth noting that the phosphorus atom has an empty 3d orbital, and the atomic radius of this atom is higher than that of the C. [87-89]. More importantly, mismatched bond lengths can lead to severely distorted results on carbon substrates, but the lesser electronegativity of phosphorus atoms can also cause charge redistribution between them and carbon atoms. [89]. These results are consistent with a study by Wang's group in which "protruding" type P-doped graphene exhibited better performance than N-doped graphene in sodium batteries (Figure 1-15). According to their DFT calculations, the P-doped metallic properties of graphene remain largely unchanged after Na adsorption, which leads to fast electron transport insertion and extraction during Na ion process [90].

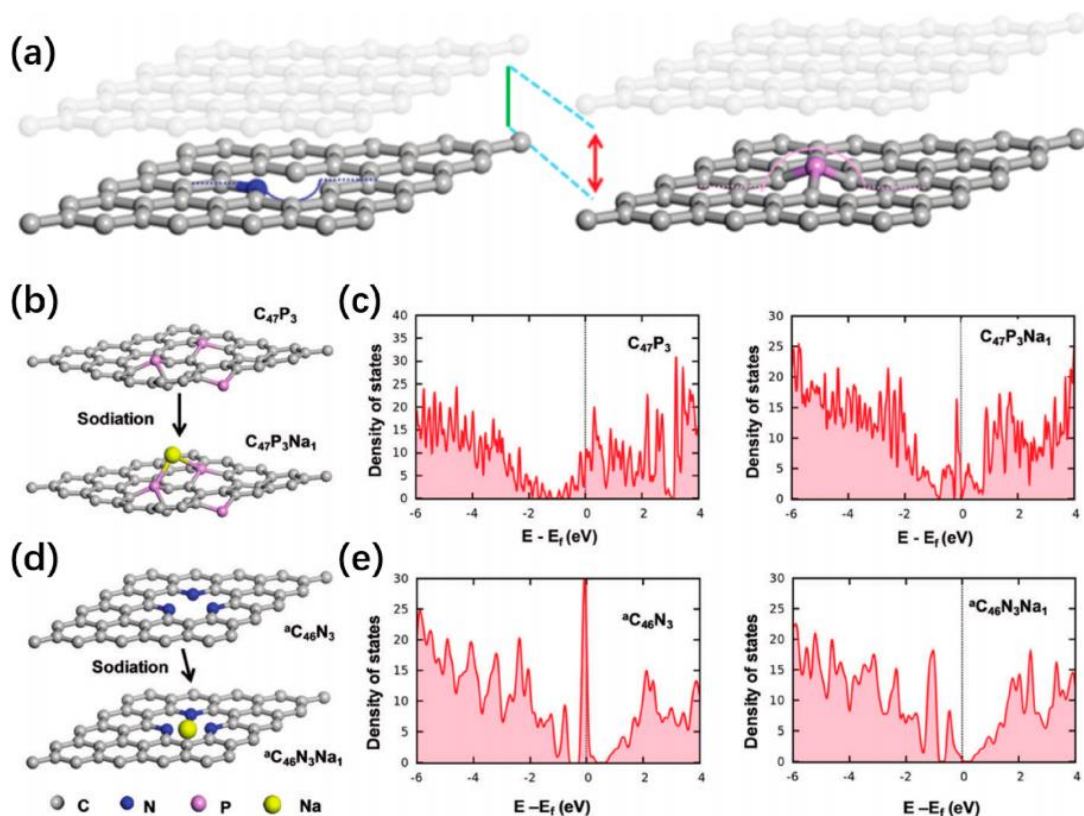


**Figure 1-15.** (a) The constructed model of graphene with pyridinic N and P doping. (b, d) Schematic illustrations of P-doped states in graphene before and after sodiation. (c, e) Partial density of states (PDOS) of P-doped states in graphene before and after sodiation. Reproduced with permission from ref 49. Copyright 2017 Royal Society of Chemistry.

On the other hand, heteroatoms N, P co-doped metal-free carbon materials with synergistic effects of dopants is one of the most promising none precious-metal catalysts for oxygen redox reaction due to their competitive activity and no concerns on potential detrimental impact of dissolved metal species from transition metal based electrocatalysts.

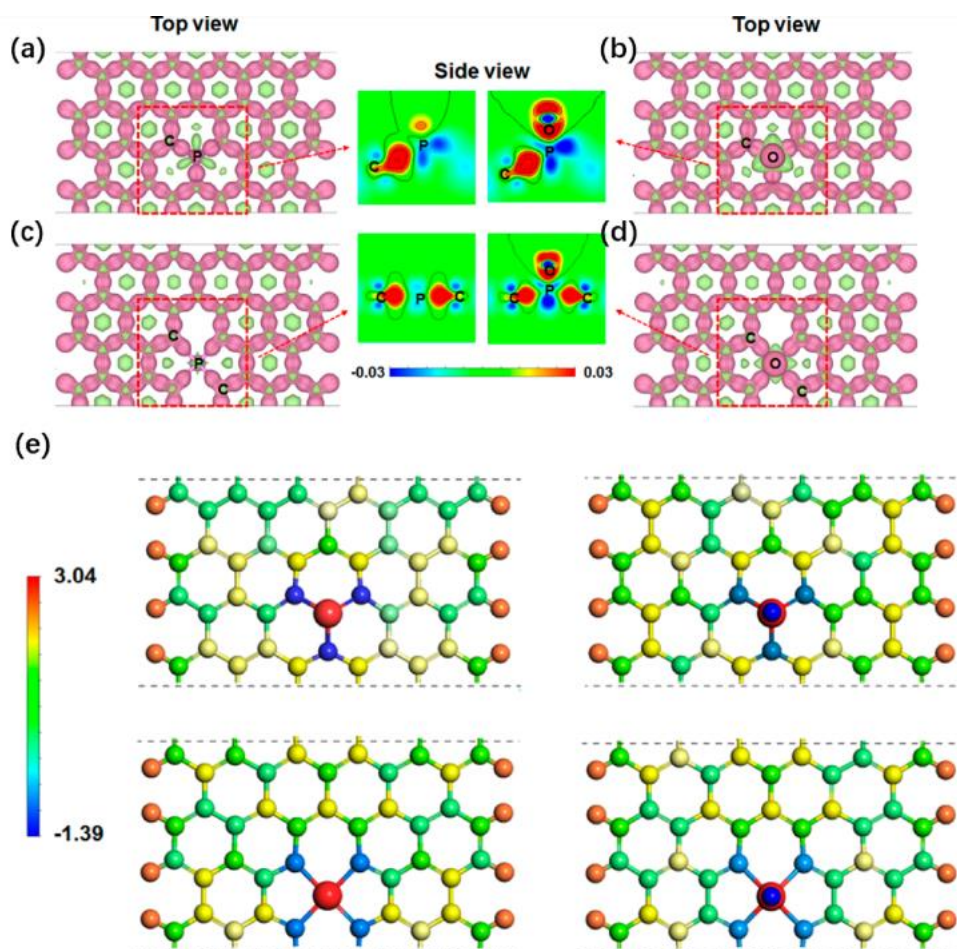


**Figure 1-16.** Deformation electronic density of hypothetical (a) PC3G, (b) OPC3G, (c) PC4G, and (d) OPC4G. (e) Bader charges of the constructed models. Reproduced with permission from ref 232. Copyright 2017 American Chemical Society.

Researchers proposed an effective active sites engineering strategy of bottom-up synthesized N, P co-doped graphene (NPG) nanosheets with 1,3-Diaminobenzene as adjustable N-containing precursor platform, phytic acid was selected as P source (Figure 1-16). It is worth noting that the superior electrocatalytic performance mainly derived from the optimization of intermediates energy in each reaction pathway in the specific configurations constructed by N and P dopants.

#### 2.4.3.3 N, B co-doped carbon materials as highly efficiency electrocatalysts

Compared with traditional pure carbon materials as substrates, boron-doped carbon materials show great advantages, which not only greatly improve the electrocatalytic

activity, but also greatly improve the stability of the catalysts. Due to the direct Pt-B interaction and the high stability of the nanorods [92-96].

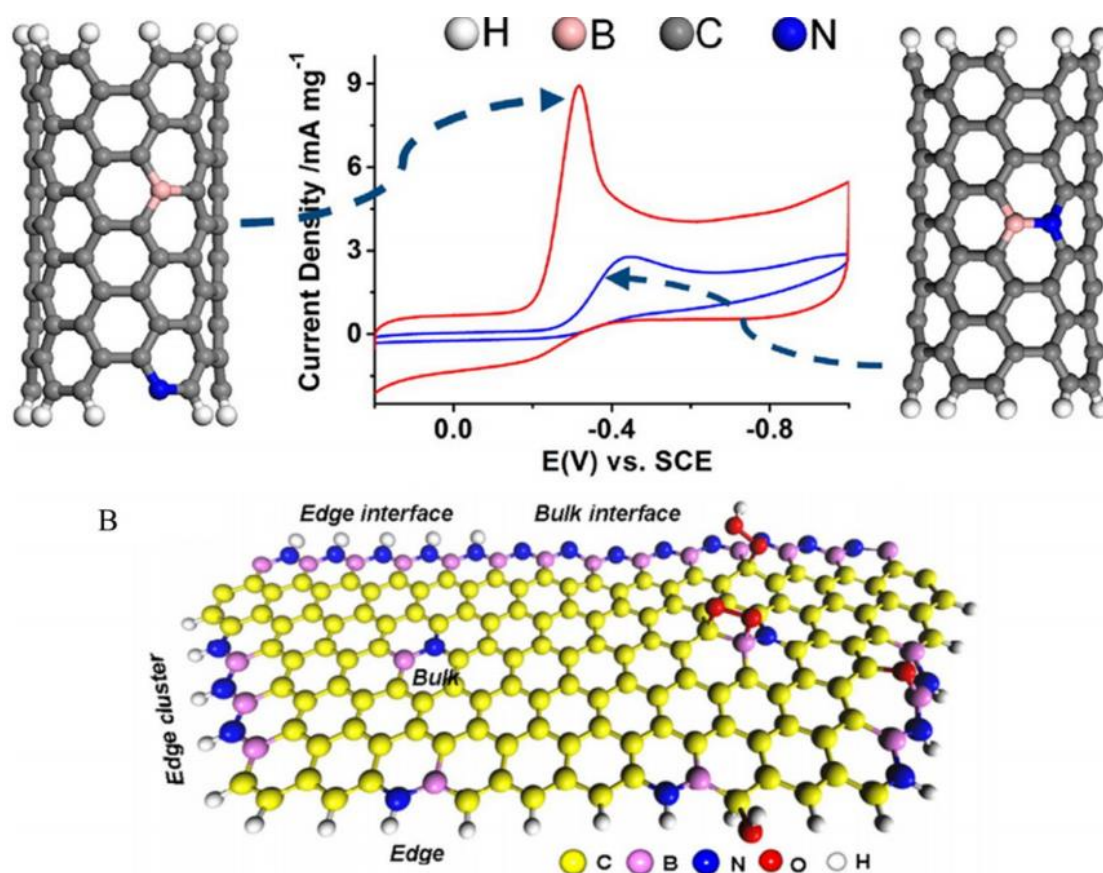


**Figure. 1-17.** Illustration of different N, B configurations and their catalytic performance for ORR. (Reprinted with permission from Ref. 48. Copyright 2015 American Chemical Society)

At the same time, the boron-doped carbon material also exhibits excellent electrocatalytic selectivity and good anti-poisoning ability. In order to deeply study the internal mechanism of the increased catalytic activity brought about by boron doping, the researchers performed theoretical calculations, which showed that the enhanced catalytic activity should be attributed to the synergistic effect between boron and nitrogen [97-99]. In addition to the carbon materials doped with boron atoms alone, the carbon materials co-doped with boron and nitrogen have also attracted extensive attention of researchers. For example, researchers such as Ozaki used melamine



carbonized polymer particles and boron trifluoride as reactants to obtain very interesting boron-nitrogen co-doped carbon materials as efficient point catalysts [100].

The carbon materials showed more

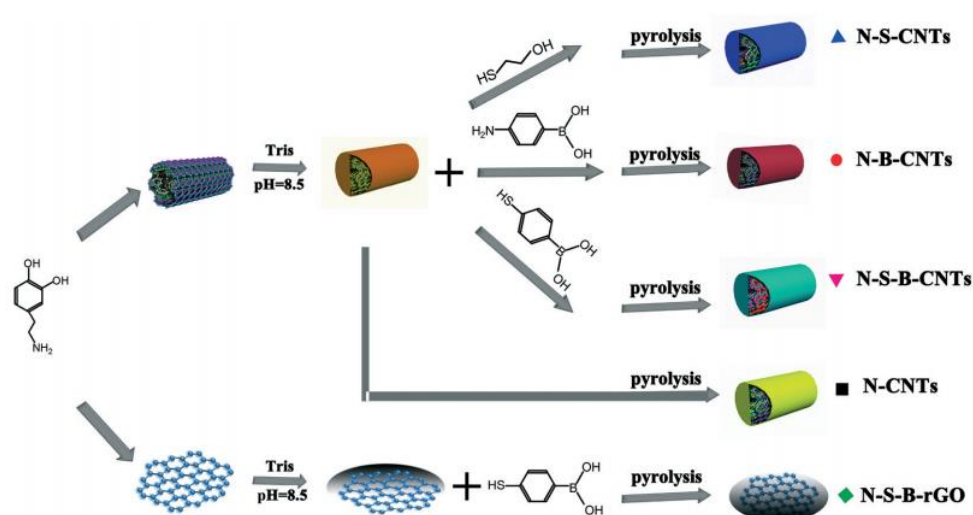


**Figure 1-18.** The diagrammatic sketch of the N, B co-doped graphene materials by one-pot hydrothermal route [51]. Copyright (2020) Elsevier.

Excellent catalytic activity than the nitrogen-doped carbon materials alone. However, it is worth noting that the catalytic activity exhibited by the boron-nitrogen co-doped carbon material still has a certain gap with the traditional platinum-based noble metal catalyst. The key factor is the adjustment of the BNC configuration. In the process of pyrolysis, the BNC configuration cannot be controlled, and there are few studies on this aspect at present. With the deepening of research, if the BNC configuration can be specifically studied and accurately controlled, the boron nitrogen co-doped, the performance of carbon materials is expected to be further improved. Researchers strengthen their study by performing direct comparative measurements on pure N-doped, pure B-doped and B,N-co-doped carbons, all derived from the same precursor,

which once again demonstrate that doping of boron has a significant effect on the electrochemical catalytic activity of carbon materials plays a crucial role as list in Figure 1-18. For example, directly bonded boron and single atoms do not seem to bring the desired catalytic effect. Based on this, Woo *et al.* used a chemical vapor deposition synthesis method to prepare a high-efficiency B-N co-doped carbon catalyst system with a precursor composed of dicyandiamide and boric acid, although it was observed that boron-nitrogen co-doping can indeed lead to higher catalytic activity, but the level of this activity is closely related to the type of B-N doping.

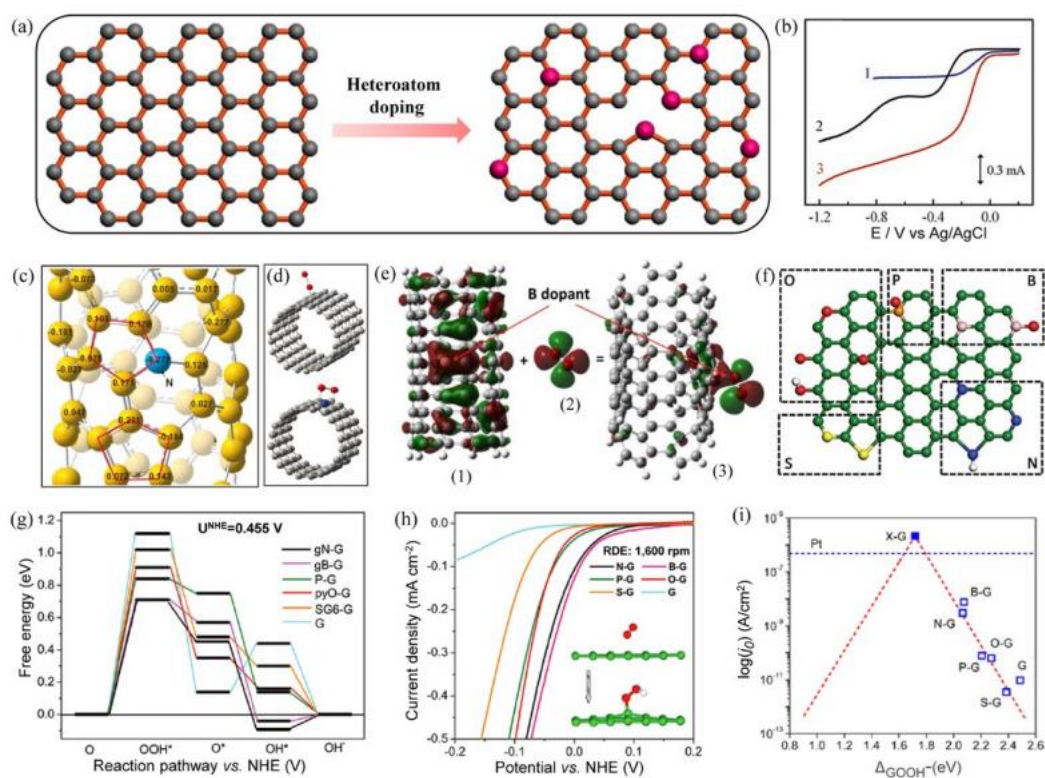


**Figure 1-19.** The diagrammatic sketch of heteroatom doping on carbon matrix. Copyright 2014, American Chemistry Society.

The researchers further extended the application of boron-nitrogen co-doped carbon materials to two widely used allotropes of carbon: graphene and carbon nanotubes as present in Figure 1-19. Especially with regard to boron-nitrogen co-doped carbon

nanotubes, Dai *et al.* reported a method to synthesize boron-nitrogen double-doped carbon nanotubes with a vertical array structure using melamine diborate as a single precursor by vapor deposition acid treatment of the metals applied during the reaction [101]. XPS results showed that the as-synthesized boron-nitrogen co-doped carbon nanotubes had no traces of metal residues. Excitingly, the boron-nitrogen co-doped carbon nanotube material with a vertical array structure exhibits very excellent electrocatalytic activity, which even exceeds that of the comparative platinum-carbon catalyst. This result clearly shows that boron-nitrogen co-doping has great potential for application. The results of Hu *et al.* further elucidate the B-N co-doping synergistic effect in more detail [102]. Based on this, the authors prepared two species of co-doped carbon nanotubes. One method is chemical vapor deposition by direct incorporation of boron and subsequent introduction of additional nitrogen atoms in ammonia, maintaining a previously established boron binding site. On the contrary, when the doping sites of boron and nitrogen are in the meta-position, the catalytic activity shows a gradual upward trend. These findings suggest that the configuration of the boron-nitrogen doping site is very sensitive to the catalytic activity. For both elements, boron and nitrogen, due to the opposite electronegativity properties of the two dopants, their effects can compensate each other. To achieve the optimization of the direct synergistic effect of boron and nitrogen. It can be concluded that boron-doped carbon materials represent a promising class of high-efficiency electrocatalyst candidates. The results discussed throughout this article are self-explanatory, and based on extensive research experience, the synergistic effect between the two can be optimized by trying different

synthetic methods and precisely tuning the configuration between the two elements.

## **2.5 Development status and problems to be solved for heteroatom-doped carbon materials.**

In recent years, people have explored the incorporation of various heteroatoms into carbon materials to change the properties of electron donors or electron acceptors, thereby changing or improving capacitance or catalysis. Especially for nitrogen act as the most attractive doping element that tune electronic structure therefore tuning electrocatalysts' electrochemical properties. This is because nitrogen doping can generate local strains in the carbon hexagonal network, leading to the formation of structural defects, and the additional lone pair electrons of nitrogen can bring negative charges to the delocalized structure of the  $Sp^2$ -hybridized carbon network, which promotes the electron transport properties and electrochemical reactivity of carbon materials (Figure 1-20). In spite of tremendous efforts have been made on theoretical and experimental exploration for synthesizing highly efficient heteroatoms doped metal-free electrocatalyst for ORR, OER and HER, they still suffer from low catalytic activity compared with transition metal based nitrogen doped carbon materials (M-N-C) and precious metal-based counterparts [103-106]. And the unclear correlation between N and other heteroatoms configurations and their electrocatalytic activity and selectivity for water-cycled reactions is a bottleneck for developing highly efficient and functional-oriented heteroatoms co-doped electrocatalysts.



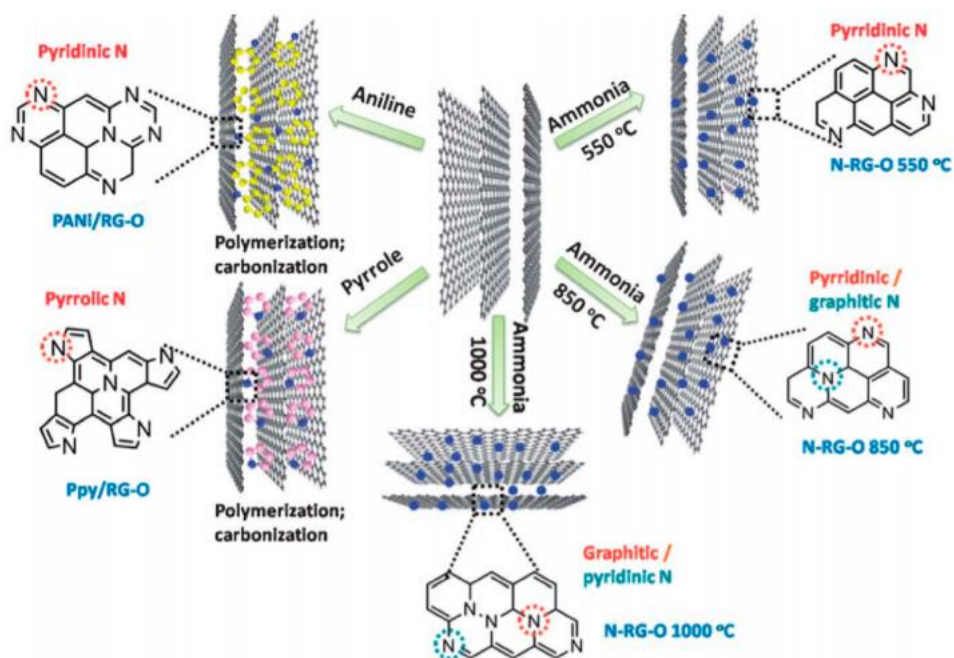


**Figure 1-20.** Surface doping of graphene materials with certain polymer precursors and temperatures. Reproduced with permission from ref 91. Copyright 2012 Royal Society of Chemistry.

It is known that the electrocatalytic performance of these materials depends to a large extent on the structure and composition of the materials. This in turn depends on the carbon precursor and synthesis conditions used to make the material, as well as the presence or absence of metals during synthesis. However, more research is still needed to identify the exact catalytic active site responsible for its catalytic performance and to explore the effect of different parts of the material, including possibly trace metals, on its catalytic activity. More research is needed to improve the electrocatalytic performance (activity, stability, and selectivity) of the material.

## 2.6 Summary and Perspective

Heteroatom-doped metal-free carbon materials are widely used in fuel cells and various other electrocatalytic reactions due to their excellent catalytic properties that attracted people's wide attention around the world. Summarizing the previous research

experience, we can know that the catalytic activity of heteroatom-doped non-metallic carbon materials as electrocatalysts depends on the elemental composition and structural characteristics. At the same time, the synthesis conditions and synthesis strategies of catalyst materials have a great influence on the catalytic active site, and the configuration of the active site is the decisive factor to determine the final catalytic activity. Heteroatom doped metal-free carbon materials is one of the most promising substitutes for precious-metal catalysts for ORR, OER and HER in electrochemical energy conversion devices such as fuel cells and metal-air batteries due to their competitive activity, excellent durability and satisfactory cost. One direct reason is lacking for elucidating the relationship between polymer precursors and active sites configurations and clarifying synergistic effects of multi-heteroatom induced hybrid active species in metal-free catalysts. This issue seriously impedes the development of scientific molecular-level design strategy for synthesizing highly efficient metal-free catalysts. Topics that are going to be explored are shown as follows.

(a) To discover the ways to control the N specific as effective sites in nitrogen doped carbon materials for ORR.

(b) To explore the intrinsic relationship between specific N species coordinated with other heteroatoms and tuning the electrocatalytic activity of co-doped carbon-based metal free electrocatalysts for the three important reactions in energy conversion technologies.

(c) Providing a new insight and effective strategy for engineering the desired coordination environment and tuning the geometric and electronic structures of

catalytic sites in single atomic carbon materials for electrochemical energy conversions and storage applications.

## Reference

- (1) Paraknowitsch, J. P.; Thomas, A. *Energy Environ. Sci.* 2013, 6, 2839–2855.
- (2) Gawande, M. B.; Fornasiero, P.; Zboril, R. *ACS Catal.* 2020, 10, 2231–2259.
- (3) Zhao, D.; Zhuang, Z.; Cao, X.; Zhang, C.; Peng, Q.; Chen, C.; Li, Y. *Chem. Soc. Rev.* 2020, 49, 2215–2264.
- (4) Zheng, B.; Lin, X.; Zhang, X.; Wu, D.; Matyjaszewski, K. *Adv. Funct. Mater.* 2019, 1907006.
- (5) Zhou, Y. Q.; Sharma, S. K.; Peng, Z. L.; Leblanc, R. M. *Polymers* 2017, 9, 67–86.
- (6) Wood, K. N.; O’Hayre, R.; Pylypenko, S. *Energy Environ. Sci.* 2014, 7, 1212–1249.
- (7) Gottlieb, E.; Matyjaszewski, K.; Kowalewski, T. *Adv. Mater.* 2019, 31, 1804626.
- (8) Gottlieb, E.; Matyjaszewski, K.; Kowalewski, T. In Dai, L., Ed.; *Chem. Soc. Rev.* 2020, 8, 30.
- (9) Ma, T. Y.; Liu, L.; Yuan, Z. Y. *Chem. Soc. Rev.* 2013, 42, 3977–4003.
- (10) Yang, W. P.; Li, X. X.; Li, Y.; Zhu, R. M.; Pang, H. *Adv. Mater.* 2018, 31, 1804740.
- (11) Liang, C. D.; Li, Z. J.; Dai, S. *Angew. Chem., Int. Ed.* 2008, 47, 3696–3717.
- (12) Chai, G. S.; Shin, I. S.; Yu, J. S. *Adv. Mater.* 2004, 16, 2057–2061.
- (13) Baumann, T. F.; Satcher, J. H. J. *Non-Cryst. Solids* 2004, 350, 120–125.
- (14) Wan, Y.; Shi, Y. F.; Zhao, D. Y. *Angew. Chem., Int. Ed.* 2008, 20, 932–945.
- (15) Wan, Y.; Yang, H. F.; Zhao, D. Y. *Acc. Chem. Res.* 2006, 39, 423–432.
- (16) Li, Z. J.; Jaroniec, M. *J. Am. Chem. Soc.* 2001, 123, 9208–9209.

- (17) Yoon, S. B.; Chai, G. S.; Kang, S. K.; Yu, J. S.; Gierszal, K. P.; Jaroniec, M. *J. Am. Chem. Soc.* 2005, 127, 4188–4189.
- (18) Jang, J.; Lim, B. *Adv. Mater.* 2002, 14, 1390–1393.
- (19) Kyotani, T.; Tsai, L. F.; Tomita, A. *Chem. Mater.* 1996, 8, 2109–2113.
- (20) Li, J.; Papadopoulos, C.; Xu, J. M.; Moskovits, M. *Appl. Phys. Lett.* 1999, 75, 367–369.
- (21) Lee, J.; Sohn, K.; Hyeon, T. *J. Am. Chem. Soc.* 2001, 123, 5146–5147.
- (22) Oda, Y.; Fukuyama, K.; Nishikawa, K.; Namba, S.; Yoshitake, H.; Tatsumi, T. *Chem. Mater.* 2004, 16, 3860–3866.
- (23) Han, L.-N.; Wei, X.; Zhu, Q.-C.; Xu, S.-M.; Wang, K.-X.; Chen, J.-S. *J. Mater. Chem. A* 2016, 4, 16698–16705.
- (24) Kyotani, T. *Carbon* 2000, 38, 269–286.
- (25) Han, S. J.; Hyeon, T. *Chem. Commun.* 1999, 1955–1956.
- (26) Han, S. J.; Sohn, K.; Hyeon, T. *Chem. Mater.* 2000, 12, 3337–3341.
- (27) Wang, Z. Y.; Li, F.; Ergang, N. S.; Stein, A. *Chem. Mater.* 2006, 18, 5543–5553.
- (28) Han, S.; Lee, K. T.; Oh, S. M.; Hyeon, T. *Carbon* 2003, 41, 1049–1056.
- (29) Lu, Y. F. *Angew. Chem., Int. Ed.* 2006, 45, 7664–7667.
- (30) Liang, Y. R.; Liu, H.; Li, Z. H.; Fu, R. W.; Wu, D. C. *J. Mater. Chem. A* 2013, 1, 15207–15211.
- (31) Yuan, D. S.; Zeng, F. L.; Yan, J.; Yuan, X. L.; Huang, X. J.; Zou, W. J. *RSC Adv.* 2013, 3, 5570–5576.
- (32) Gu, H.; Cao, D.; Wang, J.; Lu, X.; Li, Z.; Niu, C.; Wang, H. *Mater. Today Energy.*

2017, 4, 75–80.

(33) Chen, S.; Bi, J. Y.; Zhao, Y.; Yang, L. J.; Zhang, C.; Ma, Y. W.; Wu, Q.; Wang, X. Z.; Hu, Z. *Adv. Mater.* 2012, 24, 5593–5597.

(34) Fan, H.; Wang, Y.; Gao, F. J.; Yang, L. Q.; Liu, M.; Du, X.; Wang, P.; Yang, L. J.; Wu, Q.; Wang, X. Z.; Hu, Z. *J. Energy Chem.* 2019, 34, 64–71.

(35) Gong, K.; Du, F.; Xia, Z.; Durstock, M.; Dai, L. *Science* 2009, 323, 760.

(36) Meng, X. J.; Xiao, F. S. *Chem. Rev.* 2014, 114, 1521–1543.

(37) Zhang, A.; Qu, T.; Cao, S. B.; Li, Y. Y.; Zhao, Y. B.; Chen, A. H. *Adv. Mater. Interfaces* 2018, 5, 1701390.

(38) Li, W.; Zhao, D. Y. *Chem. Commun.* 2013, 49, 943–946.

(39) Enterría, M.; Pereira, M. F. R.; Martins, J. I.; Figueiredo, J. L. *Carbon* 2015, 95, 72–83.

(40) Wan, Y.; Zhao, D. Y. *Chem. Rev.* 2007, 107, 2821–2860.

(41) Hassan, M.; Wu, D. D.; Song, X. D.; Qiu, W. W.; Mao, Q.; Ren, S. Z.; Hao, C. J. *Electroanal. Chem.* 2018, 829, 157–167.

(42) Kowalewski, T.; Tsarevsky, N. V.; Matyjaszewski, K. *J. Am. Chem. Soc.* 2002, 124, 10632–10633.

(43) Zhong, M. J.; Natesakhawat, S.; Baltrus, J. P.; Luebke, D.; Nulwala, H.; Matyjaszewski, K.; Kowalewski, T. *Chem. Commun.* 2012, 48, 11516–11518.

(44) Zhou, Z. P.; Liu, T. Y.; Khan, A. U.; Liu, G. L. *Sci. Adv.* 2019, 5, 6852.

(45) Bates, F. S.; Fredrickson, G. H. *Phys. Today* 1999, 52, 32–38.

(46) Bockstaller, M. R.; Thomas, E. L. *Phys. Rev. Lett.* 2004, 93, 166106.

- (47) Templin, M.; Franck, A.; DuChesne, A.; Leist, H.; Zhang, Y. M.; Ulrich, R.; Schadler, V.; Wiesner, U. *Science* 1997, 278, 1795–1798.
- (48) Morkved, T. L.; Lu, M.; Urbas, A. M.; Ehrichs, E. E.; Jaeger, H. M.; Mansky, P.; Russell, T. P. *Science* 1996, 273, 931–933.
- (49) Liang, C. D.; Dai, S. J. *Am. Chem. Soc.* 2006, 128, 5316–5317.
- (50) Gao, L.; Chandra, A.; Nabae, Y.; Hayakawa, T. *Polym. J.* 2018, 50, 389–396.
- (51) Liu, C. Y.; Li, L. X.; Song, H. H.; Chen, X. H. *Chem. Commun.* 2007, 757–759.
- (52) Tian, H.; Lin, Z. X.; Xu, F. G.; Zheng, J. X.; Zhuang, X. D.; Mai, Y. Y.; Feng, X. L. *Small* 2016, 12, 3155–3163.
- (53) Meng, Y.; Gu, D.; Zhang, F.; Shi, Y.; Yang, H.; Li, Z.; Yu, C.; Tu, B.; Zhao, D. *Angew. Chem.* 2005, 117, 7215–7221.
- (54) Meng, Y.; Gu, D.; Zhang, F. Q.; Shi, Y. F.; Cheng, L.; Feng, D.; Wu, Z. X.; Chen, Z. X.; Wan, Y.; Stein, A.; Zhao, D. Y. *Chem. Mater.* 2006, 18, 4447–4464.
- (55) Lee, W. J.; Choi, D.S.; Lee, S.H.; Lim, J.; Kim, J.E.; Li, D.J.; Lee, G.Y. Kim, S.O. Electroless Bimetal Decoration on N-Doped Carbon Nanotubes and Graphene for Oxygen Reduction Reaction Catalysts. *Part. Part. Syst. Charact.*, 2014, 31, 965-970
- (56) Elezovic, N. R.; Babi, B. M.; Ercius, P.; Radmilovic, V.R.; Vracard, Lj.M.; Krstajic, N.V. Y. *Appl. Catal. B.* 2012, 125, 390–397.
- (57) Guan, B. Y.; Yu, L.; Lou, X. W. J. *Am. Chem. Soc.* 2016, 138, 11306–11311.
- (58) Kawashima, D.; Aihara, T.; Kobayashi, Y.; Kyotani, T.; Tomita, A. *Chem. Mater.* 2000, 12, 3397–3401.
- (59) Pang, J. B.; Li, X.; Wang, D. H.; Wu, Z. W.; John, V. T.; Yang, Z. Z.; Lu, Y. F.

*Adv. Mater.* 2004, 16, 884–886.

(60) Zhang, J. A.; Song, Y.; Zhao, Y. P.; Zhao, S.; Yan, J. J.; Lee, J.; Wang, Z. Y.; Liu, S. Y.; Yuan, R.; Luo, D. L.; Kopec, M.; Gottlieb, E.; Kowalewski, T.; Matyjaszewski, K.; Bockstaller, M. R. *Chem. Mater.* 2018, 30, 2208–2212.

(61) Ding, W.; Li, L.; Xiong, K.; Wang, Y.; Li, W.; Nie, Y.; Chen, S. G.; Qi, X. Q.; Wei, Z. D. *J. Am. Chem. Soc.* 2015, 137, 5414–5420.

(62) Gong, J.; Zhang, J. S.; Lin, H. J.; Yuan, J. Y. *Appl. Mater. Today* 2018, 12, 168–176.

(63) Wang, F.; Song, S. Y.; Li, K.; Li, J. Q.; Pan, J.; Yao, S.; Ge, X.; Feng, J.; Wang, X.; Zhang, H. J. *Adv. Mater.* 2016, 28, 10679–10683.

(64) Tang, J.; Wang, T.; Salunkhe, R. R.; Alshehri, S. M.; Malgras, V.; Yamauchi, Y. *Chem. - Eur. J.* 2015, 21, 17293–17298.

(65) Almeida, V. C.; Silva, R.; Acerce, M.; Pezoti, O.; Cazetta, A. L.; Martins, A. C.; Huang, X. X.; Chhowalla, M.; Asefa, T. *J. Mater. Chem. A* 2014, 2, 15181–15190.

(66) Dai L. Graphene: Tunable superdoping. *Nat Energy.* 2016; 1:16041.

(67) Chang, Y. Q.; Hong, F.; Liu, J. X.; Xie, M. S.; Zhang, Q. L.; He, C. X.; Niu, H. B.; Liu, J. H. *Carbon* 2015, 87, 424–433.

(68) Park, J.; Nabaee, Y.; Hayakawa, T.; Kakimoto, M. A. *ACS Catal.* 2014, 4, 3749–3754.

(69) Chen, A. B.; Yu, Y. F.; Zhang, Y.; Zang, W. W.; Yu, Y. H.; Zhang, Y. X.; Shen, S. F.; Zhang, J. *Carbon* 2014, 80, 19–27.

(70) To, J. W. F.; He, J.; Mei, J.; Haghpanah, R.; Chen, Z.; Kurosawa, T.; Chen, S.;

Bae, W.-G.; Pan, L.; Tok, J. B. H.; Wilcox, J.; Bao, Z. *J. Am. Chem. Soc.* 2016, 138, 1001–1009.

(71) Zhang, J.; Zhao, Z.; Xia, Z.; Dai, L. *Nat. Nanotechnol.* 2015, 10, 444–452.

(72) Jing, F.; Chen, M.; Tang, Y. P.; Xu, Z. X.; Huang, T.; Su, Y. Z.; Wu, D. Q. *J. Colloid Interface Sci.* 2017, 492, 8–14.

(73) Zhong, M.; Kim, E. K.; McGann, J. P.; Chun, S. E.; Whitacre, J. F.; Jaroniec, M.; Matyjaszewski, K.; Kowalewski, T. *J. Am. Chem. Soc.* 2012, 134, 14846–14857.

(74) A. K. Shukla, M. K. Ravikumar, A. Roy, S. R. Barman, D. D. Sarma, A. S. Arico, Y. Antonucci, L. Pino and N. Giordano, *J. Electrochem. Soc.*, 1994, 141, 1517–1522.

(75) S. C. Roy, P. A. Christensen, A. Hammelt, K. M. Thomas and V. Trapp, *J. Electrochem. Soc.*, 1996, 143, 3073–3079

(76) Chen, H. C.; Sun, F. G.; Wang, J. T.; Li, W. C.; Qiao, W. M.; Ling, L. C.; Long, D. H. *J. Phys. Chem. C* 2013, 117, 8318–8328.

(77) Liu, D.; Cheng, G.; Zhao, H.; Zeng, C.; Qu, D. Y.; Xiao, L.; Tang, H. L.; Deng, Z.; Li, Y.; Su, B. L. *Nano Energy* 2016, 22, 255–268.

(78) Liu, J.; Wang, H. Q.; Antonietti, M.; *Chem. Soc. Rev.*, 2016, 45, 2308–2326.

(79) Huang, X. X.; Zhou, L. J.; Voiry, D.; Chhowalla, M.; Zou, X. X.; Asefa, T. *ACS Appl. Mater. Interfaces* 2016, 8, 18891–18903.

(80) Yang, T. Y.; Liu, J.; Zhou, R. F.; Chen, Z. G.; Xu, H. Y.; Qiao, S. Z.; Monteiro, M. J. *J. Mater. Chem. A* 2014, 2, 18139–18146.

(81) Liu, H. J.; Wang, J.; Wang, C. X.; Xia, Y. Y. *Adv. Energy Mater.* 2011, 1, 1101–1108.



- (82) Sheng, Z. H.; Shao, L.; Chen, J. J.; Bao, W. J.; Wang, F. B.; Xia, X. H. *ACS Nano* 2011, 5, 4350–4358.
- (83) Shrestha, S.; Mustain, W. E. *J. Electrochem. Soc.* 2010, 157, B1665–B1672.
- (84) Li, X. L.; Wang, H. L.; Robinson, J. T.; Sanchez, H.; Diankov, G.; Dai, H. J. *J. Am. Chem. Soc.* 2009, 131, 15939–15944.
- (85) Lin, Z. Y.; Waller, G.; Liu, Y.; Liu, M. L.; Wong, C. P. *Adv. Energy Mater.* 2012, 2, 884–888.
- (86) Hou, S. C.; Cai, X.; Wu, H. W.; Yu, X.; Peng, M.; Yan, K.; Zou, D. C. *Energy Environ. Sci.* 2013, 6, 3356–3362.
- (87) Choi, C. H.; Chung, M. W.; Park, S. H.; Woo, S. I. *RSC Adv.* 2013, 3, 4246–4253.
- (88) Ma, F. W.; Zhao, H.; Sun, L. P.; Li, Q.; Huo, L. H.; Xia, T.; Gao, S.; Pang, G. S.; Shi, Z.; Feng, S. H. *J. Mater. Chem.* 2012, 22, 13464–13468.
- (89) Fan, Z.; Ding, B.; Guo, H.; Shi, M.; Zhang, Y.; Dong, S.; Zhang, T.; Dou, H.; Zhang, X. *Chem. - Eur. J.* 2019, 25, 10710–10717.
- (90) Liu, X. H.; Zhou, L.; Zhao, Y. Q.; Bian, L.; Feng, X. T.; Pu, Q. S. *ACS Appl. Mater. Interfaces* 2013, 5, 10280–10287.
- (91) Wang, S. P.; Zhang, J. N.; Shang, P.; Li, Y. Y.; Chen, Z. M.; Xu, Q. *Chem. Commun.* 2014, 50, 12091–12094.
- (92) Seredych, M.; Rodriguez-Castellon, E.; Biggs, M. J.; Skinner, W.; Bandosz, T. J. *Carbon* 2014, 78, 540–558.
- (93) Peng, H.; Ma, G. F.; Sun, K. J.; Mu, J. J.; Zhang, Z.; Lei, Z. Q. *J. Phys. Chem. C* 2014, 118, 29507–29516.

- (94) Wei, J. S.; Ding, H.; Wang, Y. G.; Xiong, H. M. *ACS Appl. Mater. Interfaces* 2015, 7, 5811–5819.
- (95) Jiang, J. G.; Chen, H.; Wang, Z.; Bao, L. K.; Qiang, Y. W.; Guan, S. Y.; Chen, J. *D. J. Colloid Interface Sci.* 2015, 452, 54–61.
- (96) Guo, Y.; Zeng, Z.; Li, Y.; Huang, Z.; Cui, Y. *Catal. Today* 2018, 307, 12–19.
- (97) Wei, H.; Xu, M. W.; Bao, S. J.; Yang, F.; Chai, H. *RSC Adv.* 2014, 4, 16979–16984.
- (98) Park, S. H.; Kang, Y. J.; Majd, S. *Adv. Mater.* 2015, 27, 7583–7619.
- (99) Jin, C.; Nagaiah, T. C.; Xia, W.; Spliethoff, B.; Wang, S. S.; Bron, M.; Schuhmann, W.; Muhler, M. *Nanoscale* 2010, 2, 981–987.
- (100) Wu, G.; More, K. L.; Johnston, C. M.; Zelenay, P. *Science* 2011, 332, 443–447.
- (101) Gong, K.; Du, F.; Xia, Z.; Durstock, M.; Dai, L. *Science* 2009, 323, 760–764.
- (102) Yuan, C. Q.; Liu, X. H.; Jia, M. Y.; Luo, Z. X.; Yao, J. N. *J. Mater. Chem. A* 2015, 3, 3409–3415.
- (103) Shin, Y. S.; Fryxell, G.; Um, W. Y.; Parker, K.; Mattigod, S. V.; Skaggs, R. *Adv. Funct. Mater.* 2007, 17, 2897–2901.
- (104) Sevilla, M.; Fuertes, A. B. *Microporous Mesoporous Mater.* 2012, 158, 318–323.
- (105) He, Y. Z.; Han, X. J.; Du, Y. C.; Song, B.; Zhang, B.; Zhang, W.; Xu, P. *Nano Res.* 2018, 11, 2573–2585.
- (106) Liu, Y. L.; Ai, K. L.; Lu, L. H. *Chem. Rev.* 2014, 114, 5057–5115.

***Every reasonable effort has been made to acknowledge the owners of copyright material. I would be pleased to hear from any copyright owner who has been omitted or incorrectly acknowledged.***



### **Chapter 3: Precursor modulated active sites of nitrogen doped graphene-based carbon catalysts via one-step pyrolysis method for the enhanced oxygen reduction reaction**

#### **Abstract**

Tuning active configurations of different nitrogen (N) species and elucidating their influence on the catalytic activity for oxygen reduction reaction (ORR) is important to develop N-doped carbon (N/C) as efficient metal-free catalysts. The challenge is to selectively control the active N sites of N/C. Herein, we approach this challenge by modulating N active species in graphene structured N/C with specific precursors via a one-step pyrolysis process. In this method, 5-aminouracil is selected as the N-containing precursor platform to modulate the Pyridinic N ( $N_P$ ), while 2,6-diaminopyridine and 1,3-diaminobenzene are used to modulate Graphitic N ( $N_G$ ) and Pyrrolic N ( $N_{PY}$ ), respectively.  $N/C-N_P+N_G$ ,  $N/C-N_P+N_P$  and  $N/C-N_P+N_{PY}$  are successfully synthesized and identified by microstructure and phase characterization. Electrochemical results demonstrate that  $N/C-N_P+N_G$  exhibits the best ORR performance, which is comparable to commercial Pt/C. By contrast,  $N/C-N_P+N_{PY}$  exhibits the lowest activity for ORR. Density functional theory (DFT) simulation further validates that the  $N_P+N_G$  configuration produces strong electronic distribution on carbon matrix that leads to high charge and high spin density on surrounding carbon atoms. This work provides a facile approach to design N doped graphene structured carbon materials with active N configurations for ORR.

*\*Reprinted (adapted) with permission from Xiaoran Zhang, Xiao Zhang, Shiyong*

*Zhao, Yunqiu Wang, Zhi Qun Tian\*, Pei Kang Shen, San Ping Jiang\* Precursor modulated active sites of nitrogen doped graphene-based carbon catalysts via one-step pyrolysis method for the enhanced oxygen reduction reaction. Electrochim. Acta 2020, 370, 137712. Copyright 2020 Elsevier.*

### **3.1. Introduction**

Oxygen reduction reaction (ORR) is of paramount importance to construct green and renewable energy technologies, such as fuel cells and rechargeable metal–air batteries systems [1-3]. The state-of-the-art electrocatalysts for ORR are precious metal-based materials such as Pt, but their practical application is seriously suffered from the high cost and limited resources [4-6]. There are significant research efforts in the development of alternative electrocatalysts for ORR and among them heteroatom doped carbon materials are considered as promising candidates to replace Pt-based catalysts to achieve highly efficient activity for ORR [7][8]. Nevertheless, carbon based metal-free catalysts still suffer from low catalytic activity for ORR compared with their noble metal-based counterparts [9][10]. The key reason is the lack of precise synthesis process to control and modulate the active sites with strong synergistic effect between heteroatoms and surrounding carbon matrix for ORR.

Among the reported heteroatoms such as nitrogen, phosphate and sulfur (N, P, and S) in carbon, N-dopant is the most attractive and extensively studied due to their characteristic of similar size with carbon atoms [11][12], which contributes to tune electronic structure on the carbon matrix and therefore provides a promising way for increased ORR performance of heteroatoms doped carbon materials [13][14]. The

doped nitrogen in the graphitic lattice of nitrogen doped carbon (N/C) can exist in several different configurations, including pyridinic nitrogen ( $N_P$ ), pyrrolic nitrogen ( $N_{PY}$ ), quaternary nitrogen ( $N_Q$ ), nitrile nitrogen ( $N_N$ ) and primary amine nitrogen ( $N_A$ ) [15][16]. It has been shown that planar  $N_P$  with a lone electron pair is active to improve the electron-donating capability and weaken the O-O bond, and the carbon atoms with Lewis basicity adjacent to  $N_P$  are considered as active sites for ORR [17]. In addition,  $N_G$  has been considered as one of the most important active components due to its significant contribution to the conductivity [18]. The electrical conductivity of the catalysts is important for the electrocatalytic activity of N/C. However, the coexistence of different N configurations in N/C-doped catalysts leads to diverse active as well as non-active site configurations that causes a great challenge to precisely tuning synergetic effect between different N dopants in carbon matrix for ORR [19]. The challenge is to develop a facile and scalable synthesis method to modulate N configurations and explore their correlated synergetic effect on the catalytic activity for ORR.

In this study, we approach the controlled synthesis of N/C with specific N configurations through precursor modulation, based on the close correlation between the structure and composition of precursors and formed N configurations in carbon matrix [20][21]. Therefore, using suitable N-containing precursors to modulate the N/C materials with specific N configurations is a promising way to synthesize performance-oriented N-doped metal-free catalysts for ORR. In this work, an effective active site engineering strategy of synthesis of active N/C with specific N

configurations was developed via a facile pyrolysis of the selected N-containing precursors. In this process, 5-Aminouracil precursor was selected to modulate the  $N_P$  formation, while 2, 6-Diaminopyridine and 1, 3-Diaminobenzene precursors were used to modulate the content of  $N_G$  and  $N_{PY}$ , respectively. The results indicate the successful synthesis of N-doped graphene structured carbon with specific N configurations and demonstrate their close correlation with the electrocatalytic activity for ORR.

## 3.2. Experimental

### 3.2.1 Materials and synthesis

N-containing precursors, 1, 3-Diaminobenzene ( $C_6H_8N_2$ , Macklin) with the conventional aromatic benzene ring, 2, 6-Diaminopyridine ( $C_5H_7N_3$ , Macklin) with one N atom replaced in benzene ring and 5-Aminouracil ( $C_4H_5N_3O_2$ , Macklin) with aromatic pyridine and pyrimidine ring were purchased and used without further treatment. In the synthesis of N-doped carbon (N/C) materials, 5-Aminouracil, and 5-Aminouracil mixed with 2,6-diaminopyridine and 5-Aminouracil mixed with 1,3-diaminobenzene (with the molar ratio of 1:1) were ground for 20 minutes. The specific pyrolysis process for these samples is as follow: from room temperature ( $30^\circ C$ ) heat to  $350^\circ C$  and retained at  $350^\circ C$  for 1h and then heat to  $650^\circ C$  and retained at  $650^\circ C$  for 1h and then heat to  $950^\circ C$  and retained at  $950^\circ C$  for 1h, and then cool naturally to room temperature. The heating rate during the whole process was set at  $5^\circ C/min$ . And the reason for setting heat preservation at  $350^\circ C$ ,  $650^\circ C$  and  $950^\circ C$  for 1h is to ensure the fully polymerization of these N-containing precursors. Black powders were obtained after cooling and denoted as N/C-Pyridinic N+Graphitic N ( $N/C-N_P+N_G$ ) obtained from

mixed 5-Aminouracil and 2,6-diaminopyridine, N/C-Pyridinic N+Pyridinic N (N/C-N<sub>P</sub>+N<sub>P</sub>) from 5-Aminouracil and N/C-Pyridinic N+Pyrrolic N (N/C-N<sub>P</sub>+N<sub>PY</sub>) from mixed 5-Aminouracil and 1,3-diaminobenzene, respectively. Figure 3-1 shows the synthesis processes of precursor modulated N-doped graphene structured carbon materials via one-pot pyrolysis process.

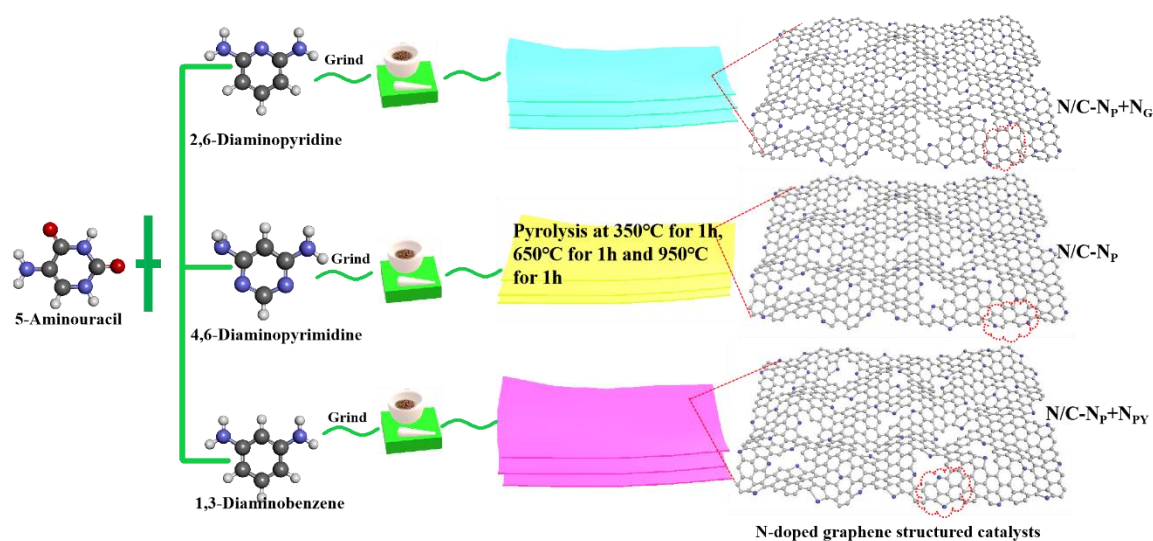


**Figure 3-1.** Scheme of the synthesis process of precursor modulated N-doped carbon materials.

### 3.2.2 Characterization

The SEM and TEM images of as-synthesized N/C materials were collected by Hitach SU8220 (SEM) and Titan ETEM G2 80-300 (TEM). The Raman spectra were determined on Horiba jobin Yvon Company with 532 nm incident laser Raman spectrometer. The BET of the N/C catalyst was obtained using Corp ASAP 2460. The CO<sub>2</sub> adsorption test was performed on RS485 Z-TEK. XRD was determined on RIGAKU Co with Cu k $\alpha$  ( $\lambda = 1.5405\text{\AA}$ ) as radiation source. Temperature-programmed desorption (TPD) were performed on a Micromeritics ChemiSorb 2750 instrument



equipped with a thermalconductivity (TCD) detector. Electrical conductivity were conducted on Conductivity Analyzer (DDS-11A), the test pressure is 25MPa. Electrochemical tests in this study were conducted with rotating ring disk electrode (RRDE) system (Pine Instrumentation, USA) on a bipotentiostat WD-20 BASIC in a three-electrode cell at 25°C in O<sub>2</sub>-saturated 0.1 M KOH solution. Reversible hydrogen electrode (RHE) and graphite rod were used as the reference and counter electrodes, respectively. Glassy carbon electrode with of diameter 5.61 mm (GCE) with a Pt ring was used as the working electrode. Catalyst loading of the N/C was 600 μg cm<sup>-2</sup>. For comparison, commercial Pt/C catalyst (46.7% Pt/C, Tanaka) was also tested with catalyst loading of 40 μg cm<sup>-2</sup>. The specific experimental conditions of the Pt based catalyst in the battery test: 10 mg of 40 wt.% Pt/C was mixed using 0.035 mL of 5 wt% Nafion solution and 1 mL of ethanol followed by 30 min sonication to form a homogeneous ink. The obtained catalyst ink was uniformly placed onto the water-proof porous carbon paper with an effective area of 0.785 cm<sup>-2</sup> with using drop-cast method and dried at room temperature. In ORR measurements, the electron-transfer number and the yield of hydrogen peroxide (% HO<sub>2</sub><sup>-</sup>) of catalysts were determined using Eqs.

(1) and (2) as below:

$$n = 4 \times \frac{I_r}{I_d + I_r/N} \quad (1)$$

$$\text{H}_2\text{O}_2 (\%) = 200 \times \frac{I_r/N}{I_r/N + I_d} \quad (2)$$

where I<sub>d</sub> represents the disk current density of work disk, I<sub>r</sub> refers to the ring current density around the work disk, and N with 0.38 is the current collection efficiency.

To evaluate the practical electrochemical application of the as-synthesized N/C catalysts, a home-made Zn-air battery was built. The catalyst ink was made from 10mg N/C mixed with 0.035 ml of Nafion (5wt%) solution followed by 30 min sonication. The catalyst ink was applied on carbon fiber paper (0.785 cm<sup>2</sup>) with loading of 1.0 mg cm<sup>-2</sup> to form the air cathode. A polished zinc foil was used as the anode and 6M KOH solution as electrolyte .

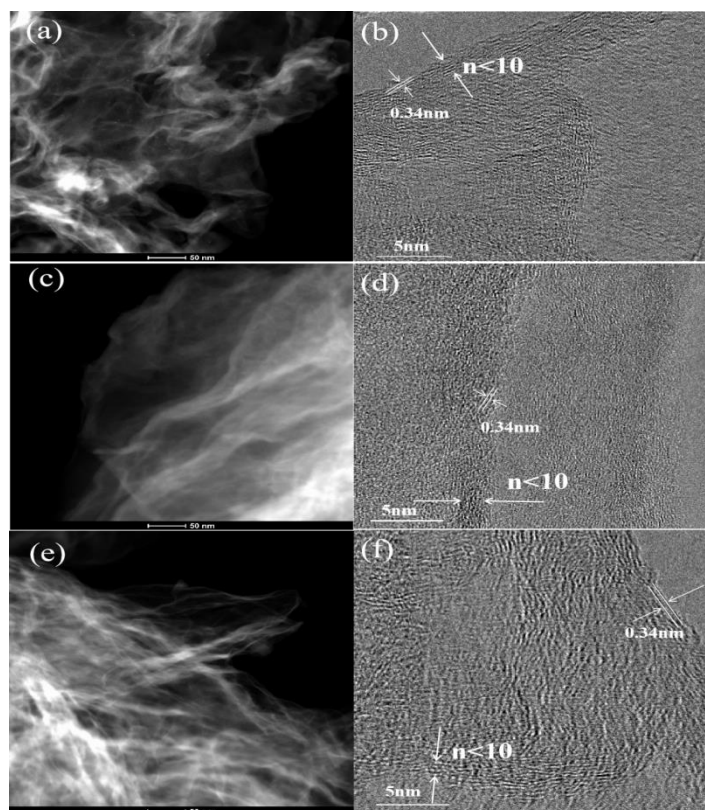
### 3.2.3 Density functional theory calculation

DFT calculations in the work adopt by Vienna *ab initio* simulation package (VASP) code. Supermodel is constructed with lattice parameters of a=35 Å, b=25 Å. The Brillouin zone was sampled with Monkhorst-Pack 3×3×1 k-points. The energy convergence tolerance is 1.0×10<sup>-5</sup> eV/atoms. The Gaussian smearing was set to 0.1 eV.

## 3.3 Results and discussion

### 3.3.1 Synthesis and characterization of graphene structured N/C

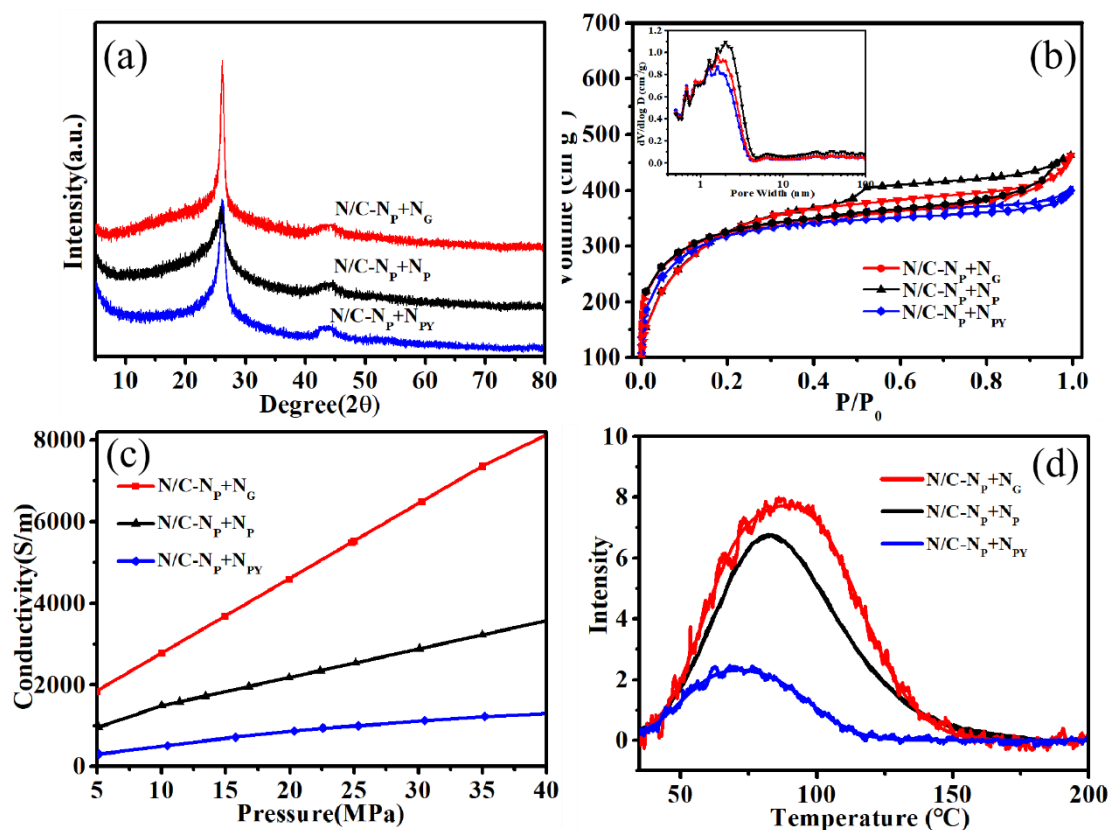
Figure 3-2 shows the TEM images of as-prepared N/C. The as-synthesized N/C exhibits similar graphene structured morphology. The formation mechanism of such graphene like structure is most likely to be induced by polymerization during the staged pyrolysis process [22]. The structure is characterized by a typical graphene lattice spacing of 0.34 nm (see Figure 3-2b, 3-2d and 3-2f). Furthermore, it is found that the number of carbon layers is around 10 (Figure 3-2f), indicating the highly graphitized structure. The result indicates the feasibility of the one-step synthesis of graphene like structure N/C via mixed N-containing precursors.



**Figure 3-2.** TEM images of (a,b) N/C-N<sub>P</sub>+N<sub>G</sub>, (c,d) N/C-N<sub>P</sub>+N<sub>P</sub>, and (e,f) N/C-N<sub>P</sub>+N<sub>PY</sub>.

Figure 3-3a shows XRD patterns of the as-synthesized N/C. There are obvious sharp diffraction peaks located at  $26^\circ$  and  $43.3^\circ$  in as-synthesized N/C, which can be attributed to (002) and (100) of graphitic carbon, respectively. The high intensity of the peak sharp carbon characteristic demonstrate its highly graphitized nature in the N doped graphene structured carbon materials [23]. Meanwhile, these N/C materials display similar XRD spectra, indicating that there is no obvious difference of structures among these N/C materials. The pore structure of the as-synthesized N/C was analyzed by N<sub>2</sub> adsorption and desorption isotherms (Figure 3-3b). The as-synthesized N/C possesses type-IV characteristic with H4 hysteresis loops, indicating the existence of micropores and mesopores with majority of pores in the range of 1-2 nm and a small portion of mesopores with diameter below 10 nm [24]. The BET surface area of the as-

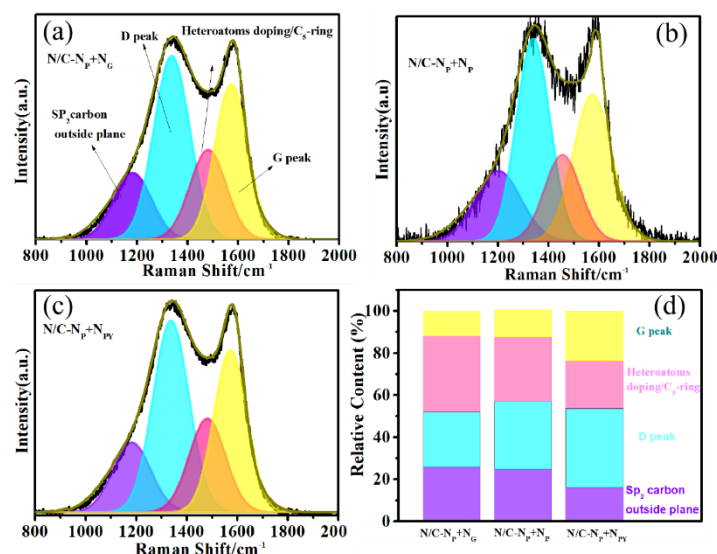
synthesized N/C-N<sub>P</sub>+N<sub>G</sub>, N/C-N<sub>P</sub>+N<sub>P</sub> and N/C-N<sub>P</sub>+N<sub>PY</sub> N/C is 864, 932, and 1062 m<sup>2</sup>g<sup>-1</sup>, respectively. Electrical conductivity of the N/C was also measured at 25MPa (Figure 3-3c). Among the N/C materials, N/C-N<sub>P</sub>+N<sub>G</sub> exhibits the highest conductivity of 5196 S m<sup>-1</sup>, followed by N/C-N<sub>P</sub>+N<sub>P</sub> (3064 S m<sup>-1</sup>) and N/C-N<sub>P</sub>+N<sub>PY</sub> (2485 S m<sup>-1</sup>). The high electrical conductivity is important for highly active catalyst materials for ORR[25].



**Figure 3-3.** (a) XRD patterns, (b) nitrogen adsorption-desorption isotherms and the inset is pore size distribution, (c) conductivity curves at room temperature and (d) CO<sub>2</sub> TPD profiles of N/C-N<sub>P</sub>+N<sub>G</sub>, N/C-N<sub>P</sub>+N<sub>P</sub> and N/C-N<sub>P</sub>+N<sub>PY</sub> catalysts.

To further study the chemical environment of carbon atoms of the as-synthesized N/C, Temperature Programmed Desorption (TPD) of CO<sub>2</sub> is conducted to analysis the Lewis base sites of the samples, based on the fact that the percentage of Lewis base sites plays a significant role that influences electronic distribution of graphene matrix[26]. As shown in Figure 3-3d, N/C-N<sub>P</sub>+N<sub>G</sub> and N/C-N<sub>P</sub>+N<sub>P</sub> exhibit the large CO<sub>2</sub> desorption peak, demonstrating their strong basicity. This is most likely derived

from the high content of graphitic N and pyridinic N, which are considered as the contributor to the ORR catalytic activity [27][28].



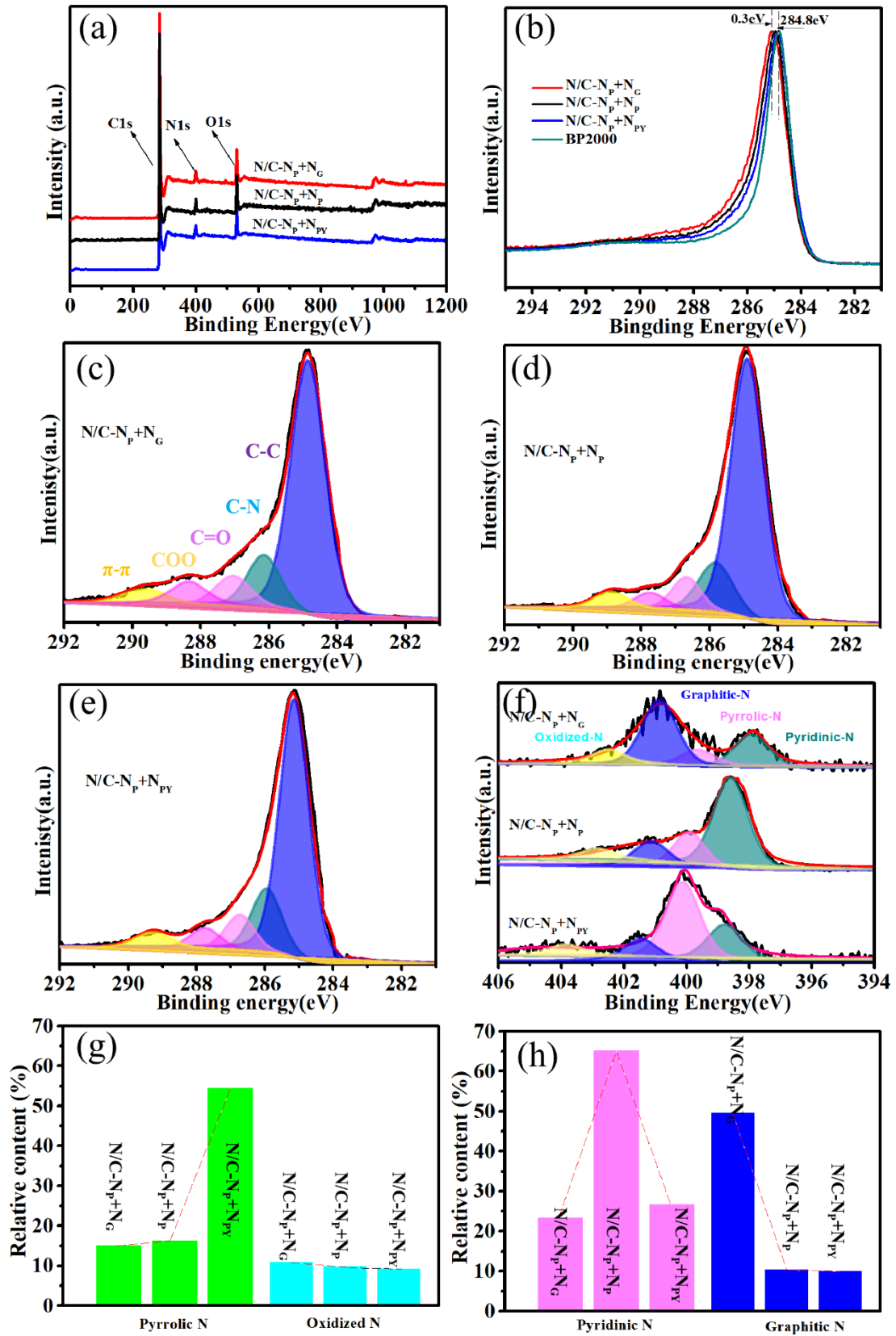
**Figure 3-4.** Raman spectrum of as-synthesized (a) N/C-N<sub>P</sub>+N<sub>G</sub>, (b) N/C-N<sub>P</sub>+N<sub>P</sub>, (c) N/C-N<sub>P</sub>+N<sub>Py</sub> and (d) distribution of specific percentage of each peaks.

Figure 3-4 shows the Raman spectroscopy responses of the as-synthesized N/C. There are two main peaks D (1350 cm<sup>-1</sup>) and G (1580 cm<sup>-1</sup>)[29] and peaks located at ~1190 and 1500 cm<sup>-1</sup> can be associated with the heteroatom doping degree of these graphene structured carbon matrix[30-32]. The peak ratio of I<sub>D</sub>/I<sub>G</sub> is 1.178, 1.14, and 1.132 obtained on N/C-N<sub>P</sub>+N<sub>G</sub>, N/C-N<sub>P</sub>+N<sub>P</sub> and N/C-N<sub>P</sub>+N<sub>Py</sub>, respectively. A gradual decrease of the I<sub>D</sub>/I<sub>G</sub> ratio from N/C-N<sub>P</sub>+N<sub>G</sub>, N/C-N<sub>P</sub>+N<sub>P</sub> to N/C-N<sub>P</sub>+N<sub>Py</sub> indicates the decreased defects in the N/C. The percentage of peak density at 1500 cm<sup>-1</sup> is 24.8%, 23.09% and 18.76% for N/C-N<sub>P</sub>+N<sub>G</sub>, N/C-N<sub>P</sub>+N<sub>P</sub> and N/C-N<sub>P</sub>+N<sub>Py</sub>, respectively, consistent with the change of the I<sub>D</sub>/I<sub>G</sub> ratio. Overall, the as-synthesized N/C-N<sub>P</sub>+N<sub>G</sub> displays the highest doping degree followed by that of N/C-N<sub>P</sub>+N<sub>P</sub> and N/C-N<sub>P</sub>+N<sub>Py</sub>.

### 3.3.2. Distribution of N configurations of N/C

The element content and distribution of the as-synthesized N/C were analyzed by XPS

and the results are shown in Figure 3-5. From survey spectrum, N, C, O elements were detected, and observation of obvious peaks of N1s indicates the successful N doping. There is no obvious difference on the C, N and O contents of the as-synthesized N/C derived from different precursors, indicating that precursors do not have a remarkable impact on the overall composition. For XPS, to calibrate the peak of C1s, in the XPS test, the commercial BP 2000 carbon black was introduced as an internal standard for the calibration of C1s peak with 284.6 eV, and the XPS spectrum of BP2000 was listed as reference curve. Furthermore, all our samples and BP 2000 were tested in the same instrument at one time to eliminate possible binding energy shift error of C1s. The main C1s peak was allocated at 284.85, 284.97 and 285.13 eV in N/C-N<sub>P</sub>+N<sub>PY</sub>, N/C-N<sub>P</sub>+N<sub>P</sub> and N/C-N<sub>P</sub>+N<sub>G</sub>, respectively. C1s spectra in the N/C can be fitted into five peaks of 285.5, 286.42, 284.3, 288.4 and 291 eV, respectively, corresponding to C-C, C-N, C=O, -COO and  $\pi$ - $\pi$ , respectively[33] (see Figure 3-5c-e). The N1s spectra were fitted with four peaks located at 398.25, 399.79, 401.12 and 403.5 eV, respectively (Figure 3-5f), which can be assigned to N<sub>P</sub>, N<sub>PY</sub>, N<sub>G</sub>, and oxidized N or N<sub>O</sub>, respectively [34][35]. The percentage of specific N species is shown in Figure 3-5g and 3-5h. For N/C-N<sub>P</sub>+N<sub>G</sub>, the N configuration is dominated by the 23% N<sub>P</sub> and 50% N<sub>G</sub> with relatively small 15% N<sub>PY</sub> and 12% N<sub>O</sub>. N/C-N<sub>P</sub>+N<sub>P</sub> contains 65% N<sub>P</sub> with



**Figure 3-5.** (a) The survey, (b) main peaks of C1s, high-resolution XPS spectra of C1s for (c) N/C-N<sub>p</sub>+N<sub>G</sub>, (d) N/C-N<sub>p</sub>+N<sub>p</sub>, (e) N/C-N<sub>p</sub>+N<sub>py</sub>, (f) Peak fitting for high-

resolution, N1s of N/C catalysts, and (g,h) the bar charts of distributions of N configurations and species in the N/C catalysts.

16%  $N_{PY}$  and only 10%  $N_G$  while N/C- $N_P+N_{PY}$  contains 55%  $N_{PY}$  and 27%  $N_P$  with only 10% $N_G$ . 5-Aminouracil contributes to high content of  $N_P$  (65%) than that of pyridine based precursor (23%) (mixture of 5-Aminouracil and 2,6-diaminopyridine) and 27% on benzene based precursors (mixture of 5-Aminouracil and 1,3-diaminobenzene) in N/C. On the other hand, pyridine based precursor produces the highest content of  $N_G$  (50%), but, benzene based precursor derived N/C catalyst has higher content of  $N_{PY}$  (55%). Table 1 gives the content and compositions of graphene structured N/C materials synthesized in this study. It is worth noting that although there is no obvious difference on overall N content but the N dopant species are very different among the as-synthesized N/C, indicating that there is close correlation between the formed N configurations and precursors [36].

It has been shown that the thermal decomposition process of the precursors with different N/C ratio can be an indication of the preferential modulation of the specific N configuration formation [37]. Elemental analysis data of 5-aminouracil, 2,6-diaminopyridine and 1,3-diaminobenzene were conducted at temperatures between 200°C and 900°C. The N content decreased strongly with the increase in temperatures from 200-400°C for 5-aminouracil and 1,3-diaminobenzene precursors, while the N content in 2,6-diaminopyridine showed a slow descent at the same temperature range, but sharply declined when the temperature was above 500°C. A high decomposition temperature represents a relatively good thermal stability of polymer precursor, which means that more N atoms in aromatic benzene rings retained and participate in the



carbon matrix-forming process. Thus, 2,6-diaminopyridine exhibits a better thermal stability during the pyrolysis process than that of 5-aminouracil and 1,3-diaminobenzene, therefore, more N atoms in pyridine based aromatic benzene rings would be expected to be doped into carbon lattice and attribute to form  $N_G$  as compared with 5-aminouracil and 1,3-diaminobenzene precursors. The observed high content  $N_P$  and  $N_{PY}$  in N/C derived from 5-aminouracil and 1,3-diaminobenzene precursor mixtures may be due to the fact that the rapid thermal decomposition would produce a large number of free N and H atom from unstable aromatic benzene rings and aromatic pyrimidine rings and their connected  $NH_2$  moieties. The high concentration of C-N and N-H bonding contributes to edge and defect doping to form high content of  $N_P$  and  $N_{PY}$  [38][39]. This is in general consistent with XPS results as shown above.

### 3.3.3. *Electrochemical activity for ORR*

Figure 3-6 shows the electrochemical catalytic activity of the as-synthesized N/C for ORR. Among the N/C catalysts, N/C- $N_P+N_G$  displays the highest performance for ORR with the onset potential ( $E_{onset}$ ) of 1.01 V vs RHE and half-wave potential ( $E_{1/2}$ ) of 0.86 V vs. RHE, respectively, followed by N/C- $N_P+N_P$  with  $E_{onset}$  and  $E_{1/2}$  of 0.95 and 0.80 V, and N/C- $N_P+N_{PY}$  with  $E_{onset}$  and  $E_{1/2}$  of 0.92V and 0.75 V. The electrochemical activity of N/C- $N_P+N_G$  is comparable to conventional Pt/C electrocatalysts with  $E_{onset}$  and  $E_{1/2}$  of 1.01 and 0.86 V, respectively. The differences in ORR catalytic activity of N/C catalysts are further demonstrated by the kinetic current density ( $J_k$ ) measured at 0.9 V (see Figure 6b). Among them, N/C- $N_P+N_G$  catalyst shows the best kinetic current density, achieving  $0.254 \text{ mAcm}^{-2}$ , significantly higher

than  $0.115 \text{ mAcm}^{-2}$  obtained on N/C-N<sub>P</sub>+N<sub>P</sub> and  $0.056 \text{ mAcm}^{-2}$  on N/C-N<sub>P</sub>+N<sub>PY</sub>, respectively.

The superior catalytic activity for ORR is also validated by the Tafel slope of the reaction, achieving 75, 85, and 101  $\text{mV dec}^{-1}$  on N/C-N<sub>P</sub>+N<sub>G</sub>, N/C-N<sub>P</sub>+N<sub>P</sub> and N/C-N<sub>P</sub>+N<sub>PY</sub>, respectively (Figure 3-6c). The corresponding electron-transfer numbers and H<sub>2</sub>O<sub>2</sub> yield for the reaction were also measured and calculated (see Figure 3-6d). N/C-N<sub>P</sub>+N<sub>G</sub> shows the highest electron transfer number of 3.97, followed by 3.86 for the reaction on N/C-N<sub>P</sub>+N<sub>P</sub> and 3.79 on N/C-N<sub>P</sub>+N<sub>PY</sub>. In addition, the maximum of H<sub>2</sub>O<sub>2</sub> yield at 0.1-0.8 V in N/C-N<sub>P</sub>+N<sub>G</sub> is about 2.5%, almost identical with that on Pt/C electrocatalysts. This indicates the preferable 4 electron transfer process for ORR on N/C-N<sub>P</sub>+N<sub>G</sub>. On the other hand, for the reaction on N/C-N<sub>P</sub>+N<sub>P</sub> and N/C-N<sub>P</sub>+N<sub>PY</sub>, the H<sub>2</sub>O<sub>2</sub> yield increases with the polarization voltage, reaching 10% to 13% at 0.8 V (Figure 6d). This indicates the increased two-electron process for ORR on N/C-N<sub>P</sub>+N<sub>P</sub> and N/C-N<sub>P</sub>+N<sub>PY</sub> in the kinetic polarization regions. The results show that observed activity and performance of N/C-N<sub>P</sub>+N<sub>G</sub> catalysts for ORR are among the highest active heteroatom doped carbon based metal-free electrocatalysts reported in the literature. For example, N/C-N<sub>P</sub>+N<sub>G</sub> reported in this study exhibits the highest onset potential of 0.98V vs. RHE for ORR. On the other hand, the reported carbon based electrocatalysts usually display low limiting current density, below  $5 \text{ mAcm}^{-2}$ .

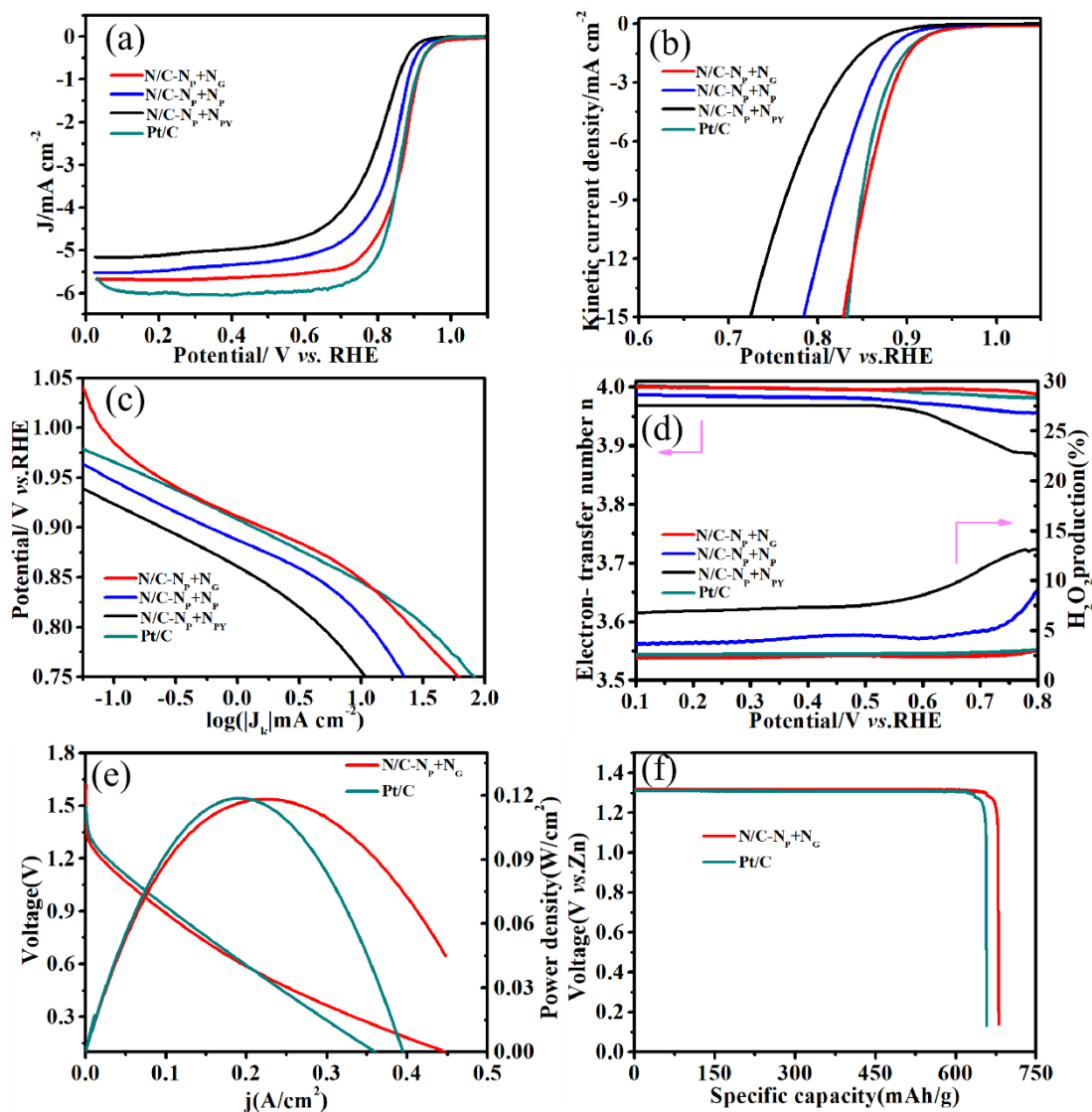


**Figure 3-6.** (a) Linear scanning voltammetry (LSV) curves, (b) plots of kinetic current density as a function of applied voltage, (c) Tafel slope, (d) electron transfer number  $n$  and  $\text{H}_2\text{O}_2$  production of  $\text{N/C-N}_\text{P}+\text{N}_\text{G}$ ,  $\text{N/C-N}_\text{P}+\text{N}_\text{P}$ ,  $\text{N/C-N}_\text{P}+\text{N}_\text{PY}$ , and  $\text{Pt/C}$  measured in  $0.1 \text{ M KOH}$ , (e) polarization curves and (f) the corresponding power density plots of a Zn-air battery with  $\text{N/C-N}_\text{P}+\text{N}_\text{G}$  and  $\text{Pt/C}$  cathode catalysts. Curves specific capacities at current densities  $10 \text{ mA cm}^{-2}$  of the Zn-air batteries using  $\text{N/C-N}_\text{P}+\text{N}_\text{G}$  and  $\text{Pt/C}$  as ORR electrocatalysts.

However,  $\text{N/C}$  electrocatalysts in this study exhibit a high limiting current  $>5.3 \text{ mAcm}^{-2}$ , and in the case of  $\text{N/C-N}_\text{P}+\text{N}_\text{G}$ , the limiting current is  $5.85 \text{ mAcm}^{-2}$ . More importantly, the half-wave potential of  $\text{N/C-N}_\text{P}+\text{N}_\text{G}$  for ORR is also among the highest value as compared with those carbon based metal-free catalysts.

Zn-air battery test was conducted on the as-synthesized  $\text{N/C-N}_\text{P}+\text{N}_\text{G}$  cathode and

Pt/C cathode and the performance is shown in Figure 3-6e. The Zn-air battery based on N/C-N<sub>P</sub>+N<sub>G</sub> cathode displays an open-circuit voltage of 1.70 V which is higher than that of conventional Pt/C (1.54 V). The peak power density of 126 mW cm<sup>-2</sup> is also slightly higher than 121 mW cm<sup>-2</sup> of the battery with Pt/C cathodic electrode. Galvanostatic discharge curves show that the battery with N/C-N<sub>P</sub>+N<sub>G</sub> air electrode displays a high voltage of 1.33 V as well as a long discharge time of 31.8 h, in comparison with 1.30 V and 29.7 h of the battery with Pt/C cathode. The specific capacities of the batteries is 707.6 mAh g<sup>-1</sup>, also higher than that with conventional Pt/C (669.4 mAh g<sup>-1</sup>) (Figure 3-6f). The result demonstrates the promising practical application of N/C-N<sub>P</sub>+N<sub>G</sub> in Zn-air batteries.

#### 3.3.4. DFT calculation of the origin of catalytic activity

DFT calculations were conducted to understand the effect of N configurations on surrounding carbon atoms. Four different N configurations, including N<sub>P</sub>, N<sub>P</sub>+N<sub>G</sub>, N<sub>P</sub>+N<sub>P</sub>, and N<sub>P</sub>+N<sub>PY</sub> on graphene matrix, were constructed as illustrated in Figure 3-7. The criterion of model establishment with N-doped sites was based on the results of XPS data (see Figure 3-5). It has been known that C atoms with high charge density or positive spin density are considered as promising active sites for ORR[40][41]. It is noticed that graphene+N<sub>P</sub>+N<sub>G</sub> configuration shows the high percentage (12.49%) of carbon atoms with high charge density and has the highest value of positive spin density with 46.68% among the configurations studied. This indicates that graphene+N<sub>P</sub>+N<sub>G</sub> has a significant effect on the electronic structure of carbon matrix. As for as graphene+N<sub>P</sub>+N<sub>PY</sub>, the content of carbon atoms with high charge density is 8.14% only.

By contrast, there is a low content (5.03%) of carbon atoms with positive spin density  $>0$ . On the other hand, the partial density of state (PDOS) of these configurations were analyzed and compared (Figure 3-7e-h). It is clearly shown that the P-state partial DOS overlap at the Fermi level (0 eV) of  $N_P+N_G$  configuration exhibits the higher value than that of  $N_P+N_P$  and  $N_P+N_{PY}$  configurations, consistent with that reported [42-44]. This indicates the high electrical conductivity and easy charge transfer of  $N_P+N_G$  configuration and the superior conductivity is clearly due to its high content of  $N_G$  which is considered as the contributor to the enhanced electrical conductivity[45-47]. Meanwhile, the high P-state partial DOS overlap at the Fermi level (0 eV) of  $N_P+N_G$  configuration demonstrate their superior catalytic activity due to its high electron- or spin redistribution in pristine  $sp^2$  conjugated graphene framework which induces atomic orbital hybridization [48][49]. This conclusion is supported by the high ORR performance of  $N/C-N_P+N_G$  catalysts (see Figure 3-6). For more intuitive discussion, several carbon atoms with surrounding doped N atoms with high charge and spin densities were selected as promising active sites and free-energy for the reaction steps of ORR was calculated (see Figure 3-7i). The ORR in alkaline media can be written as following steps[50]:



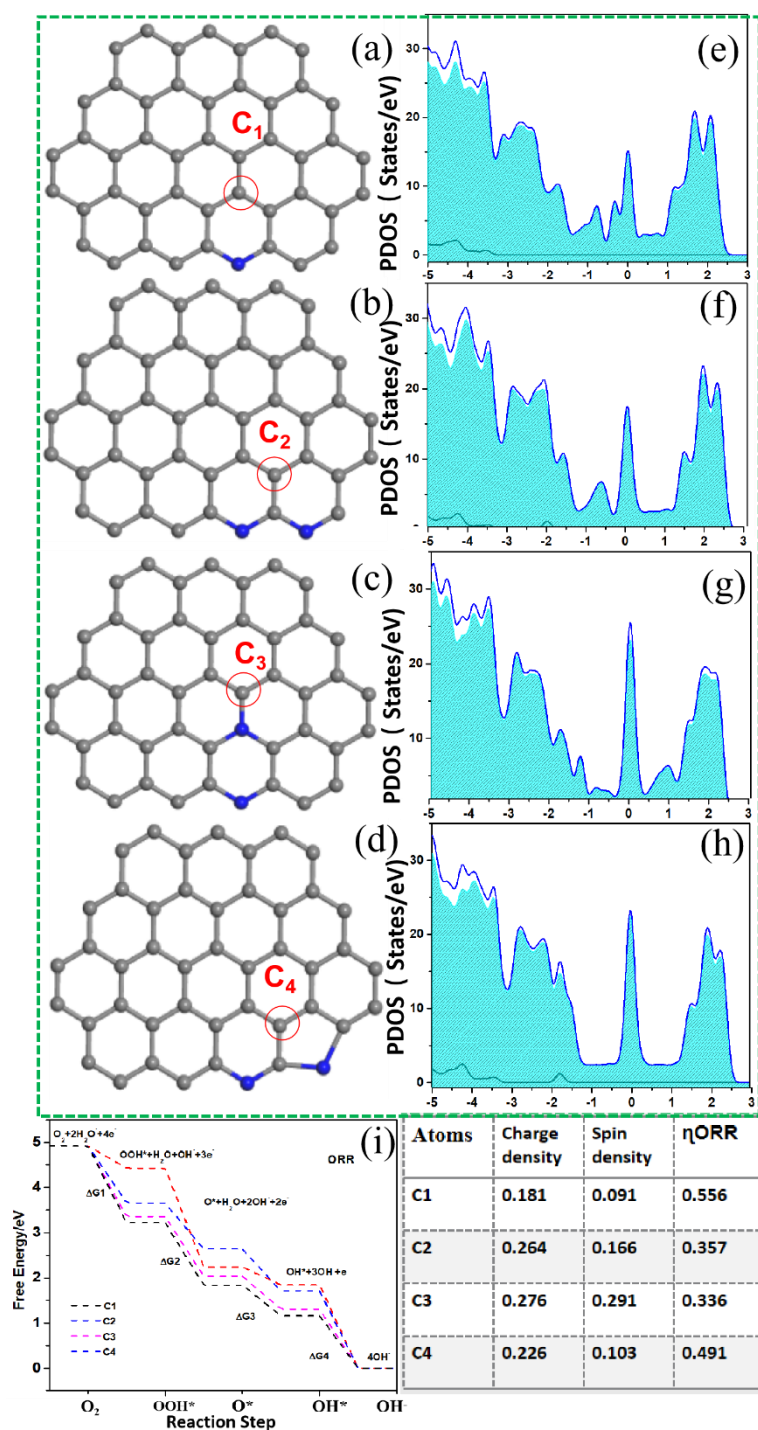


**Figure 3-7.** Constructed configurations/models and corresponding partial density of state (PDOS) of state (PDOS) of (a,e) graphene+NP, (b,f) graphene+NP+NP, (c,g) graphene+NP+NG and (d,h) graphene+NP+NPY. C<sub>1</sub>, C<sub>2</sub>, C<sub>3</sub> and C<sub>4</sub> are C atoms surrounded by single NP, NP+NP, NP+NG and NP+NPY, respectively. The Gibbs free energy of ORR and the specific values  $\eta_{\text{ORR}}$ , charge density and spin density values of the models are given in (i). Color scheme: C-grey balls and N-blue balls.

Carbon atom C<sub>3</sub> in the graphene+NP+NG configuration exhibits the  $\eta_{\text{ORR}}$  of 0.336 eV among all the configurations studied, followed by  $\eta_{\text{ORR}}$  0.357eV for C<sub>2</sub> of

graphene+N<sub>P</sub>+N<sub>P</sub>. The calculated free energy diagram illustrates that the adsorption of O<sub>2</sub> (Step 1) are rate-limiting for ORR in an alkaline solution, in this case, protonation of OO\* are the most sluggish steps for ORR in this work.[51-53] By contrast, in the case of graphene+N<sub>P</sub>+N<sub>PY</sub> configuration, the η<sub>ORR</sub> of ORR is 0.491 eV, significantly higher than that on both graphene+N<sub>P</sub>+N<sub>G</sub> and graphene+N<sub>P</sub>+N<sub>P</sub> configurations. In the case of single Pyridinic N doped configuration, graphene+N<sub>P</sub> the η<sub>ORR</sub> is highest, 0.556 eV. The free energy calculation indicates the highest catalytic potential of graphene+N<sub>P</sub>+N<sub>G</sub> configuration, consistent with experimental performance for ORR as discussed above (Figure 3-6).

### 3.4 Conclusion

In this study, three N-doped carbon catalysts with different N configurations, N/C-N<sub>P</sub>+N<sub>G</sub>, N/C-N<sub>P</sub>+N<sub>P</sub> and N/C-N<sub>P</sub>+N<sub>PY</sub> were successfully synthesized via a one-step pyrolysis method using specific precursor modulations of 5-Aminouracil, 2, 6-diaminopyridine and 1, 3-diaminobenzene. The microstructure, composition and N configurations were characterized in detail by various techniques such as TEM, XRD, TGA, Raman, XPS, and CO<sub>2</sub> adsorption and the electrochemical activity for ORR was measured in 0.1 M KOH solution.

The results indicate that the N/C-N<sub>P</sub>+N<sub>G</sub> containing a high content of 50% N<sub>G</sub> and 23% N<sub>P</sub> (23%) shows the best electrocatalytic activity for ORR, compatible to that of Pt/C. The high activity is attributed to the combined N<sub>G</sub> and N<sub>P</sub> configuration that introduce high spin and charge density on surrounding carbon atoms, thus reducing the energy barrier, supported by the DFT calculation. On the other hand, in the case of N/C-

$N_P+N_P$ , high content of  $N_P$  (65%) but low  $N_G$  will contribute to high charge density but not the spin density, leading to relatively low catalytic activity for ORR. The combined  $N_P+N_G$  configuration produce a significant effect on activating surrounding carbon atoms than that of pure  $N_P+N_P$  configuration. In the case of N/C- $N_P+N_{PY}$ , it possess the low content of 27%  $N_P$ , very low account for  $N_G$  (10%) but high percentage of 55%  $N_{PY}$ . According to the DFT calculation, such configuration induces a weak electron transfer with surrounding carbon atoms, indicated by a low values of charge density and spin density of the surrounding C atoms, therefore, leading to a relatively weak catalytic activity for ORR.

This study introduces a precursor modulated N/C via a facile and one-pot synthesis with controlled formation of N configurations. The result reveals the correlation between N configurations of N/C and the catalytic activity for ORR, providing a new insight on the design of N/C catalysts via easy and facile N-containing precursors to enhance ORR.

**Table 1.** The specific content of each element of these samples.

Samples	C%	O%	N % (% in N configurations)				total
			$N_{PY}$	$N_P$	$N_G$	$N_O$	
N/C- $N_P+N_G$	89.67	5.31	0.75 (15%)	1.15 (23%)	2.51 (50%)	0.61 (12%)	5.02 (100%)
N/C- $N_P+N_P$	89.02	6.02	0.79 (16%)	3.22 (65%)	0.5 (10%)	0.45 (9%)	4.96 (100%)
N/C- $N_P+N_{PY}$	90.68	4.45	2.68 (55%)	1.31 (27%)	0.49 (10%)	0.39 (8%)	4.87 (100%)

## References

[1] A. S. Arico, P. Bruce, B. Scrosati, J. M. Tarascon, W. Van Schalkwijk,



Nanostructured materials for advanced energy conversion and storage devices. *Nature Materials* 2005, 4 (5), 366-377.

[2] U. Martinez, S. K. Babu, E. F. Holby, H. T. Chung, X. Yin, P. Zelenay, Progress in the Development of Fe-Based PGM-Free Electrocatalysts for the Oxygen Reduction Reaction, *Advanced Materials*, 2019, 31(31)1806545 .

[3] F. Cheng, J. Chen, Metal-air batteries: from oxygen reduction electrochemistry to cathode catalysts. *Chemical Society Reviews* 2012, 41 (6), 2172-2192.

[4] L. Chai, L. Zhang, X. Wang, L. Xu, C. Han, T.-T. Li, Y. Hu, J. Qian, S. Huang, Bottom-up synthesis of MOF-derived hollow N-doped carbon materials for enhanced ORR performance, *Carbon*, 2019, 146(7) 248-256.

[5] X. Zhong, W. Yi, Y. Qu, L. Zhang, H. Bai, Y. Zhu, J. Wan, S. Chen, M. Yang, L. Huang, M. Gu, H. Pan, B. Xu, Co single-atom anchored on Co<sub>3</sub>O<sub>4</sub> and nitrogen-doped active carbon toward bifunctional catalyst for zinc-air batteries, *Applied Catalysis B-Environmental*, 2020, 260(8) 267-272.

[6] W. Liu, J. Zhang, Z. Bai, G. Jiang, M. Li, K. Feng, L. Yang, Y. Ding, T. Yu, Z. Chen, ;A. Yu, Controllable Urchin-Like NiCo<sub>2</sub>S<sub>4</sub> Microsphere Synergized with Sulfur-Doped Graphene as Bifunctional Catalyst for Superior Rechargeable Zn-Air Battery. *Advanced Functional Materials* 2018, 28 (11).

[7] W. Zhang, H. Sun, Z. Zhu, R. Jiao, P. Mu, W. Liang, A. Li, N-doped hard carbon nanotubes derived from conjugated microporous polymer for electrocatalytic oxygen reduction reaction, *Renewable Energy*, 2020, (146),2270-2280.

[8] C. Hu, L. Dai, Multifunctional Carbon-Based Metal-Free Electrocatalysts for Simultaneous Oxygen Reduction, Oxygen Evolution, and Hydrogen Evolution, *Advanced Materials*, 2017, (29), 1604942

[9] H. Zhang, H.T. Chung, D. A. Cullen, S. Wagner, U. I. Kramm, K.L. More, P. Zelenay, G. Wu, High-performance fuel cell cathodes exclusively containing atomically dispersed iron active sites, *Energy & Environmental Science*, 2019,(12), 2548-2558.

[10] Q. Hu, G. Li, G. Li, X. Liu, B. Zhu, X. Chai, Q. Zhang, J. Liu, C. He, Trifunctional Electrocatalysis on Dual-Doped Graphene Nanorings-Integrated Boxes for Efficient

Water Splitting and Zn-Air Batteries, *Advanced Energy Materials*, 2019, 9(14) 1803867.

[11] Y. Shao, J.-P. Dodelet, G. Wu, P. Zelenay, PGM-Free Cathode Catalysts for PEM Fuel Cells: A Mini-Review on Stability Challenges, *Advanced Materials*, 2019,31(31) 1807615.

[12]N. T. Suen, S. F. Hung, Q. Quan, N. Zhang, Y. J. Xu,H. M. Chen, Electrocatalysis for the oxygen evolution reaction: recent development and future perspectives. *Chemical Society Reviews* 2017, 46 (2), 337-365.

[13] X. Ren, Q. Lv, L. Liu, B. Liu, Y. Wang, A. Liu, G. Wu, Current progress of Pt and Pt-based electrocatalysts used for fuel cells, *Sustainable Energy & Fuels*, 2020, 14 (3) 15-30.

[14] Y. Jiao, Y. Zheng, K. Davey, S. Z. Qiao, Activity origin and catalyst design principles for electrocatalytic hydrogen evolution on heteroatom-doped graphene, *Nature Energy*, 2016,12 (4).

[15] Y. Zhang, M. Luo, Y. Yang, Y. Li, S. Guo, Advanced Multifunctional Electrocatalysts for Energy Conversion, *ACS Energy Letters*, 2019, (4) 1672-1680.

[16] Q. B. Javier, E. Morallón, C. A. Diego. Metal-free heteroatom-doped carbon-based catalysts for ORR: A critical assessment about the role of heteroatoms. *Carbon* 2020, 165, 434-454.

[17] X. Li, X. Duan, C. Han, X. Fan, Y. Li, F. Zhang, G. Zhang, W. Peng, S. Wang, Chemical activation of nitrogen and sulfur co-doped graphene as defect-rich carbocatalyst for electrochemical water splitting, *Carbon*, 2019, (148) 540-549.

[18] M. Melchionna, P. Fornasiero, M. Prato, The Rise of Hydrogen Peroxide as the Main Product by Metal-Free Catalysis in Oxygen Reductions, *Advanced Materials*, 2019, 31(13),1802920.

[19] Q. B. Javier, M. F. Manuel, S. F. Emilio, M. Emilia, C. A. Diego, Towards understanding the active sites for the ORR in N-doped carbon materials through fine-tuning of nitrogen functionalities: an experimental and computational approach. *Journal of Materials Chemistry A*, 2019, (7), 24239-24250.

[20] H. Cui, Z. Zhou, D. Jia, Heteroatom-doped graphene as electrocatalysts for air

cathodes. *Materials Horizons* 2017, 4 (1), 7-19.

[21] L. S. Panchakarla, K. S. Subrahmanyam, S. K. Saha, A. Govindaraj, H. R. Krishnamurthy, U. V. Waghmare, C. N. R. Rao, Synthesis, Structure, and Properties of Boron- and Nitrogen-Doped Graphene, *Advanced Materials*, 2009, 21(46), 4726-4730 .

[22] W. Zhou, J. Jia, J. Lu, L. Yang, D. Hou, G. Li, S. Chen, Recent developments of carbon-based electrocatalysts for hydrogen evolution reaction, *Nano Energy*, 2016, (28) 29-43.

[23] S.K. Singh, K. Takeyasu, J. Nakamura, Active Sites and Mechanism of Oxygen Reduction Reaction Electrocatalysis on Nitrogen-Doped Carbon Materials, *Advanced Materials*, 2019,31 (13), 1804297.

[24] Z. Luo, S. Lim, Z. Tian, J. Shang, L. Lai, B. MacDonald, C. Fu, Z. Shen, T. Yu, J. Lin, Pyridinic N doped graphene: synthesis, electronic structure, and electrocatalytic property, *Journal of Materials Chemistry*, 2011, 21(22) , 8038-8044.

[25] X. Wang, A. Vasileff, Y. Jiao, Y. Zheng, S.-Z. Qiao, Electronic and Structural Engineering of Carbon-Based Metal-Free Electrocatalysts for Water Splitting, *Advanced Materials*, 2019, 31(13), 1803625.

[26] K. Qu, Y. Zheng, Y. Jiao, X. Zhang, S. Dai, S. Z. Qiao, Polydopamine-Inspired, Dual Heteroatom-Doped Carbon Nanotubes for Highly Efficient Overall Water Splitting. *Advanced Materials*, 2017, 7(9), 1602068.

[27] H. Xu, S. Ci, Y. Ding, G. Wang, Z. Wen, Recent advances in precious metal-free bifunctional catalysts for electrochemical conversion systems, *Journal of Materials Chemistry A*, 2019, (7) 8006-8029.

[28] Y. Zhou, Y. Leng, W. Zhou, J. Huang, M. Zhao, J. Zhan, C. Feng, Z. Tang, S. Chen, H. Liu, Sulfur and nitrogen self-doped carbon nanosheets derived from peanut root nodules as high-efficiency non-metal electrocatalyst for hydrogen evolution reaction, *Nano Energy*, 2015, (16) 357-366.

[29] R. Paul, Q. Dai, C. Hu, L. Dai, Ten years of carbon-based metal-free electrocatalysts, *Carbon Energy*, 2019, (1) 19-31.

[30] P. Li, H. Jang, J. Zhang, M. Tian, S. Chen, B. Yuan, Z. Wu, X. Liu, J. Cho, A Metal-Free N and P-Codoped Carbon Nanosphere as Bifunctional Electrocatalyst for

Rechargeable Zinc-Air Batteries. *Chemelectrochem* 2019, 6 (2), 393-397.

[31] L. Yang, J. Shui, L. Du, Y. Shao, J. Liu, L. Dai, Z. Hu, Carbon-Based Metal-Free ORR Electrocatalysts for Fuel Cells: Past, Present, and Future, *Advanced Materials*, 2019, 31 (13)1804799 .

[32] Y. Ito, W. Cong, T. Fujita, Z. Tang, M. Chen, High Catalytic Activity of Nitrogen and Sulfur Co-Doped Nanoporous Graphene in the Hydrogen Evolution Reaction, *Angewandte Chemie-International Edition*, 2015, 54 (13) 2131-2136.

[33] Chai. G. L, Qiu. K, Qiao. M, M. M.Titirici, C. Shang, Z. Guo, Active sites engineering leads to exceptional ORR and OER bifunctionality in P, N Co-doped graphene frameworks. *Energy & Environmental Science* 2017, 10 (5), 1186-1195.

[34] X. Zheng, J. Wu, X. Cao, J. Abbott, C. Jin, H. Wang, P. Strasser, R. Yang, X. Chen, G. Wu, N-, P-, and S-doped graphene-like carbon catalysts derived from onium salts with enhanced oxygen chemisorption for Zn-air battery cathodes, *Applied Catalysis B-Environmental*, 2019, (241) 442-451.

[35] M. Inagaki, M. Toyoda, Y. Soneda, T. Morishita, Nitrogen-doped carbon materials. *Carbon* 2018, 132, 104-140.

[36] Y. He, S. Hwang, D.A. Cullen, M.A. Uddin, L. Langhorst, B. Li, S. Karakalos, A.J. Kropf, E.C. Wegener, J. Sokolowski, M. Chen, D. Myers, D. Su, K.L. More, G. Wang, S. Litster, G. Wu, Highly active atomically dispersed CoN<sub>4</sub> fuel cell cathode catalysts derived from surfactant-assisted MOFs: carbon-shell confinement strategy, *Energy & Environmental Science*, 2019, (12) 250-260.

[37] H. Jiang, J. Gu, X. Zheng, M. Liu, X. Qiu, L. Wang, W. Li, Z. Chen, X. Ji, J. Li, Defect-rich and ultrathin N doped carbon nanosheets as advanced trifunctional metal-free electrocatalysts for the ORR, OER and HER, *Energy & Environmental Science*, 2019, (12) 322-333.

[38] D. Li, Y. Jia, G. Chang, J. Chen, H. Liu, J. Wang, Y. Hu, Y. Xia, D. Yang, X. Yao, A Defect-Driven Metal-free Electrocatalyst for Oxygen Reduction in Acidic Electrolyte, *Chem*, 2018, (4) 2345-2356.

- [39] K. P. Gong, F. Du, Z. H. Xia, M. Durstock, L. M. Dai, Nitrogen-Doped Carbon Nanotube Arrays with High Electrocatalytic Activity for Oxygen Reduction. *Science*, 2009, (323) 760-764.
- [40] R. Shibuya, T. Kondo, J. Nakamura, Bottom-Up Design of Nitrogen-Containing Carbon Catalysts for the Oxygen Reduction Reaction, *ChemCatChem*, 2018, (10) 2019-2023.
- [41] Q. Qin, H. Jang, P. Li, B. Yuan, X. Liu, J. Cho, A Tannic Acid-Derived N-, P-Codoped Carbon-Supported Iron-Based Nanocomposite as an Advanced Trifunctional Electrocatalyst for the Overall Water Splitting Cells and Zinc-Air Batteries, *Advanced Energy Materials*, 2019, (9) 1167-1173.
- [42] C. Hu, L. Dai, Carbon-Based Metal-Free Catalysts for Electrocatalysis beyond the ORR, *Angew Chem Int Ed Engl*, 2016, (55) 11736-11758.
- [43] J. Sun, S.E. Lowe, L. Zhang, Y. Wang, K. Pang, Y. Wang, Y. Zhong, P. Liu, K. Zhao, Z. Tang, H. Zhao, Ultrathin Nitrogen-Doped Holey Carbon@Graphene Bifunctional Electrocatalyst for Oxygen Reduction and Evolution Reactions in Alkaline and Acidic Media, *Angewandte Chemie-International Edition*, 2018, (57) 16511-16515.
- [44] H. F. Wang, C. Tang, Q. Zhang, A Review of Precious-Metal-Free Bifunctional Oxygen Electrocatalysts: Rational Design and Applications in Zn-Air Batteries, *Advanced Functional Materials*, 2018, 28 (46) 1803329.
- [45] X. Yan, Y. Jia, X. Yao, Defects on carbons for electrocatalytic oxygen reduction, *Chemical Society Reviews*, 2018, (47) 7628-7658.
- [46] Z. Pei, H. Li, Y. Huang, Q. Xue, Y. Huang, M. Zhu, Z. Wang, C. Zhi, Texturing in situ: N,S-enriched hierarchically porous carbon as a highly active reversible oxygen electrocatalyst, *Energy & Environmental Science*, 2017, (10) 742-749.
- [47] K. Gao, B. Wang, L. Tao, B. V. Cunniff, Z. Zhang, S. Wang, R. S. Ruoff, L. Qu, Efficient Metal-Free Electrocatalysts from N-Doped Carbon Nanomaterials: Mono-Doping and Co-Doping. *Advanced Materials*, 2019, (31), 1805121.
- [48] M. Borghei, J. Lehtonen, L. Liu, O.J. Rojas, Advanced Biomass-Derived Electrocatalysts for the Oxygen Reduction Reaction, *Advanced Materials*, 2018, 30 (24)

1703691.

[49] B. C. Hu, Z. Y. Wu, S. Q. Chu, H. W. Zhu, H. W. Liang, J. Zhang, S.-H. Yu, SiO<sub>2</sub>-protected shell mediated templating synthesis of Fe-N-doped carbon nanofibers and their enhanced oxygen reduction reaction performance, *Energy & Environmental Science*, 2018, (11) 2208-2215.

[50] M. Li, C. Liu, H. Zhao, H. An, H. Cao, Y. Zhang, Z. Fan, Tuning sulfur doping in graphene for highly sensitive dopamine biosensors, *Carbon*, 2015, (86) 197-206.

[51] S. Mu, G. D. Samolyuk, S. Wimmer, C. M. Troparevsky, S. N. Khan, S. M. George, M. Stocks. Uncovering electron scattering mechanisms in NiFeCoCrMn derived concentrated solid solution and high entropy alloys. *Computational Materials* 2019, (1), 78-83.

[52] Q. J. Ju, R. G. Ma, Y. F. Hu, B. B. Guo, Q. Liu, T. J. Thomas, T. Zhang, M. H. Yang, W. Chen, J. C. Wang. Highly Localized C-N<sub>2</sub> Sites for Efficient Oxygen Reduction. *ACS Catalysis* 2020, (16), 9366-9375.

[53] Q. B. Javier, M. F. Manuel, S. F. Emilio, M. Emilia, C. A. Diego, Towards understanding the active sites for the ORR in N-doped carbon materials through fine-tuning of nitrogen functionalities: an experimental and computational approach. *Journal of Materials Chemistry A*, 2019, (7), 24239-24250.

*Every reasonable effort has been made to acknowledge the owners of copyright material. I would be pleased to hear from any copyright owner who has been omitted or incorrectly acknowledged.*



## **Chapter 4: Precursor modulated active sites of N, P Co-doped graphene-structured based carbon catalysts via One-step pyrolysis method for Enhanced Oxygen Reduction Reaction and Oxygen Evolution Reaction**

### **Abstract**

Elucidating the correlation of active sites configuration of binary heteroatoms-doped carbon materials and the catalytic activity for oxygen reduction reaction (ORR) and Oxygen evolution reaction (OER) is essential to develop performance-oriented metal-free catalysts for effective energy conversion technologies. Herein, heteroatom N and P doped graphene-like carbon (NP-G) catalysts with configurations of different N species coordinate with P (Pyridinic N+Graphitic N+P, Pyridinic N+Pyrrolic N+P, and Pyridinic N+Pyridinic N+P) were successfully synthesized via one-step pyrolysis of N-containing precursors mixture. 5-aminouracil was selected as one of the N-containing precursor platform due to their preference on formation of high percentage of Pyridinic N among all N types and phytic acid as P source. 2,6-diaminopyridine and 1,3-diaminobenzene were act as another precursors mixed with 5-aminouracil respectively. Electrochemical results demonstrate that the catalyst with Pyridinic N+Graphitic N+P configuration exhibits the highest ORR catalytic activity among all these configurations. By contrast, Pyridinic N+Pyrrolic N+P configuration contribute greatly for OER performance of the NP-G catalysts. Density functional theory calculation (DFT) further validated that these different N, P configurations produce different electronic structure



on surrounding carbon atoms that leads to significant differences cover ORR and OER activity of the NP-G catalysts, and thus function control from ORR to OER is realized via tuning active sites configuration of different N species and P. This study shed new light on the intrinsic relationship between specific N species coordinated with P and tuning the electrocatalytic activity for ORR and OER in co-doped carbon-based metal free electrocatalysts for energy conversion technologies.

*\*Reprinted (adapted) with permission from Xiaoran Zhang, Xiao Zhang, Xue Xiang, Can Pan, Qinghao Meng, Chao Hao, Zhi Qun Tian, Pei Kang Shen, San Ping Jiang\*  
Nitrogen and Phosphate Co-doped Graphene as Efficient Bifunctional Electrocatalysts by Precursor Modulation Strategy for Oxygen Reduction and Evolution Reactions. ChemElectroChem. DOI10.1002/celec.202100599.*

## **4.1 Introduction**

Heteroatom doped metal-free carbon materials is one of the most promising substitutes for metal based catalysts for electrochemical energy conversion devices such as fuel cells and metal-air battery [1-3]. Oxygen reduction reaction (ORR) and oxygen evolution reaction (OER) are crucial reactions for fuel cells. The application of heteroatom doped metal-free carbon materials as electrocatalysts for ORR and OER attracted wide attention. Especially, carbon based electrocatalysts aroused great concern as an magical material due to their intriguing physical, chemical and mechanical properties originating from its unique electronic band structures which

exhibits extremely promising tunable characteristics via chemical modification that can potentially achieve the required control for diversity of applications [4-6].

In the past decades, heteroatoms doped carbon materials have been developed as metal-free catalysts for ORR and OER[7-13]. Doping with heteroatoms could modulate the electronic surface of carbon and fine tunes the ORR and OER catalytic activity [14]. Both theoretical calculations and experimental studies have confirmed that introducing a heteroatom such as N, P, S, *etc.* into the carbon lattice improves the carbon's ORR activity greatly[15]. Dai's group first reported in 2009 that vertically aligned nitrogen-doped carbon nanotube arrays (VA-NCNTs) exhibits considerable ORR activity.[16] And this has led to significant research and development activities of heteroatoms-doped carbon-based electrocatalysts [17]. The high electronegativity of nitrogen induces increased positive charge density in carbon, creating active sites for ORR and OER. Moreover, N-doping, due to its size similarity with carbon, provides favorable improvements in electron transport properties of the carbon matrix and is therefore a preferred dopant for realizing highly efficient electrocatalysts for applications in fuel cells[18-19]. Especially, the introducing of N leads to asymmetrical charge distributions on the adjacent carbon atoms and cause larger polarizations, due to its strong electronegativity[20]. In the case of N-doped carbon, planar pyridinic N with a lone electron pair is considered to be the active configuration to improve the electron-donating capability and weaken the O-O bond [21], and the carbon atoms with Lewis basicity adjacent to pyridinic N are the most active sites for ORR[22-24]. Besides, graphitic N is considered as one of the most important active site components due to

their great contributes to high conductivity which is critical for the ORR and OER catalytic performance. However, single heteroatom doping is usually difficult to achieve optimal electronic and geometric structures favorable for the ORR. Therefore, by introducing a secondary element or fabricating specific defect structures in the pristine carbon framework, engineering of electron- or spin redistribution in the  $sp^2$  conjugated carbon matrix could be achieved for wide application as multifunctional electrocatalysis [25]. It has been found that doping with two or more heteroatoms such as nitrogen-sulfur (NS), nitrogen-phosphate (NP), and nitrogen-boron (NB) are more effective to improve the electrocatalytic activity of carbon-based catalysts [26]. Among of them, NP co-doped carbon-based catalysts for ORR and OER have attracted a significant attention[27]. Compared to N, P has the same number of valence electrons but a higher electron-donating ability due to its larger atomic radius (110 pm). Moreover, the electronegativity of P is 2.19, lower than that of C (2.55), and the charged sites of  $P^+$  are created when P is doped in carbon. In addition, P with a larger atomic radius favors the  $sp^3$ -orbital configuration, generating a high distortion of carbon structures and forming large number of open edge sites, which enhance the ORR activity of carbon[28-30]. Despite of great efforts in the development of N-doped carbon-based catalysts, there is still a big gap on catalytic activity between N-doped metal-free catalysts and Pt/C catalysts. One of the main reasons is related to the difficulty in the control of various N species in the doped catalysts for ORR. The synergistic effects of the different N species configuration with P and their correlation with the catalytic activity for ORR and OER are not clear. Therefore, research on

configuration of P coordinate with different N species, especially, Pyridinic N based N types and the influence they produced on tuning catalytic activity for ORR and OER is highly desirable.

In this study, N, P configuration in graphene based carbon materials are controlled by reasonable selecting 5-Aminouracil as precursors platform as its preference on producing high content of Pyridinic N, 2,6-Diaminopyridine and 1,3-Diaminobenzene was selected as another reactant N-containing precursors, and phytic acid as P source. It is notable that. all these nitrogen-containing precursors have a conjugated system of connected *p*-orbitals with delocalized electrons in molecules with alternating single and double bonds[31-32]. This delocalization of *p* electrons makes them highly effective as desired carbon/nitrogen sources to convert to different C-N bonding during heat treatment process derived from their different nitrogen locations and amount in the carbon host, which endows these six-membered heterocyclic precursors with high electronic flexibility, capable of designing and tuning active sites configuration for performance-oriented heteroatoms doped electrocatalysts[33]. In this study, three N,P co-doped graphene-based catalysts featured with different Pyridinic N based N species configuration coordinate with P (Graphitic N+ Pyridinic N+P, Pyridinic N+Pyrrolic N+P and Pyridinic N+ Pyridinic N+P) were successfully prepared via direct Pyrolysis of N-containing precursors mixture with phytic acid as P source.

## **4.2 Experimental**

### *4.2.1. Materials and synthesis*

A series of six-membered heterocyclic compounds with aromatic rings connected

through NH<sub>2</sub> groups were selected as typical N-containing precursors. 1,3-Benzenediamine(Macklin) with the conventional aromatic benzene ring, 2,6-Diaminopyridine(Macklin) (one N atom replaced in benzene ring) and 5-Aminouracil(Macklin)with aromatic pyridine and pyrimidine ring, these chemicals were purchased and used without further treatment.

In the synthesis of NP co-doped graphene catalysts (NP-G), 5-Aminouracil was mixed with 2,6-diaminopyridine, and 1,3-diaminobenzene (with the molar ratio of 1:1), respectively, and grind for twenty minutes, Phytic acid was added as P source. After heat treatment at 350 °C for 1 h, 650 °C for 1 h and 950 °C for 1 h in the presence of N<sub>2</sub> gas flow, a series of catalysts were obtained and denoted as NP/C-Pyridinic N+Graphitic N or N<sub>P</sub>+N<sub>G</sub>/PG obtained from precursor 5-Aminouracil+2,6-diaminopyridine+ Phytic acid mixture, NP/C-Pyridinic N+Pyridinic N or N<sub>P</sub>/PG from precursor 5-Aminouracil+ Phytic acid and NP/C-Pyridinic N+Pyrrolic N or N<sub>P</sub>+N<sub>PY</sub>/PG from precursor 5-Aminouracil+1,3-diaminobenzene + Phytic acid mixture, respectively.

Figure 4-1 shows the synthesis processes of N,P-Co-doped graphene via the control of the selection of precursors. Three kinds of precursors were obtained with mixture of 5-Aminouracil with 2,6-diaminopyridine, 5-Aminouracil with 1,3-diaminobenzene, single 5-Aminouracil as precursors respectively with Phytic acid as P source. Sectional heating control at 350 °C, 650 °C and 950 °C for 1h respectively were used to realize self-polymerization of amino-group. The final products NP/C-Pyridinic

N+Graphitic N( $N_P+N_G/PG$ ), NP/C-Pyridinic N+Pyridinic N( $N_P/PG$ ) and NP/C-Pyridinic N+Pyrrolic N( $N_P+N_{PY}/PG$ ) were obtained after cooling.

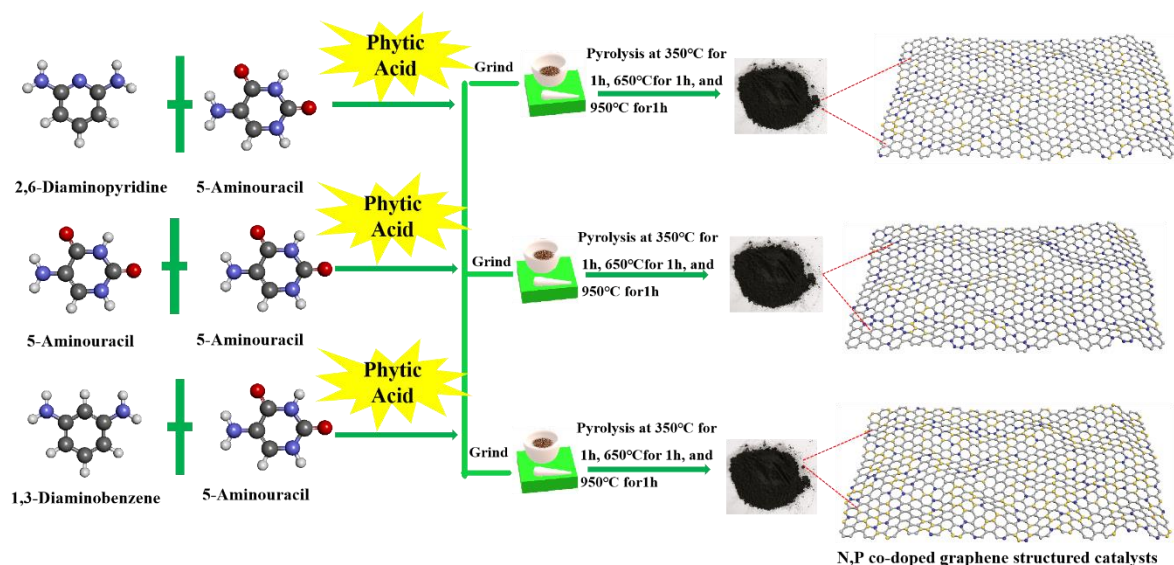


**Figure 4-1.** Illustration of the synthesis process of N,P Co-doped graphene structured catalysts.

#### 4.2.2 Materials characterization

The morphologies of these catalysts were characterized by Scanning Electron Microscopy (SEM and FESEM) using a Hitach SU8220 field emission scanning electron microscope and Transmission Electron Microscopy (TEM) using Titan ETEM G2 80-300 electron microscope operating at 300 kV). X-ray diffraction (XRD) was carried out on a Smart Lab diffractometer using a Cu  $K\alpha$  ( $\lambda=1.5405 \text{ \AA}$ ) radiation source (Rigaku Co.). Raman spectra were measured on a Lab Ram HR Evolution Raman spectrometer with 532 nm wavelength incident laser light (Horiba Jobin Yvon Co.). Brunauer-Emmett-Teller (BET) surface area and pore size distribution of catalysts was analysed using a Micromeritics instrument (CORP ASAP 2460). X-ray photoelectron spectroscopy (XPS) measurements were carried out on an ESCALAB 250 system to determine the composition and chemical states of the catalysts.

### 4.2.3 Electrochemical Measurements

All electrochemical measurements were conducted on bipotentiostat WD-20 BASIC with rotating ring disk electrode (RRDE) system (Pine Instrumentation, USA) in a thermostatically-controlled three-electrode cell at 25°C. The three-electrode cell constitutes of a reversible hydrogen electrode (RHE) electrode that were corrected before measurements as the reference electrode and a graphite rod as the counter electrode, in order to eliminate possible of Pt contamination on the catalysts, RRDE with a glassy carbon as the working electrode (diameter 5.61mm). The estimated catalyst loading on the working electrode was 600.0  $\mu\text{g cm}^{-2}$ . For comparison, the commercial Pt/C catalyst (46.7% Pt/C, Tanaka) is used. The Pt loading is 40  $\mu\text{g cm}^{-2}$ . ORR activity of the catalysts was evaluated in O<sub>2</sub>-saturated 0.1 M KOH. Linear sweep voltammetry (LSV) was performed from 0 V to 1.10 V at a scan rate of 5 mV s<sup>-1</sup> at a rotating rate of 1600 rpm, while the Pt ring electrode was held at 1.2 V vs. RHE.

#### *Test of Zn-air batteries.*

The electrochemical performance of Zn-air batteries was evaluated in a home-made electrochemical devices. 10 mg of catalysts (or 40 wt.% Pt/C) was mixed using 0.035 mL of 5 wt% Nafion solution and 1 mL of ethanol followed by 30 min sonication to form homogeneous ink. For the air cathode, as-prepared electrocatalyst ink was coated onto carbon fiber paper (0.785 cm<sup>2</sup>) with loading of 1.0 mg cm<sup>-2</sup> by electrospinning spray. A polished zinc foil and 6 M KOH were used as the anode and electrolyte, respectively. Polarization curves and galvanostatic discharge tests were carried out on a bipotentiostat WD-20 BASIC electrochemical workstation.

#### 4.2.4 Density functional theory calculation

The system energy DFT calculations are performed by using the Vienna *ab initio* simulation package (VASP) code. The Projector Augmented Wave (PAW) and the Perdew-Burke-Ernzerhof (PBE) functional was used to describe the exchange-correlation interaction. The supermodel was built with the lattice parameters of  $a=35 \text{ \AA}$ ,  $b=25 \text{ \AA}$ . The vacuum slab of  $15 \text{ \AA}$  was applied in  $z$  direction to avoid the periodic interactions. The energy cut-off for the plane-wave basis set was set to 450 eV for all relaxation, energy and electronic properties calculations. The Brillouin zone was sampled with Monkhorst-Pack  $3 \times 3 \times 1$  k-points generated manually. A Gaussian smearing with a width of 0.1 eV was used in all calculations. The convergence tolerance of energy was set to  $1.0 \times 10^{-5}$  eV/atoms. The maximal displacement and force is  $1.0 \times 10^{-3} \text{ \AA}$  and  $0.02 \text{ eV/\AA}$ , respectively.

### 4.3 Results and discussion

#### 4.3.1 Microstructure and phase of N, P co-doped graphene catalysts.

The morphological features of as-prepared N doped graphene catalysts were first observed using transmission electron microscopy (TEM) and Scanning Electron Microscope (SEM). As shown in Figure 4-2(a-i), Transmission electron microscope (TEM) images of NP/C-Pyridinic N+Graphitic N( $N_P+N_G/PG$ ) catalyst shows “fluffy”porous-graphene structure, meanwhile, the high-resolution TEM image manifests measured graphene lattice fringe layers below 10 layers with its typical graphene lattice spacing of 0.34 nm. In addition, NP/C-Pyridinic N+Pyridinic N( $N_P/PG$ ) and NP/C-Pyridinic N+Pyrrolic N( $N_P+N_{PY}/PG$ ) samples exhibit similar graphene



morphological structure, indicating that co-doped of N,P catalysts derived from different N-containing precursors produce little impact on final morphological structure.

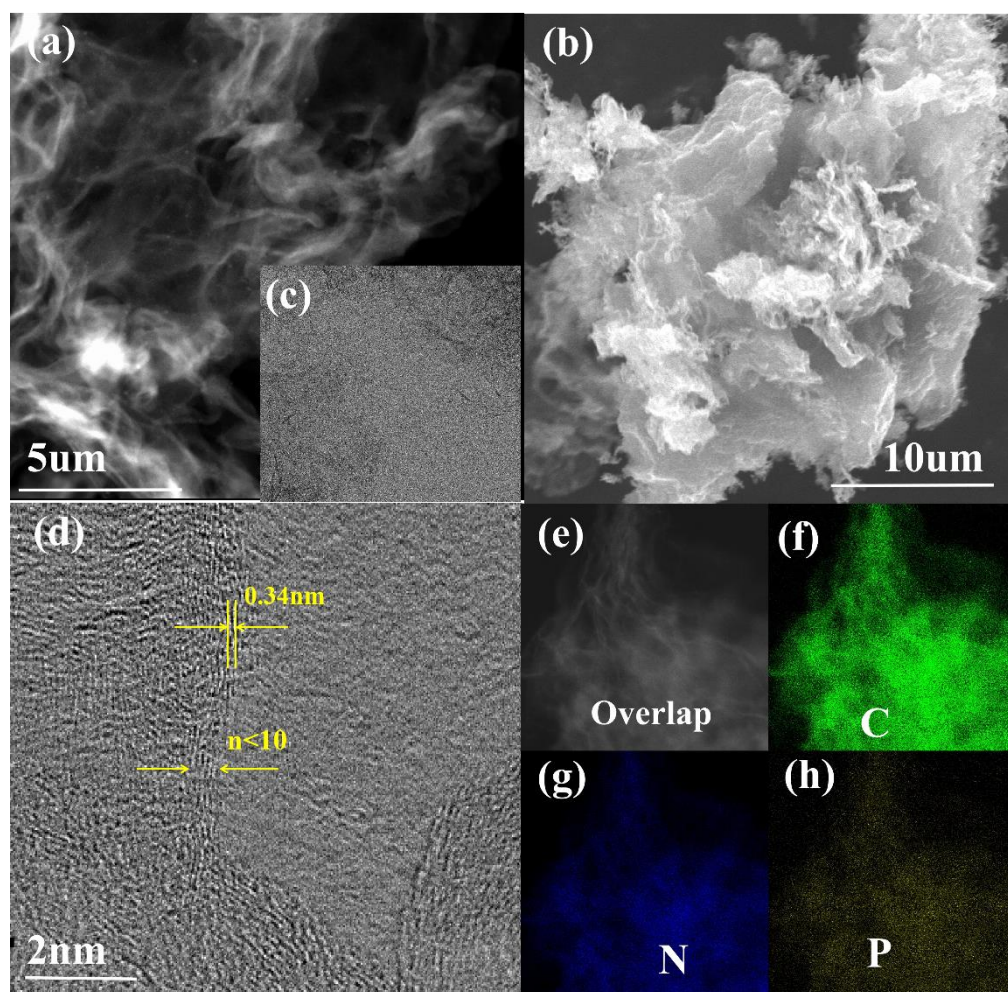


**Figure 4-2.** TEM images of NP/C-Graphitic N+ Pyridinic N (a,c,d) SEM image(b) and elements mapping(e, f, g, h) of NP/C-Graphitic N+ Pyridinic N.

Figure 4-3a shows X-ray diffraction (XRD) patterns of the as-prepared NP-G catalysts. All of them possess a sharp diffraction peak at around  $26^\circ$  and broad peak at  $43.3^\circ$  which are attributed to (002) and (100) of graphite, suggesting the highly graphitized nature of these NP co-doped graphene catalysts. Raman spectroscopy provides a sensitive probe for electronic and phonon structures of heteroatoms-doped carbon materials [36]. Figure 4-3b shows the Raman spectra of the as-prepared NP-G catalysts. The two main peaks at  $\sim 1350$  and  $1580\text{ cm}^{-1}$  are ascribed to the defective

peak (D) and graphitic peak (G), respectively [37]. As shown in Figure 4-3b, the ratio of D and G peaks is an important parameter to reflect the doping degree of these carbon matrix. The ID/IG ratio is 1.172, 1.136, 1.241 for NP/C-Pyridinic N+Graphitic N( $N_P+N_G/PG$ ), NP/C-Pyridinic N+Pyridinic N( $N_P/PG$ ) and NP/C-Pyridinic N+Pyrrolic N( $N_P+N_{PY}/PG$ ) respectively. The results indicate that different N species configurations play a significant role in the disorder degree of their corresponding N doped carbon materials. The  $N_2$  adsorption and desorption isotherms of these catalysts display characteristics of type-IV with obvious  $H_4$  hysteresis loops, indicating the coexistence of micropore and mesopore in the structure of the NP-G catalysts (Figure 3c). BET surface areas of NP/C-Pyridinic N+Graphitic N( $N_P+N_G/PG$ ), NP/C-Pyridinic N+Pyridinic N( $N_P/PG$ ) and NP/C-Pyridinic N+Pyrrolic N( $N_P+N_{PY}/PG$ ) are, 987, 1114, 1062  $m^2g^{-1}$  respectively. The pore size distribution of the samples is also similar with a large portion of pore size in the 1-2 nm region and a small portion of mesopores with diameter at 2-10nm (Figure 4-3d). The hierarchical pore structure could enhance the electrochemical performance of catalysts by providing fast mass transportation.

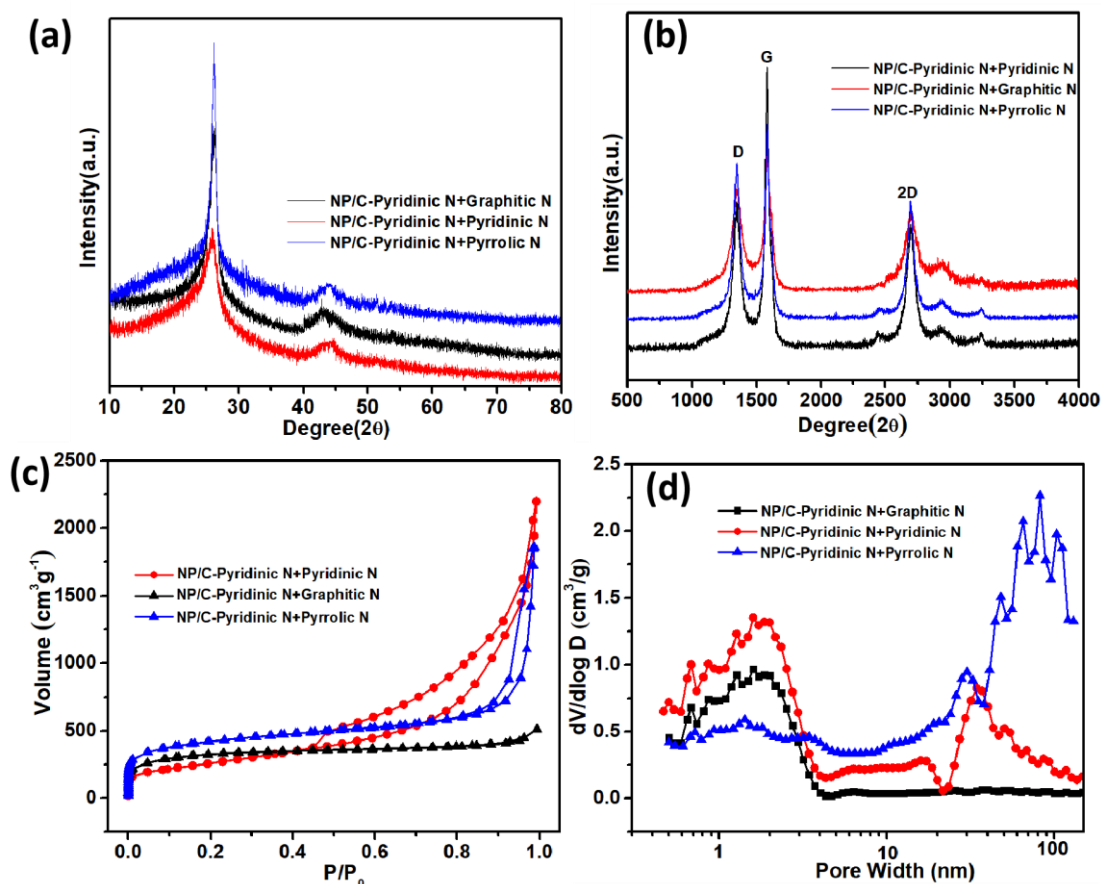


**Figure 4-3.** XRD (a) and Raman patterns (b) and Nitrogen adsorption-desorption isotherms (c) and Pore size distribution (d) of NP/C-Pyridinic N+Graphitic N(N<sub>P</sub>+N<sub>G</sub>/PG), NP/C-Pyridinic N+Pyridinic N(N<sub>P</sub>/PG) and NP/C-Pyridinic N+Pyrrolic N(N<sub>P</sub>+N<sub>PY</sub>/PG) respectively.

#### 4.3.2 Element analysis of NP-G catalysts

X-ray photoelectron spectroscopy (XPS) was conducted to elucidate the chemical composition and element content and the results are shown in Figure 4-4a. It can be found that N, P were successfully doped in these NP-G catalysts. From the high-resolution XPS spectra of C1s (Figure 4-4b), it is obvious that the binding energy (BE) of C1s of NP/C-Pyridinic N+Pyrrolic N is 284.85eV, shifted positively to 284.97eV and 285.13eV for NP/C-Pyridinic N+Pyridinic N and NP/C-Pyridinic N+Graphitic N, respectively. Such increase in the binding energy of C1s implies that there is a strong interaction between carbon atoms and doped N, P heteroatoms [40-41]. The high

resolution of C1s spectra of the catalysts can be deconvoluted into five main peaks at 285.5, 286.42, 284.3, 288.4 and 291 eV, which is assignable to C-C, C-N, C=O, -COO and  $\pi$ - $\pi$ , respectively[42]. Among them, C-C component has the largest proportion, followed by that of C-N with 4.87%, 4.76%, 4.53% in NP/C-Pyridinic N+Graphitic N, NP/C-Pyridinic N+Pyridinic N and NP/C-Pyridinic N+Pyrrolic N, respectively.

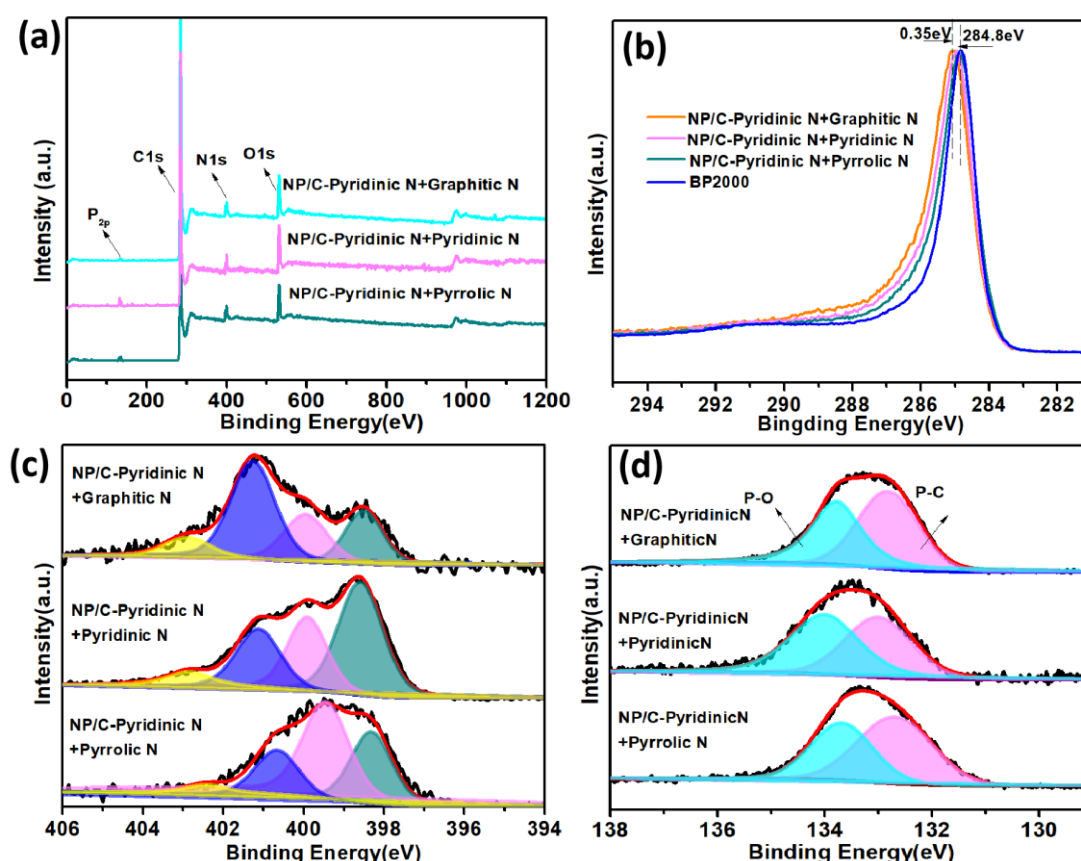


**Figure 4-4.** The survey (a) and main peaks of C1s (b) high-resolution XPS spectra of N1s(c) and P<sub>2p</sub>(d) for NP/C-Pyridinic N+Graphitic N(N<sub>P</sub>+N<sub>G</sub>/PG), NP/C-Pyridinic N+Pyridinic N(N<sub>P</sub>/PG) and NP/C-Pyridinic N+Pyrrolic N(N<sub>P</sub>+N<sub>PY</sub>/PG).

Nitrogen is an important doping element that influences catalytic performance greatly. The doped N atomic content of NP/C-Pyridinic N+Graphitic N(N<sub>P</sub>+N<sub>G</sub>/PG), NP/C-Pyridinic N+Pyridinic N(N<sub>P</sub>/PG) and NP/C-Pyridinic N+Pyrrolic N(N<sub>P</sub>+N<sub>PY</sub>/PG) catalysts is 4.52%, 5.08%, and 5.14%, respectively. As shown in Figure 4-4c, N1s spectra of the samples could be deconvoluted into four main peaks at 398.25, 399.79,

401.12 and 403.5 eV, which can be assigned to pyridinic N, pyrrolic N, graphitic N, and oxidized N, respectively[43-44]. In addition, as shown in Figure 4-5c, it is clear that NP/C-Pyridinic N+Pyridinic N( $N_P/PG$ ) possess high content of pyridinic N with 61.8%, significantly higher than 31.08% of NP/C-Pyridinic N+Graphitic N( $N_P+N_G/PG$ ) and 20.21% from NP/C-Pyridinic N+Pyrrolic N( $N_P+N_{PY}/PG$ ). On the other hand, NP/C-Pyridinic N+Graphitic N( $N_P+N_G/PG$ ) tends to produce high content of graphitic N, 56.57%, highest among all three N, P co-doped graphene materials. By contrast, NP/C-Pyridinic N+Pyrrolic N( $N_P+N_{PY}/PG$ ) possess highest content of Pyrrolic N, 53.81%. This indicates the content of doped N configuration or species such as pyridinic N, pyrrolic N, graphitic N can be controlled in certain degree by using different N precursors. The specific content of these N species in three N, P co-doped catalysts are shown in Figure 4-5c. P was successfully doped into graphene materials with similar P content. The specific content of P doping is 0.67at%, 0.65at% and 0.71at% in NP/C-Pyridinic N+Graphitic N( $N_P+N_G/PG$ ), NP/C-Pyridinic N+Pyridinic N( $N_P/PG$ ) and NP/C-Pyridinic N+Pyrrolic N( $N_P+N_{PY}/PG$ ), respectively. The P2p spectra show two typical P species at 133 eV for P-C and 134 eV for P-O (Figure 4-4d).

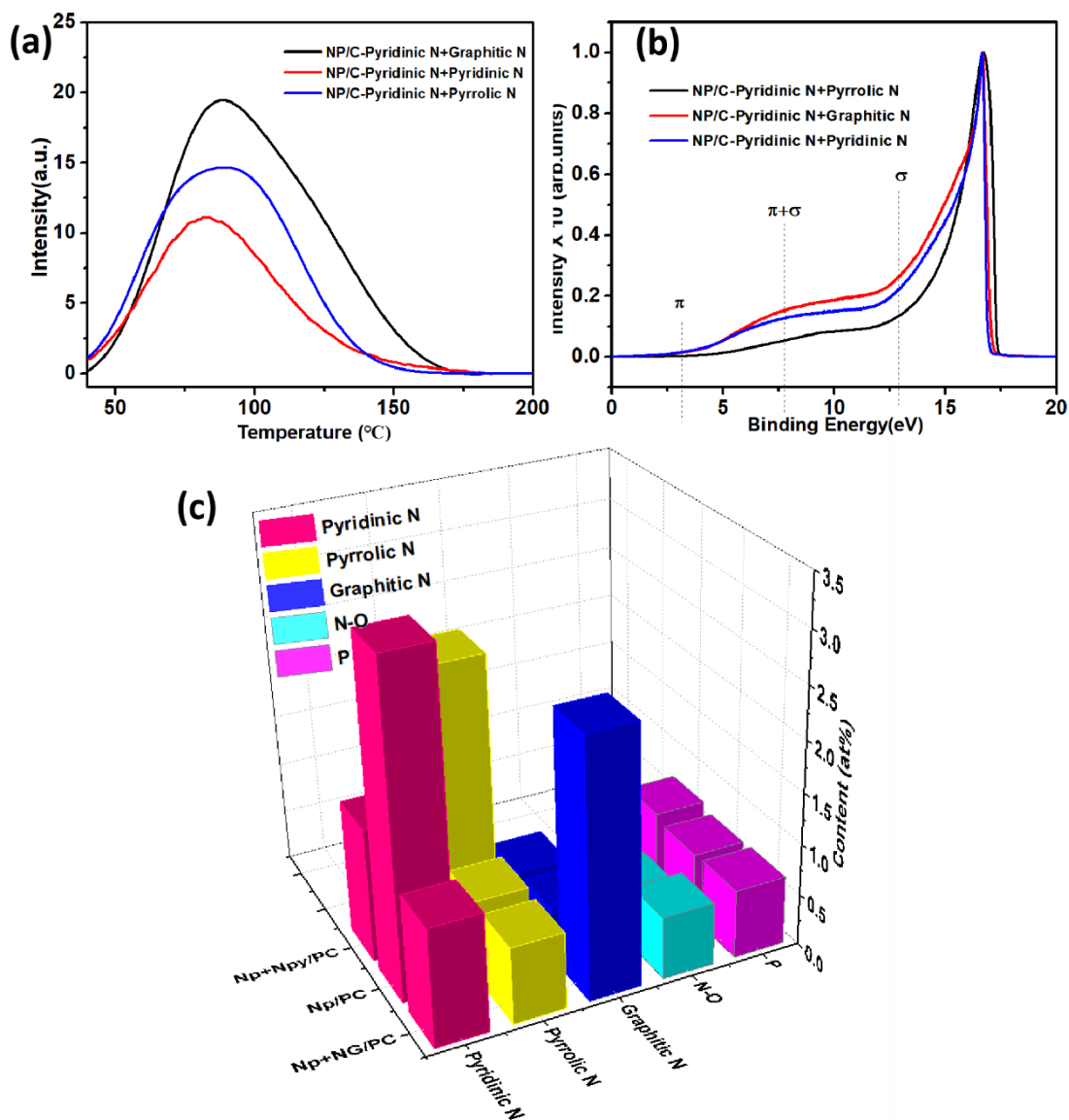


**Figure 4-5.** CO<sub>2</sub> TPD profiles(a) and UPS spectra (b), The 3D bar charts of specific percentage of each species of N and P in NP/C-Pyridinic N+Graphitic N(N<sub>P</sub>+N<sub>G</sub>/PG), NP/C-Pyridinic N+Pyridinic N(N<sub>P</sub>/PG) and NP/C-Pyridinic N+Pyrrolic N(N<sub>P</sub>+N<sub>PY</sub>/PG), respectively (c).

To further study the relationship between active sites and the chemical environment of carbon atoms, Temperature Programmed Desorption (TPD) of CO<sub>2</sub> was conducted on NP/C catalysts as a probe of the Lewis base site to clarify the basicity characteristic of the catalysts. As shown in Figure 4-5a. Because Lewis base sites is an important property of doped carbon that reflects electronic distribution around carbon atoms and is considered as important active origin for carbon based catalysts[44]. Based

on the TPD profiles of CO<sub>2</sub> of N, P co- doped graphene catalysts, it is obvious that NP/C-Pyridinic N+Pyridinic N catalyst exhibits the largest CO<sub>2</sub> desorption peak, demonstrating its strong basicity, due to the highest content of Pyridinic N instead of NP/G-Pyridinic N+Pyridinic N that possess the highest catalytic activity for ORR among these three samples. Pyridinic N dopant is generally claimed as the most contribution to the basicity of N doped carbon due to the fact that its adjacent carbons feature a localized density of states in the occupied region near the Fermi level<sup>45</sup>. Combining with the results of XPS, CO<sub>2</sub> adsorption results, it is demonstrated that no matter Lewis base site that closely linked with active sites configuration or final catalytic activity for ORR could be reflected well via electronic structural characteristics of surrounding carbon atoms around doping atom.

Ultraviolet photoelectron spectroscopy (UPS) was employed as a credible measurement for further investigating electronic structures, valence band edges and work functions of doped N,P co-doped samples. As displayed in Figure 4-5b, three peaks can be observed for these samples. A broad peak at around 3 eV is assigned as a 2p- $\pi$  state. The 2p- $\pi$  peaks of NP/C-Pyridinic N+Graphitic N(N<sub>P</sub>+N<sub>G</sub>/PG), NP/C-Pyridinic N+Pyridinic N(N<sub>P</sub>/PG) and NP/C-Pyridinic N+Pyrrolic N(N<sub>P</sub>+N<sub>PY</sub>/PG) slightly shift to the lower binding energy. This may be attributed to the electron transfer from carbon to sulfur(electron deficiency), leading to a lower shift of the Fermi level (EF). The weakening of the 2p- $\pi$  +  $\sigma$  peak of these samples at about 7 eV can be explained by the  $\pi$ -doping effect. For N,S co-doping, all valence electrons of S and N will participate in the bonding with

neighboring carbons, while the additional electron for  $\pi$  bonding will vanish. Additionally, a more prominent  $2\sigma$  peak of NP/C-Pyridinic N+Graphitic N(N<sub>P</sub>+N<sub>G</sub>/PG) compared with that of NP/C-Pyridinic N+Pyridinic N(N<sub>P</sub>/PG) and NP/C-Pyridinic N+Pyrrolic N(N<sub>P</sub>+N<sub>PY</sub>/PG) at the nominal binding energy (about 13 eV) is due to a higher density of states (DOSs) in the unoccupied states originating from the interlayer band that has larger charge densities between N,P and carbon plane.

#### 4.3.2 Electrochemical activity for ORR and OER

ORR and OER performance was evaluated by Linear Sweep Voltammetry (LSV) in 0.1M KOH solution, using Rotating Ring Disk Electrode (RRDE). The catalyst loading was 0.6mg/cm<sup>2</sup>. As shown in Figure 4-6a, NP/C-Pyridinic N+Graphitic N catalyst exhibits the best performance for ORR with the onset and half-wave potentials ( $E_{\text{onset}}$  and  $E_{1/2}$ ) of 1.01 and 0.89 V vs. RHE, respectively (in this study,  $E_{\text{onset}}$  is defined as the potential of current density at 1 $\mu$ A cm<sup>-2</sup>). The activity of NP/C-Pyridinic N+Graphitic N catalyst is even superior to commercial Pt/C with  $E_{\text{onset}}$ =1.0 V and  $E_{1/2}$ =0.86 V. In the case of NP/C-Pyridinic N+Pyridinic N and NP/C-Pyridinic N+Pyrrolic N catalysts,  $E_{\text{onset}}$  and  $E_{1/2}$  are 0.94 and 0.85 V, and 0.91 and 0.81 V, respectively. Tafel slope is 71.54, 80.5 and 109.2 mV decade<sup>-1</sup> for the ORR on NP/C-Pyridinic N+Graphitic N, NP/C-Pyridinic N+Pyrrolic N and NP/C-Pyridinic N+Pyridinic N, respectively (Figure 7b). This indicates that the different configuration of P and N species in the carbon-based materials has a significant influence on their catalytic activity for ORR.



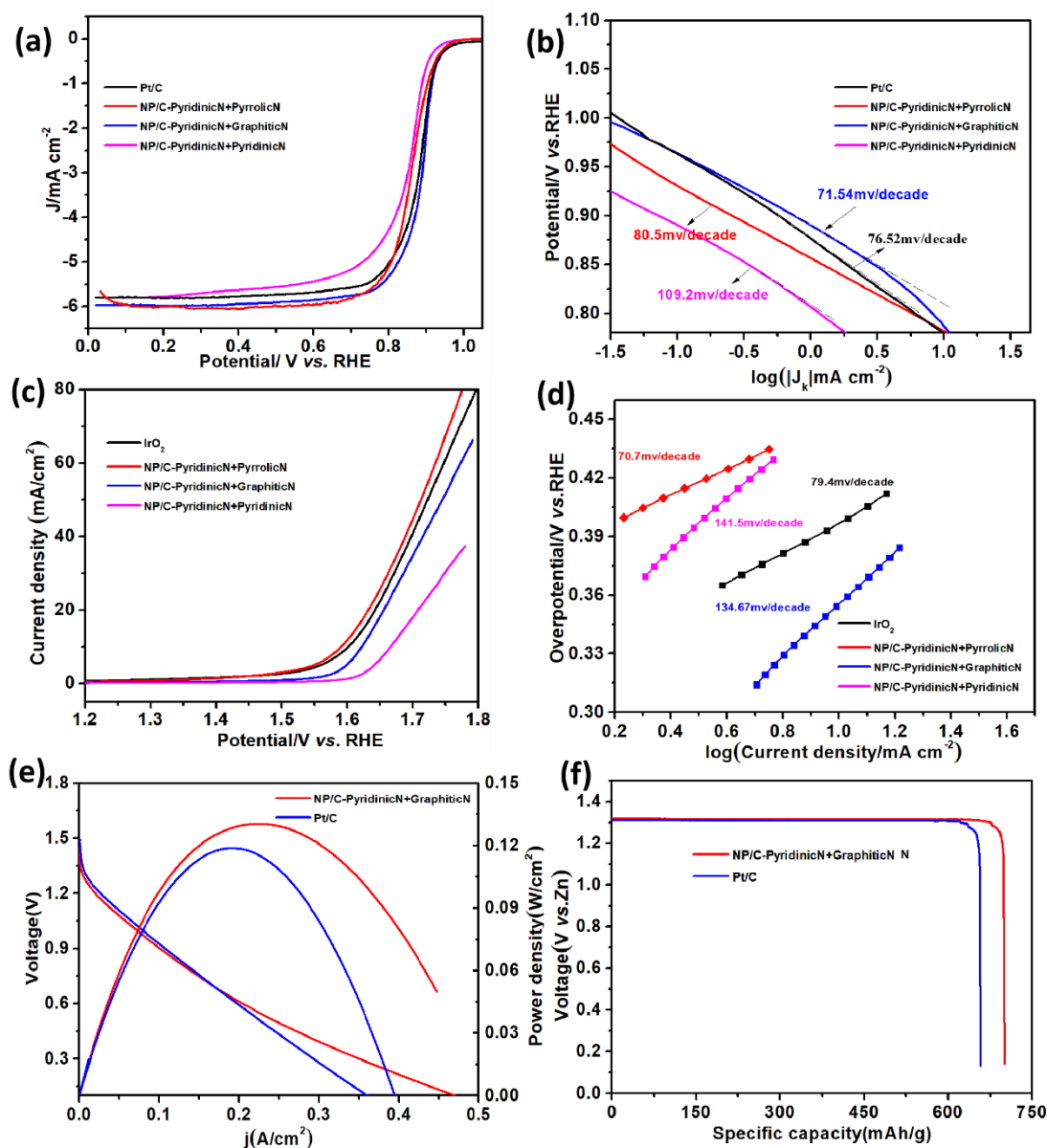


**Figure 4-6.** LSV curves of ORR (a), The kinetic current density (b), LSV curves of OER(c), Tafel slope (d) of NP/C-Pyridinic N+Graphitic N(N<sub>P</sub>+N<sub>G</sub>/PG), NP/C-Pyridinic N+Pyridinic N(N<sub>P</sub>/PG) and NP/C-Pyridinic N+Pyrrolic N(N<sub>P</sub>+N<sub>PY</sub>/PG) and Pt/C in 0.1MKOH. . Polarization curves and the corresponding power density plots of NP/C-Pyridinic N+Graphitic N and Pt/C (e), Curves specific capacities at current densities 10 mA cm<sup>-2</sup> of the Zn-air batteries (f).

On the other hand, to further demonstrate the potential application of these N, P-co-doped graphene catalysts for OER, these catalysts were measured by sweeping the RRDE with potential between 1.2 and 1.8 V in a 0.1 MKOH electrolyte. The LSV curves obtained are shown in Figure 4-6c. It is notable that NP/C-Pyridinic N+Pyrrolic

N displays the highest catalytic activity for OER with the potential of 1.58V at the current of 10.0 mA cm<sup>-2</sup> (i.e.,  $E_j = 10$ ), among all these N,P co-doped catalysts, which is lower than that of IrO<sub>2</sub>(1.61V at the current of 10.0 mA cm<sup>-2</sup>) followed by NP/C-Pyridinic N+Graphitic N with the potential of 1.63V at the current of 10.0 mA cm<sup>-2</sup>. By contrast, NP/C-Pyridinic N+Pyridinic N exhibits the lowest catalytic activity for OER with the potential of 1.64V at the current of 10.0 mA cm<sup>-2</sup>. Tafel plots as shown in Figure 4-6d, the corresponding Tafel slope for these catalysts are 70.7 mV/dec for NP-G-Pyridinic N+Pyrrolic N which is even lower than that of the state-of-the-art IrO<sub>2</sub> (79.4 mV /dec) followed by NP/C-Pyridinic N+Graphitic N of 134.7 mV/dec, NP/C-Pyridinic N+Pyridinic N of 141.5 mV/dec.

To investigate the practical application of these N, P co-doped catalysts, the best performed NP/C-Pyridinic N+Graphitic N catalyst was selected and tested in a Zn-air battery by using NP/C-Pyridinic N+Graphitic N as air cathode electrocatalyst and the results are shown in Figure 4-6e, f. As shown in Figure 6e, the Zn-air battery with NP/C-Pyridinic N+Graphitic N as air cathode exhibits an open-circuit voltage of 1.70 V, higher than 1.54V observed on the Zn-air battery with commercial Pt/C cathode catalysts. Moreover, the peak power density of 133 mW cm<sup>-2</sup> at 0.22 mA cm<sup>-2</sup> obtained on the Zn-air battery with NP/C-Pyridinic N+Graphitic N cathode is also higher than 121 mW cm<sup>-2</sup> at 0.18 mA cm<sup>-2</sup>, obtained with Pt/C cathode (Figure 4-6e). More importantly, Galvanostatic discharge curves reveal that the battery with NP/C-Pyridinic N+Graphitic N catalyst displays a high voltage of 1.32 V and longer discharge time of 31.7 h, as compared with 1.30 V and 29.6 h obtained on the battery with Pt/C

electrocatalyst at a current density of  $5 \text{ mA cm}^{-2}$  (Figure 4-6f). The specific capacities of the battery with NP/C-Pyridinic N+Graphitic N is  $720.3 \text{ mAh g}^{-1}$  at  $5 \text{ mA cm}^{-2}$ , also better than that catalyzed by commercial Pt/C ( $669.4 \text{ mAh g}^{-1}$ ). The high discharging voltages and specific capacities demonstrates excellent electrocatalytic performance of NP/C-Pyridinic N+Graphitic N catalyst in practical application in Zn-air batteries.

#### 4.3.4 Density functional theory (DFT) calculations

Density functional theory (DFT) calculations were performed to further explore the influence of N, P configurations produced on carbon atoms. In this work, a  $\text{C}_{63}\text{H}_{18}$  cluster as the initial model and its derived models with single doping site for pyridinic N, graphitic N and pyrrolic N dopant and P co-doped sites were built up and shown in Figure 4-8a. The doping site for pyridinic N and pyrrolic N species is located on the edge of such graphene cluster model, graphitic N is inside the graphene. The P doping atom, is squeezed out of the carbon plane because of its relatively larger radius. Five graphene networks models doped by different N species and P configurations have been constructed for computational simulation as illustrated in Figure 4-8. According to the results reported in the literature, the ORR activity mainly originates from the C atoms surrounding heteroatoms with high charge density or positive spin density [46], and the carbon atoms with positive spin or charge density larger than 0.15 are most likely to serve as catalytic active sites [47]. And spin density is considered as the crucial evaluation criterion of active carbon atoms which is more important than charge density<sup>48</sup>. Thus, the number of carbon atoms with large charge density or positive spin

density could serve as a barometer to evaluate the catalytic capability of the materials for ORR as well as the chemical environment change of surrounding carbon atomic.

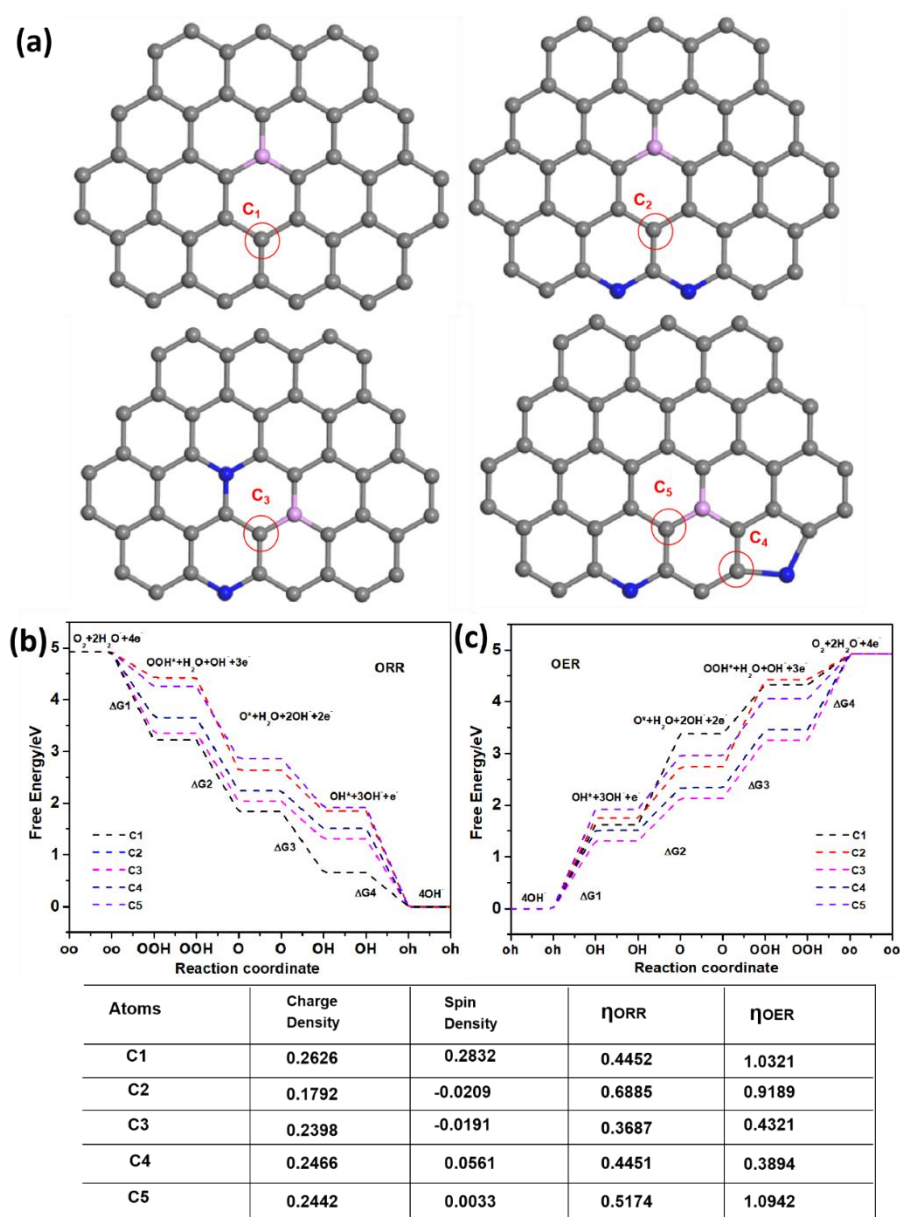


**Figure 4-7.** Models for graphene+ P, graphene+P+ Pyridinic N+Graphitic N, graphene+P+Pyridinic N+Pyridinic N and graphene+P+Pyridinic N+Pyrrolic N (a), and the Gibbs free energy of ORR (b) and OER (c) and the specific values of corresponding overpotential and the specific values  $\eta_{\text{ORR}}$ ,  $\eta_{\text{OER}}$ , in these models.

It is clear that among all these models, model of pristine graphene exhibits the low percentage (5.15%) of active carbon atoms with charge density  $>0.15$  among these models and the content of spin density  $>0$  is 48.03%. Meanwhile, with the addition of

P, it is notable that the percentage of active carbon atoms with charge density  $> 0.15$  increased to 8.16%, but the content of spin density  $> 0$  decreased to 45.03%. When dual doping of different N species were introduced, the model of graphene+ Graphitic N+ Pyridinic N+P exhibits high content of active sites carbon atoms with charge density  $> 0.15$  of 35.16% and the highest percentage of active carbon atoms with positive spin density of 56.78% among all these models. This indicates that configuration of graphene+ Graphitic N+ Pyridinic N+P produces great influence on electronic structure of surrounding carbon atoms. In model of graphene+ Pyrrolic N+ Pyridinic N+P, the ratio of carbon atoms with charge density  $> 0.15$  and spin density  $> 0$  is 11.11% and 35.16%, respectively. As for as model of graphene+ Pyridinic N+ Pyridinic N+P, the percentage of effective carbon atoms with charge density  $> 0.15$  and spin density  $> 0$  is 7.94% and 48.09%, respectively. It is observed that carbon atoms with the highest charge or spin density in these models usually located near at doped N and P atoms, indicating that electronic redistribution induced by heteroatoms focus on the area near doping sites.

For more intuitive expression, Reaction Gibbs free energy, as a fundamental thermodynamic parameter of a reaction, was calculated to analyze the overpotential of crucial catalytic steps as shown in Figure 4-8. The calculated free energy diagram illustrates that the adsorption of  $O_2$  (Step 1) are rate-limiting for ORR in alkaline solution, in this case, protonation of  $OO^*$  are the most sluggish steps for ORR and the overpotentials are crucial parameters for reversible oxygen electrocatalysis<sup>47-50</sup>. According to DFT results, carbon atom of  $C_3$  in model of graphene+ Graphitic N+

Pyridinic N+P displays the least value of overpotential (0.368) among all these models, followed by carbon atom C<sub>4</sub> in model of graphene+ Pyrrolic N+ Pyridinic N+P shows the overpotential of 0.445. By contrast, C<sub>2</sub> in the model of graphene+ Pyridinic N+ Pyridinic N+P exhibits the highest value of 0.688, indicating that the configuration of graphene+ Pyridinic N+ Graphitic N+P contributes to enhance catalytic activity for ORR greatly among all these N, P configurations. The result is in good accordance with electrochemical test results discussed above.

On the other hand, OER proceeds in an opposite pathway from the ORR, according to calculated free energy diagram discussed above, the OER overpotentials were calculated and compared among these promising active atoms. According to Gibbs free-energy diagram of OER, it is found that carbon atom of C<sub>4</sub> in model of graphene+ Pyrrolic N+ Pyridinic N+P displays the least value of overpotential (0.389eV) among all these models, followed by carbon atom C<sub>3</sub> in model of graphene+ Graphitic N+ Pyridinic N+P with overpotential of 0.432eV. And C<sub>2</sub> in model of graphene+ Pyridinic N+ Pyridinic N+P possess the highest overpotential of 0.918. According to DFT results as discussed, it can be well explained the significant enhancement of ORR catalytic activity of Pyridinic N+Graphitic N+P catalyst compared to Pyridinic N+Pyridinic +P and Pyridinic N+Pyrrolic N +P configurations in this study. As well as explained the best catalytic activity of Pyridinic N+Pyrrolic N +P for OER.

In summary, DFT calculations well explained the function control mechanism via tuning the configuration of N and P with different ratio. At first, according to UPS results, the N, P co-doping catalysts display different work function (F), indicating

that different N, P configurations provide different energetic barrier needed to motivate electrons escape during catalysis process. Meanwhile, the result is validated by XPS analysis, the shift of C1s is a clue that different electron distribution in carbon matrix derived from different N, P configurations. DFT result is a solid evidence to support the excellent catalytic activity for ORR of NP/C-Pyridinic N+Graphitic N with high content of Graphitic N, Pyridinic N and P according to XPS results. By contrast, when more Pyrrolic N was added, due to the lower value of OER overpotentials derived from Pyrrolic N+Pyridinic N and P, the catalyst of NP/C-Pyridinic N+Pyrrolic N exhibits the higher catalytic activity for OER than that of NP/C-Pyridinic N+Graphitic N. This study evidently demonstrates the correlation between the configuration of active sites (Graphitic N+ Pyridinic N+P, Pyridinic N+Pyrrolic N+P and Pyridinic N+ Pyridinic N+P) and catalytic activity for ORR and OER of as-synthesized NP-G catalysts. The results of the study show a new platform for the design and development of highly efficient N, P co-doped metal free carbon based electrocatalysts for effective energy conversion technologies.

#### **4. 4 Conclusion**

Three kinds of N, P co-doped graphene based catalysts featured with different Pyridinic N based N species configuration coordinate with P (Graphitic N+ Pyridinic N+P, Pyridinic N+Pyrrolic N+P and Pyridinic N+ Pyridinic N+P) were successfully prepared via direct Pyrolysis of N-containing precursors mixture with phytic acid as P source. It demonstrates that the configuration of Pyridinic N +Graphitic N+P prefer to producing enhanced catalytic activity for ORR. Meanwhile, Pyridinic N +Graphitic

N+P contributes to promoting OER performance greatly. This study reveals the correlation between different N, P configurations with final catalytic activity for ORR and OER as well as provides a new insight on molecular-level design of performance-oriented N, P co-doped catalysts via reasonably selecting N-containing precursors to tune N, P species configurations.

## Reference

1. Escala, M.; Zumbuhl, T.; Koller, C.; Junge, R.; Krebs, R., Hydrothermal Carbonization as an Energy-Efficient Alternative to Established Drying Technologies for Sewage Sludge: A Feasibility Study on a Laboratory Scale. *Energy & Fuels* 2013, 27, 454-460.
2. Wang, N.; Lu, B. Z.; Li, L. G.; Niu, W. H.; Tang, Z. H.; Kang, X. W.; Chen, S. W., Graphitic Nitrogen Is Responsible for Oxygen Electroreduction on Nitrogen-Doped Carbons in Alkaline Electrolytes: Insights from Activity Attenuation Studies and Theoretical Calculations. *Acs Catalysis* 2018, 8, 6827-6836.
3. Lewis, N. S.; Nocera, D. G., Powering the Planet: Chemical Challenges in Solar Energy Utilization. *Proc. Natl. Acad. Sci. U. S. A.* 2006, 103, 15729-15735.
4. Chu, S.; Cui, Y.; Liu, N., The Path Towards Sustainable Energy. *Nature materials* 2017, 16, 16-22.
5. Hosseini, S. E.; Wahid, M. A., Hydrogen Production from Renewable and Sustainable Energy Resources: Promising Green Energy Carrier for Clean Development. *Renewable & Sustainable Energy Reviews* 2016, 57, 850-866.



6. Ramli, Z. A. C.; Kamarudin, S. K., Platinum-Based Catalysts on Various Carbon Supports and Conducting Polymers for Direct Methanol Fuel Cell Applications: A Review. *Nanoscale Research Letters* 2018, 13.
7. Grey, C. P.; Tarascon, J. M., Sustainability and in Situ Monitoring in Battery Development. *Nature materials* 2017, 16, 45-56.
8. Ge, X. M.; Sumboja, A.; Wu, D.; An, T.; Li, B.; Goh, F. W. T.; Hor, T. S. A.; Zong, Y.; Liu, Z. L., Oxygen Reduction in Alkaline Media: From Mechanisms to Recent Advances of Catalysts. *Acs Catalysis* 2015, 5, 4643-4667.
9. Jiao, Y.; Zheng, Y.; Jaroniec, M. T.; Qiao, S. Z., Design of Electrocatalysts for Oxygen- and Hydrogen-Involving Energy Conversion Reactions. *Chem. Soc. Rev.* 2015, 44, 2060-2086.
10. He, C. Y.; Zhang, J. J.; Shen, P. K., Nitrogen-Self-Doped Graphene-Based Non-Precious Metal Catalyst with Superior Performance to Pt/C Catalyst toward Oxygen Reduction Reaction. *Journal of Materials Chemistry A* 2014, 2, 3231-3236.
11. Tian, Z. Q.; Lim, S. H.; Poh, C. K.; Tang, Z.; Xia, Z. T.; Luo, Z. Q.; Shen, P. K.; Chua, D.; Feng, Y. P.; Shen, Z. X.; Lin, J. Y., A Highly Order-Structured Membrane Electrode Assembly with Vertically Aligned Carbon Nanotubes for Ultra-Low Pt Loading Pem Fuel Cells. *Advanced Energy Materials* 2011, 1, 1205-1214.
12. Tang, H. L.; Shen, P. K.; Jiang, S. P.; Fang, W.; Mu, P., A Degradation Study of Nation Proton Exchange Membrane of Pem Fuel Cells. *J. Power Sources* 2007, 170, 85-92.
13. Jaouen, F.; Jones, D.; Coutard, N.; Artero, V.; Strasser, P.; Kucernak, A., Toward

Platinum Group Metal-Free Catalysts for Hydrogen/Airproton-Exchange Membrane Fuel Cells. Johnson Matthey Technology Review 2018, 62, 231-255.

14. Wei, W.; Liang, H. W.; Parvez, K.; Zhuang, X. D.; Feng, X. L.; Mullen, K., Nitrogen-Doped Carbon Nanosheets with Size-Defined Mesopores as Highly Efficient Metal-Free Catalyst for the Oxygen Reduction Reaction. *Angewandte Chemie-International Edition* 2014, 53, 1570-1574.

15. Qin, L.; Wang, L. C.; Yang, X.; Ding, R. M.; Zheng, Z. F.; Chen, X. H.; Lv, B. L., Synergistic Enhancement of Oxygen Reduction Reaction with Bc3 and Graphitic-N in Boron- and Nitrogen-Codoped Porous Graphene. *Journal of Catalysis* 2018, 359, 242-250.

16. Chung, H. T.; Cullen, D. A.; Higgins, D.; Sneed, B. T.; Holby, E. F.; More, K. L.; Zelenay, P., Direct Atomic-Level Insight into the Active Sites of a High-Performance Pgm-Free Orr Catalyst. *Science* 2017, 357, 479-483.

17. Zhang, J. T.; Zhao, Z. H.; Xia, Z. H.; Dai, L. M., A Metal-Free Bifunctional Electrocatalyst for Oxygen Reduction and Oxygen Evolution Reactions. *Nature Nanotechnology* 2015, 10, 444-452.

18. Sun, T.; Wang, J.; Qiu, C. T.; Ling, X.; Tian, B. B.; Chen, W.; Su, C. L., B, N Codoped and Defect-Rich Nanocarbon Material as a Metal-Free Bifunctional Electrocatalyst for Oxygen Reduction and Evolution Reactions. *Advanced Science* 2018, 5.

19. Wang, H. F.; Tang, C.; Zhang, Q., Template Growth of Nitrogen-Doped Mesoporous Graphene on Metal Oxides and Its Use as a Metal-Free Bifunctional

Electrocatalyst for Oxygen Reduction and Evolution Reactions. *Catalysis Today* 2018, 301, 25-31.

20. Mamtani, K.; Jain, D.; Dogu, D.; Gustin, V.; Gunduz, S.; Co, A. C.; Ozkan, U. S., Insights into Oxygen Reduction Reaction (Orr) and Oxygen Evolution Reaction (Oer) Active Sites for Nitrogen-Doped Carbon Nanostructures (Cnx) in Acidic Media. *Applied Catalysis B-Environmental* 2018, 220, 88-97.

21. Wang, Q. C.; Ji, Y. J.; Lei, Y. P.; Wang, Y. B.; Wang, Y. D.; Li, Y. Y.; Wang, S. Y., Pyridinic-N-Dominated Doped Defective Graphene as a Superior Oxygen Electrocatalyst for Ultrahigh-Energy-Density Zn-Air Batteries. *Acs Energy Letters* 2018, 3, 1183.

22. Guo, D. H.; Shibuya, R.; Akiba, C.; Saji, S.; Kondo, T.; Nakamura, J., Active Sites of Nitrogen-Doped Carbon Materials for Oxygen Reduction Reaction Clarified Using Model Catalysts. *Science* 2016, 351, 361-365.

23. Xu, Y.; Mo, Y. P.; Tian, J.; Wang, P.; Yu, H. G.; Yu, J. G., The Synergistic Effect of Graphitic N and Pyrrolic N for the Enhanced Photocatalytic Performance of Nitrogen-Doped Graphene/Tio<sub>2</sub> Nanocomposites. *Applied Catalysis B-Environmental* 2016, 181, 810-817.

24. Xing, T.; Zheng, Y.; Li, L. H.; Cowie, B. C. C.; Gunzelmann, D.; Qiao, S. Z.; Huang, S. M.; Chen, Y., Observation of Active Sites for Oxygen Reduction Reaction on Nitrogen-Doped Multilayer Graphene. *Acs Nano* 2014, 8, 6856-6862.

25. Borghei, M.; Laocharoen, N.; Kibena-Poldsepp, E.; Johansson, L. S.; Campbell, J.; Kauppinen, E.; Tammeveski, K.; Rojas, O. J., Porous N,P-Doped Carbon from Coconut

Shells with High Electrocatalytic Activity for Oxygen Reduction: Alternative to Pt-C for Alkaline Fuel Cells. *Applied Catalysis B-Environmental* 2017, 204, 394-402.

26. Chai, G. L.; Qiu, K. P.; Qiao, M.; Titirici, M. M.; Shang, C. X.; Guo, Z. X., Active Sites Engineering Leads to Exceptional Orr and Oer Bifunctionality in P,N Co-Doped Graphene Frameworks. *Energy & Environmental Science* 2017, 10, 1186-1195.

27. Pu, Z. H.; Amiin, I. S.; Zhang, C. T.; Wang, M.; Kou, Z. K.; Mu, S. C., Phytic Acid-Derivative Transition Metal Phosphides Encapsulated in N,P-Codoped Carbon: An Efficient and Durable Hydrogen Evolution Electrocatalyst in a Wide Ph Range. *Nanoscale* 2017, 9, 3555-3560.

28. Zhang, J.; Fang, J. H.; Han, J. L.; Yan, T. T.; Shi, L. Y.; Zhang, D. S., N, P, S Co-Doped Hollow Carbon Polyhedra Derived from Mof-Based Core-Shell Nanocomposites for Capacitive Deionization. *Journal of Materials Chemistry A* 2018, 6, 15245-15252.

29. Qin, Q.; Jang, H.; Li, P.; Yuan, B.; Liu, X.; Cho, J., A Tannic Acid-Derived N-, P-Codoped Carbon-Supported Iron-Based Nanocomposite as an Advanced Trifunctional Electrocatalyst for the Overall Water Splitting Cells and Zinc-Air Batteries. *Advanced Energy Materials* 2019, 9.

30. Zheng, X. J.; Wu, J.; Cao, X. C.; Abbott, J.; Jin, C.; Wang, H. B.; Strasser, P.; Yang, R. Z.; Chen, X.; Wu, G., N-, P-, and S-Doped Graphene-Like Carbon Catalysts Derived from Onium Salts with Enhanced Oxygen Chemisorption for Zn-Air Battery Cathodes. *Applied Catalysis B-Environmental* 2019, 241, 442-451.

31. Schon, T. B.; McAllister, B. T.; Li, P. F.; Seferos, D. S., The Rise of Organic

Electrode Materials for Energy Storage. *Chemical Society Reviews* 2016, 45, 6345-6404.

32. Gu, C.; Huang, N.; Gao, J.; Xu, F.; Xu, Y. H.; Jiang, D. L., Controlled Synthesis of Conjugated Microporous Polymer Films: Versatile Platforms for Highly Sensitive and Label-Free Chemo- and Biosensing. *Angewandte Chemie-International Edition* 2014, 53, 4850-4855.

33. Chen, X.; Huang, N.; Gao, J.; Xu, H.; Xu, F.; Jiang, D. L., Towards Covalent Organic Frameworks with Predesignable and Aligned Open Docking Sites. *Chemical Communications* 2014, 50, 6161-6163.

34. Lin, Z. Y.; Waller, G. H.; Liu, Y.; Liu, M. L.; Wong, C. P., 3d Nitrogen-Doped Graphene Prepared by Pyrolysis of Graphene Oxide with Polypyrrole for Electrocatalysis of Oxygen Reduction Reaction. *Nano Energy* 2013, 2, 241-248.

35. Cao, C. A.; Zhuang, X. D.; Su, Y. Z.; Zhang, Y.; Zhang, F.; Wu, D. Q.; Feng, X. L., 2d Polyacrylonitrile Brush Derived Nitrogen-Doped Carbon Nanosheets for High-Performance Electrocatalysts in Oxygen Reduction Reaction. *Polymer Chemistry* 2014, 5, 2057-2064.

36. Shi, P. C.; Guo, J. P.; Liang, X.; Cheng, S.; Zheng, H.; Wang, Y.; Chen, C. H.; Xiang, H. F., Large-Scale Production of High-Quality Graphene Sheets by a Non-Electrified Electrochemical Exfoliation Method. *Carbon* 2018, 126, 507-513.

37. Eddaoudi, M.; Kim, J.; Rosi, N.; Vodak, D.; Wachter, J.; O'Keeffe, M.; Yaghi, O. M., Systematic Design of Pore Size and Functionality in Isoreticular Mofs and Their Application in Methane Storage. *Science* 2002, 295, 469-472.

38. Zhao, Y.; Hu, C. G.; Song, L.; Wang, L. X.; Shi, G. Q.; Dai, L. M.; Qu, L. T., Functional Graphene Nanomesh Foam. *Energy & Environmental Science* 2014, 7, 1913-1918.
39. Liang, H. W.; Wei, W.; Wu, Z. S.; Feng, X. L.; Mullen, K., Mesoporous Metal-Nitrogen-Doped Carbon Electrocatalysts for Highly Efficient Oxygen Reduction Reaction. *Journal of the American Chemical Society* 2013, 135, 16002-16005.
40. Zhang, X. R.; Wang, Y. Q.; Du, Y. H.; Qing, M.; Yu, F.; Tian, Z. Q.; Shen, P. K., Highly Active N,S Co-Doped Hierarchical Porous Carbon Nanospheres from Green and Template-Free Method for Super Capacitors and Oxygen Reduction Reaction. *Electrochimica Acta* 2019, 318, 272-280.
41. Liang, J.; Jiao, Y.; Jaroniec, M.; Qiao, S. Z., Sulfur and Nitrogen Dual-Doped Mesoporous Graphene Electrocatalyst for Oxygen Reduction with Synergistically Enhanced Performance. *Angew. Chem.-Int. Edit.* 2012, 51, 11496-11500.
42. Yang, Z.; Yao, Z.; Li, G. F.; Fang, G. Y.; Nie, H. G.; Liu, Z.; Zhou, X. M.; Chen, X.; Huang, S. M., Sulfur-Doped Graphene as an Efficient Metal-Free Cathode Catalyst for Oxygen Reduction. *Acs Nano* 2012, 6, 205-211.
43. Zhang, M.; Dai, L. M., Carbon Nanomaterials as Metal-Free Catalysts in Next Generation Fuel Cells. *Nano Energy* 2012, 1, 514-517.
44. Qu, K. G.; Zheng, Y.; Zhang, X. X.; Davey, K.; Dai, S.; Qiao, S. Z., Promotion of Electrocatalytic Hydrogen Evolution Reaction on Nitrogen-Doped Carbon Nanosheets with Secondary Heteroatoms. *Acs Nano* 2017, 11, 7293-7300.
45. Li, D. H.; Jia, Y.; Chang, G. J.; Chen, J.; Liu, H. W.; Wang, J. C.; Hu, Y. F.; Xia,

Y. Z.; Yang, D. J.; Yao, X. D., A Defect-Driven Metal-Free Electrocatalyst for Oxygen Reduction in Acidic Electrolyte. *Chem* 2018, 4, 2345-2356.

46. Hu, C. G.; Dai, L. M., Multifunctional Carbon-Based Metal-Free Electrocatalysts for Simultaneous Oxygen Reduction, Oxygen Evolution, and Hydrogen Evolution. *Advanced Materials* 2017, 29.

47. Duan, X. G.; O'Donnell, K.; Sun, H. Q.; Wang, Y. X.; Wang, S. B., Sulfur and Nitrogen Co-Doped Graphene for Metal-Free Catalytic Oxidation Reactions. *Small* 2015, 11, 3036-3044.

48. Liu, Z.; Nie, H. G.; Yang, Z.; Zhang, J.; Jin, Z. P.; Lu, Y. Q.; Xiao, Z. B.; Huang, S. M., Sulfur-Nitrogen Co-Doped Three-Dimensional Carbon Foams with Hierarchical Pore Structures as Efficient Metal-Free Electrocatalysts for Oxygen Reduction Reactions. *Nanoscale* 2013, 5, 3283-3288.

49. Ai, W.; Luo, Z. M.; Jiang, J.; Zhu, J. H.; Du, Z. Z.; Fan, Z. X.; Xie, L. H.; Zhang, H.; Huang, W.; Yu, T., Nitrogen and Sulfur Codoped Graphene: Multifunctional Electrode Materials for High-Performance Li-Ion Batteries and Oxygen Reduction Reaction. *Advanced Materials* 2014, 26, 6186.

50. Choi, C. H.; Park, S. H.; Woo, S. I., Binary and Ternary Doping of Nitrogen, Boron, and Phosphorus into Carbon for Enhancing Electrochemical Oxygen Reduction Activity. *Acs Nano* 2012, 6, 7084-7091.

*Every reasonable effort has been made to acknowledge the owners of copyright material. I would be pleased to hear from any copyright owner who has been omitted or incorrectly acknowledged.*





## **Chapter 5: Revealing the dependence of active site configuration of N doped and N, S-co-doped carbon nanospheres on six-membered heterocyclic precursors for oxygen reduction reaction**

### **Abstract**

Elucidating the correlation of the polymer precursors and active sites formation of multi-heteroatom doped based carbon for oxygen reduction reaction (ORR) is essential to develop molecular-level design of highly efficient metal-free carbon catalysts. Herein, two series of N doped and N, S co-doped carbon nanospheres were synthesized via pyrolysis of self-polymerized compounds of three analogous precursors of 2,6-Diaminopyridine, 4,6-Diaminopyrimidine and 1,3-Diaminobenzene as nitrogen source initiated by hydrogen peroxide and ammonium persulfate as sulfur source respectively. The results demonstrate that nitrogen atoms in the six-membered rings of three precursors play a critical role on the formation of N-doping types and synergistic effects of N and S dopants in their derived carbon nanospheres for ORR. Among the three precursors, 2,6-Diaminopyrimidine prefers to form the Pyridinic N doped carbon, resulting in the highest activity for ORR in N doped nanospheres, in contrast, 2,6-Diaminopyridine facilitates the formation of a more content of graphitic-N dopant, which has stronger synergy with thiophenic-S dopant in carbon matrix than Pyridinic N dopants. This unique characteristics endow 2,6-Diaminopyrimidine derived N, S co-doped nanospheres with excellent ORR activity of a higher half-wave potential of 0.87V vs RHE in 0.1M KOH and Zn-Air battery power output performance than that of the same loading of commercial Pt/C catalyst. This revealing the dependence of

specific active sites determined by precursors with very similar molecular structures will shed light on the precise design strategy based on the precursors-selecting guidance for the development of advanced multi-heteroatom doped carbon ORR catalysts.

*\*Reprinted (adapted) with permission from Xiaoran Zhang, Sixian. Yao, Pinsong. Chen, Yunqiu. Wang, Dandan. Lyu, Feng. Yu, Ming. Qing, Zhi Qun Tian\*, Pei Kang Shen, , Revealing the dependence of active site configuration of N doped and N, S-co-doped carbon nanospheres on six-membered heterocyclic precursors for oxygen reduction reaction, J. Catal. 2020, 389, 677-689.*

## 5.1 Introduction

Oxygen reduction reaction (ORR) is the key process for sustainable energy conversion technologies such as fuel cells and metal-air batteries [1,2]. Pt-based precious catalysts as the most efficient ORR catalysts are widely employed to promote the sluggish kinetics of oxygen reduction reaction [3,4]. However, their intrinsic limitation of prohibitive cost contributes to the bottleneck of large-scale application of these technologies [5,6]. Therefore, tremendous efforts have been devoted to developing non-precious catalysts to replace Pt based catalysts and several promising materials have been successfully screened out such as transition metals based nitrogen doped carbon materials (M-N-C) [7], metal carbides [8], as well as metal nitrides [9]. However, there is a common concern on the dissolution of transition metal from hosts during the practical application that would result in poor durability of fuel cells [10,11].

Since Dai' s group first reported vertically aligned nitrogen-doped carbon nanotube arrays (VA-NCNTs) exhibits considerable ORR activity in 2009 [12], a series

of heteroatoms-doped nanocarbon materials have emerged and attracted wide attention due to their enhanced and promising catalytic activity for ORR [13,14]. The doping of carbon by heteroatoms of N, B, P, and S etc. is an effective strategy to promote ORR reactions, as it creates catalytic active sites by a modulation of charge and spin densities of carbon near the dopant atoms [15]. In instance, N doping, by virtue of its size similarity with carbon, provides favorable improvements in electron transport properties of the carbon matrix and is therefore a preferred dopant for realizing highly efficient electrocatalysts for applications in fuel cells [16,17]. Moreover, the high electronegativity of nitrogen induces increased positive charge density in carbon, creating active sites for electrochemical reduction of O<sub>2</sub>. To further develop carbon-based heteroatom-doped electrocatalysts for achieving their competitiveness with commercial Pt/C catalysts, a wide diversity of multi-heteroatoms co-doped carbon based catalysts were developed due to their increased number of efficient active sites and so-called “synergistic coupling” effect [18]. Especially, N, S co-doped carbon materials can induce asymmetrical spin and charge density leading to excellent ORR performance [19]. Much efforts have been made on the synthesis of highly efficient N, S co-doped carbon materials with well-defined electronic structures, heteroatom doping and desired active sites [20].

Generally, direct pyrolysis of heteroatom-containing precursors is an effective strategy to realize a homogeneous incorporation of heteroatoms into the carbon matrix. Precursors’ type is a kind of powerful mean to tune dopants’ types and their coordination of doped heteroatom into carbon matrix for achieving enhanced catalytic

activity for ORR [21]. It has been revealed that the intrinsic nature of an organic precursor plays a significant role in aspects ranging from physical and chemical properties of the resultant carbon framework, including conductivity, basicity, microcrystalline structure, morphology, and functionalities to final performance of the heteroatoms doped catalysts [22]. Especially, N-containing precursors are considered to be a crucial factor on determining doped N species in resultant catalysts. So far a series of N-containing precursors were used for designing nitrogen doped catalysts for ORR via direct pyrolysis precursors, such as polyaniline (PANI) [23], polydopamine (PDA) [24], polypyrrole (PPy) [25], and polyacrylonitrile (PAN) [26], phenanthroline [27], cyanamide [28], ethylenedi-amine [29] ect. Furthermore, metal-organic frameworks (MOF) [30], covalent organic polymers (COPs) [31] and covalent organic framework (COFs) [32] have been explored as promising precursors for preparing low-cost and highly active ORR electrocatalysts with well-defined morphology. In spite of tremendous efforts have been made, to date, there is still a big gap between their catalytic activity and the benchmarked Pt/C catalyst for ORR and the correlation between precursor structures, especially the type of C-N bonding in precursor, and final active sites species remains unclear, which seriously impede the accomplishment of a precise molecular-level design of advanced heteroatom doped carbon materials for efficient ORR.

In this study, three analogous six-membered heterocyclic compounds (benzene, pyridine, pyrimidine) are selected as precursors to directly synthesize N doped and N, S co-doped carbon nanospheres using hydrogen peroxide and ammonium persulfate as

initiators respectively with no use of any shape-directing agents in water for elucidating the relation between active sites of N doped and N, S-co doped carbon and precursors. The three six-membered heterocyclic precursors possess the same amount of NH<sub>2</sub> groups, but different aromatic ring species, in which 1,3-Benzenediamine has a conventional aromatic benzene ring, 2,6-Diaminopyridine and 2,6-Diaminopyrimidine has an aromatic pyridine (one N atom replaced in benzene ring) and pyrimidine ring (two N atoms replaced in benzene ring) respectively. Their respectively corresponding derived N doped and N, S-co-doped carbon nanospheres are characterized comprehensively by various measurements such as BET, TEM, XPS and CO<sub>2</sub> adsorption *ect* to reveal the correlation between active sites configuration and the molecular structure of precursors as well as final catalytic activity for ORR. Meanwhile, the electronic structure properties and ORR reaction pathway of the most possible configurations with N and N, S co-doped carbon are simulated by density functional theory calculation (DFT) to clarify the significant discrepancy in ORR activity.

## 5. 2 Experimental

### 5. 2.1 Synthesis of N doped and N, S co-doped nanospheres

For N, S co-doped carbon nanospheres, firstly, 10 mmol of 2,6-diaminopyridine (2,4-diaminopyrimidine or 1,3-Diaminobenzene) was dissolved into 200 ml of deionized water under vigorous stirring in an ice water bath (0-5°C), followed by the addition of 3.5 mmol of ammonium persulfate and stirring for 4 h until to obtain the dark green, wine red and black precipitates respectively. These as-received precipitates were collected by filtration and dried under 80°C for 12h. Finally, the collected powder

was thermally treated at 900°C for 1 h with the ramp rate of 5 °C min<sup>-1</sup> in N<sub>2</sub>. The corresponding N doped carbon nanospheres were synthesized using the same above procedure and hydrogen peroxide was used to replace ammonium persulfate as initiator.

### *5.2.2 Materials characterization*

The morphologies of N doped and N, S co-doped carbon nanospheres were characterized by Scanning Electron Microscopy (SEM and FESEM) using a Hitach SU8220 field emission scanning electron microscope and Transmission Electron Microscopy (TEM) using Titan ETEM G2 80-300 electron microscope operating at 300 kV). X-ray diffraction (XRD) was carried out on a Smart Lab diffractometer using a Cu K $\alpha$  ( $\lambda=1.5405$  Å) radiation source (Rigaku Co.). Raman spectra were measured on a Lab Ram HR Evolution Raman spectrometer with 532 nm wavelength incident laser light (Horiba Jobin Yvon Co.). Brunauer-Emmett-Teller (BET) surface area and pore size distribution of catalysts was analysed using a Micromeritics instrument (CORP ASAP 2460). X-ray photoelectron spectroscopy (XPS) measurements were carried out on an ESCALAB 250 system to determine the composition and chemical states of N doped and N, S co-doped carbon nanospheres. CO<sub>2</sub> adsorption evaluation was performed on RS485 Z-TEK from 25°C to 200°C with heating rate of 5°C/min, and all CO<sub>2</sub> adsorption evaluation test for these catalysts were conducted using the same mass loading of 30 mg.

### *5.2.3 Electrochemical measurements*

All electrochemical measurements were conducted on bipotentiostat WD-20 BASIC with rotating ring disk electrode (RRDE) system (Pine Instrumentation, USA)

in a thermostatically-controlled three-electrode cell at 25°C. The cell constitutes of a reversible hydrogen electrode (RHE) electrode as the reference electrode, a graphite rod as the counter electrode, a glassy carbon (diameter 5.61mm) with a Pt ring as the working electrode. The estimated catalyst loading on the working electrode was 600.0  $\mu\text{g cm}^{-2}$ . For comparison, the commercial Pt/C catalyst (46.7% Pt/C, Tanaka) was used. The Pt loading was 40  $\mu\text{g cm}^{-2}$ . ORR activity of the catalysts was evaluated in  $\text{O}_2$ -saturated 0.1 M KOH. Linear sweep voltammetry (LSV) was performed from 0 V to 1.10 V at a scan rate of 5  $\text{mV s}^{-1}$  at a rotating rate of 1600 rpm, while the Pt ring electrode was held at 1.2 V vs. RHE. The yield of hydrogen peroxide (%  $\text{HO}_2^-$ ) and the number of electron transfer (n) for ORR were calculated using the Equation (1) and (2) as below:

$$H_2O_2\% = 200 \times \frac{\frac{I_R}{N}}{I_D + \left(\frac{I_R}{N}\right)} \quad (1)$$

$$n = \frac{4I_D}{I_D + \left(\frac{I_R}{N}\right)} \quad (2)$$

where  $I_D$  represents an absolute value of the disk current,  $I_R$  represents an absolute value of the loop current, and the current collecting efficiency N is 0.38.

The kinetic current ( $I_k$ ) can be calculated using the following Koutecky-Levich equation (3):

$$\frac{1}{I_k} + \frac{1}{I_d} = \frac{1}{I} \quad (3)$$

Where I refer to the measured current and  $I_d$  is the diffusion limited current.

Zn-Air Battery Measurements: The electrochemical performance of Zn-air

batteries was evaluated in a home-made electrochemical device. For the air cathode, as-prepared electrocatalyst ink was coated onto carbon fiber paper ( $0.785 \text{ cm}^2$ ) with loading of  $1.0 \text{ mg cm}^{-2}$  by electrospinning spray. A polished zinc foil and 6.0 M KOH were used as the anode and electrolyte, respectively. Polarization curves and galvanostatic discharge tests were carried out on a bipotentiostat WD-20 BASIC electrochemical workstation.

#### *5.2.4 Density functional theory calculation*

The system energy DFT calculations are performed by using the Vienna *ab initio* simulation package (VASP) code. The Projector Augmented Wave (PAW) and the Perdew-Burke-Ernzerhof (PBE) functional was used to describe the exchange-correlation interaction. The supermodel was built with the lattice parameters of  $a=35 \text{ \AA}$ ,  $b=25 \text{ \AA}$ . The vacuum slab of  $15 \text{ \AA}$  was applied in z direction to avoid the periodic interactions. The energy cut-off for the plane-wave basis set was set to 450 eV for all relaxation, energy and electronic properties calculations. The Brillouin zone was sampled with Monkhorst-Pack  $3 \times 3 \times 1$  k-points generated manually. A Gaussian smearing with a width of 0.1 eV was used in all calculations. The convergence tolerance of energy was set to  $1.0 \times 10^{-5}$  eV/atoms. The maximal displacement and force is  $1.0 \times 10^{-3} \text{ \AA}$  and  $0.02 \text{ eV/\AA}$ , respectively.

### **5.3 Results and discussion**

#### *5.3.1 Synthesis and characterization of N doped and N, S co-doped carbon nanospheres*



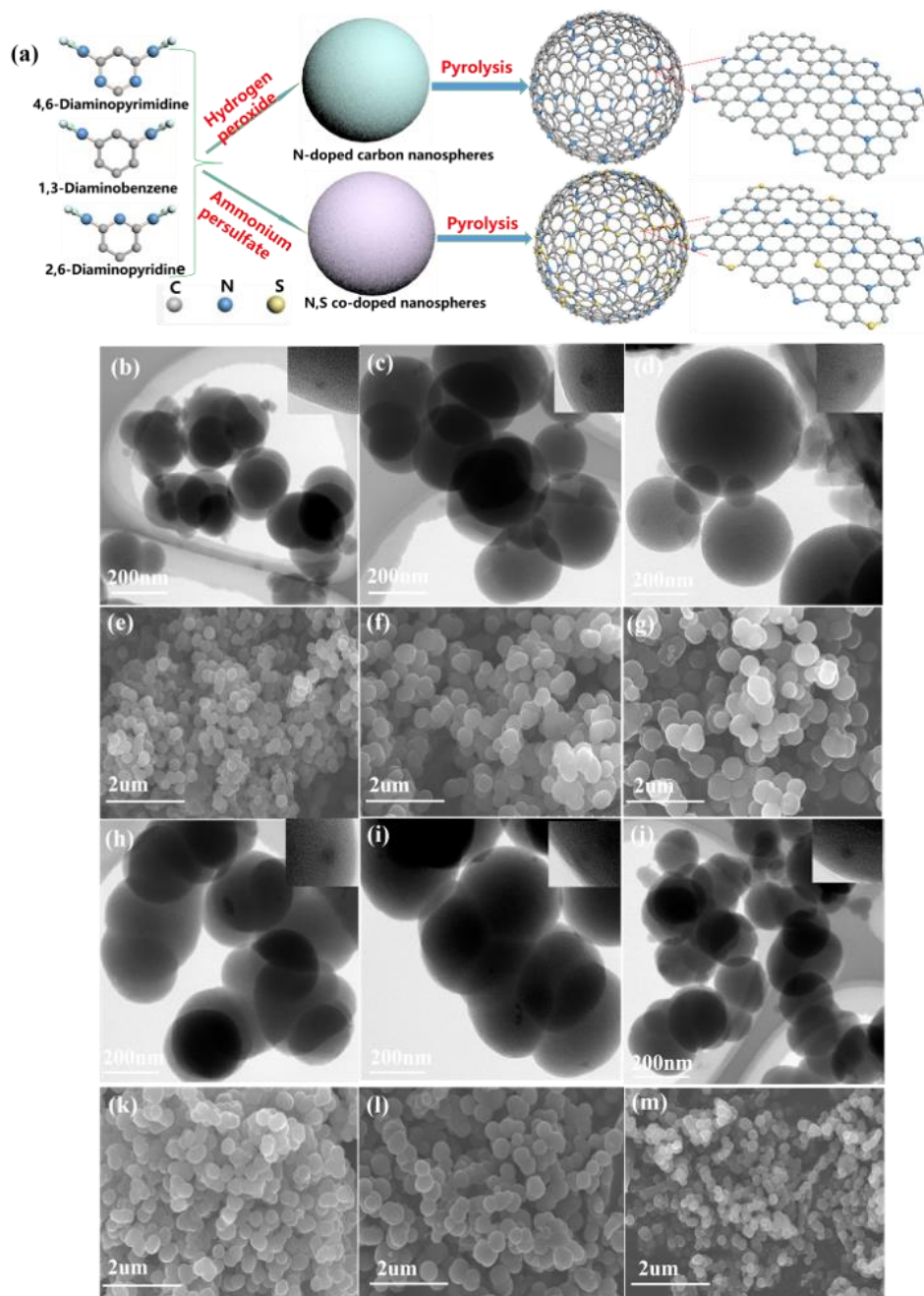


**Figure 5-1.** Illustration of the synthesis process of N,S co-doped and single N doped nanospheres with 2,6-Diaminopyridine, 4,6-Diaminopyrimidine, and 1,3-Diaminobenzene as precursors (a). TEM images and their corresponding SEM images respectively of N,S co-doped and single N doped nanospheres: N-C-Pyridine (b, e), N-C-Pyrimidine (c, f), N-C-Benzene (d, g) and N/S-C-Pyridine (h, k), N/S-C Pyrimidine (i, l), N/S-C-Benzene (j, m).

Figure 5-1(a) schematically illustrates the synthesis of N doped and N, S co-doped carbon nanospheres using our previously reported methods [33], in which 2,6-Diaminopyridine, 4,6-Diaminopyrimidine and 1,3-Diaminobenzene as precursors were

polymerized using hydrogen peroxide and ammonium persulfate as initiator respectively, followed by filtration and dry to obtain corresponding polymer nanospheres. After heat treatment at 900 °C for 1 h in the presence of N<sub>2</sub> gas flow, a series of catalysts were obtained and denoted as N-C-Pyridine, N-C-Pyrimidine, N-C-Benzene, N/S-C-Pyridine, N/S-C-Pyrimidine, and N/S-C-Benzene, respectively.

The morphological features of these prepared carbon spheres were observed using transmission electron microscopy (TEM) and scanning electron microscope (SEM). As shown in Figure 5-1(b-m), all these N and N, S co-doped carbon samples display a uniform nanospherical structure. The formation of spherical structure is mostly like due to that heterocyclic compounds with meta-amino group is easily to form cross-linked molecules via a hydrogen bond from amino groups or steric effect under chemical oxidation processes [34, 35]. It is notable that although these samples exhibit a similar spherical structure, the diameter of these spheres are different, which may be attributed to the difference of location and quantity of nitrogen groups in heterocyclic precursors. For N doped carbon nanospheres with hydrogen peroxide as initiator. N-C-Benzene has the biggest size (around 300nm), among all the three samples, followed by N-C-pyrimidine with about 250nm, and N-C-pyridine has a relatively small diameter of about 150nm (Figure 5-1b, e). As for N, S co-doped carbon nanospheres with ammonium persulfate as initiator, the diameter of N/S-C-pyrimidine nanospheres is about 350nm (Figure 5-1h, k), followed by N/S-C-pyridine with about 300nm (Figure 5-1i,l) and N/S-C-Benzene with about 200nm (Figure 5-1j,m) respectively. The high magnification TEM images (insert images) of these samples show that there are a large

number of microporous and mesoporous structures existing into these nanospheres. Element Mapping results demonstrate that C, N, O and C, N, O and S elements are homogeneously distributed into N doped and N, S co-doped nanospheres, respectively, indicating the success of uniform heteroatom doping.

Figure 5-2a shows XRD (X-ray diffraction) patterns of these N doped and N, S co-doped carbon nanospheres. All of them possess two weak and broad diffraction peaks at around  $25^\circ$  and  $43^\circ$ , which are attributed to (002) and (100) of graphite, suggesting the amorphous nature of these carbon nanospheres [36]. It can be also found that different precursors have no significant effect on the crystal structure of these carbon nanospheres. The specific surface area and pore structure analysis were shown in Figure 5-2b. All these  $N_2$  adsorption and desorption isotherms display characteristics of type-IV with obvious  $H_4$  hysteresis loops, indicating the coexistence of micropore and mesoporous structure. All the samples have a similar BET surface area, wherein N-C-Pyridine, N-C-Pyrimidine, N-C-Benzene are N/S-C-Pyridine, N/S-C-Pyrimidine, N/S-C-Benzene are  $1260\text{ m}^2/\text{g}$ ,  $1190\text{ m}^2/\text{g}$ ,  $1184\text{ m}^2/\text{g}$  and  $1024\text{ m}^2/\text{g}$ ,  $966\text{ m}^2/\text{g}$ ,  $1146\text{ m}^2/\text{g}$  respectively. According to the pore size distribution results (insert of Figure 5-2b), these samples also have similar pore size distribution. A large portion of pore size concentrates on 1-2nm, combining with a small part of mesopores with diameter at 2-10nm, which is consistent with TEM results as discussed above. It

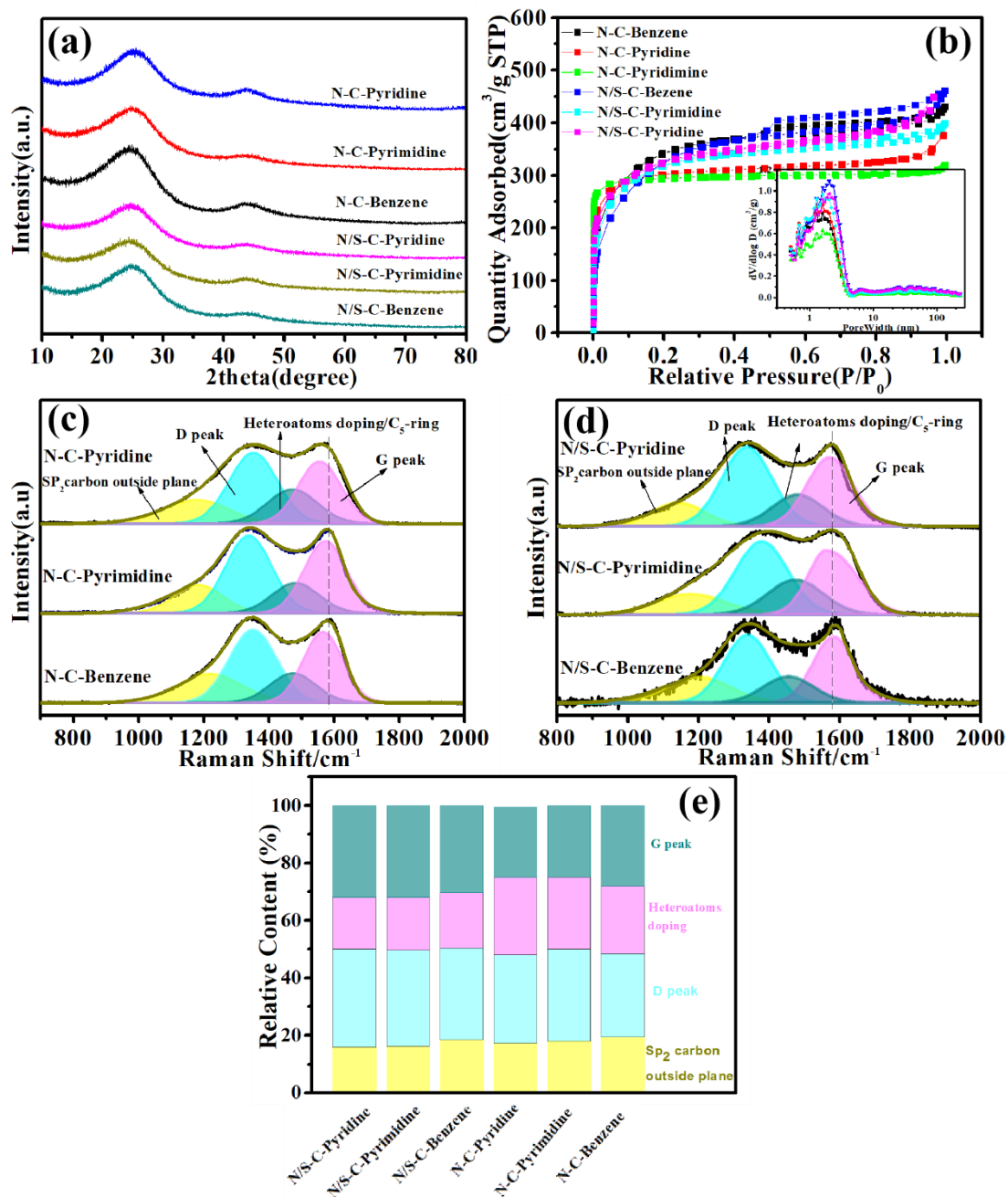


**Figure 5- 2.** XRD patterns (a) and Nitrogen adsorption-desorption isotherms (b) and Pore size distribution (insert) of N,S co-doped and N doped nanospheres (N-C-Pyridine, N-C-Pyrimidine, N-C-Benzene-900 and N/S-C-Pyridine, N/S-C-Pyrimidine, N/S-C-Benzene). Raman spectrum of N/C-Pyridine, N/C-Pyrimidine and N/C-Benzene (c) N/S-C-Pyridine, N/S-C-Benzene and N/S-C-Pyrimidine (d) and their specific content of each peaks (e).

is generally known that the hierarchical pore structure contributes to enhance the electrochemical performance of catalysts due to providing fast mass transportation [37].

Meanwhile, it is worth noting that the main pore size distribution of N, S co-doped

nanospheres positively shifts a bit, compared with their corresponding N doped nanospheres, indicating that addition of S can generate the formation of bigger pore structure. Raman spectroscopy provides a sensitive probe for electronic and phonon structures of heteroatoms doped carbon materials [38]. The doping-induced shifts of the Raman-active tangential G band can reflect the change of the electronic structure (Fermi level) in carbon matrix [39]. More importantly, the positive shift of the G band is correlated with the decreases of electrical resistivity of carbon based materials [40]. As shown in Figure 5-2c, d, it can be seen that for the N doped system, the specific value of G peak in these catalysts are 1578.7, 1581.9 and 1583.1 corresponding to N-C-Pyridine, N-C-Pyrimidine and N-C-Benzene respectively. For N, S co-doped samples, there exhibits relative negative shift of G peak compared to single N doped nanospheres, the specific position of G peak are 1577.6, 1580.3 and 1582.4 in N/S-C-Pyridine, N/S-C-Pyrimidine and N/S-C-Benzene respectively, indicating that nanospheres with S addition are endowed with enhanced electrical conductivity. Especially, among all these catalysts, no matter in the N, S co-doped system or in single N doped system, pyridine based samples displays an obvious negative shift of the main G peak compared with other samples, signifying that they have best electrical conductivity, mostly like due to their specific doping configuration. Meanwhile, the power conductivity measurements of these resultant nanospheres also confirm the above Raman results. It is clear that the conductivity increased with S doping compared with single N doped nanospheres, which may derive from increased metallic characteristic of carbon based materials with addition of S. Among all these samples, N/S-C-Pyridine exhibits the

highest conductivity of 5589 S/m at 25MPa, followed by N-C-Pyridine, greatly higher than N/S-C-Pyrimidine (2556 S/m) and N-C-Pyrimidine (2203 S/m), the nanospheres from Benzene based precursors displays the lowest conductivity among all these nanospheres. In addition, all Raman spectra can be further fitted to four carbon species via Gaussian fitting (Figure 5-2c, d). The two main peaks at about 1350 and 1580  $\text{cm}^{-1}$  are ascribed to the defective peak (D) and graphitic peak (G) respectively [41]. In addition, two another small peaks at around 1190 and 1500  $\text{cm}^{-1}$  are associated with heteroatom doping degree in carbon matrix, which is corresponding to carbon atoms outside of a perfectly planar  $\text{sp}^2$  carbon network and heteroatoms in carbon matrix or integrated five-number rings, respectively [42]. The specific content of these four species are calculated and shown in Figure 5-2e. The ratio of D peak and G peak is an important parameter to reflect the doping degree of these carbon matrix. The value of  $I_{\text{D}}/I_{\text{G}}$  is 1.073, 1.052, 1.048 and 1.158, 1.182, 1.15 corresponding to N-C-Pyrimidine, N-C-Pyridine, N-C-Benzene and N/S-C-Pyrimidine, N/S-C-Pyridine, N/S-C-Benzene respectively. It is obvious that the N doped nanospheres have higher  $I_{\text{D}}/I_{\text{G}}$  ratio than that of N, S-co-doped nanospheres, indicating that the S doping further increases disorder degree of carbon matrix [43]. In addition, there is an obviously gradually decrease for the integrated area of peak intensity at 1500  $\text{cm}^{-1}$ , compared to their individual total area, in which the portion for N/S-C-Pyrimidine, N/S-C-Pyridine, N/S-C-Benzene and N-C-Pyrimidine, N-C-Pyridine and N-C-Benzene is 25.9%, 23.14%, 21.08%, 17.67%, 18.45% and 19.16% respectively, indicating that the doping degree of heteroatoms decreases gradually. That is basically consistent with defect change

tendency from the ratio of ID/IG. Overall, precursors species play significant influence on the disorder degree of their corresponding N and N, S co-doped carbon nanospheres. The nanospheres with Pyrimidine based polymer as precursor displays the highest doping degree and Benzene based polymer derived carbon nanospheres have the lowest disorder degree of carbon matrix. These disorder degree of samples would lead to the big difference for their ORR activity.

### 5.3.2 Electrochemical evaluation for ORR

ORR performance was evaluated by Linear Sweep Voltammetry (LSV) using Rotating Ring Disk Electrode (RRDE) system. As shown in Figure 5-3a, for N doping carbon nanospheres, N-C-Pyrimidine exhibits the best performance for ORR with the onset and half-wave potential of 0.97 and 0.79 V *vs.* RHE respectively, followed by N-C-Pyridine with 0.94 and 0.76 V *vs.* RHE, and N-C-Benzene shows the lowest catalytic activity for ORR with 0.92 and 0.71 V *vs.* RHE respectively (in this study, E<sub>onset</sub> is defined as the potential of current density at 1  $\mu\text{A cm}^{-2}$ ). Meanwhile, their ORR catalytic performance are also supported by Tafel slope of 64.26, 75.83 and 87.62 mV decade<sup>-1</sup>, corresponding to N-C-Pyrimidine, N-C-Pyridine and N-C-Benzene, respectively, as shown in Figure 3c. The corresponding electron-transfer numbers and H<sub>2</sub>O<sub>2</sub> yield was shown in Figure 3e. N-C-Pyrimidine exhibits the biggest average of the electron transfer numbers with 3.84, followed by that of N-C-Pyridine with 3.769 and N-C-Pyridine with 3.75. Correspondingly, the maximum of H<sub>2</sub>O<sub>2</sub> yield at 0.1V RHE in is 14%, 17% and 22% respectively. The change tendency of electron transfer numbers and H<sub>2</sub>O<sub>2</sub> production in N doped carbon nanospheres is consistent with LSV results for

### ORR of N-C-Pyridimine, N-C-Pyridine and N-C-Benzene.

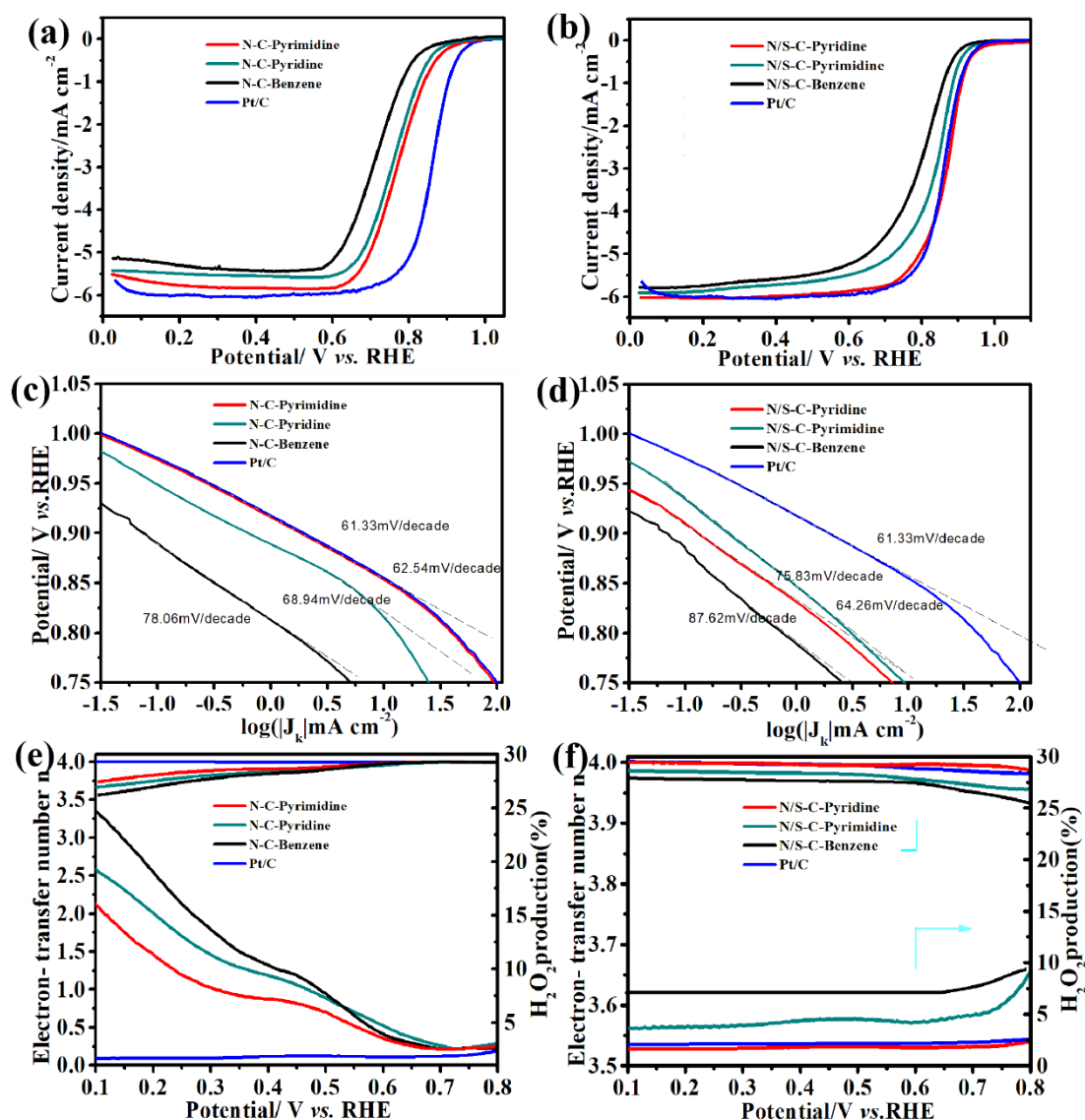


**Figure 5-3.** LSV curves (a), Tafel slope (c) and Electron transfer number  $n$  and  $H_2O_2$  production (e) of N-C-Pyrimidine, N-C-Pyridine, N-C-Benzene and Pt/C in 0.1 M KOH. LSV curves (b), Tafel slope (d) and Electron transfer number  $n$  and  $H_2O_2$  production (f) of N/S-C-Pyridine, N/S-C-Pyrimidine, N/S-C-Benzene and Pt/C in 0.1 M KOH.

Meanwhile, it should be noted that ORR activity of N-doped nanospheres is fairly low due to their partial 4 electron transfer process. On the other hand, as for N-S-co-doped nanospheres, their ORR activity is significantly higher than that of N doped nanospheres derived from the same precursors. N/S-C-Pyridine shows the best catalytic activity. Its onset and half-wave potentials of 1.01 V and 0.87 V vs. RHE respectively



is higher than 0.97 V and 0.82 V for N/S-C-Pyrimidine and 0.93V, 0.78V for N/S-C-Benzene and even better than that of commercial Pt/C catalysts (1.01 V and 0.86 V *vs.* RHE) in 0.1 M KOH (Figure 5-3b). The N/S-C-Pyridine ORR activity is also superior to the most of previously reported meta-free carbon based materials prepared using other N-containing precursors with other hetero atom such as P and S. The efficient ORR catalytic performance of N/S-C-Pyridine is also validated by its smallest Tafel slope ( $62.54\text{mV decade}^{-1}$ ), which is comparable to those of Pt/C ( $61.33\text{mV decade}^{-1}$ ) and significantly lower than  $68.94\text{ mV decade}^{-1}$ ,  $78.06\text{ mV decade}^{-1}$  of N/S-C-Pyrimidine, N/S-C-Benzene respectively (Figure 5-3d). And in Figure 5-3f, the  $\text{H}_2\text{O}_2$  yield and electron-transfer number ( $n$ ) of oxygen reduction of N/S-C-Pyridine at all electrode potentials is almost similar to that of the commercial Pt/C catalyst, which is less than 5% and 3.99 respectively, indicating its highly efficient oxygen reduction via the four-electron process into water, which is desirable for fuel cells application. Moreover, a low  $\text{H}_2\text{O}_2$  yield ( $< 10\%$ ) in the diffusion-limiting current region and a high electron transfer number (3.975 and 3.96 respectively) are achieved in N/S-C-Pyrimidine, N/S-C-Benzene, indicating a partial two-electron pathway involved in the ORR process of N/S-C-Pyrimidine and N/S-C-Benzene. The stability performance of N/S-C-Pyridine was also evaluated by accelerated durability tests within a cycling range of 0.6 to 1.0 V in  $\text{O}_2$ -saturated alkaline media. After 10,000 cycles accelerated stability test, the half-wave potential shifted negatively by only 8 mV compared to 17 mV on Pt/C in 0.1MKOH, indicating N/S-C-Pyridine catalysts exhibits superior stability than commercial Pt/C. Generally, oxygen reduction activity of N-doped and N, S co-doped

nanospheres is critically relied on the structure of precursors. N-doped nanospheres and N, S co-doped nanospheres derived from pyrimidine and pyridine based polymer respectively show the best catalytic performance among all these three N-containing heterocyclic precursors, which is mostly like due to their derived specific active site configurations.

To investigate the practical application of N/S-C-Pyridine nanospheres, the discharge behaviors were investigated in a homemade Zn-air battery by using N/S-C-Pyridine as air cathode electrocatalyst and its schematic configuration is shown in Figure 5-4a. The home-built Zn-air battery with N/S-C-Pyridine exhibits comparable and higher performance to that of commercial Pt/C catalyst at the current density of less than  $0.2 \text{ A cm}^{-2}$  and more than  $0.2 \text{ A cm}^{-2}$ , as in Figure 5-4b. In addition, the peak power density of  $125 \text{ mW cm}^{-2}$  at  $0.22 \text{ mA cm}^{-2}$  are slightly higher than that of Pt/C electrocatalyst ( $121 \text{ mW cm}^{-2}$  at  $0.18 \text{ mA cm}^{-2}$ ). Meanwhile, Galvanostatic discharge curves reveal that N/S-C-Pyridine nanospheres based battery displays a higher voltage (1.32 V) and longer discharge time (31.7 h) compared with that (1.30 V, 29.6 h) of Pt/C electrocatalyst at a current density of  $10 \text{ mA cm}^{-2}$ . The specific capacities were calculated (Figure 5-4c) of the batteries are  $705.3 \text{ mAh g}^{-1}$  at  $10 \text{ mA cm}^{-2}$ , which is better than that catalyzed by commercial Pt/C ( $669.4 \text{ mAh g}^{-1}$ ). The high discharging voltage and specific capacity demonstrates excellent electrocatalytic performance of

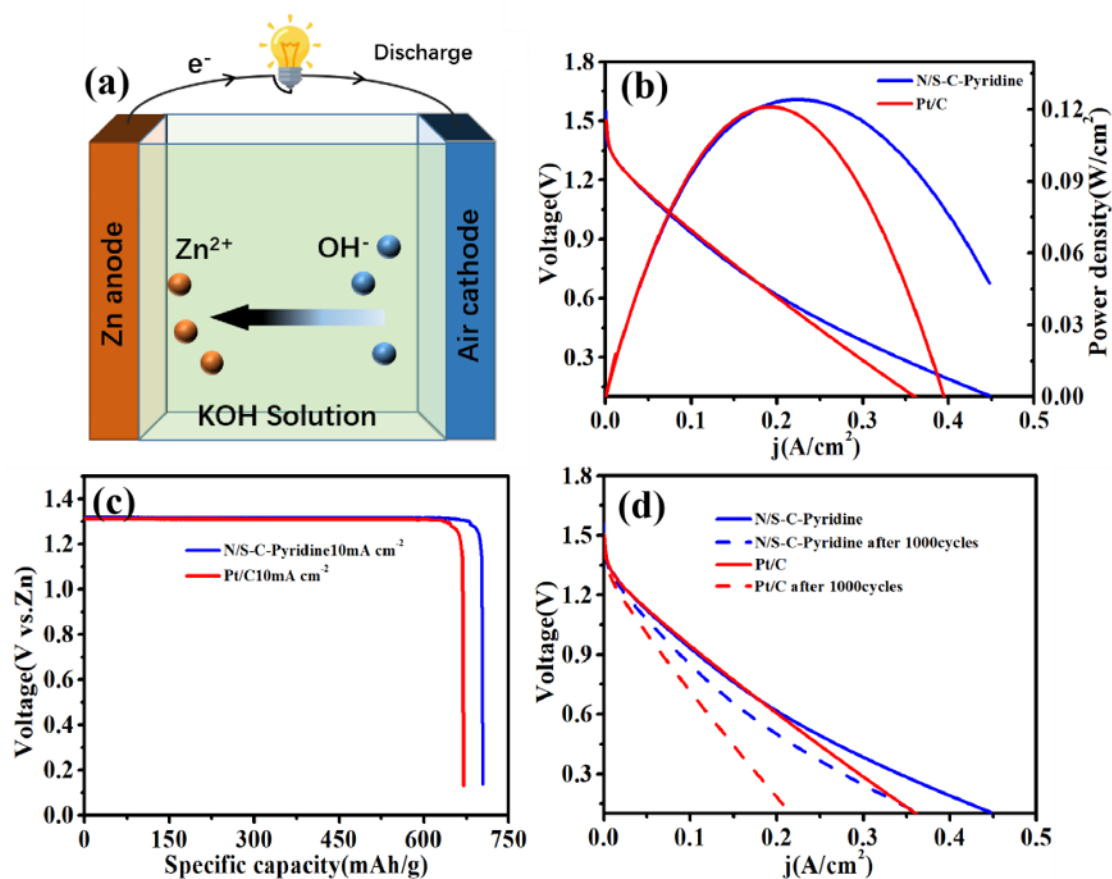


**Figure 5-4.** Schematic of Zinc-Air battery(a), Polarization curves and the corresponding power density plots of N/S-C-Pyridine and Pt/C (b), Curves of specific capacities at current densities 10 mA cm<sup>-2</sup> of the Zn-air batteries using N/S-C-Pyridine and Pt/C as ORR electrocatalysts (c) and long-term galvanostatic discharge test at a current density of 10 mA cm<sup>-2</sup> for the Zn-air batteries using N/S-C-Pyridine and Pt/C as the ORR electrocatalyst before and after 1000 cycles (d).

N/S-C-Pyridine in practical application in Zn-air batteries. The stability performance was evaluated by durability tests within a CV cycling range of 0.6 -1.0 V for 1000cycles. As observed, there is less voltage drop occurred in N/S-C-Pyridine during the test process compared with Pt/C (Figure 5-4d), the result is consistent with durability testing in half-cell testing discussed above, indicating excellent stability of N/S-C-Pyridine electrocatalyst. It should be noted that the performance Zn-Air performance with N/S-C-Pyridine is accomplished using the same loading as Pt/C catalyst with 0.1mg/cm<sup>2</sup>, strongly indicating its outstanding activity and great promise for practical application.

### 5.3.3 *The origin of catalytic activity difference for ORR*

To further clarify the exact reasons for the big difference in ORR performance of these doped carbon nanospheres. X-ray photoelectron spectroscopy (XPS) was conducted to elucidate the chemical composition, and in the measurement, the commercial BP 2000 carbon black was introduced as a internal standard for the calibration of C1s peak with 284.6 eV to eliminate the binding energy shift error of elements induced by instruments. From the full scan survey spectra (Figure 5-5a), there are N, C, O elements in N doped nanospheres and N, S, C, O elements in N, S co-doped nanospheres, indicating the successful doping of N and S. The specific N atomic content of catalysts are 4.85%, 5.23% and 4.71% corresponding to N/S-C-pyridine, N/S-C-pyrimidine, N/S-C-Benzene and 4.74%, 4.96%, 4.60% corresponding to N-C-pyridine, N-C-pyrimidine, N-C-Benzene respectively. It is clearly that with the addition of S, the content of N increases slightly compared to single N doped catalyst, which is consistent with previous work that S plays the role of fixing N element [46]. However, ORR test results clearly demonstrate their significant distinction. It portends that these difference should be mostly originated from the fine structure of active sites formed from the three precursors.

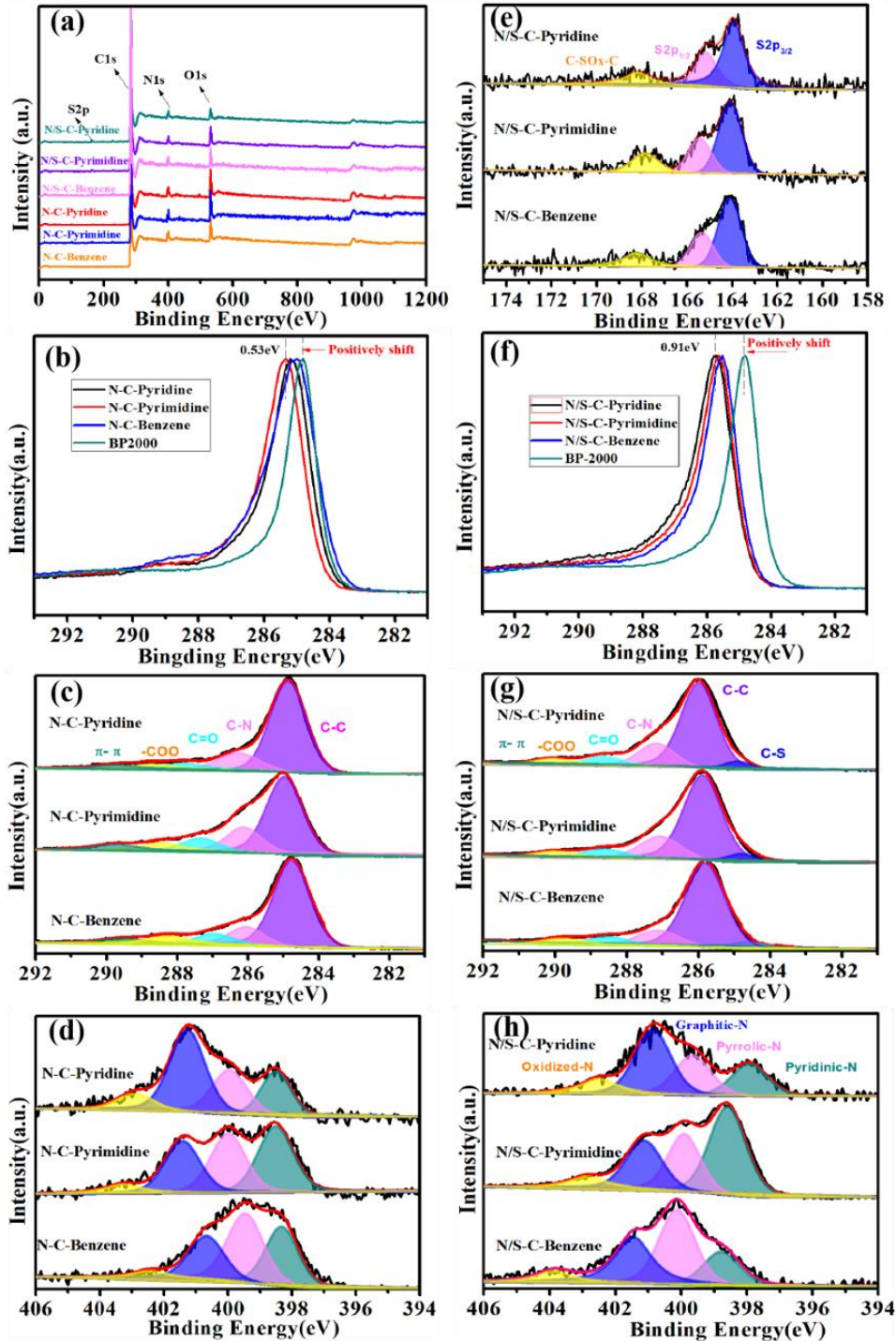


**Figure 5-5.** XPS full scan Survey of N and N, S co-doped nanospheres (a); The main peak shifts of C1s (b), the high-resolution XPS spectra of C1s (c) and N1s(d) of N doped nanospheres; The main peak shifts of C1s (b), the high-resolution XPS spectra of C1s (c) and N1s(d) of N doped nanospheres; The high-resolution XPS spectra of S2p (e), the main peak shifts of C1s (f), the high-resolution XPS spectra of C1s (g) and N1s (h) of N, S co-doped nanospheres.

As for N doped carbon nanospheres, from the comparison of high-resolution XPS spectra of C1s (Figure 5-5b), it is obvious that the peak position of C1s gradually shifts

to bigger binding energy with 284.75eV, 284.85eV and 284.98eV, corresponding to N-C-Benzene, N-C-Pyridine, and N-C-Pyrimidine respectively, compared to the standard of BP-2000. This various binding energy increasement of carbon implies that there is a strong interaction between C atoms and doped N heteroatom [44]. By further analysis, high resolution of C1s spectra of these three samples could be deconvoluted into five main peaks of 285.5eV, 286.42eV, 284.3eV, 288.4eV and 291eV, which is assignable to C-C, C-N, C=O, -COO and  $\pi$ - $\pi$  respectively, as shown in Figure 5-5c. It is worth noting that C-C accounts for the largest proportion among all compositions, followed by that of C-N with 4.88%, 5.76%, 4.5%, in N-C-Pyridine, N-C-Pyridimine, N-C-Benzene respectively, and the percentage of the fitted peak of C-N is also basically consistent with the corresponding content of N according to XPS full survey results. As for N, S co-doped nanospheres, there is a whole positive shift of the main peak of C1s compared to corresponding single N doped carbon nanospheres (Figure 5-5f). It is a clue that higher charge densities is produced by N, S co-doping than that of single N doping, which is consistent with the increased catalytic activity after S doping. Meanwhile, N/S-C-Pyridine shows highest binding energy (285.75eV) of C1s peak. The higher charge density around C atoms in N/S-C-Pyridine could explain its best catalytic performance for ORR. Considering tremendous previously reported research results that heteroatoms doping effect is usually closely linked with carbon atoms surrounding heteroatoms via creating the net positive charge density or doping-induced spin redistribution effect on adjacent carbon atoms for changing the oxygen adsorption mode to facilitate ORR[45]. Therefore, the obvious shift of C1s in these samples may

attribute to the co-introduction of doped heteroatoms S and N. Meanwhile, there is an obvious fitted peak of C-S in N/S-C-Pyridine, N/S-C-Pyrimidine and N/S-C-Benzene, displaying the successful co-doping of N and S. The C-N doping content is 4.76%, 5.64%, 4.32% and C-S dopants is 2.05%, 1.8% and 1.44% for N/S-C-Pyridine, N/S-C-Pyrimidine and N/S-C-Benzene respectively.

Nitrogen is a kind of crucial doped element that influences final catalytic performance greatly. The specific high resolution of N1s of these catalysts were shown in Figure 5-5d and 5-5h. XPS spectra of N1s of these samples can be deconvoluted into four main peaks of 398.25, 399.79, 401.12 and 403.5, assignable to pyridinic N, pyrrolic N, graphitic N, and oxidized N dopant respectively[47]. It is clear that pyrimidine based precursor prefers to form more pyridinic N (31.8%) than that of pyridine (16.08%) and benzene (14.21%) based precursors in single N doped carbon nanospheres. Pyridine based precursor tends to afford more graphitic N (56.57%) among all three precursors. By contrast, N doped nanospheres derived from Benzene based precursor possess more content of Pyrrolic N (26.81%). Even for N/S co-doped catalysts, this formation preference of N dopant types is consistent with single N doped samples. The deconvolution of S 2p for N/S-C-Pyridine, N/S-C-Pyrimidine and N/S-C-Benzene (Figure 5-5e) shows that three different peaks at the binding energy of 164.0, 165.1 and 168.4 eV, respectively. The former two peaks can be assigned to S2p<sub>3/2</sub> and S2p<sub>1/2</sub> of the C-S-C covalent bond of the thiophenic-S caused by spin-orbit coupling, while the third peak arises from oxidized S [48]. It is notable that N/S-C-Pyridine show the

relatively highest content of thiophenic-S up to 0.49at%, followed by N/S-C-Pyrimidine (0.43at%) and N/S-C-Benzene (0.42at%).

Generally, as for single N doping samples, it is obvious that N-C-Pyrimidine exhibits the highest value of pyridinic-N (1.61at%) followed by N-C-Pyridine (0.77at%) and N-C-Benzene (0.69at%). Previous research and density functional calculations (DFT) proved that the configuration of pyridinic-N bonded to two adjacent carbon atoms can produce more active sites for oxygen adsorption, and plays important role in the catalytic process of ORR[49], therefore, the high content of Pyridinic N in N-C-Pyrimidine attributes its excellent performance for ORR. After addition of S, N/S-C-Pyrimidine still shows the highest value of Pyridinic N with content of (1.12at%) followed by 0.91at% and 0.75at% in N/S-C-Pyridine and N/S-C-Benzene respectively. However, according to electrocatalytic activity for ORR discussed above, N/S-C-Pyrimidine displays lower catalytic activity for ORR than N/S-C-Pyridine in spite of that the former has higher pyridinic N content than the latter, which is contrary to that in single N doping system. Meanwhile, it should be noted that N/S-C-Pyridine with the highest catalytic activity displays the highest content of graphitic N and thiophenic S (C-S-C). As the similar electronegativity between S ( $x = 2.58$ ) and C atoms ( $x = 2.55$ ) would result in a negligible charge transfer between S and C[50] and the DFT calculations indicated that the dual doping of S and N induces a asymmetrical spin and charge density distribution in the N-S-Graphene models with different relative positions of the S and N atoms, leading to the excellent ORR performance [51]. We can therefore deduce that the part of the superior catalytic activity of N/S-C-Pyrimidine comes from



the synergistic effect between graphitic N and thiophenic S. Considering that graphitic N were reported as the major factor that greatly promote for conductivity and combining with conductivity test results discussed above, N/S-C-Pyridine exhibits the highest conductivity among all these samples, which may attribute to high content of graphitic N derived from Pyridine based precursors, the result is in good accordance with Raman and conductivity results discussed above.

To further study the relationship between active sites and the chemical environment of carbon atoms reflected by XPS results, Temperature Programmed Desorption (TPD) of CO<sub>2</sub> was conducted as a probe of the Lewis base site to clarify the basicity characteristic of each samples sample. Because Lewis base sites is a kind of important property of doped carbon that reflects electronic distribution around carbon atoms and be considered as important active origin for carbon based catalysts[52]. TPD profiles of CO<sub>2</sub> of N doped and N, S co doped carbon nanospheres. For N doped nanospheres, it is obvious that N-C-Pyrimidine exhibits the largest CO<sub>2</sub> desorption peak and area, demonstrating its strong basicity, which is also consistent with the highest content of Pyridinic N as well as the highest catalytic activity of N-C-Pyrimidine among these three samples. Pyridinic N dopant is generally claimed as the most contribution to the most basicity of N doped carbon due to that its adjacent carbons features a localized density of states in the occupied region near the Fermi level[53]. After S addition, it is clear that the area of CO<sub>2</sub> desorption increases more significant than that of corresponding single N doped carbon nanospheres, indicating that the incorporation of S can result in more basic adsorption sites. Moreover, in N, S-co-doped carbon

nanospheres, N/S-C-Pyridine exhibits the highest area of CO<sub>2</sub> desorption, indicating that the strong electronic capabilities among all these three samples, which is consistent with the most positive shift of binding energy of C1s. Generally speaking, Lewis base property is related to pyridinic N, however, according to XPS analysis above, the N/S-C-Pyrimidine with the highest content of pyridinic N, by contrary, displays relatively weak Lewis base property compared to N/S-C-Pyridine with high graphitic N and thiophenic S. Therefore, the high content of graphitic N and thiophenic S may could act as the role of pyridinic N producing Lewis base sites by changing charge distribution of surrounding carbon atoms.

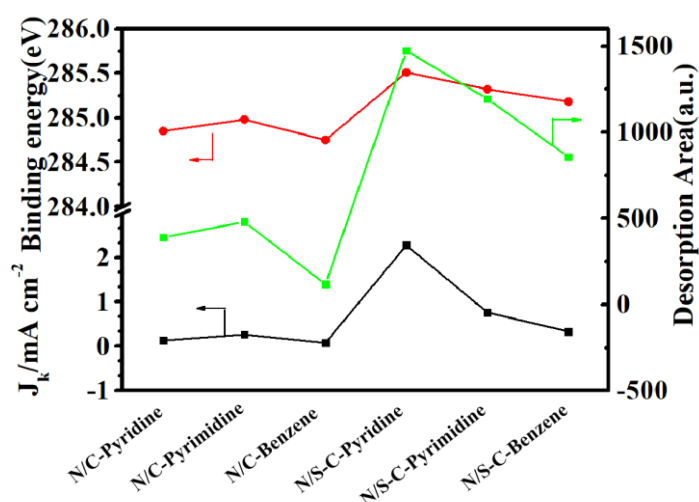


**Figure 5-6.** Correlation of binding energy of C1s, kinetic current density ( $J_k$ ) at 0.9V vs RHE and desorption area of CO<sub>2</sub> of N/S-C-Pyridine, N/S-C-Pyrimidine, N/S-C-Benzene and N-C-Pyridine, N-C-Pyrimidine, N-C-Benzene.

Combing with the analysis results of XPS, CO<sub>2</sub> adsorption and electrochemical activity of these catalysts as shown in Figure 5-6, it clearly demonstrates that the binding energy of C1s of these doped carbon nanospheres are positively correlated with the change tendency of kinetic current density at 0.9V as well as that of desorption area of CO<sub>2</sub>, indicating that no matter Lewis base site that closely linked with active sites

configuration or final catalytic activity for ORR could be reflected well via electronic structural characteristics of surrounding carbon atoms around doping atom. In other words, binding energy of C1s could be act as one of the intuitive indicators for judging catalytic activity of metal free doped carbon for ORR.

Density functional theory (DFT) calculations were performed to further explore the specific influence of N, S configuration produced on carbon atoms. In this work, a  $C_{63}H_{18}$  cluster as the initial model and its derived models with single doping site for pyridinic N, pyrrolic N, graphitic N and thiophenic S dopant and dual doping site with Thiophenic S and three respective N doping type were built up. It is believed that the ORR activity mainly originates from surrounding C atoms of doped heteroatoms as catalytic activity promoter for ORR due to the electronic structure changes of carbon atoms induced by heteroatoms doping [54]. More importantly, carbon atoms with positive spin or charge density larger than 0.15 have been identified as an key indicator for the judgement of catalytic active sites for ORR[55]. Thus, the number of carbon atoms with large charge density or positive spin density could be served as a barometer to evaluate the catalytic capability of the materials for ORR as well as reflects chemical environment change of doped carbon matrix. On the other hand, the maximum charge and spin density appeared in carbon matrix reflects the maximum electron transfer capability induced by corresponding heteroatom doping. More importantly, the distribution state change of the most active carbon atom' location in these models demonstrates transfer of electron transfer center with the doping of specific heteroatoms configurations [56]. Therefore, the analysis and comparison of charge and spin density

values in eight models focus on two aspects: 1. the percentage of carbon atoms with large charge density  $> 0.15$  or spin density  $> 0$  in all carbon atoms. 2. the transfer of carbon atom location with the highest charge or spin density. It is clear that among all these models, the model with pristine graphene exhibits the low percentage (4.76%) of active carbon atoms with charge density  $>0.15$  among these models. Meanwhile, it is notable that the percentage of active carbon atoms with charge density  $> 0.15$  increased to 7.94%, 11.11% and 12.5% with the addition of pyridinic N, graphitic N and pyrrolic N respectively. By contrast, there is almost no change on spin density in model of Graphene + Pyridinic N compared with pristine graphene, even there is an obvious decline of percentage of carbon with spin density  $>0$  with the addition of pyrrolic N. When the dual doping of S and N are introduced, the model of Graphene + Graphitic N+ Thiophenic S exhibits high content of active sites carbon atoms with charge density  $> 0.15$  of 11.11% and the highest percentage of active carbon atoms with positive spin density of 55.97% among all these models, indicating that the configuration of graphene+ Graphitic N+ Thiophenic S produces a great influence on electronic structure for the surrounding carbon atoms. In the model of Graphene + Pyrrolic N + Thiophenic S, the ratio of carbon atoms with charge density  $> 0.15$  and spin density  $> 0$  are 8.93% and 51.78% respectively. As for as the model of Graphene + Pyridinic N + Thiophenic S, it is notable that although it displays relatively maximum high charge but the percentage of effective carbon atoms with spin density  $>0$  is low, only 4.03%, and the spin density is considered as one of the crucial evaluation criterion of active carbon atoms which more important than charge density [57].

On the other hand, it is observed that carbon atoms with the highest charge or spin density in these models usually located near at doped heteroatoms, indicating that electronic redistribution induced by heteroatoms focus on the area near doping sites. Specifically, in the model of pristine graphene, both carbon atoms of C<sub>42</sub> and C<sub>45</sub> with the highest charge (0.182) and spin density (0.388) respectively at the edge of graphene, and C<sub>42</sub> are adjacent to C<sub>45</sub>. With addition of pyridinic N, carbon atom C<sub>42</sub> bonding to doped N atom in model of Graphene + Pyridinic N exhibits the highest charge density of 0.252, and the largest spin density with the value of 0.297. In the model of Graphene + Graphitic N, the carbon atom (C<sub>33</sub>) bonding to doped graphitic N displays the highest charge density of 0.256, among all carbon atoms in the model. It is notable that spin density in the model are 0, which may attribute to the disappeared edge polarization effect with doping of graphitic N [58]. When pyrrolic N is doped in graphene, the carbon atom of C<sub>17</sub> in the opposite position of the same hexagon ring as the doped pyrrolic N has the largest spin density 0.293 while C<sub>14</sub> separated by a carbon ring with pyrrolic N possess the largest spin density of 0.158. It is worth noting that in the model of single S doping, the spin density is 0 and the carbon atom (of C<sub>24</sub>) possess the highest charge density (0.181), far away from the doped S site. By contrast, the carbon atoms around S show relatively low charge and spin density, indicating that the single S doping produces almost negligible electron transfer on the whole carbon matrix. When N and S were co-doped, the charge and spin density are further increased, compared to single heteroatom doping. Specifically, in the model of Pyridinic N + Thiophenic S, C<sub>39</sub> bonded to pyridinic N site possess the high charge density of 0.184, and doped S

site exhibits the highest charge density of 0.241, meanwhile, the spin density of all carbon atoms are 0 in the model. When graphitic N and thiophenic S is co-doped, the carbon atom of C<sub>10</sub>, the neighbor of Graphitic N, shows the largest charge density of 0.245 and the highest spin density of 0.34 appeared in C<sub>33</sub>, which locates at junction of two carbon rings that contains doped graphitic N and thiophenic S respectively. In the model of Pyrrolic N + Thiophenic S, C<sub>16</sub> and C<sub>20</sub> that bonding to pyrrolic N, but far away from S, displays the highest charge and spin density of 0.269 and 0.185 respectively. In order to further confirm the most active sites in N, S co-doped models and their influence on specific progress of ORR. The free-energy diagrams under alkaline conditions was calculated to analyze the overpotential of crucial ORR steps.

Through the analysis of charge and spin density discussed above, the introduction of N, S in carbon framework can break the neutrality and redistribute the charges, facilitating the ORR process. According to charge and spin distribution in four models, the most promising four carbon atoms marked by yellow circles as ORR

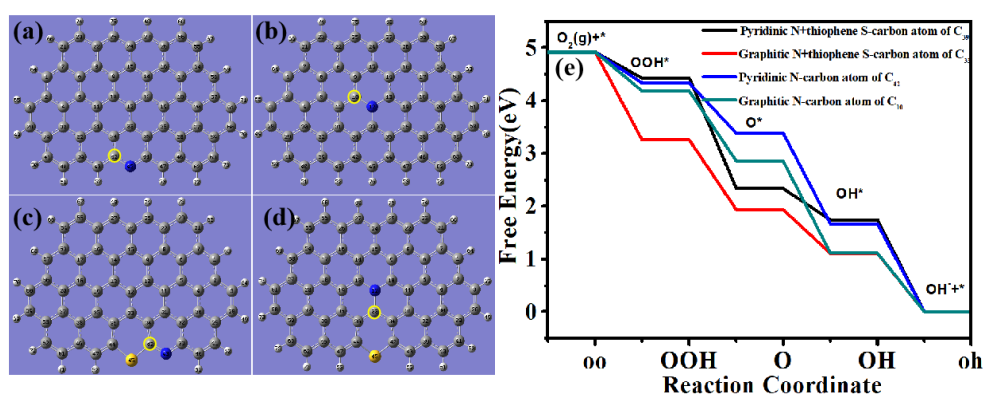


**Figure 5-7.** Models of Graphene + Pyridinic N + thiophenic S (a), Graphene + Graphitic N + thiophenic S (b), Graphene + Pyridinic N (c), Graphene + Graphitic N (d) and their corresponding free-energy diagram for ORR (e)

active sites in models of Graphene + Pyridinic N, Graphene + Graphitic N, Graphene + Pyridinic N + Thiophenic S, and Graphene + Graphitic N + Thiophenic S (Figure 5-

7 a-d) for ORR were selected for free energy calculation. As shown in Figure 5-7e, the calculated free energy diagram illustrates that the adsorption of O<sub>2</sub> (Step 1) are rate-limiting for ORR in an alkaline solution, in this case, protonation of OO\* are the most sluggish steps for ORR and the overpotentials are crucial parameters for reversible oxygen electrocatalysis [59,60]. According to DFT results, carbon atom C<sub>33</sub> in model of Graphene + Graphitic N + thiophenic S displays the least value of overpotential (0.403eV) among all these models, followed by carbon atom C<sub>42</sub> in model of Graphene + Graphitic N (0.45eV) and carbon atom C<sub>10</sub> in Graphene + Pyridinic N(0.5eV), and carbon atom 39 in model of Graphene + Pyridinic N + Thiophenic S shows high overpotential of 0.53eV. The results demonstrate that configuration of the model of Graphitic N + Thiophenic S is more conducive to the kinetic process of ORR, compared with other single or co-doped N, S configuration, which may attribute to the synergy effect from the electronic distribution change of surrounding carbon atoms of graphitic N plus thiophenic S, leading to carbon atoms polarization with positive charge, therefore, producing enhanced ability of oxygen adsorption.

**Table 1.** The specific parameters of N and N, S co-doped carbo nanospheres.

Samples	BET Surface area (m <sup>2</sup> ·g <sup>-1</sup> )	Pyridinic N content (at%)	Graphitic N content (at%)	Thiophenic S content (at%)	ORR E <sub>1/2</sub> 3.0 mA cm <sup>-2</sup> (V vs RHE)
N-C-Pyridine	1260	0.82	2.38	NA	0.76

N-C-Pyrimidine	1190	1.58	2.03	NA	0.79
N-C-Benzene	1184	0.68	2.13	NA	0.71
N,S-C-Pyridine	1024	0.926	2.02	0.50	0.87
N,S-C-Pyrimidine	966	1.16	1.85	0.46	0.82
N,S-C-Benzene	1146	0.87	1.2	0.48	0.78
Pt/C					0.86

Combining DFT results discussed above and the summary of key physical properties and ORR activity of N and N, S co-doped carbon nanospheres (table 1), it can be well explained the significant enhancement of ORR catalytic activity of N/S-C systems relative to that on single N doped catalysts in this study. As for as single N doped nanospheres, N-C-Pyrimidine exhibits the best catalytic activity for ORR among single N doped catalysts, due to its highest content of pyridinic N that induces high charge and spin density. While, N-C-Pyridine featured with the highest content of graphitic N but low content of pyridinic N displays relatively low ORR performance than N-C-Pyrimidine, and N-C-Benzene possess the lowest activity for ORR due to relatively weak electron transfer of around carbon atoms. The result is consistent with previous related reports [60]. Meanwhile, it could be well explained that N/S-C-Pyridine with relatively low content Pyridinic N but high content of Graphitic N



displays higher catalytic activity than N/S-C-Pyrimidine-900 with the highest content of pyridinic N due to the stronger synergistic effect between pyridinic N and thiophene S than that of graphitic N and thiophene S.

#### **5.4 Conclusion**

Single N doped and N, S co-doped carbon nanospheres have been successfully prepared using three typical heterocyclic nitrogen groups (Pyridine, Pyrimidine, Benzene) as precursors using a green and template-free chemical method for correlating precursor types with active sites configuration for ORR catalysis. N atoms in rings of precursors have an vital role in final catalytic activity via the significant effect on the content of each doping species and their specific configuration that closely related to catalytic performance for ORR. Pyrimidine based precursors prefer to form high content of Pyridinic N that contributes to its highest catalytic activity for ORR among single N doped carbon nanospheres, meanwhile, Pyridine based precursor tends to afford more graphitic N and the carbon nanospheres derived from Benzene based precursor possess more content of Pyrrolic N. Furthermore, N, S co-doped carbon nanospheres with Pyridine based precursor exhibits the best catalytic activity for ORR in N, S co-doped carbon nanospheres that attributes to the configuration of graphitic N and thiophenic S dopants induces strongly increased charge and spin distribution on surrounding carbon atoms, that promote catalytic activity for ORR. This synergistic effect is much more significant than the configuration of pyridinic N and thiophenic S. The clear elucidation between analogous N-containing precursors and active site configuration as well as final ORR activity in this study not only strengthens the

molecular-level understanding of the critical role precursors on active sites, but also provides a new highlight for precise synthesis of advanced multi-heteroatom doped carbon ORR electrocatalysts with synergistically enhancing effect through purposefully selecting precursors and doping elements.

## References

- [1] M. S. Dresselhaus, I. L. Thomas, Alternative Energy Technologies. *Nature* **2001**, *414*, 332–337.
- [2] N. Wang, B. Z. Lu, L. G. Li, W. H. Niu, Z. H. Tang, X.W. Kang, S. W. Chen, Graphitic Nitrogen Is Responsible for Oxygen Electroreduction on Nitrogen-Doped Carbons in Alkaline Electrolytes: Insights from Activity Attenuation Studies and Theoretical Calculations. *ACS Catal.* **2018**, *8*, 6827-6836.
- [3] N. S. Lewis, D. G. Nocera, Powering the Planet: Chemical Challenges in Solar Energy Utilization. *Proc. Natl. Acad. Sci. U. S. A.* **2006**, *103*, 15729-15735.
- [4] J. A. Turner, Sustainable Hydrogen Production. *Science* **2004**, *305*, 972-974.
- [5] S. Chu, Y. Cui, N. Liu, The Path towards Sustainable Energy. *Nat. Mater.* **2017**, *16*, 16-22.
- [6] C. P. Grey, J. M. Tarascon, Sustainability and In Situ Monitoring in Battery Development. *Nat. Mater.* **2017**, *16*, 45-56.
- [7] X. Ge, A. Sumboja, D. Wu, T. An, B. Li, F. W. T. Goh, T. S. A. Hor, Y. Zong, Z. Liu, Oxygen Reduction in Alkaline Media: From Mechanisms to Recent Advances of Catalysts. *ACS Catal.* **2015**, *5*, 4643-4667.
- [8] Z. Cui, G. Fu, Y. Li, J. B. Goodenough, Ni<sub>3</sub>FeN-Supported Fe<sub>3</sub>Pt Intermetallic

Nanoalloy as a High-Performance Bifunctional Catalyst for Metal-Air Batteries. *Angew. Chem. Int. Ed.* **2017**, *56*, 9901-9905.

[9] C. Y. He, J. J. Zhang, P. K. Shen, Nitrogen-Self-Doped Graphene-Based Non-Precious Metal Catalyst with Superior Performance to Pt/C Catalyst toward Oxygen Reduction Reaction. *J. Mater. Chem. A* **2014**, *2*, 3231-3236.

[10] W. Wei, H. Liang, K. Parvez, X. Zhuang, X. Feng, K. Muellen, Nitrogen-Doped Carbon Nanosheets with Size-Defined Mesopores as Highly Efficient Metal-Free Catalyst for the Oxygen Reduction Reaction. *Angew. Chem. Int. Ed.* **2014**, *53*, 1570-1574.

[11] L. Qin, L. C Wang, X. Yang, R. M. Ding, Z. F. Zheng, X. H. Chen, B. L. Lv, Synergistic Enhancement of Oxygen Reduction Reaction with BC<sub>3</sub> and Graphitic-N in Boron-and Nitrogen-Codoped Porous Graphene. *J. Catal.* **2018**, *359*, 242-250.

[12] H. T. Chung, D. A. Cullen, D. Higgins, B. T. Sneed, E. F. Holby, K. L. More, P. Zelenay, Direct Atomic-Level Insight into the Active Sites of a High-Performance PGM-free ORR Catalyst. *Science* **2017**, *357*, 479-484.

[13] Z. Q. Tian, S. H. Lim, C. K. Poh, Z. Tang, Z. Xia, Z. Luo, P. K. Shen, D. Chua, Y. P. Feng, Z. Shen, J. Lin, A Highly Order-Structured Membrane Electrode Assembly with Vertically Aligned Carbon Nanotubes for Ultra-Low Pt Loading PEM Fuel Cells. *Adv. Energy Mater.* **2011**, *1*, 1205-1214.

[14] Y. Jiao, Y. Zheng, M. Jaroniec, S. Z. Qiao, Chem. Design of Electrocatalysts for Oxygen- and Hydrogen-involving Energy Conversion Reactions. *Soc. Rev.* **2015**, *44*, 2060-2086.

- [15] K. Gong, F. Du, Z. Xia, M. Durstock, L. Dai, Nitrogen-Doped Carbon Nanotube Arrays with High Electrocatalytic Activity for Oxygen Reduction. *Science* **2009**, *323*, 760–764.
- [16] J. Zhang, Z. Zhao, Z. Xia, L. Dai, A Metal-Free Bifunctional Electrocatalyst for Oxygen Reduction and Oxygen Evolution Reactions. *Nat. Nanotechnol.* **2015**, *10*, 444–452.
- [17] Y. Ito, W. Cong, T. Fujita, Z. Tang, M. Chen, High Catalytic Activity of Nitrogen and Sulfur Co-Doped Nanoporous Graphene in the Hydrogen Evolution Reaction. *Angew. Chem., Int. Ed.* **2015**, *54*, 2131–2136.
- [18] M. T. Li, L. P. Zhang, Q. Xu, J. B. Niu, Z. H. Xia, N-doped Graphene as Catalysts for Oxygen Reduction and Oxygen Evolution Reactions: Theoretical Considerations. *J. Catal.* **2018**, *314*, 66-72.
- [19] L. Yu, X. L. Pan, X. M. Cao, P. Hu, X. H. Bao, Oxygen Reduction Reaction Mechanism on Nitrogen-doped Graphene: A Density Functional Theory Study. *J. Catal.* **2011**, *282*, 183-190.
- [20] A. Arunchander, S. G. Peera, S. K. Panda, S. Chellammal, A. K. Sahu, Simultaneous co-doping of N and S by A Facile in-situ Polymerization of 6-N, N-dibutylamine-1,3,5-triazine-2,4-dithiol on Graphene Framework: An Efficient and Durable Oxygen Reduction Catalyst in Alkaline Medium, *Carbon* **2017**, *118*, 531-544.
- [21] P. H. Matter, L. Zhang, U. S. Ozkan, The Role of Nanostructure in Nitrogen-containing Carbon Catalysts for The Oxygen Reduction Reaction. *J. Catal.* **2006**, *239*, 83-96.

- [22] L. M. Dai, Y. H. Xue, L. T. Qu, H. J. Choi, J. B. Baek, Metal-Free Catalysts for Oxygen Reduction Reaction. *Chem. Rev.* **2015**, *115*, 4823- 4892.
- [23] D. Guo, R. Shibuya, C. Akiba, S. Saji, T. Kondo, J. Nakamura, Active Sites of Nitrogen-Doped Carbon Materials for Oxygen Reduction Reaction Clarified Using Model Catalysts. *Science* **2016**, *351*, 361–365.
- [24] L. Lai, J. R. Potts, D. Zhan, L. Wang, C. K. Poh, C. Tang, H. Gong, Z. Shen, J. Lin, R. S. Ruoff, Exploration of the Active Center Structure of Nitrogen-Doped Graphene-Based Catalysts for Oxygen Reduction Reaction. *Energy Environ. Sci.* **2012**, *5*, 7936–7942.
- [25] H. B. Yang, J. Miao, S. F. Hung, J. Chen, H. B. Tao, X. Wang, L. Zhang, R. Chen, J. Gao, H. M. Chen, Identification of Catalytic Sites for Oxygen Reduction and Oxygen Evolution in N Doped Graphene Materials: Development of Highly Efficient Metal-Free Bifunctional Electrocatalyst. *Sci. Adv.* **2016**, *2*, 1501122.
- [26] J. Liang, Y. Jiao, M. Jaroniec, S. Z. Qiao, Sulfur and Nitrogen Dual-Doped Mesoporous Graphene Electrocatalyst for Oxygen Reduction with Synergistically Enhanced Performance. *Angew. Chem., Int. Ed.* **2012**, *51*, 11496–11500.
- [27] Y. Zheng, Y. Jiao, L. Ge, M. Jaroniec, S. Z. Qiao, Two-Step Boron and Nitrogen Doping in Graphene for Enhanced Synergistic Catalysis. *Angew. Chem., Int. Ed.* **2013**, *52*, 3110–3116.
- [28] R. Silva, D. Voiry, M. Chhowalla, T. Asefa, Efficient Metal-Free Electrocatalysts for Oxygen Reduction: Polyaniline-Derived N- and O-Doped Mesoporous Carbons. *J. Am. Chem. Soc.* **2013**, *135*, 7823-7826.

- [29] W. Wei, H. W. Liang, K. Parvez, X. D. Zhuang, X. Feng, K. Müllen, Nitrogen-Doped Carbon Nanosheets with Size-Defined Mesopores as Highly Efficient Metal-free Catalyst for the Oxygen Reduction Reaction. *Angew. Chem., Int. Ed.* **2014**, *53*, 1570-1574.
- [30] Z. Lin, G. H. Waller, Y. Liu, M. Liu, C. P. Wong, 3D Nitrogen-doped Graphene Prepared by Pyrolysis of Graphene Oxide with Polypyrrole for Electrocatalysis of Oxygen Reduction Reaction. *Nano Energy* **2013**, *2*, 241-248.
- [31] C. A. Cao, X. Zhuang, Y. Su, Y. Zhang, F. Zhang, D. Wu, X. Feng, 2D Polyacrylonitrile Brush Derived Nitrogen-doped Carbon Nanosheets for High-performance Electrocatalysts in Oxygen Reduction Reaction. *Polym. Chem.* **2014**, *5*, 2057-2064.
- [32] Z. Xiang, D. Cao, L. Huang, J. Shui, M. Wang, L. Dai, Nitrogen-Doped Holey Graphitic Carbon from 2D Covalent Organic Polymers for Oxygen Reduction. *Adv. Mater.* **2014**, *26*, 3315-3320.
- [33] P. Shi, J. Guo, X. Liang, S. Cheng, H. Zheng, Y. Wang, Large-scale Production of High-quality Graphene Sheets by A Non-Electrified Electrochemical Exfoliation Method. *Carbon* **2018**, *126*, 507-513.
- [34] M. Eddaoudi, J. Kim, N. Rosi, D. Vodak, J. Wachter, M. O’Keeffe, O. M. Yaghi, Systematic Design of Pore Size and Functionality in Isoreticular MOFs and Their Application in Methane Storage. *Science* **2002**, *295*, 469-472.
- [35] Y. Zhao, C. Hu, L. Song, L. Wang, G. Shi, L. Dai, L. Qu, Functional Graphene Nanomesh Foam. *Energy Environ. Sci.* **2014**, *7*, 1913-1918.

- [36] H. Liang, W. Wei, Z. Wu, X. Feng, K. Muellen, Mesoporous Metal-Nitrogen-Doped Carbon Electrocatalysts for Highly Efficient Oxygen Reduction Reaction. *J. Am. Chem. Soc.* **2013**, *135*, 16002-16005.
- [37] G. Wu, N. H. Mack, W. Gao, S. G. Ma, R. Q. Zhong, J. T. Han, J. K. Baldwin, P. Zelenay, Nitrogen-Doped Graphene-Rich Catalysts Derived from Heteroatom Polymers for Oxygen Reduction in Nonaqueous Lithium-O<sub>2</sub> Battery Cathodes. *ACS Nano* **2012**, *6*, 9764-9776.
- [38] G. Wu, C. M. Johnston, N. H. Mack, K. Artyushkova, M. Ferrandon, M. Nelson, J. S. L. Pacheco, S. D. Conradson, K. L. More, D. J. Myersd, P. Zelenay, Synthesis-structure-performance Correlation for Polyaniline-Me-C Non-Precious Metal Cathode Catalysts for Oxygen Reduction in Fuel Cells. *J. Mater. Chem.* **2011**, *21*, 11392-11405.
- [39] S. Mukherjee, D. A. Cullen, S. Karakalos, K. Liu, H. Zhang, S. Zhao, H. Xu, K. L. More, G. F. Wang, G. Wu, Metal-organic Framework-derived Nitrogen-doped Highly Disordered Carbon for Electrochemical Ammonia Synthesis using N<sub>2</sub> and H<sub>2</sub>O in Alkaline Electrolytes. *Nano Energy* **2018**, *48*, 217-226.
- [40] X. R. Zhang, Y. Q. Wang, Y. H. Du, M. Qing, F. Yu, Z. Q. Tian, P. K. Shen, Highly Active N, S co-doped Hierarchical Porous Carbon Nanospheres from Green and Template-free Method for Super Capacitors and Oxygen Reduction Reaction. *Electrochim. Acta*, **2019**, *20*, 272-280.
- [41] J. Li, Y. Zhang, X. Zhang, J. Huang, J. Han, Z. Zhang, S, N Dual-doped Graphene-like Carbon Nanosheets as Efficient Oxygen Reduction Reaction Electrocatalysts. *ACS Appl. Mater. Interfaces* **2017**, *9*, 398-405.

- [42] J. Liang, Y. Jiao, M. Jaroniec, S. Z. Qiao, Sulfur and Nitrogen Dual-Doped Mesoporous Graphene Electrocatalyst for Oxygen Reduction with Synergistically Enhanced Performance. *Angew. Chem., Int. Ed.*, **2012**, *51*, 11496-11500.
- [43] Z. Yang, Z. Yao, G. F. Li, G. Y. Fang, H. G. Nie, Z. Liu, X. M. Zhou, X. Chen, S. M. Huang, Sulfur-Doped Graphene as an Efficient Metal-free Cathode Catalyst for Oxygen Reduction. *ACS Nano*, **2012**, *6*, 205-211.
- [44] T. Akhter, M. M. Islam, S. N. Faisal, E. Haque, A. I. Minett, H. K. Liu, Self-assembled N/S co-doped Flexible Graphene Paper for High Performance Energy Storage and Oxygen Reduction Reaction. *ACS Appl. Mater. Interfaces* **2016**, *8*, 2078-2087.
- [45] K. G. Qu, Y. Zheng, X. X. Zhang, K. Davey, S. Dai, S. Z. Qiao, Promotion of Electrocatalytic Hydrogen Evolution Reaction on Nitrogen-Doped Carbon Nanosheets with Secondary Heteroatoms. *ACS Nano* **2017**, *11*, 7293–7300.
- [46] Z. Wu, R. Liu, J. Wang, J. Zhu, W. Xiao, C. Xuan, W. Lei, D. Wang. Nitrogen and Sulfur Co-doping of 3D Hollow-structured Carbon Spheres as an Efficient and Stable Metal Free Catalyst for the Oxygen Reduction Reaction. *Nanoscale*, **2016**, *45*, 19086-19092.
- [47] L. Zhang, Z. Xia. Mechanisms of Oxygen Reduction Reaction on Nitrogen-doped Graphene for Fuel Cells. *J. Phys. Chem. C*, **2011**, *115*, 11170-11176.
- [48] D. W. Chang, H. J. Choi, J. B. Baek. Wet-chemical Nitrogen-doping of Graphene Nanoplatelets as Electrocatalysts for The Oxygen Reduction Reaction. *J. Mater. Chem.*, **2015**, *14*, 7659-7665.



- [49] T. Xing, Y. Zheng, L. H. Li, B. C. C. Cowie, D. Gunzelmann, S. Z. Qiao, S. Huang, Y. Chen. Observation of Active Sites for Oxygen Reduction Reaction on Nitrogen-doped Multilayer Graphene. *ACS Nano*, **2014**, *8*, 6856-6862.
- [50] M. Vikkisk, I. Kruusenberg, U. Joost, E. Shulga, I. Kink, K. Tammeveski, Electrocatalytic Oxygen Reduction on Nitrogen-doped Graphene in Alkaline Media. *Appl. Catal., B*, **2014**, *147*, 369-376.
- [51] C. V. Rao, C. R. Cabrera, Y. Ishikawa. In Search of the Active Site in Nitrogen-doped Carbon Nanotube Electrodes for the Oxygen Reduction Reaction. *J. Phys. Chem. Lett.*, **2010**, *18*, 2622-2627.
- [52] S. Wang, L. Zhang, Z. Xia, A. Roy, D. W. Chang, J. B. Baek, L. Dai. BCN Graphene as Efficient Metal-Free Electrocatalyst for The Oxygen Reduction Reaction. *Angew. Chem. Int. Ed.*, **2012**, *51*, 4209-4212.
- [53] Z. Yang, Z. Yao, G. Li, G. Fang, H. Nie, Z. Liu, X. Zhou, X. a. Chen, S. Huang, Sulfur-doped Graphene as an Efficient Metal-free Cathode Catalyst for Oxygen Reduction. *ACS Nano*, **2011**, *6*, 205-211.
- [54] X. Wu, Z. Xie, M. Sun, T. Lei, Z. Zuo, X. Xie, Edge-rich and (N, S)-doped 3D Porous Graphene as an Efficient Metal-free Electrocatalyst for the Oxygen Reduction Reaction. *RSC Adv.* **2016**, *6*, 90384-90387.
- [55] T. Jiang, Y. Wang, K. Wang, Y. Liang, D. Wu, P. Tsiakaras, S. Song. A Novel Sulfur-Nitrogen Dual Doped Ordered Mesoporous Carbon Electrocatalyst for Efficient Oxygen Reduction Reaction. *Appl. Catal., B*, **2016**, *189*, 1-11.
- [56] A. Arunchander, S. G. Peera, S.K. Panda, S. Chellammal, A. K. Sahu,

Mechanisms of Oxygen Reduction Reaction on Nitrogen-Doped Graphene for Fuel Cells. *Carbon* **2017**, *118*, 531-544.

[57] F. Sun, X. Chen, Sulfur and Nitrogen Dual-doped Mesoporous Graphene Electrocatalyst for Oxygen Reduction with Synergistically Enhanced Performance. *Electrochem. Commun.* **2017**, *82*, 89-92.

[58] X. Chen, J. Chang, Q. Ke, Supramolecular Polymerization-Assisted Synthesis of Nitrogen and Sulfur Dual-doped Porous Graphene Networks from Petroleum Coke as Efficient Metal-free Electrocatalysts for the Oxygen Reduction Reaction. *Carbon* **2018**, *126*, 53-57.

[59] L. Zhang, Z. Xia, Mechanisms of Oxygen Reduction Reaction on Nitrogen-Doped Graphene for Fuel Cells. *J. Phys. Chem. C* **2011**, *115*, 11170-11176. [60] J. Liang, Y. Jiao, M. Jaroniec, S. Z. Qiao. Sulfur and Nitrogen Dual-Doped Mesoporous Graphene Electrocatalyst for Oxygen Reduction with Synergistically Enhanced Performance. *Angew. Chem. Int. Ed.*, **2012**, *51*, 11496-11500.

# **Chapter 6: Active Sites Engineering via Tuning Configuration between Graphitic-N and Thiophenic-S Dopants in one-step Synthesized Graphene Nanosheets for Efficient Water-Cycled Electrocatalysis**

## **Abstract**

Precisely tuning synergetic effect between multi-heteroatom dopants in carbon matrix for water-cycled reactions such as hydrogen evolution reaction (HER) and oxygen evolution reaction (OER) and oxygen reduction reaction (ORR) is critical for fuel cell technologies. Herein, an effective active site engineering strategy of bottom-up synthesized N, S co-doped graphene (NSG) nanosheets was developed via a facile pyrolysis of the mixed solid power of 2,6-diaminopyridine (DAP) as N source and ammonium persulfate (AP) as S source. All of NSG nanosheets prepared with various mass ratio of DAP and AP possess a high surface area up to more than  $1000 \text{ m}^2 \text{ g}^{-1}$  and highly degree of crystallinity, but displays significant differentiation in electrocatalytic selectivity. For instance, the NSG prepared by DAP and AP with the mass ratio of 1:1 displays the highest ORR performance with half-wave potential of  $0.87 \text{ V vs. RHE}$ , while the NSG with 3:1 and the NSG with 1:3 exhibit the highest activity for OER and HER respectively with corresponding potential at  $10 \text{ mA cm}^{-2}$  of  $1.58 \text{ V}$  and  $0.118 \text{ V vs. RHE}$ , respectively. These activities are comparable and even better than their precious metals counterparts, outperform the vast majority of reported doped carbon prepared using other strategies and precursors. The excellent electrocatalytic activities

essentially originates from the optimized intermediates energy of three reaction pathway via active sites engineering constructed by tuning the ratio of graphitic-N and thiophenic-S dopants in NSG nanosheets, realized by controlling the ratio of DAP and AP. This simple active sites tuning strategy provides an effective and convenient way to develop controllable function-orientated water-cycled electrocatalysis in one catalyst based on a certain platform of N-containing precursor.

*\*Reprinted (adapted) with permission from Xiaoran Zhang, Yunqiu Wang, Kun Wang, Yilin Huang, Dandan Lyu, Feng Yu, Shuangbao Wang, Zhi Qun Tian\*, Pei Kang Shen, San Ping Jiang,\* Active sites engineering via tuning configuration between graphitic-N and thiophenic-S dopants in one-step synthesized graphene nanosheets for efficient water-cycled electrocatalysis. Chem. Eng. J. 2021, 416, 129096.*

## **6.1 Introduction**

Fuel cells, metal-air batteries and water splitting related devices were considered as environmentally friendly and renewable energy technologies to solve energy crisis. The key water-cycled electrochemical processes involved the three important reactions: oxygen reduction reaction (ORR), oxygen evolution reaction (OER), and hydrogen evolution reaction (HER)[1-3]. To date, the most efficient and the state-of-the-art catalysts for ORR, OER and HER are platinum (Pt)-based electrocatalysts, Ru and Ir oxides respectively [4]. However, these precious metal electrocatalysts with limited resources and prohibitive cost hampered the large-scale application of these sustainable energy conversion technologies. Therefore, great efforts have been made on developing

alternative non-precious metal (NPM) electrocatalysts, such as transition metals based nitrogen doped carbon materials (M-N-C), transition metal oxides, sulfides, phosphides, metal carbides, metal nitrides, *ect.*[5]. However, these NPM catalysts suffer from the potential detrimental impact of the dissolved transition metal species on performance and stability of perfluorosulfonic acid (PFSA) polymer electrolyte membranes such as Nafion of polymer electrolyte membrane fuel cells (PEMFCs). Therefore, developing robust and highly efficient metal-free based electrocatalysts as promising candidates for metal-containing electrocatalysts is highly demand.

Carbon materials attracted researchers' wide attention due to its intrinsic structure characteristics (such as high electronic conductivity and structure tenability *ect.*) that could be modified via fine regulation for various physical and chemical properties, and they were widely used in various basic science fields [6]. Especially, heteroatom doped metal-free carbon materials shows its great application potential due to its flexible electronic band structures. The introduction of heteroatom dopants into carbon matrix provides an effective route to tailor its electronic band structure as well as produces singly-occupied donor level due to the presence of  $\pi$  and  $\pi^*$  states from the  $sp^2$  sites, leading to the new  $\pi^*$  conduction band, providing a possibility to produce multifunctional catalytic activity for various reactions via tuning electronic structure [7, 8]. Among all kinds of doped heteroatoms, N was considered as one of the most promising dopants due to its strong electronegativity and similar atomic sizes with C atoms [9, 10]. Furthermore, by introducing a secondary doped element catalytic activity of doped carbon materials can be further enhanced due to their complicated

synergistic effects of different dopants and may produce wide catalytic activity as multifunctional electrocatalysis [11,12]. Especially, N, S co-doped carbon materials attracted much attention, tremendous efforts of theoretical and experimental have been made on studying N, S co-doped carbon materials as efficient multifunctional electrocatalysts [13,14]. However, there is a hot debate on the specific catalytic mechanism and effective catalytic active sites in N, S co-doped catalysts. For HER, some researchers suggested that S doping plays a crucial role in enhancing final catalytic performance validated by the addition of S leads to marked changes of electronic energy structure on carbon matrix [15, 16]. For OER, some groups proposed that the doped S dopant may produce significant role in enhancing final catalytic activity for ORR rather than doped N dopant [17]. But, some researchers reported that pyridinic N, C-O, C-S-C and surface polar oxygen groups contributes to increased catalytic activity for OER due to their favorable adsorption of hydroxyl species [18, 19]. For ORR, some researchers proved that pyridinic N act as the effective active sites for ORR [20]. But, some others proposed that graphitic N may be responsible for the catalytic activity for ORR [21, 22].

Despite the aforementioned considerable achievements, N, S co-doped carbon materials still suffer from low catalytic activity compared to commercial precious metal catalysts, and fundamental understanding on the correlation between N, S active sites configurations and final catalytic activity for the three reactions is still keep in unclear. One of the main reasons is that the coexistence of different N (pyridinic N, graphitic N, pyrrolic N and oxidized N) and S species that leads to diversity of potential active sites

configurations that caused a great challenge to precisely tuning synergetic effect between N, S heteroatom dopants in carbon matrix for function-oriented water-cycled electrocatalysis. And the unclear correlation between N, S configurations and their electrocatalytic activity and selectivity for water-cycled reactions is a bottleneck for developing highly efficient and functional-oriented N, S co-doped catalysts.

In this work, 2,6-diaminopyridine is selected as flexible nitrogen-containing precursor platform for precisely tuning synergetic effect of N, S via tuning the ratio of graphitic N and S for function-oriented water-cycled reactions ORR, OER and HER respectively. According to our previous work [23-26], direct pyrolysis of 2,6-diaminopyridine is prefer to forming high content of graphitic N that is considered as one of the most important N species for the three reactions. Meanwhile, ammonium persulfate was introduced as S source to tune the ratio of N and S. It is found that there is a close relation between the ratio of added N, S precursors and ratio of graphitic N and thiophenic S formed in graphene matrix that provides a possibility to realize optimization of intermediates energy in each reaction pathway for ORR, OER and HER respectively. This study will shed light on one-step solid reaction bottom-up synthesized N, S co-doped functional-oriented graphene materials as promising water based electrocatalyst for tailorable catalytic capabilities on one catalyst.

## **6.2 Results and Discussion**

### *6.2.1 Structure properties*

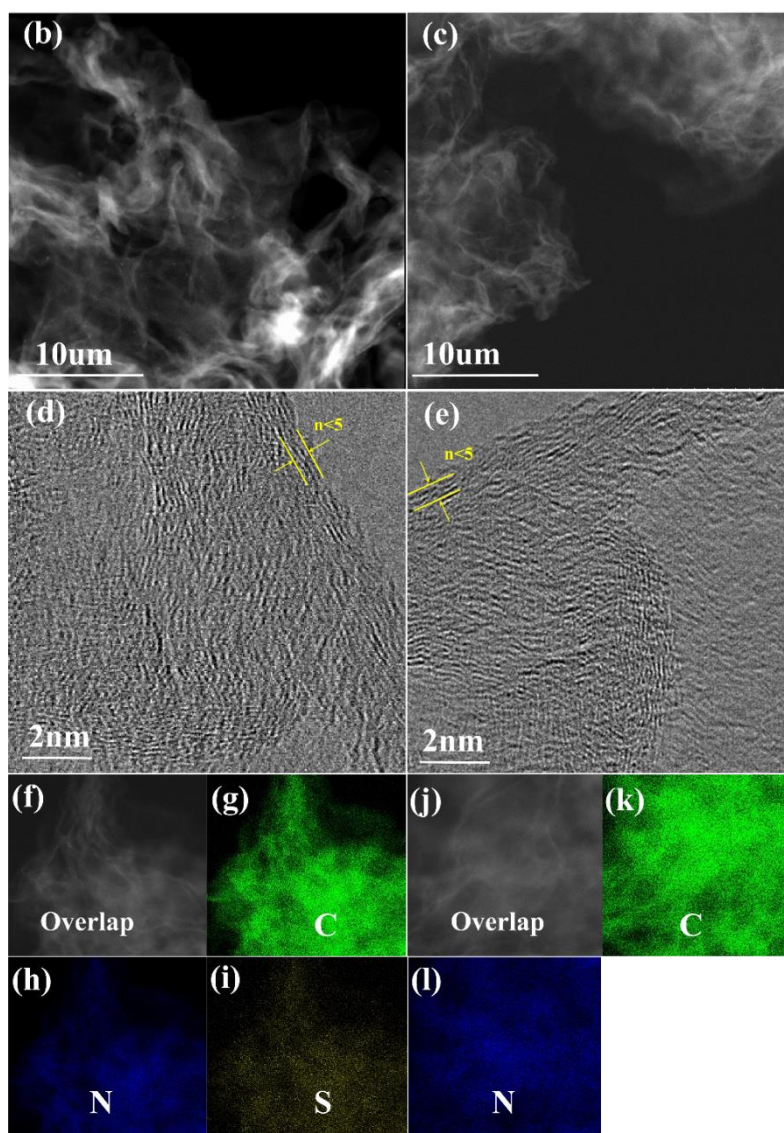
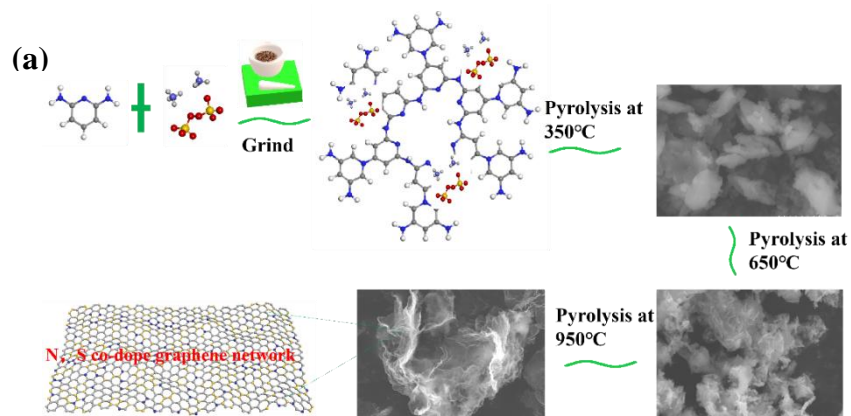


**Figure 6-1.** Illustration of the synthesis process of these N, S co-doped graphene nanosheets (a). Transmission Electron Microscope (TEM) images (b-e) and mapping images of the NSgraphene-(1:1)(f-i) and N-graphene (j-l).

Figure 6-1a illustrate the synthesis process of these N, S co-doped graphene nanosheets. From the transmission electron microscopy (TEM) images (Figure 6-1b-e).



It is found that all these N, S co-doped graphene nanosheets display uniform graphene-like structure. Transmission electron microscope (TEM) images of these N, S co-doped graphene nanosheets show “fluffy” porous-graphene structure, meanwhile, the high-resolution TEM image manifests measured graphene lattice fringe layers below 10 layers. Meanwhile, these N, S co-doped graphene nanosheets with different ratio of N/S exhibit similar graphene morphological structure, indicating that content of N, S has little impact on final morphological structure. Element Mapping images of N-graphene (Figure 6-1j-l) and N, S co-doped graphene nanosheets (Figure 6-1f-l) demonstrates C, N, S elements evenly distributed onto the graphene nanosheets.

Crystal structure information of these N, S co-doped catalysts, was further analyzed by X-ray diffraction (XRD), as shown in Figure 6-2a. It is notable that all N,S-co-doped catalysts exhibit two obvious peaks at around  $26.3^\circ$  and  $42.1^\circ$ , which corresponding to the (002) and (100) planes of graphitic carbon (PDF#41-1487) respectively[27]. More importantly, there are sharp and strong diffraction peaks a the peak at  $26.4^\circ$ , demonstrating that these N, S co-doped graphene nanosheets are highly graphitized. Meanwhile, these catalysts with different N/S ratio exhibits similar carbon crystal structure manifests different N, S doping ratios has little influence effect on carbon crystal structure of these N,S co-doped catalysts.

Raman spectra analysis has also been used extensively to probe the heteroatom doping effect of these N, S co-doped graphene nanosheets. As shown in Figure 6-2 b, There are two main peaks D ( $1350\text{ cm}^{-1}$ ) and G ( $1580\text{ cm}^{-1}$ ) [28]. The ratio of ID/IG is 0.526, 0.501, 0.742, 0.523, 0.575, 0.517, 0.796, 0.718, and 0.812 corresponding to N-

graphene, NSgraphene-(1:4), NSgraphene-(1:3), NSgraphene-(1:2), NSgraphene-(1:1), NSgraphene-(2:1), NSgraphene-(3:1), NSgraphene-(1:4) Meanwhile, all these catalysts has a obvious and sharp 2D peak at around  $2750\text{cm}^{-1}$ , indicating their highly graphitized structure, which is consistent with TEM and XRD results discussed above.

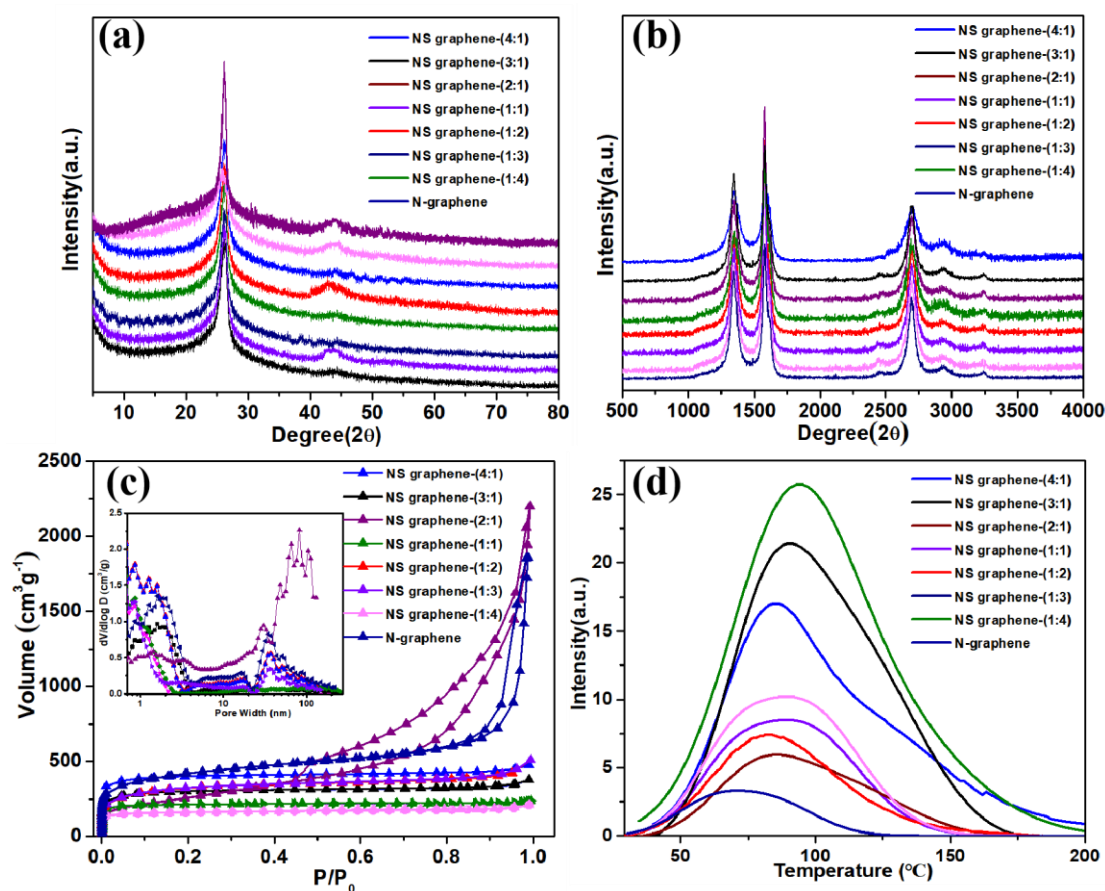


**Figure 6-2.** XRD (a), Raman spectrum(b) Nitrogen adsorption-desorption isotherms and Pore size distribution(c) CO<sub>2</sub> TPD profiles(d) of NSgraphene-(4:1), NSgraphene-(3:1), NSgraphene-(2:1), NSgraphene-(1:1), NSgraphene-(1:2), NSgraphene-(1:3), NSgraphene-(1:4) and N-graphene.

The pore structure of the as-synthesized N, S co-doped graphene nanosheets was analyzed by N<sub>2</sub> adsorption and desorption isotherms (Figure 6-2c). The as-synthesized N, S co-doped graphene nanosheets possesses type-IV with H4 hysteresis loops, indicating the coexistence of micropore and mesoporous structure [29]. BET surface

area of N-graphene, NSgraphene-(4:1), NSgraphene-(3:1), NSgraphene-(2:1), NSgraphene-(1:1), NSgraphene-(1:2), NSgraphene-(1:3), NSgraphene-(1:4) are corresponding to 923m<sup>2</sup>/g, 956m<sup>2</sup>/g, 1166 m<sup>2</sup>/g, 1210 m<sup>2</sup>/g, 1049m<sup>2</sup>/g, 1158 m<sup>2</sup>/g, 1058 m<sup>2</sup>/g and 899m<sup>2</sup>/g respectively. According to the pore size distribution results (Figure 6-2c insert), it can be seen that pore size distribution of these samples seems slightly different. The main pore size distribution focus on 1-2nm in these N,S co-doped samples, and there are small part of mesopores distributed in diameter of 2-10nm. TPD profiles of CO<sub>2</sub> was conducted to analysis the active sites adsorption information (Figure 6-2d). It is observed that N-graphene has the smallest CO<sub>2</sub> desorption intensity, demonstrating its relatively weak basicity among all these samples. More importantly, it is obvious that there are completely different CO<sub>2</sub> desorption peaks and areas of these N, S co-doped graphene nanosheets with different ratio, indicating that the different ratio of N and S influence greatly of electronic structure and acidity and basicity on carbon matrix.

X-ray photoelectron spectroscopy (XPS) as a powerful technique was used to analysis the chemical composition in these catalysts, electronic structures and element content bonding configurations (shown in Figure 6-3). It could be found that there are four element (C, N, O, S) exist in these catalysts (Figure 6-3a).

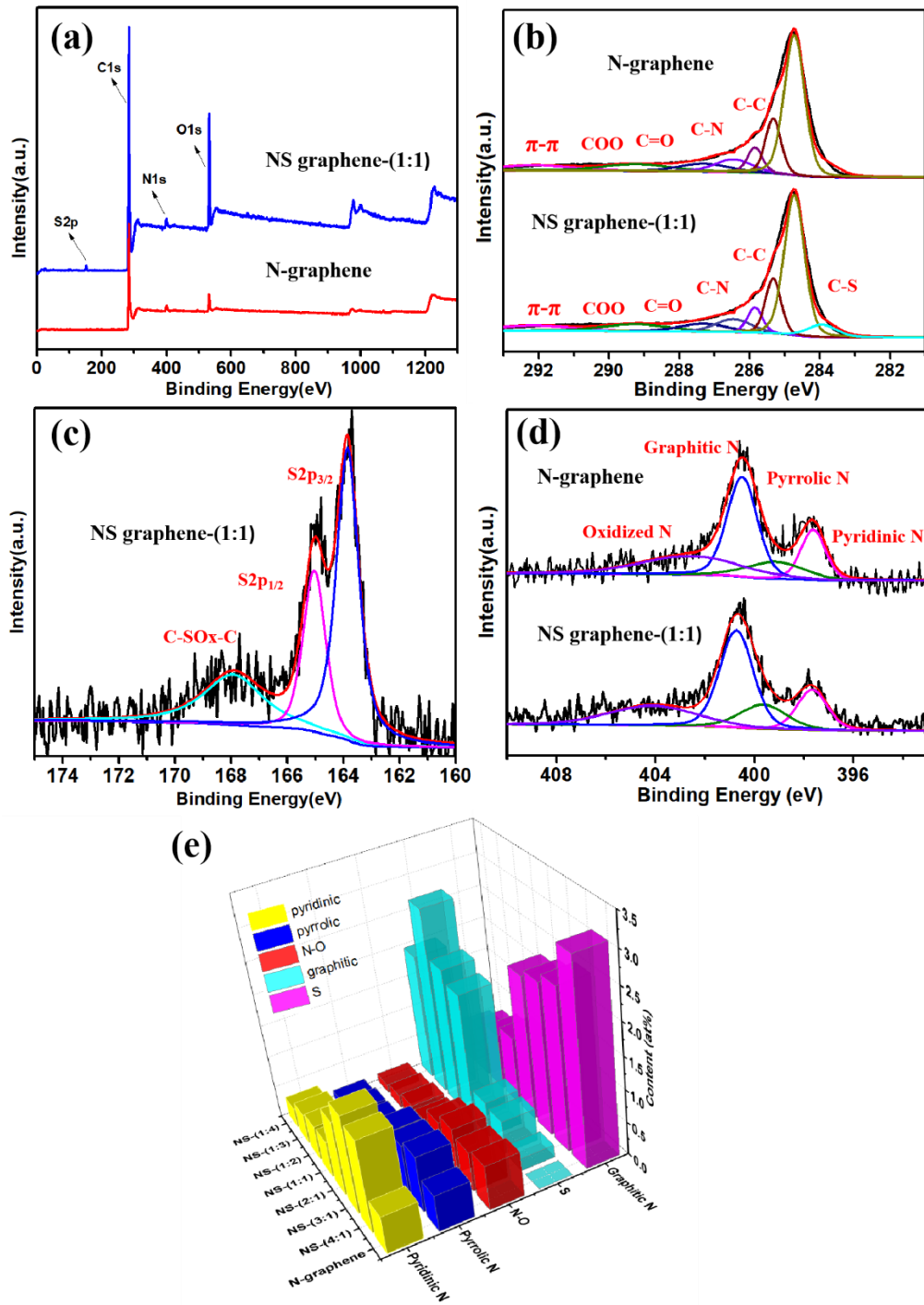


**Figure 6-3.** The XPS surveys (a) high-resolution XPS spectra for C 1s (b), S2p (c) and N1s (d) of NSgraphene-(1:1) and N-graphene.. The 3D bar charts of specific percentage of each species of N and S in NSgraphene-(4:1), NSgraphene-(3:1), NSgraphene-(2:1), NSgraphene-(1:1), NSgraphene-(1:2), NSgraphene-(1:3), NSgraphene-(1:4) and N-graphene (e).

High-resolution XPS spectra of C1s in N-graphene and NSgraphene-(1:1) (Figure 6-3 b). It is obvious that The main C1s peak was allocated at 285.41, 285.38, 285.27,

285.14, 285.02, 284.91, 284.82 and 284.71 corresponding to NSgraphene-(4:1), NSgraphene-(3:1), NSgraphene-(2:1), NSgraphene-(1:1), NSgraphene-(1:2), NSgraphene-(1:3), NSgraphene-(1:4) and N-graphene, this shift is a clue that there are the most charge density exist on central C atoms in NSgraphene-(3:1) among all these N, S co-doped graphene nanosheets. The N1s spectra were fitted with four peaks located at 398.25, 399.79, 401.12 and 403.5 eV, respectively (Figure 6-3d) [30-33]. As for as the high-resolution of S<sub>2p</sub>, three main peaks located at 164.0, 165.1 and 168.4 eV, respectively (Figure 6-3c). The three peaks can be assigned to S2p<sub>3/2</sub> and S2p<sub>1/2</sub> as well as the oxidized S [34, 35]. The doping content of S in these samples are 0.98at%, 1.51at%, 1.87at%, 0.87at%, 0.54at% and 0.19at% corresponding to NSgraphene-(1:4), NSgraphene-(1:3), NSgraphene-(1:2), NSgraphene-(1:1), NSgraphene-(2:1), NSgraphene-(3:1), NSgraphene-(4:1) as shown in Figure 6-3e. It is obvious that with the increase of doped S-containing precursors, the content of S content increased in resultant catalysts.

Ultraviolet photoelectron spectroscopy (UPS) was conducted to analysis the specific electronic structures information that can not be reflected by XPS results. As shown in Figure 6-4a, there are three typical peaks located at around 3eV, 7eV and 13eV were observed that corresponding to 2p- $\sigma$  and 2 $\sigma$ . Respectively. It is found that there is a significant shift of to the lower binding energy of the 2p- peaks in NSgraphene-(1:3), NSgraphene-(1:3) and NSgraphene-(1:1), which may derived from the electron transfer from C to the doped S dopants(electron deficiency), meanwhile, producing a lower shift of the Fermi level (E<sub>F</sub>)[36]. As

for as the peak located at about 7 eV that can be explained by the doping effect. As shown in Figure 6-4b, all valence electrons of S and N will be derived from the bonding with surrounding carbons. Furthermore, there is a more obvious peak of NSgraphene-(1:3) than that of NSgraphene-(1:1) and NSgraphene-(3:1) at about 13 eV which may contribute to a higher density of states (DOSs) in the unoccupied states derived from the interlayer band that display higher charge densities of doped N, S dopants with carbon matrix[36]. The work function ( $F$ ) is an important parameter that reflects the minimum energy barrier that needs to be overcome for inner electrons escaping from nucleus. As listed in Figure 6-4d, the calculated  $F$  value of NS graphene(1:1) is 3.90 eV, which is far less than that of N-graphene (4.32 eV), NS graphene(1:3) (4.31 eV) and NS graphene(3:1) (4.17 eV).

Excellent conductivity is one of the crucial factors for highly active catalyst materials for ORR. More importantly, the properties of carbon can be reflected by incorporated different heteroatoms types active sites species. Among all these N, S co-doped graphene nanosheets, NSgraphene-(1:3) has the highest value of conductivity of 5196 S/m at 25MPa, followed by NSgraphene-(1:2) (3064 S/m), greatly higher than that of NSgraphene-(3:1) (2485 S/m). Combining with XPS results, NSgraphene-(1:3) catalyst possess high content of graphitic N and the highest

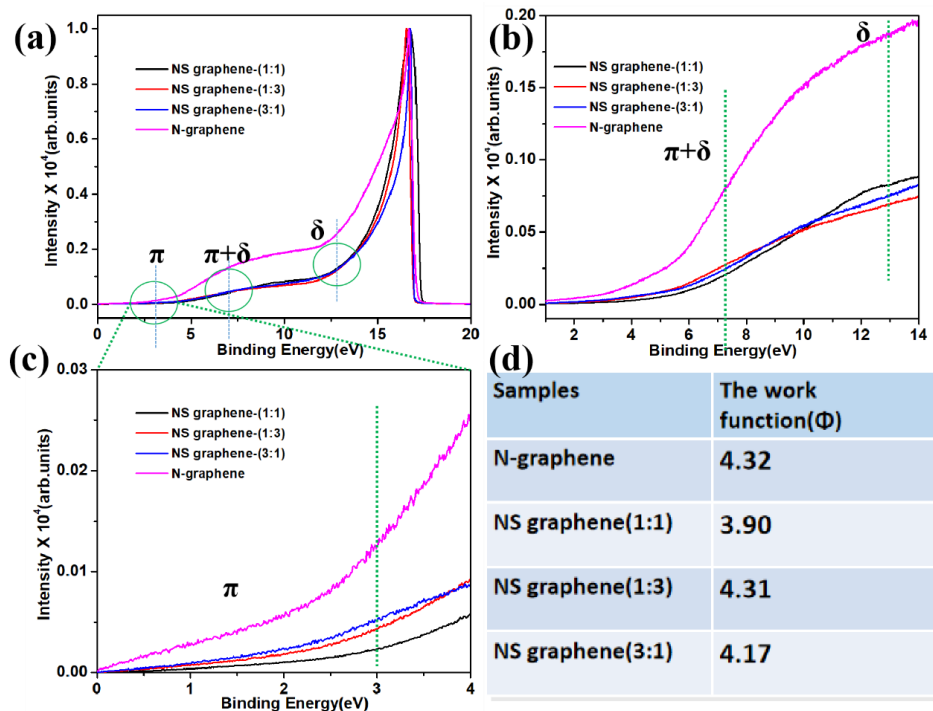


**Figure 6-4.** UPS spectra (a) Partial enlarged spectra (b, c) and the specific value of work function (d) of the NSgraphene-(4:1), NSgraphene-(3:1), NSgraphene-(2:1), NSgraphene-(1:1), NSgraphene-(1:2), NSgraphene-(1:3), NSgraphene-(1:4) and N-graphene respectively.

percentage of S doping, graphitic N were considered as conductivity contributor, therefore, high content of graphitic N attributes to excellent conductivity of catalysts greatly. More importantly, with S doping, the band gap could be lifted and metallic properties of graphene is increased as well as attributes to enhanced conductivity [37]. The excellent conductivity of NSgraphene-(1:3) is in consistent with XPS results discussed above.

### 6.2.2 Electrochemical evaluation

As shown in Figure 6-5a, for these N, S co-doped graphene nanosheets with different N/S ratio, NSgraphene-(1:1) has the highest catalytic activity for ORR among all these doped catalysts with onset and half-wave potential at 1.0 and 0.87 V vs.RHE respectively, which is even higher than that of commercial Pt/C (half-wave potential of

0.86V) followed by NSgraphene-(1:2) at 0.98 and 0.84 V vs.RHE respectively, and NSgraphene-(2:1) at 0.96 and 0.78 V vs.RHE respectively as well as NSgraphene-(3:1) shows the relatively low catalytic activity for ORR with 0.92 and 0.75 V vs.RHE respectively. In addition, it is clear that N-graphene catalyst exhibits the lowest activity with half-wave potential of 0.55 V vs.RHE for ORR compared to N,S co-doped catalysts, indicating that the addition of S induce enhanced catalytic activity for ORR. Tafel slope of NSgraphene-(4:1), NSgraphene-(3:1), NSgraphene-(2:1), NSgraphene-(1:1), NSgraphene-(1:2), NSgraphene-(1:3), NSgraphene-(4:1), and N-graphene corresponding to respectively 112.2, 109.2, 72.31, 80.5, 110.4 and 112.5 mV decade<sup>-1</sup> as shown in Figure 6-5b.

OER performance of these catalysts were measured at the potential range between 1.2 and 1.8 V in a 0.1 MKOH electrolyte, as shown in Figure 6-5c. N-graphene displays the lowest catalytic activity for OER with the potential of 1.74V at the current of 10.0 mA cm<sup>-2</sup> (i.e.,  $E_j = 10$ ), among all these N, S co-doped graphene nanosheets, NSgraphene-(3:1) with the lowest S doped content possess the best OER performance in 0.1MKOH with the lowest onset potential of 1.49 V, a value which is comparable to that of the IrO<sub>2</sub> catalyst (1.45 V) followed by 1.63 V of NSgraphene-(2:1), 1.68 V of NSgraphene-(3:1) and 1.64 V of NSgraphene-(4:1). More importantly, the value in NSgraphene-(3:1) at the current of 10.0 mA cm<sup>-2</sup> is 1.59 V, which is lower than that of NSgraphene-(2:1) (1.71 V) and NSgraphene-(3:1) (1.80 V) and ranked the highest catalytic activity for OER among reported N,S co-doped electrocatalysts. Tafel plots were shown in Figure 6-5d, the Tafel slope value of NSgraphene-(3:1) is 66.7



mV/dec which is lower than that of 71.5 mV /dec for IrO<sub>2</sub> followed by NSgraphene-(4:1) of 74.37 mV/dec, NSgraphene-(2:1) of 78.8 mV/dec, NSgraphene-(1:1) of 130.5 mV/dec, NSgraphene-(1:2) of 134.67 mV/dec, NSgraphene-(1:3) of 141.18 mV/dec, NSgraphene-(1:4) of 146.23 mV/dec and N-graphene possess the lowest OER performance with the highest Tafel slope of 152.62mV/dec. Similarly with ORR results discussed above, the co-doping of S leads to enhanced catalytic activity for OER compared with N-graphene.

As for as catalytic activity for HER, as shown in Figure 6-5e. N-graphene displays the lowest catalytic activity for HER with the potential of -0.45V at current of 10.0 mA cm<sup>-2</sup>. Among all these N, S co-doped graphene nanosheets, NSgraphene-(1:3) possess the best HER performance with onset overpotential of ≈12 mV, much lower than those of the NSgraphene-(1:2) (-23.3 mV), NSgraphene-(1:1) (-22 mV), NSgraphene-(2:1)(-137 mV), NSgraphene-(3:1) (-188 mV) and NSgraphene-(4:1) (-185.37 mV). The overpotentials to achieve the current density of 10 mA cm<sup>-2</sup> (Figure 6-5f) for the catalysts are -450mV, -436mV, -328mV, -118mV, -200mV, -157mV and -523mV respectively corresponding to NSgraphene-(4:1), NSgraphene-(3:1), NSgraphene-(2:1), NSgraphene-(1:1), NSgraphene-(1:2), NSgraphene-(1:3), NSgraphene-(1:4), N-graphene and the corresponding tafel plots are 185.37 mV/dec, 181.01 mV/dec, 142.93 mV/dec, 153.57 mV/dec, 125.23 mV/dec, 98.93 mV/dec, 147.36 mV/dec and 232.03mV/dec respectively. The specific values of overpotentials and half-wave potentials of these samples for ORR, OER and HER respectively are shown in the line charts in Figure 6-5g.

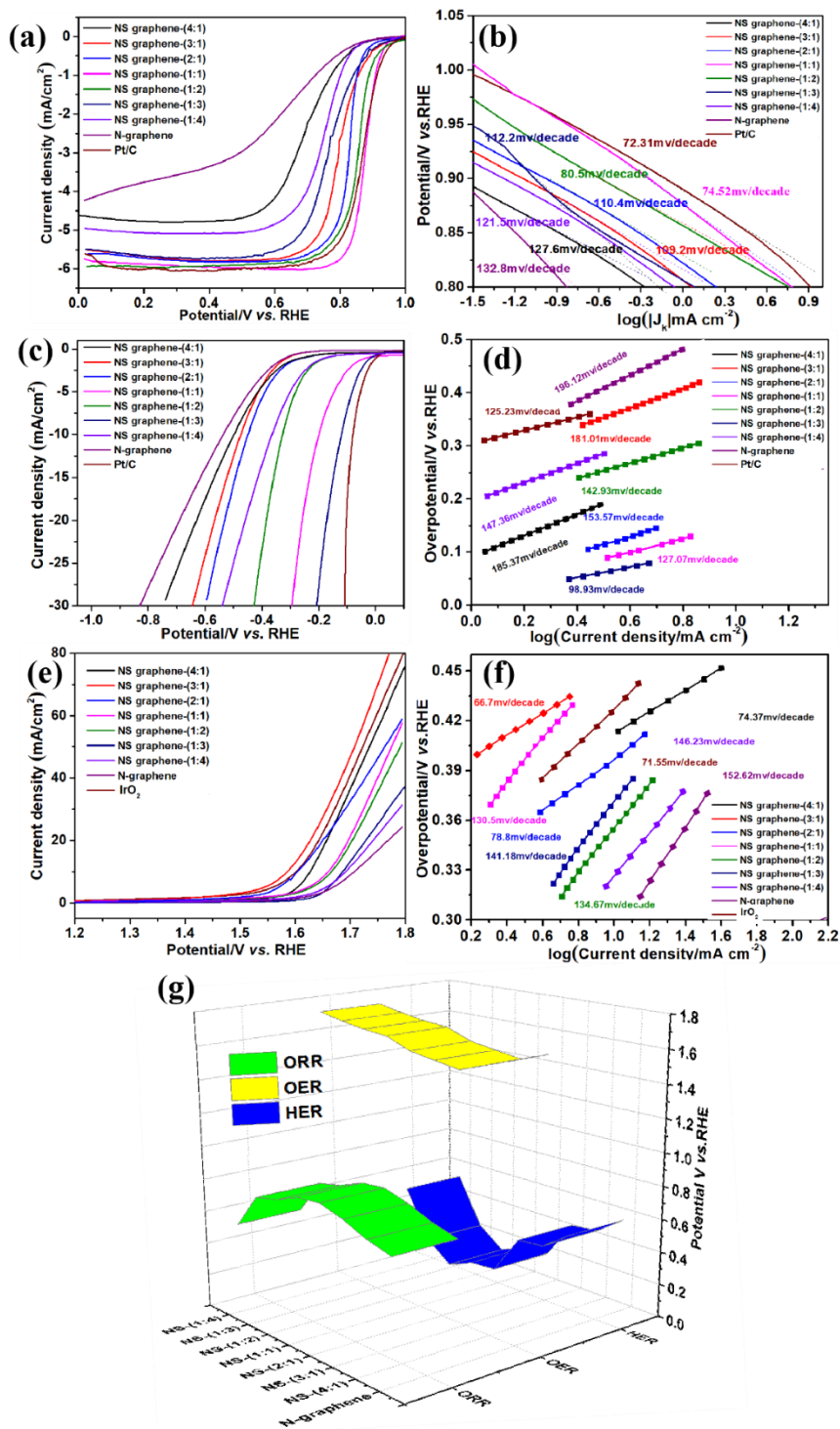


**Figure 6-5.** LSV curves of ORR (a), OER(b) and HER(c) for NSgraphene-(4:1), NSgraphene-(3:1), NSgraphene-(2:1), NSgraphene-(1:1), NSgraphene-(1:2), NSgraphene-(1:3), NSgraphene-(1:4), N-graphene and their corresponding Tafel slope of ORR (d),OER(e) and HER(f) in 0.1 M KOH. The 3D line charts of overpotentials and half-wave potentials for ORR, OER and HER of these catalysts (g).

6.2.3 Discussion on the synergistic effect of N and S with different ratio in graphene matrix for water splitting and oxygen reduction reactions.

Density functional theory (DFT) calculations were conducted to understand the effect of N, S configurations produced on enhanced catalytic activity for the three reactions respectively. And the criterion of model establishment of other models with N, S co-doped sites were based on the results of XPS discussed above as shown in Figure 6-6a. According to previous reports that carbon atoms with high spin and charge density usually hold most potential to be catalytic sites for the three reactions, due to their great contribution to adsorbing intermediates produced during ORR, OER and HER such as OH\*, OOH\* and O\* *ect.* [38, 39] It is notable that the addition of S induce more obvious uneven distribution of charge and spin density on carbon matrix compared with single pyridinic N, graphitic N doped models with increased percentage of active carbon atoms with charge density > 0.15 and spin density > 0. More importantly, the co-doping of N and S with different ratio produce different influence on charge distributions in graphene network.

Stated thus, several carbon atoms around doped atoms with high charge and spin density were selected as promising active sites in these constructed models for free-energy diagrams calculation of ORR, OER and HER respectively. As shown in Figure 6-6b, it is found that C<sub>6</sub> in model of Graphitic N + thiophenic S has the least overpotential for ORR(0.316eV), followed by carbon atom C<sub>7</sub> in model of Graphitic N + 2thiophenic S (0.324eV) and the overpotential of C<sub>8</sub> in model of 2Graphitic N + thiophenic S displays relatively high value of 0.481eV. It is worth noting that the value of overpotential for ORR is overall higher than that in configurations of Graphitic N + thiophenic S compared to PyridinicN and thiophenic S configurations, the specific

value are 0.708eV, 0.445eV and 0.589eV of C<sub>2</sub>, C<sub>4</sub> and C<sub>3</sub> respectively. On the whole, the balanced Graphitic N, thiophenic S doping in graphene matrix induce the highest catalytic activity for ORR, the result is in good accordance with electrochemical testing results. The superior activity for ORR of NSgraphene-(1:1) with high percentage of Graphitic N and thiophenic S configurations may attribute to their synergy effect that contributes to increased electronic distribution on surrounding carbon atoms, producing enhanced ability of oxygen adsorption.

#### **OER free-energy diagram.**

OER proceeds in an opposite pathway from ORR[40], according to calculated free energy diagram discussed above, the OER overpotentials of selected carbon atoms were calculated and compared of these promising active carbon atoms in graphene network. According to Gibbes free-energy diagram of OER (Figure 6-6c), it is found that carbon atom of C<sub>8</sub> in model of 2Graphitic N + thiophenic S displays the least value of overpotential (0.247eV) among all these models, followed by carbon atom C<sub>6</sub> in model of Graphitic N + thiophenic S shows high overpotential of 0.260eV, By contrast, with further introducing of thiophenic S, the overpotential of C<sub>7</sub> in model of Graphitic N + 2thiophenic S displays the highest overpotential of 0.682eV, followed by that of C<sub>3</sub> in Pyridinic N + 2thiophenic S(0.449ev) and C<sub>4</sub> in Pyridinic N + 2thiophenic S(0.389ev). It is found that when more graphitic N was added in graphene network that more configuration of 2graphitic N + thiophenic S was induced, which contributes to enhanced activity for OER instead of ORR in graphitic N + thiophenic S.

#### **HER free-energy diagram.**

As for the overall HER pathway, the Gibbs free-energy of the intermediate state,  $|DGH^*|$  was considered as a major descriptor for the HER activity [41-43]. In this work, the Gibbs free energy for  $H^*$  adsorption ( $DGH^*$ ) on single graphitic N is -0.80 eV, and  $DGH^*$  of pyridinic N are -0.95 eV. (Figure 6-6d) A largely negative value of  $\Delta GH^*$  on pyridinic N doped graphene catalyst indicates that chemical adsorption of  $H^*$  on its surface is too strong, while a largely positive  $\Delta GH^*$  1.0 on thiophenic S-graphene indicates very weak  $H^*$  adsorption and easy product desorption, which both are unfavourable for electrocatalytic HER[44]. Therefore, the chemical coupling of thiophenic S and graphitic N into a uniform hybrid can result in a mediated adsorption-desorption behaviour ( $|DGH^*|-0$ ) to facilitate the overall HER kinetics. It is validated by the decreased  $|DGH^*|$  (0.23 eV) in model of graphitic N+ thiophenic S. By contrast, the  $GH^*$  is 0.34eV with the configuration of Pyridinic N + thiophenic S. With more thiophenic S addition, graphitic N +2 thiophenic S shows the smallest  $|DGH^*|$  value of 0.12 eV among all these models (Figure 6-6e), which is a clear clue of its best electrocatalytic activity for HER from the viewpoint of thermodynamics due to its mediated adsorption-desorption behavior.

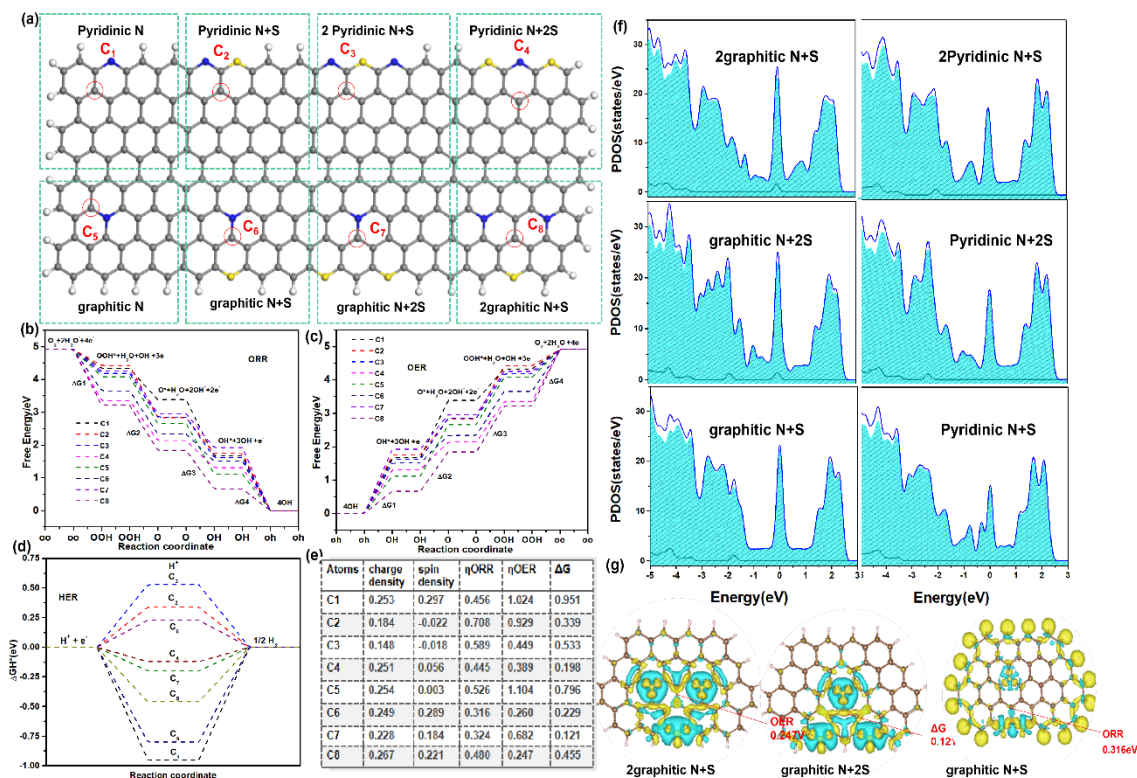


**Figure 6-6.** The constructed models(a) and the Gibbs free energy of ORR, OER, HER and corresponding overpotential (b, c, d) and the specific values of  $\eta_{\text{ORR}}$ ,  $\eta_{\text{OER}}$ , and  $\Delta G$  in these models(e), Partial density of state (PDOS)(f), Differential charge density distributions (g).

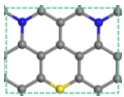
The partial density of state (PDOS) were analysis and compared of these models as shown in Figure 6-6f. It is clearly demonstrate that the P-state partial DOS overlap at the Fermi level (0 eV) of graphitic N+thiophenic S exhibits the higher value than that of pyridinic N+ thiophenic S indicates the higher electrical conductivity and easier charge transfer of graphitic N+thiophenic S compared to that of Pyridinic N+thiophenic S. When more graphitic N was introduced, the model of 2graphitic N+thiophenic S displays the highest P-state partial DOS overlap at the Fermi level (0 eV) followed by the model of graphitic N+ 2thiophenic S, demonstrating their superior catalytic potential, indicating that the configuration of graphitic N and thiophenic S may contribute mainly on final catalytic activity due to it caused higher electron- or spin redistribution in pristine sp<sup>2</sup> conjugated graphene framework which induced more

atomic orbital hybridization[45]. On the other hand, for more intuitive expression, differential charge density of selected models are shown in Figure 6-6g. It is observed that carbon atoms with the high charge or spin density in these models usually located near at doped heteroatoms, indicating that electronic redistribution induced by heteroatoms focus on the area near doping sites.

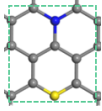
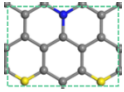
In summary, a series of N, S co-doped graphene nanosheets were obtained with combination of graphitic N, Pyridinic N and thiophenic S of different N, S ratio, which derived from pyrimidine-based precursors preferential formation of graphitic N. although, these N, S co-doped graphene nanosheets possess similar physical property but displays completely different electrochemical performance for ORR, OER and HER respectively. A series of physical characterization were conducted and DFT calculations was used to well explained the function control mechanism via tuning the configuration of N and S with different ratio. At first, according to UPS results, the N, S co-doping catalysts display lower work function ( $\Phi$ ) compared to single N doped samples, indicating that with addition of S lower energetic barrier is needed to motivate electrons escape during catalysis process. Meanwhile, the result is validated by partial density of state (PDOS) analysis, the higher value of P-state partial DOS overlap at the Fermi level was obtained with the co-doped N, S added in graphene network. Meanwhile, models with graphitic N and thiophenic S doping sites exhibits higher DOS overlap value compared with Pyridinic N and thiophenic S. The result is a solid evidence to support the excellent catalytic activity for ORR of NS graphene(1:1) with high content of graphitic N and thiophenic S according to XPS results. With

more graphitic N added, NS graphene(3:1) displays increased performance for OER with the highest PDOS overlap at the Fermi level (0 eV) demonstrating its superior catalytic potential. By contrast, when more thiophenic S was added, due to a largely positive  $\Delta GH^*$  1.0 on thiophenic S-graphene, the chemical coupling of more thiophenic S and graphitic N into a uniform hybrid leading to mediated adsorption-desorption behaviour ( $|DGH^*|-0$ ) to facilitate the overall HER kinetics, which provides a evidence from the viewpoint of thermodynamics to explain the best electrocatalytic activity of NS graphene(1:3) for HER.

**Table 1.** Summary of BET, binding energy of C1s main peak, absolutely atomic content of pyridinic-N, Pyrrolic-N, graphitic-N, thiophenic-S dopants, and electrocatalysis of water and oxygen

Samples	BET Surface area ( $m^2 \cdot g^{-1}$ )	C1s Peak Binding Energy	ORR $E_{1/2}$ 3.0 mA $cm^{-2}$ (V vs RHE)	Actual ratio of GraphiticN/thiophenic sulfur	Corresponding mode
			OER 10.0 mA $cm^{-2}$ (V vs RHE)		
			HER 10.0 mA $cm^{-2}$ (V vs RHE)		
N-graphene	923	284.71	0.550	0	
			1.745		
			-0.526		
NSgraphene-(4:1)	956	285.41	0.69	2.35	
			1.64		
			-0.516		
NSgraphene-(3:1)	923	285.38	0.765	2.23	
			1.581		
			-0.451		
		285.27	0.827	1.81	



NSgraphene- (2:1)	1166		1.625		
			-0.435		
NSgraphene- (1:1)	1210	285.14	0.870	1.1	
			1.602		
			-0.198		
NSgraphene- (1:2)	1049	285.02	0.855	0.78	
			1.683		
			-0.326		
NSgraphene- (1:3)	1158	284.91	0.795	0.524	
			1.681		
			-0.118		
NSgraphene- (1:4)	899	284.82	0.73	0.492	
			1.71		
			0.372		

### 6.3 Conclusion

Electrocatalytic functions for ORR, OER and HER respectively were successfully adjusted via fine tuning of ratio of thiophenic S and graphitic N. A series of N, S co-doped graphene electrocatalysts with controllable N,S ratio were synthesized via facile one-step solid method. These N, S co-doped graphene electrocatalysts featured with different N,S configurations that endows them display different catalytic preference from ORR, OER to HER via fine tuning of doping species in resultant carbon matrix. This study opens a new way for the development of low-cost carbon and large-scale production of N,S co-doped graphene catalysts for a controllable electrocatalytic applications, ranging from water splitting to oxygen reduction reactions.

### Acknowledgments

This work is supported by the National Key Research and Development Plan (2017YFB0103001), the National Natural Science Foundation of China (22075055), the Guangxi Science and Technology Project (AB16380030, AA17204083) and the Australian Research Council (DP180100731 and DP180100568).

## References

- [1] J. Kibsgaard, T. F. Jaramillo, Molybdenum phosphosulfide: an active, acidstable, earth-abundant catalyst for the hydrogen evolution reaction, *Angew. Chem. Int. Ed.* 53 (2014) 14433-14437.
- [2] C. Su, A. Lu, Y. Xu, F. Chen, A. Khlobystov, L. Li, High-quality thin graphene films from fast electrochemical exfoliation, *ACS Nano* 5 (2013) 2332-2339.
- [3] Z. Liu, H. Cheng, N. Li, T. Ma, Y. Su, ZnCo<sub>2</sub>O<sub>4</sub> quantum dots anchored on nitrogen-doped carbon nanotubes as reversible oxygen reduction/evolution electrocatalysts, *Adv. Mater.* 28 (2016) 3777-3784.
- [4] A. Arunchander, S. G. Peera, S. K. Panda, S. Chellammal, A.K. Sahu, Simultaneous co-doping of N and S by a facile in-situ polymerization of 6-N, N-dibutylamine-1,3,5-triazine-2,4-dithiol on graphene framework: an efficient and durable oxygen reduction catalyst in alkaline medium, *Carbon* 118 (2017) 531-544.
- [5] Y. Qian, Z. Hu, X. Ge, S. Yang, Y. Peng, Z. Kang, A metal-free ORR/OER bifunctional electrocatalyst derived from metal-organic frameworks for rechargeable Zn-Air batteries, *Carbon* 111 (2016) 641-650.
- [6] P. Shi, J. Guo, X. Liang, S. Cheng, H. Zheng, Y. Wang, Large-scale production of

high-quality graphene sheets by a non-electrified electrochemical exfoliation method, *Carbon* 126 (2018) 507-513.

[7] J. Liu, R. Wang, L. Cui, J. Tang, Z. Liu, Q. Kong, Using molecular level modification to tune the conductivity of graphene papers, *J. Phys. Chem. C* 116 (2012) 17939-17946.

[8] S. Pei, Q. Wei, K. Huang, H. M. Cheng, W. Ren, Green synthesis of graphene oxide by seconds timescale water electrolytic oxidation, *Nat. Commun.* 145 (2018),

[9] S. Yang, L. Zhi, K. Tang, X. Feng, J. Maier, K. Müllen, Efficient synthesis of heteroatom (N or S)-Doped graphene based on ultrathin graphene oxide porous silica sheets for oxygen reduction reactions, *Adv. Funct. Mater.* 22 (2012) 3634-3640.

[10] T. Akhter, M. M. Islam, S. N. Faisal, E. Haque, A.I. Minett, H. K. Liu, Self-assembled N/S co-doped flexible graphene paper for high performance energy storage and oxygen reduction reaction, *ACS Appl. Mater. Interfaces* 8 (2016) 2078-2087.

[11] J. Li, Y. Zhang, X. Zhang, J. Huang, J. Han, Z. Zhang, S, N dual-doped graphene-like carbon nanosheets as efficient oxygen reduction reaction electrocatalysts, *ACS Appl. Mater. Interfaces* 9 (2017) 398-405.

[12] K. Qu, Y. Zheng, S. Dai, S. Qiao, Graphene oxide-polydopamine derived N, S co-doped carbon nanosheets as superior bifunctional electrocatalysts for oxygen reduction and evolution, *Nanomater. Energy* 19 (2016) 373-381.

[13] X. Wang, J. Wang, D. Wang, S. Dou, Z. Ma, J. Wu, One-pot synthesis of nitrogen and sulfur co-doped graphene as efficient metal-free electrocatalysts for the oxygen reduction reaction, *Chem. Commun.* 50 (2014) 4839-4842.

- [14] X. Wu, Z. Xie, M. Sun, T. Lei, Z. Zuo, X. Xie, Edge-rich and (N, S)-doped 3D porous graphene as an efficient metal-free electrocatalyst for the oxygen reduction reaction, *RSC Adv.* 6 (2016) 90384-90387.
- [15] Z. Ma, S. Dou, A. Shen, L. Tao, L. Dai, S. Wang. Sulfur-Doped Graphene Derived from Cycled Lithium–Sulfur Batteries as a Metal-Free Electrocatalyst for the Oxygen Reduction Reaction. *Angew. Chem. Int. Ed.* 54(2015) 1888-1892.
- [16] S. Yang, X. Feng, X. Wang, K. Müllen. Graphene-Based Carbon Nitride Nanosheets as Efficient Metal-Free Electrocatalysts for Oxygen Reduction Reactions. *Angew. Chem. Int. Ed.* 123 (2011) 5451 –5455.
- [17] S. Wang, L. Zhang, Z. Xia, A. Roy, D. W. Chang, J. B. Baek, et al. BCN Graphene as Efficient Metal-Free Electrocatalyst for the Oxygen Reduction Reaction. *Angew. Chem. Int. Ed.* 124 (2012) 4285-4288.
- [18] Z. Zhang, J. Sun, C. Lai, Q. Wang, C. Hu, High-yield ball-milling synthesis of extremely concentrated and highly conductive graphene nanoplatelet inks for rapid surface coating of diverse substrates, *Carbon* 120 (2017) 411-418.
- [19] Z. Liu, J. Liu, L. Cui, R. Wang, X. Luo, C.J. Barrow, et al., Preparation of graphene/polymer composites by direct exfoliation of graphite in functionalized block copolymer matrix, *Carbon* 51 (2013) 148-155.
- [20] S. Yang, L. Zhi, K. Tang, X. Feng, J. Maier, K. Müllen, Efficient synthesis of heteroatom (N or S)-Doped graphene based on ultrathin graphene oxide porous silica sheets for oxygen reduction reactions, *Adv. Funct. Mater.* 22 (2012) 3634-3640.
- [21] T. Akhter, M.M. Islam, S.N. Faisal, E. Haque, A. I. Minett, H.K. Liu, et al., Self-

assembled N/S codoped flexible graphene paper for high performance energy storage and oxygen reduction reaction, *ACS Appl. Mater. Interfaces* 8 (2016)2078-2087.

[22] J. Li, Y. Zhang, X. Zhang, J. Huang, J. Han, Z. Zhang, et al., S, N dual-doped graphene-like carbon nanosheets as efficient oxygen reduction reaction electrocatalysts, *ACS Appl. Mater. Interfaces* 9 (2017) 398-405.

[23] X. R. Zhang, Y. Q. Wang, Y. H. Du, M. Qing, F. Yu, Z. Q. Tian, P. K. Shen, Highly Active N, S co-doped Hierarchical Porous Carbon Nanospheres from Green and Template-free Method for Super Capacitors and Oxygen Reduction Reaction. *Electrochim. Acta*, 20 (2019) 272-280.

[24] X. R. Zhang, S. X. Yao, P. S. Chen, Y. Q. Wang, Y. H. Du, M. Qing, F. Yu, Z. Q. Tian, P. K. Shen, Revealing the dependence of active site configuration of N doped and N, S-co-doped carbon nanospheres on six-membered heterocyclic precursors for oxygen reduction reaction. *J Catal*, 389 (2020) 677-689.

[25] D. D. Lyu, S. X. Yao, Y. B. Bahari, Hasan, C. Pan, X. R. Zhang, Y. Feng, Z. Q. Tian, P. K. Shen. In situ molecular-level synthesis of N, S co-doped carbon as efficient metal-free oxygen redox electrocatalysts for rechargeable Zn-Air batteries. *Appl. Mater. Today*, 20 (2020)100737.

[26] S. Zhong, L. Zhou, L. Wu, L. Tang, Q. He, J. Ahmed, Nitrogen- and Boron-Co-Doped Core-Shell Carbon Nanoparticles as Efficient Metal-Free Catalysts for Oxygen Reduction Reactions in Microbial Fuel Cells. *J. Power Sources* 272 (2014) 344-350.

[27] Lee, H.; Dellatore, S. M.; Miller, W. M.; Messersmith, P. B. Mussel-Inspired Surface Chemistry for Multifunctional Coatings. *Science* 318 (2007) 426-430.

- [28] Della Vecchia, N. F.; Avolio, R.; Alfe, M.; Errico, M. E.; Napolitano, A.; d'Ischia, M. Building-Block Diversity in Polydopamine Underpins a Multifunctional Eumelanin-Type Platform Tunable Through a Quinone Control Point. *Adv. Funct. Mater.* 23 (2013) 1331-1340.
- [29] Bernsmann, F.; Voegel, J.-C.; Ball, V. Different Synthesis Methods Allow to Tune the Permeability and Permselectivity of Dopamine-Melanin Films to Electrochemical Probes. *Electrochim. Acta* 56 (2011) 3914–3919.
- [30] B. Yu, D. A. Wang, Q. Ye, F. Zhou, W. Liu, Robust Polydopamine Nano/Microcapsules and Their Loading and Release Behavior. *Chem. Commun.* 2009, 6789–6791.
- [31] J. Cui, Y. Wang, A. Postma, J. Hao, L. Hosta-Rigau, F. Aruso, Monodisperse Polymer Capsules: Tailoring Size, Shell Thickness, and Hydrophobic Cargo Loading via Emulsion Templating. *Adv. Funct. Mater.* 20 (2010) 1625–1631.
- [32] N. F. Della Vecchia, R. Avolio, M. Alfe, M. E. Errico, A. Napolitano, d'Ischia, M. Building-Block Diversity in Polydopamine Underpins a Multifunctional Eumelanin-Type Platform Tunable Through a Quinone Control Point. *Adv. Funct. Mater.* 23 (2013) 1331-1340.
- [33] L. Zhang, Z. Y. Zhang, R. P. Liang, Y. H. Li, J. D. Qiu, Boron Doped Graphene Quantum Dots for Selective Glucose Sensing Based on the “Abnormal” Aggregation-Induced Photoluminescence Enhancement. *Anal. Chem.* 86 (2014) 4423–4430.
- [34] W. Jastrzębski, M. Sitarz, M. Rokita, K. Bułat, Infrared Spectroscopy of Different Phosphates Structures. *Spectrochim. Acta, Part A.* 79 (2011) 722–727.

- [35] K. Qu, Y. Zheng, Y. Jiao, X. Zhang, S. Dai, S. Z. Qiao, Polydopamine-Inspired, Dual Heteroatom-Doped Carbon Nanotubes for Highly Efficient Overall Water Splitting. *Adv. Energy Mater.* 2017, 7, 1602068.
- [36] R. Li, Z. Wei, X. Gou, Nitrogen and Phosphorus Dual-Doped Graphene/Carbon Nanosheets As Bifunctional Electrocatalysts for Oxygen Reduction and Evolution. *ACS Catal.* 5(2015) 4133–4142.
- [37] X. X. Wang, D. A. Cullen, Y. T. Pan, S. Hwang, M. Wang, Z. Feng, J. Wang, M. H. Engelhard, H. Zhang, Y. He, Y. Shao, D. Su, K.L. More, J.S. Spendelow, G. Wu, *Adv. Mater.* 30 (2018) 1706758.
- [38] I.-Y. Jeon, S. Zhang, L. Zhang, H.-J. Choi, J.-M. Seo, Z. Xia, L. Dai, J.-B. Baek, Edge-Selectively Sulfurized Graphene Nanoplatelets as Efficient Metal-Free Electrocatalysts for Oxygen Reduction Reaction: The Electron Spin Effect, *Adv. Mater.* , 25 (2013) 6138-6145.
- [39] Y. Tian, D. Xu, K. Chu, Z. Wei, W. Liu, Metal-free N, S co-doped graphene for efficient and durable nitrogen reduction reaction, *Journal of Materials Science*, 54 (2019) 9088-9097.
- [40] Y. Ito, W. Cong, T. Fujita, Z. Tang, M. Chen, High Catalytic Activity of Nitrogen and Sulfur Co-Doped Nanoporous Graphene in the Hydrogen Evolution Reaction, *Angew. Chem. Int. Ed.* 54 (2015) 2131-2136.
- [41] M. Li, L. Zhang, Q. Xu, J. Niu, Z. Xia, N-doped graphene as catalysts for oxygen reduction and oxygen evolution reactions: Theoretical considerations, *J Catal.* 314 (2014) 66-72.

[42] S. Sun, X. Jin, B. Cong, X. Zhou, W. Hong, G. Chen, Construction of porous nanoscale NiO/NiCo<sub>2</sub>O<sub>4</sub> heterostructure for highly enhanced electrocatalytic oxygen evolution activity, *J Catal*, 379 (2019) 1-9.

[43] F. Liu, F. Niu, T. Chen, J. Han, Z. Liu, W. Yang, Y. Xu, J. Liu, One-step electrochemical strategy for in-situ synthesis of S, N-codoped graphene as metal-free catalyst for oxygen reduction reaction, *Carbon*, 134 (2018) 316-325.

[44] D. Guo, R. Shibuya, C. Akiba, S. Saji, T. Kondo, J. Nakamura, Active sites of nitrogen-doped carbon materials for oxygen reduction reaction clarified using model catalysts, *Science*, 351 (2016) 361-365.

[45] J. Li, Y. Zhang, X. Zhang, J. Huang, J. Han, Z. Zhang, X. Han, P. Xu, B. Song, S, N Dual-Doped Graphene-like Carbon Nanosheets as Efficient Oxygen Reduction Reaction Electrocatalysts, *ACS Appl. Mater. Interfaces*. 9 (2017) 398-405.

*Every reasonable effort has been made to acknowledge the owners of copyright material. I would be pleased to hear from any copyright owner who has been omitted or incorrectly acknowledged.*

## **Chapter 7: N species tuning strategy in N, S co-doped graphene Nanosheets for electrocatalytic activity and selectivity of oxygen redox reactions**

### **Abstract**

The precise regulation of N, S doping and their synergetic effect is essential for N, S



co-doped carbon materials as efficient metal-free electrocatalysts for oxygen redox reaction (oxygen reduction reaction (ORR) and oxygen evolution reaction (OER)). Herein, an effective precursor modulated active sites engineering strategy of N, S co-doped graphene nanosheets (NSG) were developed by one step pyrolysis of 5-aminouracil (ANA) as N-containing precursor ammonium persulfate (AP), 2, 5-Dithiobiurea (DBA) as S source respectively. It is found that the specific N doping species in NSG and their synergetic effect with S dopants is strongly dependent on different S sources, which induces huge divergence of electrocatalytic activity and selectivity of NSG nanosheets for ORR and OER. The NSG prepared by ANA and AP as precursors with dominant graphitic N dopant coordinated with S possess the best ORR performance with half-wave potential of 0.87 V vs. RHE in 0.1M KOH and less OER performance with a high potential of 1.67 V at 10.0 mA cm<sup>-2</sup>, While NSG derived from ANA and DBA has the majority of pyridinic N and pyrrolic N dopants exhibits the highest bifunctional activity for both OER and ORR with  $\Delta E(\Delta E = E_{j=10} - E_{1/2})$  of 0.73V and the performance was also proved by a rechargeable Zn-Air battery fabricated by NSG with a peak power density of 146 mW·cm<sup>-2</sup>, specific capacity of 796 mAh·g<sub>Zn</sub><sup>-1</sup>, higher than that of the mixed composite of Pt/C and IrO<sub>2</sub> (1:1 wt.%) at the same catalyst loading. These excellent performance fundamentally originates from the optimized intermediates energy of ORR or/and OER via the constructed configuration of S and different N species in graphene nanosheets prepared by the specific N and S precursors. The dependence of electrocatalytic selectivity and activity for ORR or/and OER on different N, S configurations revealed in the work provides a facile strategy to

achieve specific active sites construction for developing multifunctional metal-free electrocatalysts.

*\*Reprinted (adapted) with permission from Xiaoran Zhang, Xingyu Wen, Can Pan, Xue Xiang, Chao Hao, Qinghao Meng, Zhi Qun Tian\*, Pei Kang Shen, San Ping Jiang\* N species tuning strategy in N, S co-doped Graphene Nanosheets for electrocatalytic activity and selectivity of Oxygen redox reactions. Chem. Eng. J. doi.org/10.1016/j.cej.2021.133216*

## 7.1 Introduction

Oxygen redox reaction including oxygen reduction reaction (ORR) and oxygen evolution reaction (OER) that occurs within one electrode, play a vital role in renewable energy technologies, such as regenerative fuel cell and rechargeable metal-air batteries systems [1-3]. However, the sluggish kinetics of ORR and OER with a 4-electron transfer process can be only efficiently catalyzed by precious metals (Pt, IrO<sub>2</sub>/RuO<sub>2</sub>). This kind of precious metals is suffering from low reserves, high-cost, less bifunctionality and poor stability, constructing the major contributor to hinder large-scale application of these technologies [4-6]. Therefore, it is highly desirable to develop non-precious electrocatalysts with low-cost and high performance to replace precious metal for efficient oxygen redox reaction.

Heteroatoms doped carbon materials (incorporated into carbon matrix by B, N, S, P etc.) with adjustable electronic configuration and spin angular momentum are a kind of promising active sites for electrocatalysis because of their low cost and nonmetallic properties that solves the problem of poor stability caused by the dissolution and precipitation of metals in use by the root, providing great possibilities for achieving

bifunctional materials for both ORR and OER [7-9]. Especially, N, S co-doped carbon-based materials have been recently attracted researchers' attention with great potential as highly efficient electrocatalysts via tuning active sites configurations in carbon matrix [10,11] due to the fact that the addition of doped S atoms significantly enhances the final catalytic activity via a synergetic effect with doped N atoms [12-16]. Therefore, tremendous efforts and great progress have been made on developing N, S doped metal-free catalysts for highly efficient catalytic performance for ORR and OER [17-19]. It is notable that although a lot of researches on electrocatalytic mechanism and modulation of active sites for enhanced catalytic performance for ORR and OER were conducted, the intrinsic relationship between N, S precursors and N, S active sites construction still keep in unclear, which directly leads to the uncertainty on the design of bifunctional electrocatalyst for ORR and OER, influencing the further development of practical metal-free electrocatalysts. In fact, the selection of precursors is essential to determine the formation of specific heteroatom dopants that are closed related to the final catalysts' performance for oxygen redox reactions greatly. In this regard, it is highly demanded to clarify the correlation between N, S configuration species and final catalytic activity and selectivity for oxygen redox reactions based on adjustable precursors platform for precisely design and synthesis of N, S co-doped at molecular level.

In this work, three different N, S co-doped graphene nanosheets were synthesized via one-step pyrolysis of the solid powder of 5-aminouracil as C and N precursor, mixed with 2, 5-Dithiobiurea and ammonium persulfate as precursors sources respectively, aiming to elucidate the synergetic effect between specific N species and S dopants

determined by precursors and their correlation on electrochemical performance for ORR and/or OER. The results demonstrate that the selection of S-containing precursor plays crucial role on influencing the formation of specific N doping species, and thus realizing different N, S configuration construction in these N, S co-doped samples. This work provides new understandings for tuning active sites species in N, S co-doped carbon-based materials via modulating S containing precursor types to develop bifunctional oxygen redox electrocatalysts.

## **7.2 Experimental**

### *7.2.1 Synthesis of N doped and N, S co-doped graphene nanosheets*

Three N, S co-doped graphene nanosheets were synthesized by the following procedure: 1 mmol (0.129 g) of 5-aminouracil (ANA) and 1 mmol (0.291 g) of 2, 5-Dithiobiurea (DBA), 1 mmol of 5-aminouracil (ANA) (0.129 g) and 0.5 mmol (0.114 g) ammonium persulfate (ANP) as well as 0.5 mmol (0.064 g) 5-aminouracil (ANA), 1 mmol (0.291 g) of 2, 5-Dithiobiurea (DBA) and 0.5 mmol of (0.114 g) ammonium persulfate (ANP) were firstly well-mixed via hand-grinding process in agate mortar for 20 min respectively, followed by pyrolysis at 250 °C for 1 h, 650 °C for 1 h and 950 °C for 1 h under N<sub>2</sub>. The three-stepped pyrolysis procedure was carried out for fully polymerization of these mixed polymer precursors and carbonization. After natural cooling, the obtained black powder was named as NS/G-AD (derived from 5-aminouracil (ANA) and 2, 5-Dithiobiurea (DBA) as mixed precursors), NS/G-AA (derived from 5-aminouracil (ANA) and Ammonium persulfate (AP) as mixed precursors), NS/G-AD+AA (derived from 5-aminouracil (ANA), Ammonium

persulfate (AP) and 2, 5-Dithiobiurea (DBA) as mixed precursors). Meanwhile, the single N doped graphene nanosheets (N/G-A) was prepared by 5-aminouracil (ANA) as precursor as control for comparison.

### *7.2.2 Characterization*

The morphologic structure of as-obtained NG and NSG samples were characterized by scanning electron microscope (SEM) on Hitach SU8220 and transmission electron microscope (TEM) on Titan ETEM G2 80-300. Raman spectra were obtained on Horiba jobin Yvon with 532 nm incident laser. The surface area and pore size distribution of samples were measured on Corp ASAP 2460. The CO<sub>2</sub> adsorption behavior of samples were detected using temperature programmed desorption (TPD) on RS485 Z-TEK as well as X-ray diffraction (XRD) analysis was performed on RIGAKU Co with a radiation source of Cu k $\alpha$  ( $\lambda = 1.5405\text{\AA}$ ). X-ray photoelectron spectroscopy (XPS) and Ultraviolet photoelectron spectroscopy (UPS) was carried out through Thermo Fisher Scientific, Escalab 250XI+). The powder electrical conductivity was measured by Conductivity Analyzer (DDS-11A) at various pressure.

### *7.2.3 Electrochemical Measurements*

Electrochemical ORR and OER performance of NG and NSG nanosheets were evaluated in 0.1M KOH using a three-electrode cell with bipotentiostat WD-20 BASIC and rotating ring disk electrode (RRDE) system (Pine Instrumentation, in which reversible hydrogen electrode (RHE) was used as the reference electrode and graphitic rod was used as the counter electrode, the working electrode was prepared by depositing

dispersion ink of samples onto the glassy carbon electrode with a diameter of 5.61 mm (GCE) and a Pt ring. The ink was prepared by ultrasonically dispersing 2.5 mg of samples into the mixed solution of 0.045 mL of H<sub>2</sub>O, 0.2 mL of ethanol, and 0.005 mL of 5 wt% Nafion. And then 15  $\mu$ L of well-dispersed ink was carefully dropped on the electrode surface and the mass loading of sample was 600  $\mu\text{g}\cdot\text{cm}^{-2}$ . In addition, the work electrodes of commercial Pt/C (46.7% Pt/C, Tanaka) and IrO<sub>2</sub> were also prepared using the same method. The mass loading Pt/C and IrO<sub>2</sub> was 40  $\mu\text{g}_{\text{Pt}}\cdot\text{cm}^{-2}$  and 300  $\mu\text{g}\cdot\text{cm}^{-2}$  respectively.

#### *7.2.4 Homemade Zn-Air batteries fabrication and testing*

To fabricate Zn-Air batteries, the homogeneous ink was firstly prepared by dispersing 10.0 mg of NS/G-AD with 5  $\mu$ L Nafion solution (5 wt%) and 1 mL of ethanol followed by dropping onto the water-proof carbon paper (TGP-H-060 with a microporous layer) up to the mass loading of 1.0  $\text{mg}\cdot\text{cm}^{-2}$ . For comparison, the precious metal electrode of Pt/C +IrO<sub>2</sub> (1:1) was also prepared. Meanwhile, a polished zinc sheet with a dimension of 2.0 cm x 1.0 cm x 0.3 mm was used as anode and 6.0 M KOH was used as electrolyte. Polarization curve (I-V) was collected using LSV with the voltage range of from open circuit to 0.4 V at a scan rate of 5  $\text{mV}\cdot\text{s}^{-1}$ . The specific capacity was also measured at the current densities of 50  $\text{mA}\cdot\text{cm}^{-2}$ . Battery cycling tests were carried out using the procedure of discharging (5 min) and charging (5 min) at 5  $\text{mA}\cdot\text{cm}^{-2}$ .

### **7.3 Results and discussion**

#### *7.3.1 Structural analysis of NSG nanosheets*

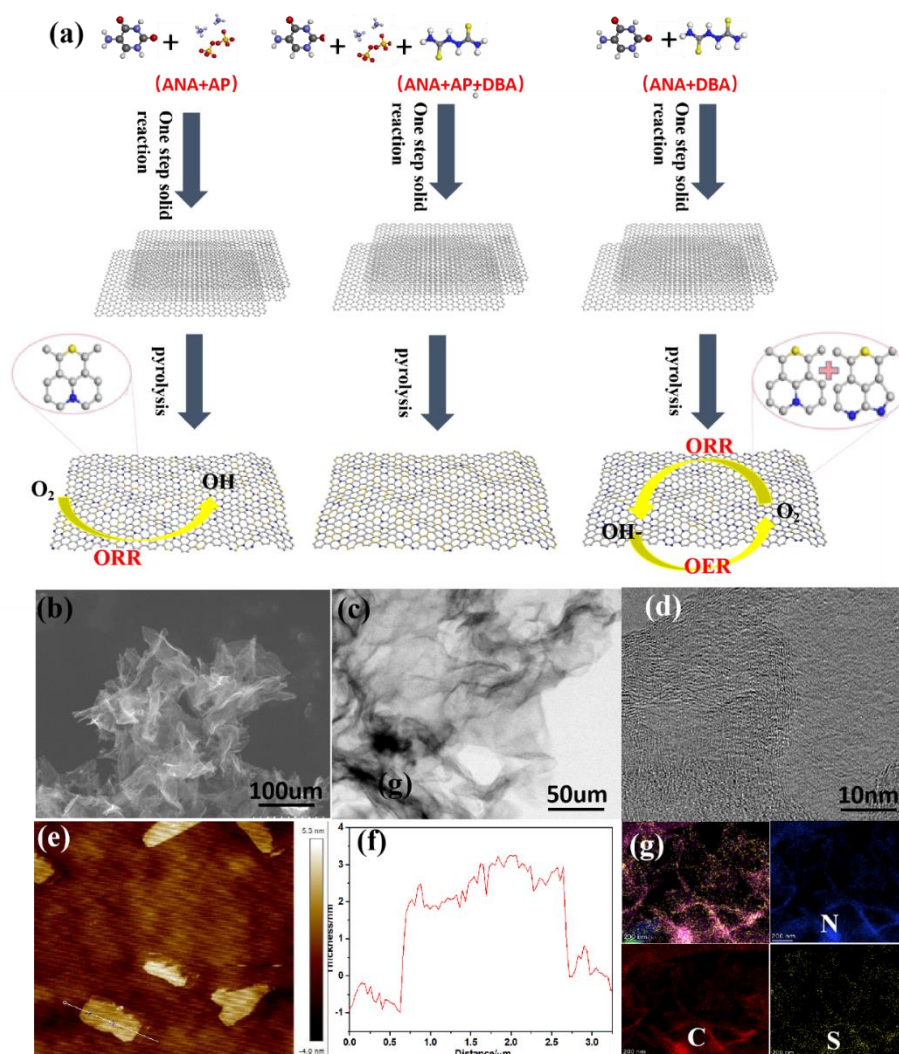


**Figure 7-1.** Illustration of the synthesis process of these NSG samples as presented by NS/G-AD (a). TEM images (b, c, d), AFM images (e) and corresponding plot of thickness (f) of NS/G-AD, Elements Mapping images (g).

Figure 7-1a illustrates the synthetic route of N doped and N, S co-doped graphene nanosheets (NG and NSG) via solid state reaction. Taking NS/G-AD as example, 5-aminouracil (ANA, C and N source) and 2, 5-Dithiobiurea (DBA, S source) powder is firstly mixed at solid state, and then the mixture is calcined at 250 °C for 1 h in N<sub>2</sub> to enhance the copolymerization of N and S sources and then carbonized at 650 °C for 1 h and final pyrolysis at 950 °C for 1 h to form N, S co-doped nanosheets. Through adjusting the kind of S precursors, four typical graphene nanosheets are prepared using this method and they are labeled as NS/G-AD (derived from 5-aminouracil (ANA) and

2, 5-Dithiobiurea (DBA) as mixed precursors), NS/G-AA (derived from 5-aminouracil (ANA) and Ammonium persulfate (AP) as mixed precursors), NS/G-AD+AA (derived from 5-aminouracil (ANA), Ammonium persulfate (AP) and 2, 5-Dithiobiurea (DBA) as mixed precursors) and N/G-A (derived from the single 5-aminouracil (ANA) as precursor).

The typical morphology characteristics of NG and NSG samples were captured by SEM and TEM and represented by the sample of NS/G-AD as shown in Figure 7-1b, c and d. From Figure 7-1b and c, NS/G-AD possess 2 D structure of nanosheet and they are self-supporting each other, avoiding restacking of conventional graphene powder. The number of graphene layer in NS/G-AD is less than 10 (Figure 7-1c), and AFM images (Figure 7-1 e and f) also validate that the average thickness of NS/G-AD focus on 2-3nm, indicating NS/G-AD is belonging to graphene. In addition, the elements mapping of NS/G-AD as presented in Figure 7-1g shows that the N, S, C elements are thoroughly distributed on nanosheets, creating the maximum possibility of producing uniform and specific synergetic effect of N and S doping. Meanwhile, it is notable that other NG and NSG samples (N/G-A, NS/G-AA, and NS/G-AD+AA) derived from no S and different S precursors exhibit similar structural characteristics of graphene, indicating that the different S precursors plays little effect on final formation of graphene structure with the same 5-aminouracil (ANA) as C and N-containing precursor platform.

Their powder X-ray diffraction (XRD) patterns in Figure 7-2a show that all samples of NS/G-AD, NS/G-AA, NS/G-AD+AA and N/G-A exhibit similar XRD patterns with



sharp and strong peaks located at around  $26^\circ$ , demonstrating that these graphene nanosheets have highly graphitized [20, 21]. Meanwhile, the similar XRD pattern of the samples manifest that the different S-containing precursors produce little influence on their crystal structure. Raman spectroscopy was conducted to further analyze the structure information of these nanosheets. It is known that the ratio of  $I_D$  (at  $1350\text{ cm}^{-1}$ ) and  $I_G$  (at  $1580\text{ cm}^{-1}$ ) is an important parameter reflecting the disorder degree of carbon. The ratio of  $I_D$  and  $I_G$  of 0.501, 0.452, 0.368 and 0.690 is corresponding to NS/G-AA, NS/G-AD, NS/G-AD+AA and N/G-A, respectively. These values with less than 1 combined with clear 2D peaks in all samples further confirm the results of highly graphitic degree of these nanosheets, while the difference at fine structure level also predicts that they would have significant dissimilarity in activity and selectivity for electrocatalysis of ORR and OER. Nitrogen adsorption/desorption isotherms of these samples (Figure 7-2c) show that they have the typical IV type isotherm [22], demonstrating that there are hierarchical pore structure in these carbon materials, which is validated by pore size distribution in Figure 7-2d that they have a bimodal pore structure, centering at micropore (less 2.0 nm) and macropore (50.0 nm-100.0 nm), And the specific BET surface area is  $881.2\text{ m}^2\text{ g}^{-1}$ ,  $845.8\text{ m}^2\text{ g}^{-1}$ ,  $926.5\text{ m}^2\text{ g}^{-1}$  and  $796.5\text{ m}^2\text{ g}^{-1}$ , which is attributed to NS/G-AD, NS/G-AA, NS/G-AD+AA and N/G-A, respectively, indicating that these graphene nanosheets have high surface area, providing more exposed active sites during the process of electrocatalysis and S incorporation can increase the surface area of graphene nanosheets.

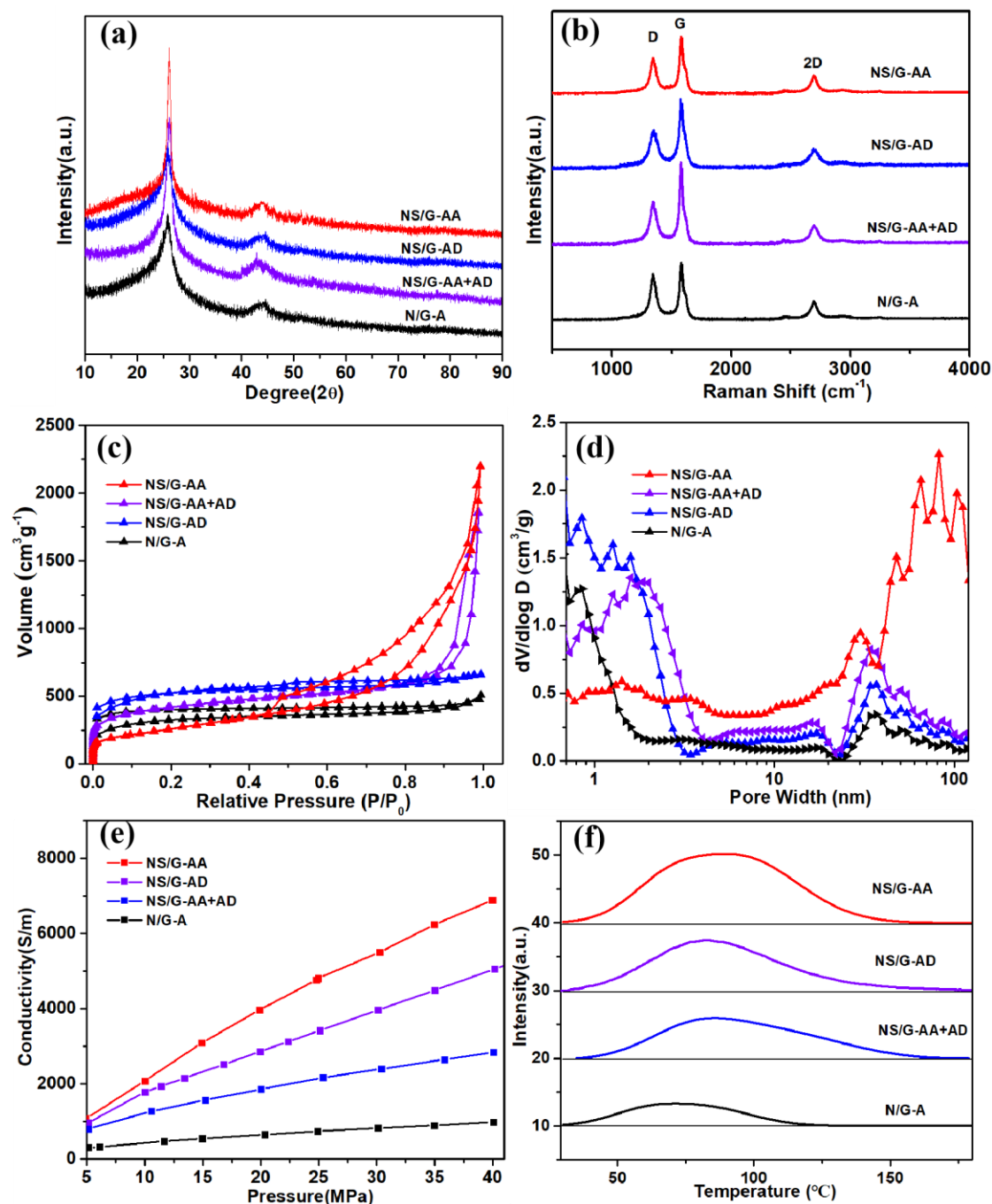


**Figure 7-2.** XRD patterns (a), Raman spectra (b), Nitrogen adsorption-desorption isotherms (c) and Pore size distribution (d), Electrical conductivity (e) and CO<sub>2</sub>-TPD (f) of NS/G-AD, NS/G-AA, NS/G-AA+AD and N/G-A.

Furthermore, Electronic conductivity of materials is also a critical parameter influencing the resistance of electrocatalysis. The powder conductivity of these samples at various pressure (Figure 7-2e) displays that all graphene nanosheets present excellent conductivity, in which N/G-AA possess the highest conductivity of 4456 S<sup>-1</sup> m at the

pressure of 25.0MPa, followed by NS/G-AD of 3068 S<sup>-1</sup> m and NS/G-AA+AD of 2130 S<sup>-1</sup> m, by contrast, N/G-A shows the lowest conductivity of 836 S<sup>-1</sup> m, manifesting that the addition of S could enhance the conductivity in these graphene nanosheets. In addition, considering that Lewis base sites is a clear indicator indirectly reflecting active sites and density of carbon atoms in heteroatoms doped carbon [23]. Temperature Programmed Desorption (TPD) of CO<sub>2</sub> was carried out to detect Lewis base sites in these samples. TPD profiles of CO<sub>2</sub> in these NG and NSG samples in Figure 7-2f demonstrate that all these NSG samples display higher desorption area of CO<sub>2</sub> than that of N/G-A, in which the desorption area of NS/G-AA is 5 times higher than N/G-A, followed by 3.5 times and 3 times of NS/G-AD and NS/G-AA+AD respectively, indicating the second doping of S can produce more active sites than single N doping. Meanwhile, different S precursors may induce discrepancy on electronic distribution of carbon atoms which may contribute by different synergetic effect between N, S dopants.

Chemical composition and state of these NSG samples were analyzed by XPS as shown in Figure 7-3a-c. The specific values of C1s position for NS/G-AD, NS/G-AA, NS/G-AD+AA and N/G-A are located at ~283.87eV, 285.19 eV, 285.92 eV, 287.35 eV, 289 eV corresponding to C-S groups, C-C (sp<sub>2</sub> centers), defect peak (sp<sub>3</sub> centers), C-N groups, and O=C-O respectively[24]as shown in Figure 7-4a. The existence of C-N and C-S group in these samples manifest that the successful doping of N and S dopants. As for as the S doping, there are three obvious fitted peaks of S exist in these NSG samples assigned to 163.8 eV, 165.2 eV, 167.8 eV corresponding to S 2p<sub>3/2</sub>, S 2p<sub>1/2</sub> and C-SO<sub>x</sub>-C respectively (Figure 7-3b). The percentages of S doping in NS/G-

AD, NS/G-AA, NS/G-AD+AA are 0.81 at%, 0.82 at% and 0.84 at% respectively as list in Table 1, indicating that different S precursors produce slight influence on final doping content of N and S dopants.

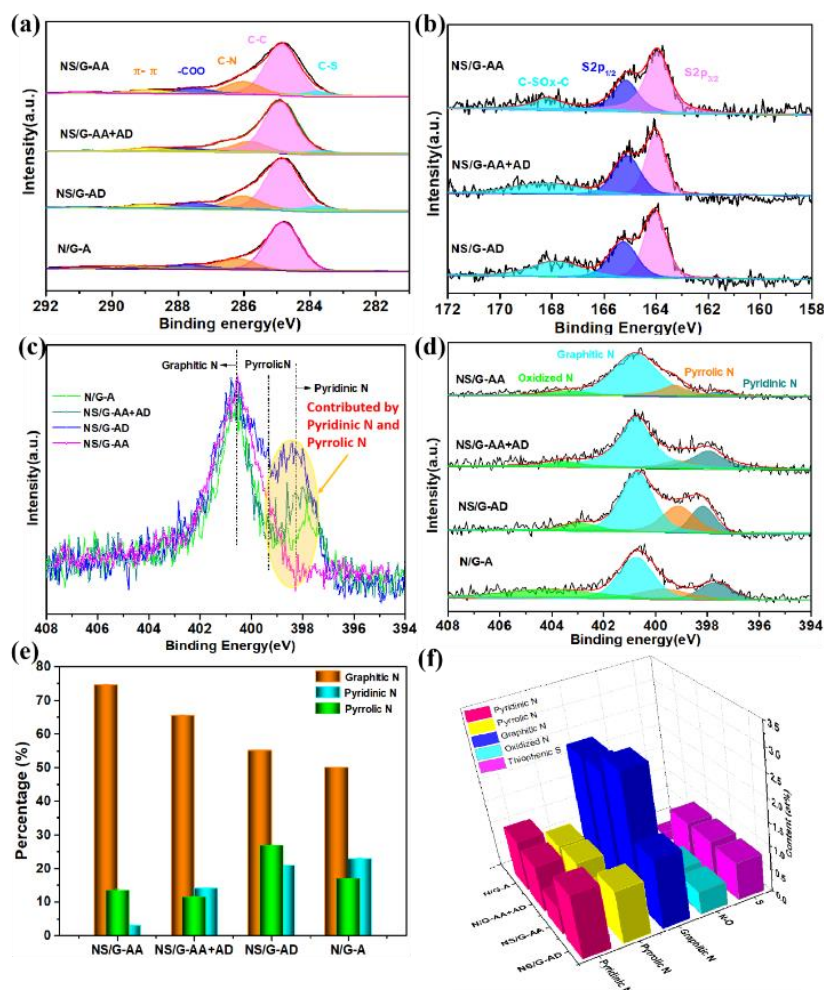


**Figure 7-3.** XPS spectra of C1s (a), S2p (b), N 1s (c) and high-resolution of fitted peaks of N 1s (d) in NS/G-AD, NS/G-AA, NS/G-AA+AD and N/G-A. The bar Graph of specific relative content of N and in these NG and NSG samples (e). The 3D bar charts of absolute content of N and in these NG and NSG samples (f).

N is kind of important doped element that plays crucial role in active sites formation of NSG nanosheets. It is found that these NSG samples display similar doping N content and the specific percentages of doped N dopants in these NSG catalysts are 4.56 at %, 4.42 at%, 4.51 at% and 4.86 at% corresponding to NS/G-AD, NS/G-AA, NS/G-AD+AA and N/G-A. However, it is notable that the specific contents

of N species in these samples are completely different as list in Figure 7-3c. The main N peaks in NS/G-AD, NS/G-AA, NS/G-AD+AA are consistent and located at about 400.95 eV, and the main peak is contributed by graphitic N. However, the N1s peak information of NS/G-AD, NS/G-AA, NS/G-AA+AD shows great difference in low binding energy region contributed by pyridinic N and pyrrolic N. It is found that a strong N1s peak (contributed by pyridinic N and pyrrolic N) at around 398.3 eV in NS/G-AD, but there is sharp decreased peak intensity in NS/G-AA+AD and the peak located at 398.3eV almost disappeared in that of NS/G-AA. It manifest that the graphitic N in these NSG samples keep in consistent basically, but the percentage of pyridinic N and pyrrolic N changed greatly in these NSG samples. As shown in Figure 7-3d, the specific percentage of N species in these samples are analyzed. By the fitted peaks of high-resolution N1s spectrum of these samples, it is found that N 1s spectrum could be fitted into pyridinic-N, pyrrolic-N, graphitic-N, and oxidized-N corresponding to 398.2 eV, 399.0 eV, 400.95 eV, and 403.0 eV, respectively [25-28] . Graphitic N is the main component and account for up to 50% in these NSG samples. The specific contents of different N species in these NSG samples are listed in Figure 7-3e, Specifically speaking, there is significant increased percentage of graphitic N at about 72% in NS/G-AA compared to other two samples, but with decreased content of pyridinic N and pyrrolic N at 3.6% and 7.4% respectively. By contrast, the percentage of graphitic N in NS/G-AA+AD slightly decreased to 64% compared to NS/G-AA with increased content of pyrrolic N and pyridinic N respectively. Furthermore, in NS/G-AD, there is the lowest content of graphitic N of 54% among these NSG samples and

with the highest percentage of pyridinic N and pyrrolic N of 18% and 22% respectively. In order to show the change of absolute value content of each N species in these NSG samples more intuitively, a 3D bar chart was listed in Figure 7-3f. According to previous reports [29-33], the doped heteroatoms in carbon matrix usually induce electronic structure redistribution on surrounding carbon atoms, based on this, the dopants of different N, S species in these different NSG samples may induce different redistribution charge and spin that influence final electrocatalytic performance for ORR or/and OER.

Ultraviolet photoelectron spectroscopy (UPS) was used to deeply analyze the internal electronic structure information of materials. From Figure 7-4a, three typical regions located at 3eV, 7eV and 13eV can be observed that is corresponding to  $\pi$ ,  $\pi + \delta$  and  $\delta$  bond in carbon matrix respectively [34, 35]. N/G-A without S dopants possess the highest intensity of  $\pi$ ,  $\pi + \delta$ ,  $\delta$  among all samples, which provides a clue that the addition of S induce great change on internal electronic structure distribution on carbon matrix. As for as the NSG samples, NS/G-AA and NS/G-AD exhibit the similar tendency in binding energy around 13 eV as shown in Figure 7-4b, NS/G-AA+AD possess relatively high intensity of  $\pi$ ,  $\pi + \delta$ ,  $\delta$  compared by NS/G-AA and NS/G-AD, which may induce less electron transfer from C to the doped S dopants (electron deficiency) in NS/G-AA+AD. As shown in Figure 7-4c, NS/G-AD possess the lowest value of the peak intensity located at about 3 eV among the three NSG samples that may

bring out the strongest doping effect of N, S dopants in NS/G-AD among all these samples [36-38].

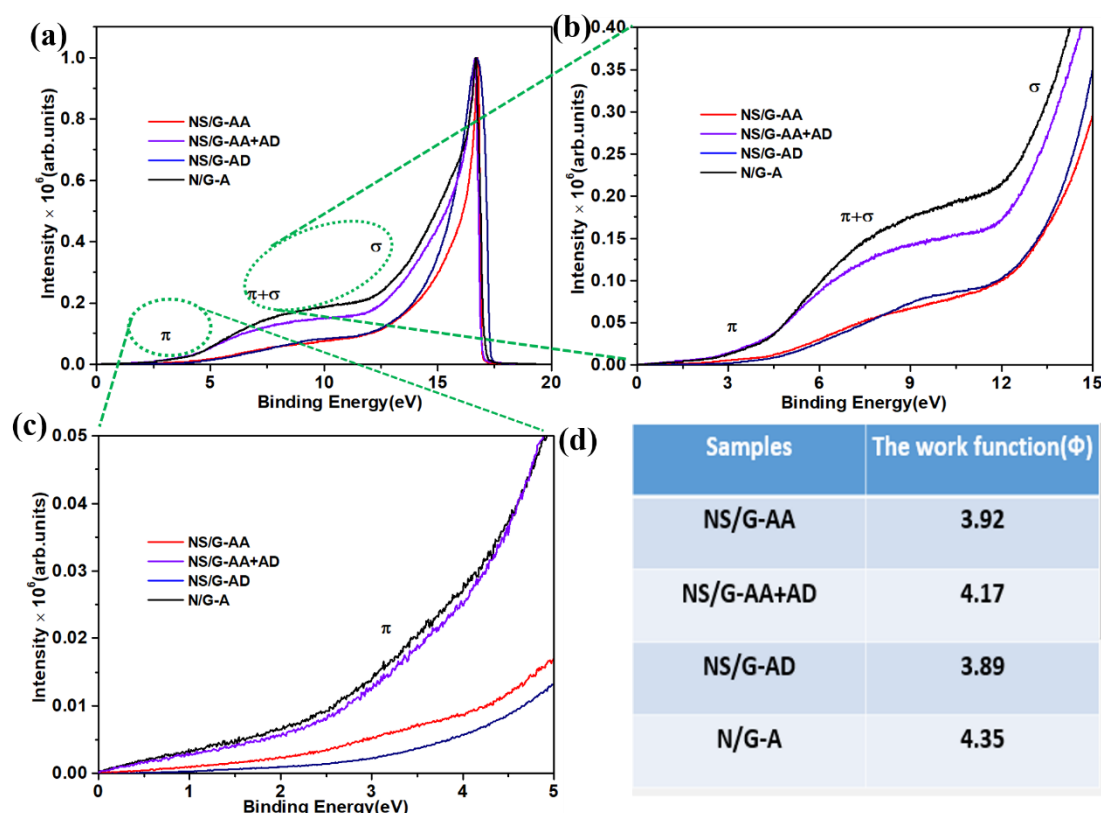


**Figure 7-4.** UPS spectra (a), Partial enlarged spectra (b, c) of the UPS spectra and the specific values of work function (d) of NS/G-AD, NS/G-AA, NS/G-AA+AD and N/G-A.

Furthermore, work function ( $F$ ) is a crucial index related to the minimum energy barrier that internal electrons escaping from the nucleus. In Figure 7-4d, N/G-A shows the biggest values of 4.35 eV, followed by 4.17 eV in NS/G-AA+AD and 3.92 eV in that of NS/G-AA. The low values of  $F$  in these NSG samples demonstrate their great potential as highly active electrocatalysts.

### 7.3.2 Electrocatalysis for ORR, OER and Zn-air battery.

Figure 7-5a shows that the electrochemical tests for ORR of these NG and NSG samples derived from the same N-containing precursor but with different S-

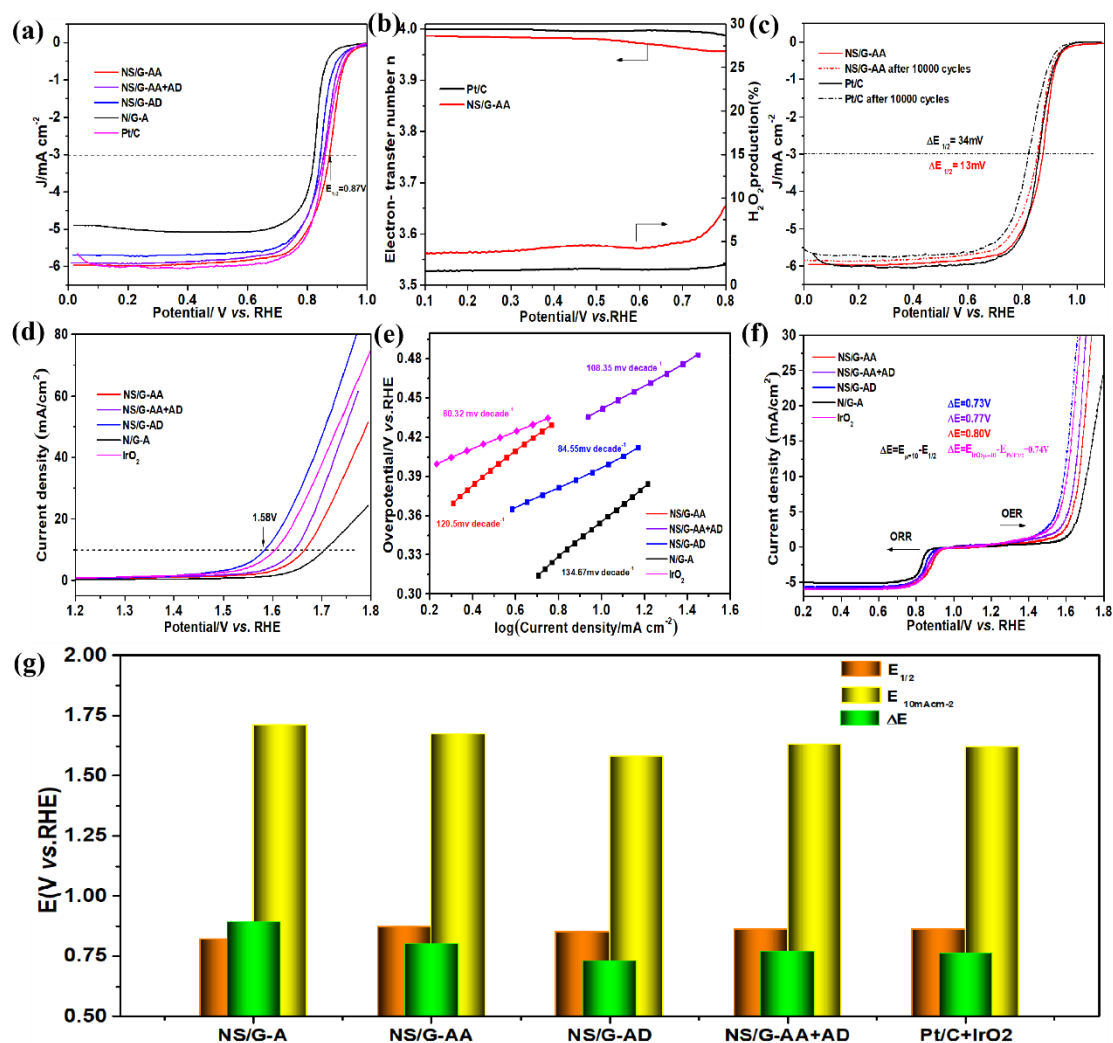


**Figure 7-5.** LSV curves of NS/G-AD, NS/G-AA, N/G-A, NS/G-AA+AD and Pt/C for ORR(a), hydrogen peroxide and electron transfer number of NS/G-AA and Pt/C (b), cycles stability test after 10000 cycles of NS/G-AA in 0.1M KOH(c), Tafel slope of NS/G-AD, NS/G-AA, N/G-A and Pt/C for OER(d) and both ORR and OER(e) and their corresponding LSV curves (g).

Containing precursors, in which the NS/G-AA has the best ORR performance with the values of  $E_{\text{onset}}$  of NS/G-AA for ORR up to 1.01 V vs. RHE and the  $E_{\text{half-wave}}$  potential up to 0.87 V vs. RHE, compared to other samples, and is also better than that of benchmarked Pt/C with  $E_{\text{half-wave}}$  potential of 0.86 V vs. RHE. In addition, NS/G-AD shows the values of  $E_{\text{onset}}$  and  $E_{\text{half-wave}}$  potential are 0.96 V vs. RHE and 0.84 V vs. RHE respectively, followed by NS/G-AA+AD with  $E_{\text{onset}}$  and  $E_{\text{half-wave}}$  potential at 0.98 vs. RHE and 0.85 V vs. RHE respectively. By contrast, N/G-A shows the poor catalytic



activity for ORR of the  $E_{\text{onset}}$  and  $E_{\text{half-wave}}$  potential at 0.88 V *vs.* RHE and 0.74 V *vs.* RHE respectively, indicating that the addition of S doping can effectively enhance catalytic performance for ORR. On the other hand, we can see that the limiting current density of NS/G-AD (5.73 mA cm<sup>-2</sup>), NS/G-AA+AD (5.80 mA cm<sup>-2</sup>) and NS/G-AA (5.99 mA cm<sup>-2</sup>) have been greatly improved compared with N/G-A (5.0 mA cm<sup>-2</sup>), which may contribute to improved electrical conductivity with S doping, the result is in consistent with conductivity test results discussed above. The superior catalytic activity of NS/G-AA for ORR is further validated by hydrogen peroxide yield and number of electron transfers (Figure 7-5b), average number of electron transfers of NS/G-AA between 0.1-0.8V is 3.975 which indicates that there are close to 4 e<sup>-</sup> transfer process in NS/G-AA during ORR reaction. Meanwhile, the hydrogen peroxide yield is around 5% between 0.1-0.8V, also displaying its high selectivity of 4 e<sup>-</sup> transfer process. The stability is an important technical index in practical application. After 10000 accelerated cycle test, there is only 13mV shift occurred in NS/G-AA far below than that of Pt/C with 34mV negative shift (Figure 7-5c), indicating that NS/G-AA possess excellent stability due to its nature of highly graphitic degree as revealed by XRD and Raman analysis.

OER performance of these samples were characterized under the potential range of 1.2 V-1.8 V in 0.1 M KOH. From Figure 7-5d and e, it is observed that among all these samples, NS/G-AD possess the best OER performance in 0.1 M KOH of the smallest potential of 1.58 V at the current of 10.0 mA cm<sup>-2</sup> (i.e.,  $E_j = 10$ ), followed by NS/G-AA+AD with 1.63 V at  $E_j = 10$  as well as NS/G-AA with 1.67 V at  $E_j = 10$ . By

contrast, N/G-A displays a biggest potential value of 1.71 V at  $E_j = 10$ . Tafel plots in Figure 7-5f further displays that the NS/G-AD have the lowest value of Tafel slope of  $66.7 \text{ mV decade}^{-1}$ , followed by NS/G-AA+AD of  $82.6 \text{ mV decade}^{-1}$ , NS/G-AA of  $98.3 \text{ mV decade}^{-1}$  and N/G-A of  $131.18 \text{ mV decade}^{-1}$ , even lower than that of  $\text{IrO}_2$  with Tafel slope is  $71.55 \text{ mV decade}^{-1}$ . As for as bifunctional performance for ORR and OER, the value of  $\Delta E = E_{j=10} - E_{1/2}$  is considered as a core parameter to evaluate the overall performance of oxygen redox reaction (both ORR and OER). Like ORR results discussed above, the co-doping of S leads to increased catalytic performance for OER, compared with single N doped ones. Interestingly, it is observed that NS/G-AD with slightly lower performance for ORR than that of NS/G-AA exhibits enhanced catalytic activity for OER than that of NS/G-AA, which endows NS/G-AD with superior bifunctional performance for ORR and OER. Accordingly, the values of  $\Delta E$  for N/G-A, NS/G-AA, NS/G-AA+AD and NS/G-AD are 0.97 V, 0.80 V, 0.77 V and 0.73 V, respectively. And the  $\Delta E$  of only 0.73 V of NS/G-AD for ORR and OER with is high than that of Pt/C+ $\text{IrO}_2$  ( $\Delta E = 0.76 \text{ V}$ ). The big gap between catalytic activity and selectivity for ORR and OER in these NSG samples may derived from different synergetic effect between N, S dopants originated from the change of different S-containing precursors. This excellent performance of NS/G-AD rank samong advanced metal-free bifunctional catalysts reported previously. In order to intuitively show the performance comparison of these samples, a 3D bar chart is list in Figure 7-5g. In addition, the electrochemically active surface areas (ECSA) of N/G-A, NS/G-AA, NS/G-AD and NS/G-AA+AD is calculated based on the double layer capacitance ( $C_{dl}$ )

from the cyclic voltammograms under the potential region of the non-Faradaic (1.04V-1.18V). The specific  $C_{dl}$  value of N/G-A, NS/G-AA, NS/G-AD and NS/G-AA+AD is 21.45  $\text{mF cm}^{-2}$ , 25.05  $\text{mF cm}^{-2}$ , 27.15  $\text{mF cm}^{-2}$  and 29.27  $\text{mF cm}^{-2}$  respectively, indicating S doping exactly promote more active sites than single N doped graphene.

The excellent bifunctional performance of NS/G-AD for both ORR and OER was also verified by a home-made Zn-air battery test, presented in Figure 7-6a. From Figure 7-6 b, the Zn-air battery with NS/G-AD as cathode produces a high power density of 146  $\text{mW cm}^{-2}$ , which is even higher than that of its counterpart of Pt/C+IrO<sub>2</sub> (135  $\text{mW cm}^{-2}$ ). In addition, its typical discharging and charging polarization curves from Figure 7-6c, displays that the charging and discharging potential gap of NS/G-AD is 1.05 V at a current density of 50  $\text{mA cm}^{-2}$ , which is much lower than that of Pt/C+IrO<sub>2</sub> (1.13 V). Meanwhile, the NS/G-AD shows excellent cycling stability, validate by 900 cycles in Figure 7-6d, in which After, the decay value of the discharging and charging potential gap of NSC-based is 27.16% at 900th cycle, whereas the value in that of Pt/C + IrO<sub>2</sub> electrode is 36.18%,. The specific discharge capacity is estimated to be 796  $\text{mAh g}_{\text{zn}}^{-1}$  (Figure 7-6e) at 50  $\text{mA cm}^{-2}$  higher than Pt/C+IrO<sub>2</sub> (767  $\text{mAh g}_{\text{zn}}^{-1}$ ). The excellent performance of NS/G-AD in Zn-air battery manifest its great potential in practical application.

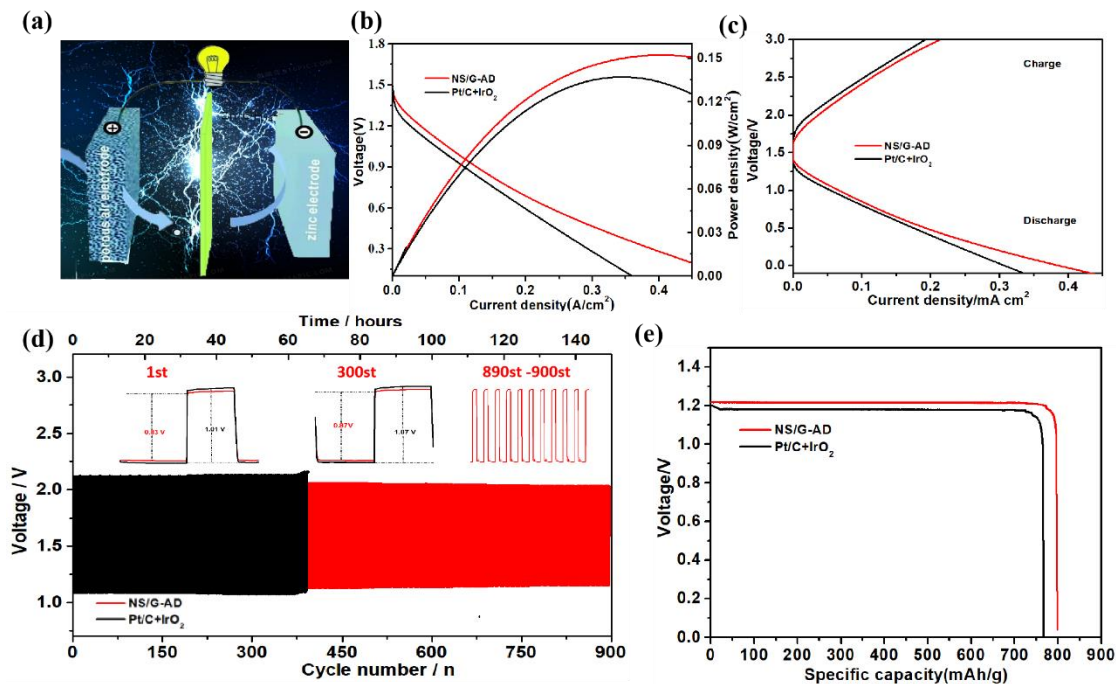


**Figure 7-6.** Illustration of the primary Zn-Air batteries (a) the discharge polarization curves and the corresponding power density plots of Zn-Air batteries driven by NS/G-AD and Pt/C+IrO<sub>2</sub> (b) charge and discharge polarization curves (c) galvanostatic discharge-charge cycling curves at 5 mA·cm<sup>-2</sup> of rechargeable Zn-Air batteries (d). Specific capacities of the Zn-Air batteries at a current density of 50 mA·cm<sup>-2</sup> (e).

### 7.3.3 Discussion on active sites in N, S co-doped graphene for ORR and OER

The synergetic effects of S coordinate with different N species in graphene for electro catalytic selectivity for ORR or/and OER are explored based on Density functional theory (DFT) calculations. In our previous work, the synergy between graphitic-N and thiophenic-S dopants in N, S co-doped graphene strongly relied on different relative position in graphene network, producing significant effect on intermediates energy of ORR and OER pathways [39]. It is notable that S atoms usually distributes on graphene edges in the built models, due to the fact that S has a much larger radius than C and N atoms, the S atoms are more likely to be located at edges or holes of carbon layer due to steric resistance effects[40]. Although most studies including

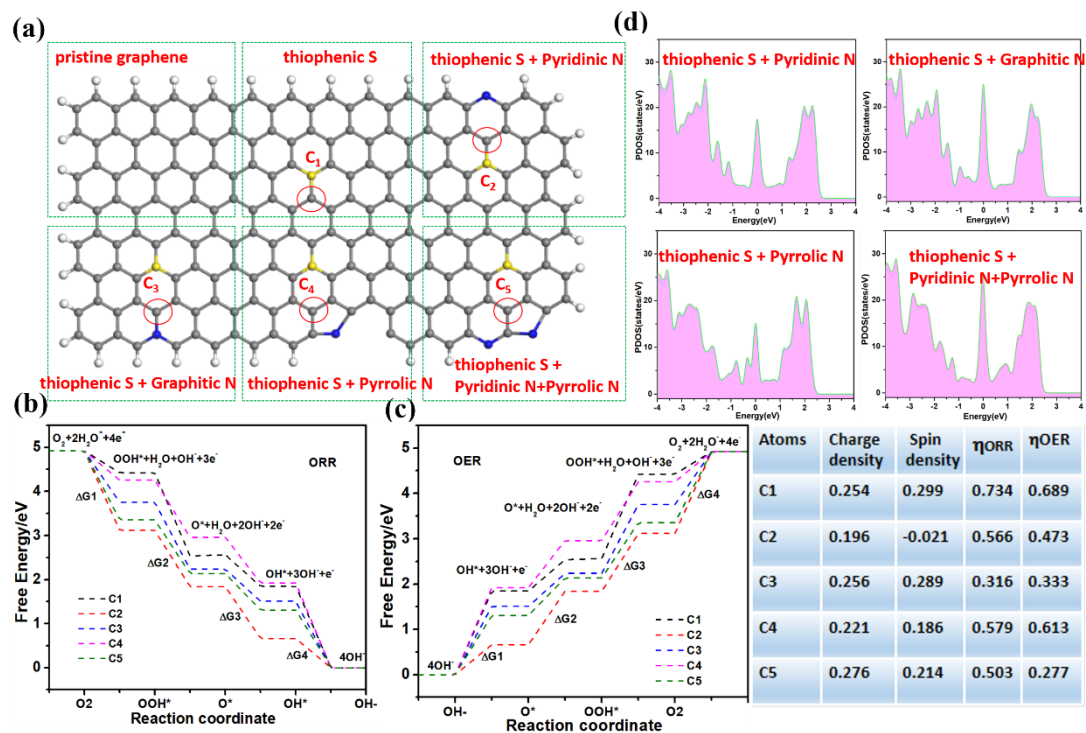


**Figure 7-7.** The constructed models (a) and the Gibbs free energy diagram of ORR (b) and the Gibbs free energy diagram of OER(c). Partial density of state of partial models (PDOS) (d) of these models.

our previous reports focus on exploring edged S and their synergy between other dopants [41,42], the possibility of S doping in the bulk of graphene replace one C atom also exist. Based on previous research results and built models, in this work, the models are further optimized with introducing bulk thiophenic S dopant as shown in Figure 7-7a. In addition, it is believed that carbon atoms featured with high spin and charge density are considered as the potential active sites for enhanced catalytic activity due to they are beneficial for adsorbing intermediates products during process for ORR or OER [43]. Based on this, some carbon atoms with high charge and spin density which usually located at surrounding the doped N, S dopants were selected as potential effective sites in built models for free-energy diagram calculations of ORR and OER respectively. The specific free-energy diagram in Figure 7-7b shows that C<sub>3</sub> located at around graphitic N coordinate with thiophenic S shows the least overpotential value of

0.316 eV for ORR. By contrast, C<sub>5</sub> in model of pyridinic N + pyrrolic N + thiophenic S exhibits relatively higher overpotential value of 0.503 eV compared to that of C<sub>3</sub>. Accordingly, C<sub>2</sub> in the model of pyridinic N coordinated with thiophenic S displays high overpotential value of 0.566 eV. C<sub>4</sub> and C<sub>1</sub> in the model of pyrrolic N+ thiophenic S and single thiophenic S possess the high values of overpotential of 0.579 eV and 0.734 eV respectively.

Correspondingly, the selected carbon atoms as potential catalytic sites were calculated for free-energy diagram of OER, which is known that featured with an opposite processing pathway from ORR[44-47], As shown in Figure 7-7c. It is notable that carbon atom of C<sub>5</sub> in model of pyridinic N + pyrrolic N + thiophenic S displays the least value of overpotential (0.277 eV) for OER among these configurations of S and N species, which is lower than that of C<sub>3</sub> in model constructed by graphitic N and thiophenic S with the value of 0.333 eV. Similarly, as for as the carbon atoms of C<sub>2</sub>, C<sub>4</sub> and C<sub>1</sub> in coordination of pyridinic N+thiophenic S, pyrrolic N+ thiophenic S and single thiophenic S display the high values of overpotentials (0.473 eV, 0.613 eV and 0.689 eV) for OER respectively.

According to previous reports, the value of partial density of state (PDOS) overlap at the Fermi level (0 eV) is kind of important parameter that could reflect the degree of atomic orbital hybridization, which is related with the catalytic activity potential for ORR and OER. From Figure 7-7d, it is observed that the coordination of graphitic N and thiophenic S bring out the high value of P-state partial DOS overlap at the Fermi level (0 eV) of than that in model of pyridinic N+ thiophenic S and pyrrolic N +

thiophenic S, which provides a clue that there may exist higher electrical conductivity and easier charge transfer in model of graphitic N+thiophenic S. Furthermore, it is notable that when pyrrolic N coordinate with pyridinic N+ thiophenic S, the P-state partial DOS value increased greatly, demonstrating that the enhanced catalytic potential may produce.

In this work, DFT calculation combined with a series of physical characterizations were conducted to reveal the origin of electrochemical performance differences of these NSG catalysts in catalytic activity and selectivity for ORR and OER. It is found that NSG catalysts possess similar graphene nanosheet morphology as well as similar specific surface area and pore size distribution. From the perspective of chemical compositions, NS/G-AD and NS/G-AA exhibit similar content of doped dopants, however, it is notable that the contents of specific N dopant species are completely different despite they derived from the same N-containing precursor platform but influenced by the addition of different S-containing precursors. Speak specifically, the addition of Ammonium persulfate induced the increased high content of graphitic N up to 65% compared to N/G-A. By contrast, the addition of Disulfide biurea as S-containing precursor bring about increased content of pyrrolic N and pyridinic N but decreased percentage of graphitic N. According to previous reports, it is known that the doped dopants act as the main components of active sites play crucial role in final catalytic performance for ORR and OER. Especially, their synergistic effect between N, S dopants contribute greatly to enhanced electrocatalytic activity. Considering that the different S precursors greatly affect the final doping species of N, therefore, the N,

S synergistic effect in the two catalysts may significantly change by the doped S precursors, which may be the root cause that influences adsorption energy during electrochemical reaction process and therefore leads to the difference of their catalytic performance for ORR and/or OER respectively. Combining with DFT calculation results, graphitic N coordinate with thiophenic S brings out the enhanced catalytic performance for ORR, by contrast, the coordination of pyridinic N + pyrrolic N + thiophenic S exhibits the increased performance for OER, which is consistent with electrochemical testing results, NSG catalyst with high content of graphitic N and thiophenic S derived from Ammonium persulfate as precursors exhibits the highest catalytic activity for ORR. By contrast, the catalyst derived from Disulfide biurea as S-containing precursor possesses relatively low performance for ORR but with enhanced catalytic activity for OER. In summary, the selection of different S-containing precursors plays an important role on the formation of doped N dopant species, therefore, producing a great effect on coordination of S and different N species which induces different synergistic effects of N and S that bring about the possibility of electrocatalytic functions tuning for ORR and OER.

**Table 1.** BET surface area, the specific content of each element and the specific performance parameters for ORR and OER of these samples.

Samples	BET Surface area (m <sup>2</sup> ·g <sup>-1</sup> )	OER	S at%	C at%	O at%	N at%				
		10.0 mA cm <sup>-2</sup> (V vs RHE)				ORR E <sub>1/2</sub> 3.0 mA cm <sup>-2</sup> (V vs RHE)	N <sub>PY(Pyrrolic N)</sub>	N <sub>P(Pyridinic N)</sub>	N <sub>G(Graphitic N)</sub>	N <sub>O(Oxidized)</sub>



		$\Delta E / V (VE_{j=10} / V - E_{j=3})$								
NS/G-AD	881.2	1.58	0.81	91.36	3.27	1.14	1.38	1.50	0.49	4.56
		0.85								
		0.73								
NS/G-AA	845.8	1.67	0.84	91.67	3.91	0.46	0.60	2.87	0.48	4.42
		0.87								
		0.8								
NS/G-AA+AD	926.5	1.63	0.82	90.65	4.02	1.00	0.78	2.48	0.25	4.51
		0.86								
		0.77								
N/G-A	796.5	1.71	0	91.27	3.87	0.72	1.11	2.43	0.6	4.86
		0.82								
		0.89								

## 7.4 Conclusion

In summary, typical NSG catalysts were obtained based on the same N-containing precursor platform but with different S-containing precursors, it is found that the different S precursors play important role on influencing the formation of N dopant species in carbon matrix, which leads to different active sites construction between S and various N species. DFT revealed that graphitic N + thiophenic S contributes to enhanced catalytic activity for ORR, but when thiophenic S coordinate with pyridinic N and pyrrolic N, it brings out increased catalytic performance for OER. The significance of this work not only relies on revealing the correlation between S-containing precursors with the resultant N species in carbon matrix but elucidating the dependence of electrocatalytic functions tuning for ORR and OER on N, S

configurations and provide a facile strategy to realize various active sites construction via adjustable precursor platform.

## References

1. Li, Y.; Dai, H., Recent advances in zinc-air batteries. *Chem. Soc. Rev.* **2014**, *43*, 5257-5275.
2. Shao, M.; Chang, Q.; Dodelet, J.-P.; Chenitz, R., Recent Advances in Electrocatalysts for Oxygen Reduction Reaction. *Chem. Rev.* **2016**, *116*, 3594-3657.
3. Wan, W. J.; Liu, X. J.; Li, H. Y.; Peng, X. Y.; Xi, D. S.; Luo, J., 3D carbon framework-supported CoNi nanoparticles as bifunctional oxygen electrocatalyst for rechargeable Zn-air batteries. *Appl. Catal. B-Environ.*, **2019**, *240*, 193-200.
4. Lei, Y. P.; Wang, Q. C.; Peng, S. J.; Ramakrishna, S.; Zhang, D.; Zhou, K. C., Electrospun Inorganic Nanofibers for Oxygen Electrocatalysis: Design, Fabrication, and Progress. *Adv. Energy Mater.* **2020**, *10*, 1902115.
5. Shi, Q.; Zhu, C.; Du, D.; Lin, Y., Robust noble metal-based electrocatalysts for oxygen evolution reaction. *Chem. Soc. Rev.* **2019**, *48*, 3181-3192.
6. Gong, K.; Du, F.; Xia, Z.; Durstock, M.; Dai, L., Nitrogen-Doped Carbon Nanotube Arrays with High Electrocatalytic Activity for Oxygen Reduction. *Science* **2009**, *323*, 760-764.
7. Yuan, K.; Luetzenkirchen-Hecht, D.; Li, L.; Shuai, L.; Li, Y.; Cao, R.; Qiu, M.; Zhuang, X.; Leung, M. K. H.; Chen, Y.; Scherf, U., Boosting Oxygen Reduction of Single Iron Active Sites via Geometric and Electronic Engineering: Nitrogen and Phosphorus Dual Coordination. *J. A. Chem. Soc.* **2020**, *142*, 2404-2412.
8. Shao, Y.; Dodelet, J.-P.; Wu, G.; Zelenay, P., PGM-Free Cathode Catalysts for PEM

Fuel Cells: A Mini-Review on Stability Challenges. *Adv. Mater.* **2019**, *31*, 1807615.

9. Liu, S.; Yang, Z.; Li, M.; Liu, L.; Wang, Y.; Lv, W.; Qin, Z.; Zhao, X.; Zhu, P.; Wang, G., FeS-decorated hierarchical porous N, S-dual-doped carbon derived from silica-ionogel as an efficient catalyst for oxygen reduction reaction in alkaline media.

*Electrochim. Acta* **2018**, *265*, 221-231.

10. Hu, X.; Min, Y.; Ma, L. L.; Lu, J. Y.; Li, H. C.; Liu, W. J.; Yu, H. Q., Iron-nitrogen doped carbon with exclusive presence of Fe<sub>x</sub>N active sites as an efficient ORR electrocatalyst for Zn-air battery. *Appl. Catal. B-Environ.*, **2020**, *268*, 118405.

11. Lv, Q.; Wang, N.; Si, W. Y.; Hou, Z. F.; Li, X. D.; Wang, X.; Zhao, F. H.; Huang, C. S., Pyridinic nitrogen exclusively doped carbon materials as efficient oxygen reduction electrocatalysts for Zn-air batteries. *Appl. Catal. B-Environ.*, **2020**, *261*, 118234,

12. Xiao, F.; Xu, G.-L.; Sun, C.-J.; Xu, M.; Wen, W.; Wang, Q.; Gu, M.; Zhu, S.; Li, Y.; Wei, Z.; Pan, X.; Wang, J.; Amine, K.; Shao, M., Nitrogen-coordinated single iron atom catalysts derived from metal organic frameworks for oxygen reduction reaction.

*Nano Energy* **2019**, *61*, 60-68.

13. Wang, Q. C.; Ye, K.; Xu, L.; Hu, W.; Lei, Y. P.; Zhang, Y.; Chen, Y.; Zhou, K. C.; Jiang, J.; Basset, J. M.; Wang, D. S.; Li, Y. D., Carbon nanotube-encapsulated cobalt for oxygen reduction: integration of space confinement and N-doping. *ChemComm*, **2019**, *55*, 14801-14804.

14. Hu, C.; Dai, L., Multifunctional Carbon-Based Metal-Free Electrocatalysts for Simultaneous Oxygen Reduction, Oxygen Evolution, and Hydrogen Evolution. *Adv. Mater.* **2017**, *29*, 1604942.

15. Wang, H.; Shao, Y.; Mei, S.; Lu, Y.; Zhang, M.; Sun, J.-k.; Matyjaszewski, K.; Antonietti, M.; Yuan, J., Polymer-Derived Heteroatom-Doped Porous Carbon Materials. *Chem. Rev.* **2020**, *120*, 9363-9419.
16. Chen, Z. Y.; Wang, Q. C.; Zhang, X. B.; Lei, Y. P.; Hu, W.; Luo, Y.; Wang, Y. B., N-doped defective carbon with trace Co for efficient rechargeable liquid electrolyte-/all-solid-state Zn-air batteries. *Sci. Bull.*, **2018**, *63*, 548-555.
17. Jiang, H.; Gu, J.; Zheng, X.; Liu, M.; Qiu, X.; Wang, L.; Li, W.; Chen, Z.; Ji, X.; Li, J., Defect-rich and ultrathin N doped graphene nanosheets as advanced trifunctional metal-free electrocatalysts for the ORR, OER and HER. *Energ. Environ. Sci.* **2019**, *12*, 322-333.
18. Wang, H.; Shao, Y.; Mei, S.; Lu, Y.; Zhang, M.; Sun, J.-k.; Matyjaszewski, K.; Antonietti, M.; Yuan, J., Polymer-Derived Heteroatom-Doped Porous Carbon Materials. *Chemical Reviews* **2020**, *120*, 9363-9419.
19. Wang, H.-m.; Wang, H.-x.; Chen, Y.; Liu, Y.-j.; Zhao, J.-x.; Cai, Q.-h.; Wang, X.-z., Phosphorus-doped graphene and (8,0) carbon nanotube: Structural, electronic, magnetic properties, and chemical reactivity. *Appl. Surf. Sci.* **2013**, *273*, 302-309.
20. Zheng, Y.; Jiao, Y.; Ge, L.; Jaroniec, M.; Qiao, S. Z., Two-Step Boron and Nitrogen Doping in Graphene for Enhanced Synergistic Catalysis. *Angew. Chem. Int. Ed.* **2013**, *52*, 3110-3116.
21. Liang, J.; Jiao, Y.; Jaroniec, M.; Qiao, S. Z., Sulfur and Nitrogen Dual-Doped Mesoporous Graphene Electrocatalyst for Oxygen Reduction with Synergistically Enhanced Performance. *Angew. Chem. Int. Ed.* **2012**, *51*, 11496-11500.

22. Zhang, J.; Zhao, Z.; Xia, Z.; Dai, L., A metal-free bifunctional electrocatalyst for oxygen reduction and oxygen evolution reactions. *Nat. Nanotechnol.* **2015**, *10*, 444-452.
23. Guo, D.; Shibuy, R.; Akib, C.; Saji, S.; Kondo, T.; Nakamura, J., Active sites of nitrogen-doped carbon materials for oxygen reduction reaction clarified using model catalysts. *Science* **2016**, *315*, 361-365.
24. Wang, Q. C.; Lei, Y. P.; Chen, Z. Y.; Wu, N.; Wang, Y. B.; Wang, B.; Wang, Y., Fe/Fe<sub>3</sub>C@C nanoparticles encapsulated in N-doped graphene-CNTs framework as an efficient bifunctional oxygen electrocatalyst for robust rechargeable Zn-air batteries. *J. Mater. Chem. A*, **2018**, *6*, 516-526.
25. Hung, C.-T.; Yu, N.; Chen, C.-T.; Wu, P.-H.; Han, X.; Kao, Y.-S.; Liu, T.-C.; Chu, Y.; Deng, F.; Zheng, A.; Liu, S.-B., Highly nitrogen-doped mesoscopic carbons as efficient metal-free electrocatalysts for oxygen reduction reactions. *J. Mater. Chem. A* **2014**, *2*, 20030-20037.
26. Guo, Y.; Yao, S.; Gao, L.; Chen, A.; Jiao, M.; Cui, H.; Zhou, Z., Boosting bifunctional electrocatalytic activity in S and N co-doped graphene nanosheets for high-efficiency Zn-air batteries. *J. Mater. Chem. A* **2020**, *8*, 4386-4395.
27. Yang, K.; Li, J.; Zhou, L.; Zhang, T.; Fu, L., Synthetic strategies of two-dimensional porous materials towards highly effective catalysts. *Flatchem* **2019**, *15*.
27. Li, J.; Zhang, Y.; Zhang, X.; Huang, J.; Han, J.; Zhang, Z.; Han, X.; Xu, P.; Song, B., S, N Dual-Doped Graphene-like Graphene nanosheets as Efficient Oxygen Reduction Reaction Electrocatalysts. *ACS Appl. Mater. Interfaces* **2017**, *9*, 398-405.
28. Qu, K.; Zheng, Y.; Jiao, Y.; Zhang, X.; Dai, S.; Qiao, S.-Z., Polydopamine-Inspired,

Dual Heteroatom-Doped Carbon Nanotubes for Highly Efficient Overall Water Splitting. *Adv. Energy Mater.* **2017**, *7*, 1602068.

29. Xiang, Z.; Cao, D.; Huang, L.; Shui, J.; Wang, M.; Dai, L., Nitrogen-Doped Holey Graphitic Carbon from 2D Covalent Organic Polymers for Oxygen Reduction. *Adv. Mater.* **2014**, *26*, 3315.

30. Li, D.; Li, C.; Zhang, L.; Li, H.; Zhu, L.; Yang, D.; Fang, Q.; Qu, S.; Yao, X., Metal-Free Thiophene-Sulfur Covalent Organic Frameworks: Precise and Controllable Synthesis of Catalytic Active Sites for Oxygen Reduction. *J. Am. Chem. Soc.* **2020**, *142*, 8104-8108.

31. Zhang, J.; Dai, L., Nitrogen, Phosphorus, and Fluorine Tri-doped Graphene as a Multifunctional Catalyst for Self-Powered Electrochemical Water Splitting. *Angew. Chem. Int. Ed.* **2016**, *55*, 13296-13300.

32. Xu, H.; Zhao, L.; Liu, X.; Li, D.; Xia, Q.; Cao, X.; Wang, J.; Zhang, W.; Wang, H.; Zhang, J., CoMoP<sub>2</sub> nanoparticles anchored on N, P doped carbon nanosheets for high-performance lithium-oxygen batteries. *Flatchem* **2021**, *25*.

33. Kresse, G.; Furthmüller, J., Efficiency of ab-initio total energy calculations for metals and semiconductors using a plane-wave basis set. *Comput. Mater. Sci.* **1996**, *6*, 15-50.

34. Blöchl, P. E., Projector augmented-wave method. *Phys. Rev. B* **1994**, *50*, 17953-17979.

35. Choi, E. Y.; Kim, D. E.; Lee, S. Y.; Kim, C. K., Electrocatalytic activity of nitrogen-doped holey carbon nanotubes in oxygen reduction and evolution reactions and their

- application in rechargeable zinc -air batteries. *Carbon* **2020**, *166*, 245-255.
36. Kong, F.; Qiao, Y.; Zhang, C.; Fan, X.; Zhao, Q.; Kong, A.; Shan, Y., Oriented Synthesis of Pyridinic-N Dopant within the Highly Efficient Multifunction Carbon-Based Materials for Oxygen Transformation and Energy Storage. *ACS Sustainable Chem. Eng.* **2020**, *8*, 10431-10443.
37. Wang, J.; Ciucci, F., In-situ synthesis of bimetallic phosphide with carbon tubes as an active electrocatalyst for oxygen evolution reaction. *Appl. Catal. B-Environ.*, **2019**, *254*, 292-299,
38. Zheng, Y.; Xua, X. X.; Chen, J.; Wang, Q., Surface O<sup>2-</sup> regulation on POM electrocatalyst to achieve accurate 2e/4e-ORR control for H<sub>2</sub>O<sub>2</sub> production and Zn-air battery assemble. *Appl. Catal. B-Environ.*, **2021**, *285*, 119788.
- 39.** Zhang, X. R.; Wang, Y. Q.; Wang, K.; Huang, Y. L.; Lyu, D. D.; Tian, Z. Q.; Shen, P. K.; Jiang, S. P., Active sites engineering via tuning configuration between graphitic-N and thiophenic-S dopants in one-step synthesized graphene nanosheets for efficient water-cycled electrocatalysis. *Chem. Eng. J.* **2021**, *416*, 129096.
40. S. Yao, D. Lyu, M. Wei, B. Chu, Y. Huang, C. Pan, X. Zhang, Z. Q. Tian\*, P. K. Shen, N, S, P co-doped graphene-like carbon nanosheets via in situ engineering strategy of carbon pz-orbitals for highly efficient oxygen redox reaction, *FlatChem* **2021**, *27*, 100250.
41. Wagh, N. K.; Shinde, S. S.; Lee, C.H.;Jung, J.Y.; Kim, D. H.; Lee, J. H., Densely colonized isolated Cu-N single sites for efficient bifunctional electrocatalysts and rechargeable advanced Zn-air batteries. *Appl. Catal. B-Environ.*, **2020**, *268*, 118746.

42. Lei, W.; Deng, Y.-P.; Li, G.; Cano, Z. P.; Wang, X.; Luo, D.; Liu, Y.; Wang, D.; Chen, Z., Two-Dimensional Phosphorus-Doped Graphene nanosheets with Tunable Porosity for Oxygen Reactions in Zinc-Air Batteries. *ACS Catal.* **2018**, *8*, 2464-2472.
43. Zhang, J.; Zhang, T.; Ma, J.; Wang, Z.; Liu, J.; Gong, X., ORR and OER of Co-N codoped carbon-based electrocatalysts enhanced by boundary layer oxygen molecules transfer. *Carbon* **2021**, *172*, 556-568.
44. Tang, C.; Zhang, Q. Nanocarbon for Oxygen Reduction Electrocatalysis: Dopants, Edges, and Defects. *Adv. Mater.* **2017**, *29*, 1604103.
45. Jia, Y.; Jiang, K.; Wang, H.; Yao, X. The Role of Defect Sites in Nanomaterials for Electrocatalytic Energy Conversion. *Chem.* **2019**, *5*, 1371-1397.
46. Jia, Y.; Zhang, L.; Zhuang, L.; Liu, H.; Yan, X.; Wang, X.; Liu, J.; Wang, J.; Zheng, Y.; Xiao, Z.; Taran, E.; Chen, J.; Yang, D.; Zhu, Z.; Wang, S.; Dai, L.; Yao, X. Identification of active sites for acidic oxygen reduction on carbon catalysts with and without nitrogen doping. *Nat. Catal.* **2019**, *2*, 688-695.
47. Yan, X.; Jia, Y.; Yao, X. Defects on Carbons for Electrocatalytic Oxygen Reduction. *Chem. Soc. Rev.* **2018**, *47*, 7628-7658.

*Every reasonable effort has been made to acknowledge the owners of copyright material. I would be pleased to hear from any copyright owner who has been omitted or incorrectly acknowledged.*



## **Chapter 8: Boosting electrocatalytic activity for oxygen reduction reaction of single atom catalysts in full pH range through doped N types engineering**

### **Abstract**

Single atomic catalysts (SACs) hold a great potential to be efficient non-precious group metal (NPGM) electrocatalysts for oxygen reduction reaction (ORR), one of the most important reactions in electrochemical energy conversion and storage technologies. However, the coordination environment of SACs embedded in heteroatoms doped carbon materials plays a crucial role in determining their electrocatalytic performance for ORR. Nitrogen (N) is the most influential heteroatom in doped carbon and, to date, the enhancing mechanism of the specific N species i.e., pyridinic N ( $N_P$ ), graphitic N ( $N_G$ ), and pyrrolic N ( $N_{PY}$ ), on the catalytic activity of SACs for ORR is still not clear due to the difficulties in the control of the types of doped N species on carbon matrix. Herein, new single cobalt atoms embedded in N-doped carbon, Co-N/C, materials through the engineering control of N species by using a precursor modulation strategy are successfully synthesized. The best performed Co-N/C is obtained on the Co-N<sub>4</sub> moieties coordinated with  $N_G$ , Co-N/C+ $N_G$ , displaying superior activity for ORR with the half-wave potential of 0.815, 0.915, 0.73 V *vs.* RHE in alkaline, acidic, and neutral media, respectively, placing it one of the best NPGM catalysts for ORR in full pH range. The Co-N/C catalysts show the order of activity as a function of coordinated N species: Co-N/C+ $N_G$  > Co-N/C+ $N_P$  > Co-N/C+ $N_{PY}$ . The results also demonstrate the superior

activity and stability of Co-N/C+N<sub>G</sub> oxygen electrodes in zinc-air batteries and proton exchange membrane fuel cells as compared to the state-of-the-art Pt/C based electrocatalysts. Density functional theory calculation indicates that coordinated N species in particular N<sub>G</sub> functions as electron donors to the Co-N<sub>4</sub> active sites, leading to the downshift of *d*-band center of Co-N<sub>4</sub> active center and weakening the binding energies of the ORR intermediates on Co-N<sub>4</sub> sites. This significantly promotes catalytic kinetics and thermodynamics for ORR. This work presents a new insight and effective strategy for engineering the desired coordination environment and tuning the geometric and electronic structures of catalytic sites in SACs for electrochemical energy conversions and storage applications.

***\*Reprinted (adapted) with permission from Xiaoran Zhang, Xiaomin Xu, Kun Wang, Yilin Huang, Zhi Qun Tian, Pei Kang Shen, San Ping Jiang, Zongping Shao. Boosting electrocatalytic activity of single atom catalysts supported on nitrogen-doped carbon through N coordination environment engineering. *Small****

## **8.1 Introduction**

Electrochemical energy conversion and storage devices, such as fuel cells and metal-air batteries, are essential technologies towards energy transition from fossil fuels to renewable energies, like solar and wind power, because they can effectively tackle the problems related to the intermittent nature of such energy resources [1]. Among the electrode reactions in the electrochemical energy conversion and storage devices, oxygen reduction reaction (ORR) is the most critical due to its sluggish reaction kinetics and high activation energies [2-3]. As core parts of these electrochemical energy

devices, electrocatalysts largely determine their efficiency and cost, consequently their competitiveness with state-of-art energy technologies. Typically precious metals such as Pt, Ru and Ir electrocatalysts are employed, for example, Pt/C for ORR and IrO and RuO<sub>x</sub> for OER[4-6].

Although high activity can be achieved on precious metal electrocatalysts, the formidable cost of precious metal catalysts greatly inhibit their large-scale applications. Thus, the development of cost-effective, highly active and durable electrocatalysts is crucial towards the effective energy transition. In recent years, tremendous efforts and great progresses have been made on the development of transition metal based nitrogen doped carbon materials (M-N/C, M= Fe, Ni and Co) as promising non-precious group metal (NPGM) electrocatalysts for ORR due to their high activity, low cost and abundant reserves[7]. Among various types of M-N/C catalysts, single atom catalysts (SACs) materials have received particular attention due to their fully exposed active sites and tunable electronic configuration [8]. Up to now, a wide range of SACs catalysts with transition metals such as Fe, Co, Ni, *etc.* have been reported as potential electrocatalysts for ORR[9]. Among them, cobalt-based SACs have attracted significant attention due to their comparable performance to Fe-based catalysts but relatively low risk of Fenton reactions induced poor stability for polymer electrolyte membrane fuel cells (PEMFCs). Both experimental and theoretical efforts have also been made in exploring the specific active sites and catalytic mechanism of Co-based SACs[10]. However, Co-based SACs suffer from insufficient catalytic activity for ORR, especially in acidic media [11].

The electrocatalytic activity of SACs supported with carbonaceous materials for ORR is critically affected by the chemical and electronic environment between the single metal atom (M) and the surrounding coordinated atoms (e.g., carbon, nitrogen, and oxygen) from the support matrix[12]. The catalytic activity of the catalyst can be optimized through tuning the electronic properties of single metal atoms via the chemical hybridization between single metal atoms and vicinal atoms in the supported carbon materials. In fact, in the case of Co-based SACs supported on nitrogen doped carbon, Co-N<sub>4</sub> clusters are shown to be active for ORR[13]. However, the catalytic activities of Co-based SACs are still much lower than that of their precious metal catalyst counterparts for ORR, especially in acid media. Therefore, tremendous efforts have been made on enhancing the activity of Co-N<sub>4</sub> clusters coordinated with other heteroatoms dopants, such as, sulfur (S)[14], phosphorus (P)[15] and boron (B)[16]. Despite a great progress has been made on enhancing catalytic performance for ORR via exploring the synergistic effect between Co-N<sub>4</sub> and heteroatoms dopants, the important role of doped nitrogen seems to have not been fully explored.

Nitrogen (N) is the most important heteroatom dopant in enhancing and manipulating the carbon based electrocatalysts [17]. N not only acts as the central element of the M-N<sub>4</sub> center, but also as the host dopant element with high content widely distributed on the carbon matrix around the M-N<sub>4</sub>. It is also well known that doped N species exist in different forms, including pyridinic N (N<sub>P</sub>), graphitic N (N<sub>G</sub>), pyrrolic N (N<sub>PY</sub>) and oxidized N (N<sub>O</sub>). The presence of various N species would have significant effect on the chemical and electronic surrounding environment of M-N<sub>4</sub>

clusters [18]. However, there are very few studies focusing on the effect of coordination environment induced by various N species on the catalytic performance for ORR. The reason is due to the fact that precisely control of doped N types on carbon matrix is very difficult to achieve due to complicated pyrolysis process. Therefore, exploring the correlation between M-N<sub>4</sub> center and surrounding N environment atoms with certain species for enhancing catalytic activity for ORR is highly desirable. The challenge is to precisely tuning synergetic effect between M-N<sub>4</sub> center and N species in carbon matrix to enhance the catalytic performance for ORR.

On the other hand, the electrocatalysts may experience very different reaction conditions in different electrochemical energy conversion/storage processes. For example, in PEMFCs, the electrocatalysts are under acidic working conditions, while in metal-air batteries, the electrolyte is a strong alkaline solution. Most of reported NPGM electrocatalysts can only perform well in alkaline electrolyte, and the activity and the stability tend to decline sharply in neutral and acidic medium upon long-term running. It is thus necessary and highly desirable that the ideal electrocatalysts should be applicable in a wide range of pH values. Accordingly, to maximize the electrocatalytic activity and improve durability in wide pH condition, tremendous efforts have been made on developing highly efficient catalysts for wide PH condition, to date, only a few reported NPGM electrocatalysts can perform well in alkaline, acid and neutral electrolytes. For instance, Zhu et al. reported a Fe-N-C catalysts exhibits excellent performance for ORR in alkaline and neutral electrolytes, but there is a big gap of its performance for ORR with Pt/C in acid media [19]. Besides, for Co-based

NPGM, Yang et al. reported a kind of Co-N/C hollow-sphere electrocatalyst which could perform in wide PH condition, but, all catalytic performance in alkaline, acid and neutral electrolytes are far below from commercial Pt/C [20]. Therefore, it is highly desirable to take the step toward successful exploration of NPGM electrocatalyst for ORR in pH-universal electrolyte for paving the way to commercial development of fuel cell systems.

Here, we report the successful synthesis of a series of N-doped carbon matrix supported Co SACs coordinated with specific N species (i.e., N<sub>P</sub>, N<sub>G</sub>, N<sub>PY</sub>) by applying precursor modulation strategy based on our previous reports [21-23]. The synthesized Co-N/C with specific N species provides an ideal platform for the investigation of N coordination environment on the electrocatalytic activity of Co SACs for ORR. The results indicate that the Co SACs with coordination of N<sub>G</sub> display a much better ORR performance as compared with the coordination of other N types, achieving one of the best NPGM electrocatalysts with comparable or better performance to the state-of-the-art Pt/C electrocatalyst in a full pH range. Density functional theory (DFT) calculations reveal that the N<sub>G</sub> located at vicinities, in particular meta-position of Co-N<sub>4</sub> site effectively donates electrons to the Co core of the Co-N<sub>4</sub> cluster, downshifts the *d*-band center of Co atoms, weakens the binding energies of the ORR intermediates (O\* and OOH\*) on Co-N<sub>4</sub> sites and thus optimizes the free energies of absorbed intermediates, leading to a significantly enhanced catalytic activity for ORR.

## **8.2 Experimental**

### *8.2.1 Synthesis of Co-based SACs nanospheres.*

2,5-dihydro-1h-pyrrole (DDP) (five membered ring with one N atom), 2,4-diaminopyrimidine (DPM) (six membered ring with two N atoms) and melamine (MM) (six membered ring with three N atoms) were selected as N-containing precursor platforms via Schiff base condensation reaction with 2, 6-diacetylpyridine (DPD) as another reactant. These N-containing precursors were homogeneously mixed with absolute ethanol as solvent, Oxalic acid was used as catalyst under magnetic stirring for 12 h, then followed by adding  $\text{CoCl}_2$  as metal source to obtain the solid precipitate. After filtration and drying treatment in a vacuum drying oven at  $80\text{ }^\circ\text{C}$  for 8 h, the as-obtained mixture was conducted to heat treatments with pyrolysis procedure of  $950\text{ }^\circ\text{C}$  for 1 h with a ramping rate of  $5\text{ }^\circ\text{C min}^{-1}$  under  $\text{N}_2$ , cool naturally to room temperature. The as-synthesized products were labeled as Co-N/C+N<sub>PY</sub> prepared from DDP and DPD as precursors, Co-N/C+N<sub>G</sub> prepared from DPM and DPD as precursors, Co-N/C+N<sub>P</sub> prepared from MM and DPD as precursors, Co-N/C+N<sub>P</sub>+N<sub>G</sub> prepared from DPM, MM and DPD as precursors. The mole ratios of these N-containing precursors are 1:1. For the purpose of comparison, samples prepared with the same synthesis process but without addition of  $\text{CoCl}_2$  were obtained and denoted as Co-N/C+N<sub>PY</sub>, Co-N/C+N<sub>P</sub>, Co-N/C+N<sub>G</sub>, Co-N/C+N<sub>P</sub>+N<sub>G</sub>, respectively.

**Characterization:** The morphologies of N/C and Co-N/C carbon based materials were characterized by Field Emission Scanning Electron Microscopy (FESEM) using a Hitach SU8220 microscope and Transmission Electron Microscopy (TEM) using Titan ETEM G2 80-300 at 300 kV. Their X-ray diffraction patterns (XRD) were obtained on a Smart Lab diffractometer using a  $\text{Cu K}\alpha$  ( $\lambda=1.5405\text{ \AA}$ ) radiation source

(Rigaku Co.). Raman spectra were measured on a Lab Ram HR Evolution Raman spectrometer with 532 nm. Brunauer-Emmett-Teller (BET) surface area and pore size distribution of samples was determined using a Micromeritics instrument (CORP ASAP 2460). The X-ray photoelectron spectroscopy (XPS) were carried out on an ESCALAB 250 XPS system with a monochromatized Al Ka X-ray source and a He discharge lamp (He I:  $h\nu$  21.22 eV) respectively.

### 8.3 Results and Discussion

#### 8.3.1 Microstructure and phase properties

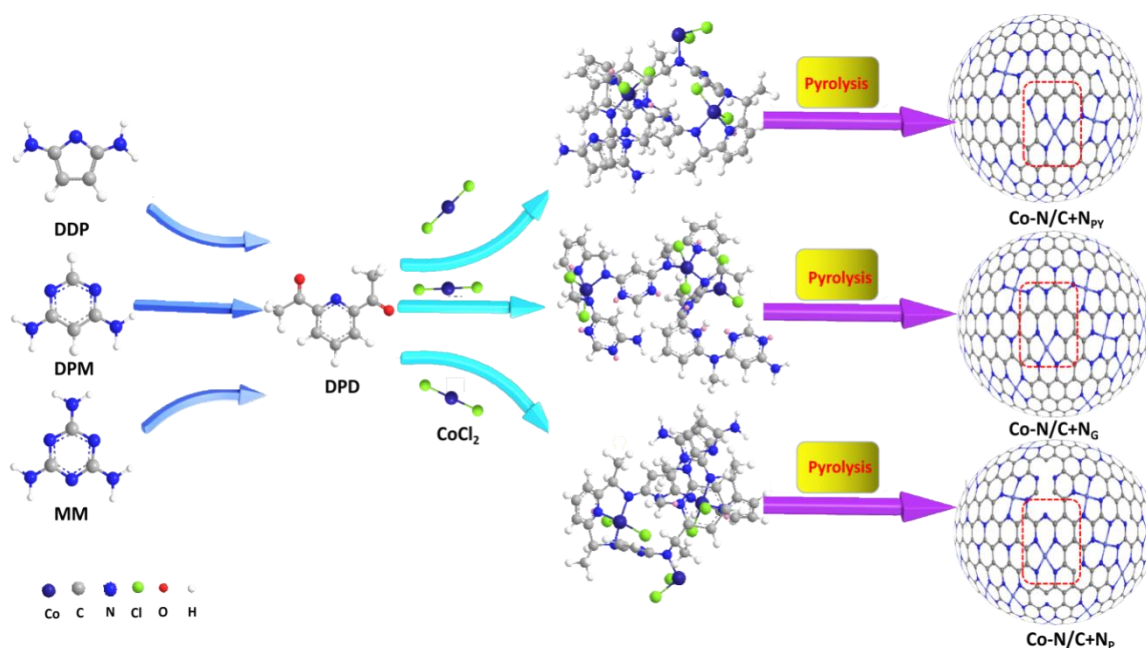


**Figure 8-1.** Illustration of the synthesis process of Co-N/C+N<sub>G</sub>, Co-N/C+N<sub>P</sub>, and Co-N/C+N<sub>PY</sub>.

Figure 8-1a illustrates the synthesis process of the Co SACs supported on carbon matrix with engineering control of doped N types. The types of doped N species were manipulated by N-containing precursor modulation, using DDP (2, 5-dihydro-1h-pyrrole with five membered ring with one N atom) for modulation of N<sub>PY</sub>, DPM (2, 4-diaminopyrimidine with six membered ring with two N atoms) for modulation of N<sub>G</sub>



and MM (melamine with six membered ring with three N atoms) for modulation of  $N_P$  as N-containing precursor platforms via Schiff base condensation reaction with DPD (2, 6-diacetylpyridine) as support precursor. These N-containing precursors were homogeneously mixed with absolute ethanol as solvent and oxalic acid as catalyst under magnetic stirring for 12 h, followed by adding  $CoCl_2$  as metal source, forming the solid precipitate. After filtration and drying treatment in a vacuum oven at 80 °C for 8 h, the as-obtained precipitate was heat-treated at 950 °C for 1 h with a ramping rate of 5 °C  $min^{-1}$  under  $N_2$ , followed by cooling naturally to room temperature. The materials after the pyrolysis treatment were denoted as Co-N/C+ $N_{PY}$  prepared from DDP and DPD precursors, Co-N/C+ $N_G$  prepared from DPM and DPD precursors, and Co-N/C+ $N_P$  prepared from MM and DPD precursors. For the purpose of comparison, a mixture of DPM, MM and DPD precursors was used and the product was denoted as Co-N/C+ $N_P+N_G$ . The mole ratios of these N-containing precursors were 1:1. Samples prepared with the same synthesis process but without addition of  $CoCl_2$  metallic precursor were also synthesized and denoted as N/C+ $N_{PY}$ , N/C+ $N_P$ , N/C+ $N_G$ , N/C+ $N_P+N_G$ , respectively.

The microstructure and microscopic chemical compositions of these Co, N co-doped samples were characterized by transmission electron microscopic (TEM) and electron energy-loss spectroscopy (EELS) and the results of selected Co-N/C+ $N_G$  and Co-N/C+ $N_P$  catalysts are shown in Figure 8-2. The Co-N/C based samples display fluffy and porous microstructure. The uniformly dispersed bright dots as shown in Fig. 2b and d are most likely the deposited Co single atoms on carbon matrix, indicating the

formation of single metallic Co atoms [24]. There are no obvious and observable large particles. HAADF-STEM images coupled with EELS provided more direct evidence of the uniform dispersion of Co atoms in the Co-N/C+N<sub>G</sub> and Co-N/C+N<sub>P</sub> catalyst [25]. Line scans conducted on selected spots in Co-N/C+N<sub>G</sub> and Co-N/C+N<sub>P</sub> clearly detected signals of Co and N (the signals of C were too strong and thus not shown in the figure) (Figure 8-2e and f), suggesting the coexistence of Co and N elements in the carbon matrix support. On the other hand, it is noted that the distance between the overlapped Co, N signal and their surrounding N signal in the samples are different, which may be derived from the change of surrounding C-N bond due to the different N species doped in carbon matrix. This implies that the coordination environments of Co-N center and neighboring N are different in Co-N/C+N<sub>G</sub> and Co-N/C+N<sub>P</sub>. This observation was confirmed in different areas throughout the catalyst. From the HAADF-STEM images of Co-N/C+N<sub>PY</sub> and Co-N/C+N<sub>P</sub>+N<sub>G</sub>, it is found that there are uniform dispersion of Co atoms in the Co-N/C+N<sub>PY</sub> and Co-N/C+N<sub>P</sub>+N<sub>G</sub> samples.

The uniform dispersion of C, N, O and Co elements over the carbon matrix was further supported by the elemental mapping of the samples as shown in Figure 8-2g and h. similar microstructure was also observed on other samples. The results indicate that the Co-N/C samples derived from different polymer precursors have similar nanosphere morphology with small differences in the size of nanospheres. On the other hand, it was observed that the samples before heat treatment also show nanosphere morphology, probably caused by crosslinking of molecular chains during the polymerization process. X-ray diffraction (XRD) and Raman spectra were conducted to examine the crystal

structure of the catalysts.

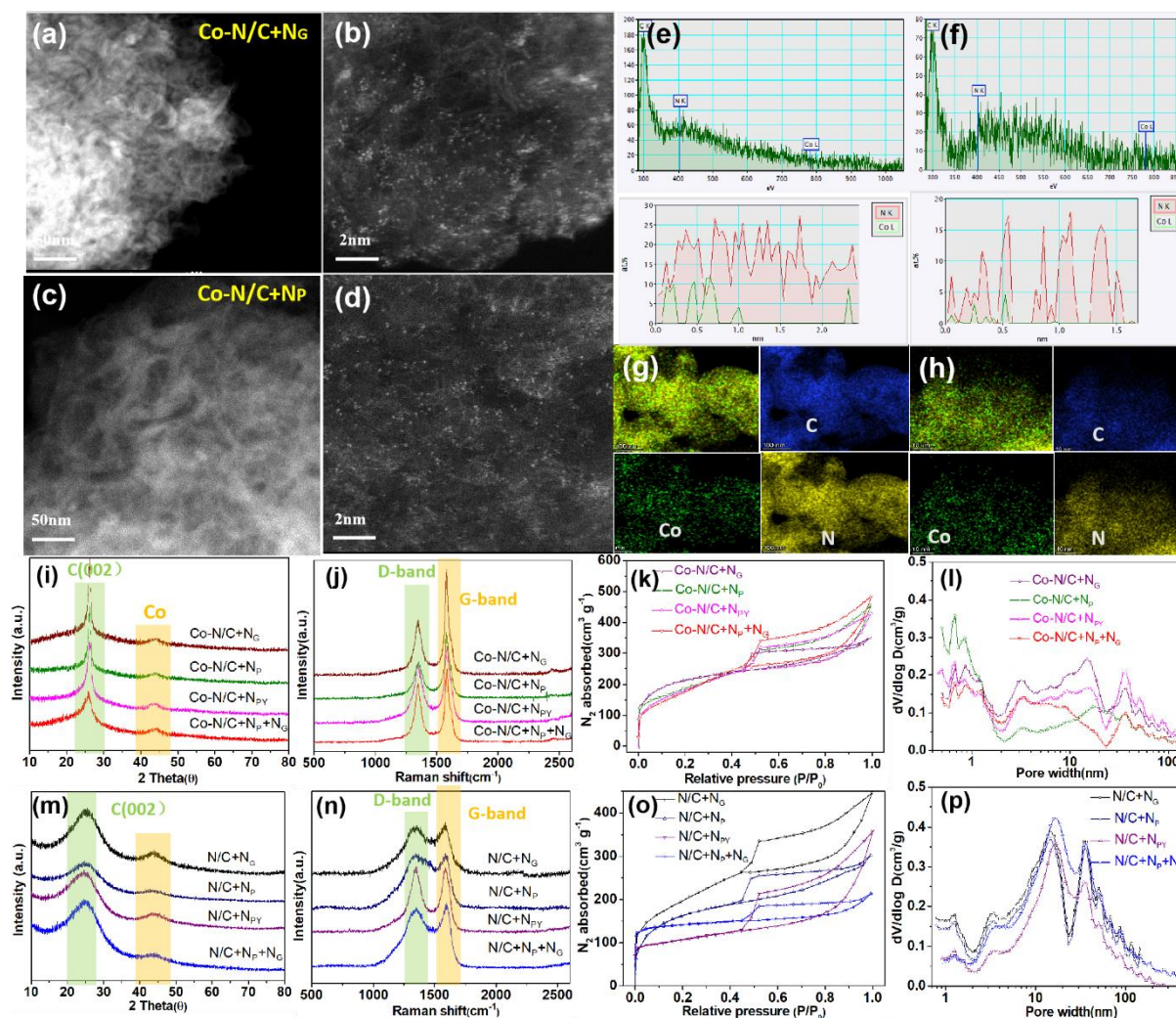


**Figure 8-2.** STEM images (a-d), element analysis element composition in line spectrum and the EELS (e, f) element mapping images (g, h) for Co-N/C+N<sub>G</sub> and Co-N/C+N<sub>P</sub>, XRD (i), Raman spectra (j), nitrogen adsorption-desorption isotherms (k) and pore size distribution (l) for Co-N/C and XRD (m), Raman spectra (n), nitrogen adsorption-desorption isotherms (o) and pore size distribution (p) for N/C.

As shown in Fig. 2i and m, the two broad peaks of graphite (PDF #75-1621) located at 26.3° and 43.5° in N/C+N<sub>G</sub>, N/C+N<sub>P</sub>, N/C+N<sub>PY</sub>, N/C+N<sub>P</sub>+N<sub>G</sub> suggest that the carbon structure in metal-free samples is amorphous [26]. Different to Co-free N/C samples, Co-N/C samples exhibit the sharp and strong peaks located at around 26.3° and 43.5° associated with (002) planes of graphitic carbon (PDF#41-1487), indicating that addition of Co metallic precursor during the pyrolysis leads to formation of highly

graphitized carbon structure [27]. Nevertheless, no diffraction peaks for metallic Co or Co compounds were observed, indicating no formation or agglomeration of cobalt metal particles. This is consistent with TEM and element mappings as discussed above. Raman spectroscopy analysis showed the presence of two typical peaks of D and G located at about  $1350\text{ cm}^{-1}$  and  $1580\text{ cm}^{-1}$ , respectively (Figure 8-2j and n). The intensity ratio of D and G bands ( $I_D/I_G$ ) is an important parameter for the evaluation of the doping and defect degree of carbon structure [28, 29]. The calculated values of  $I_D/I_G$  in N/C samples are close to 1, but for Co-N/C samples, the  $I_D/I_G$  values are in the range of 0.35~0.71, far below to 1. This again indicates that with the addition of Co, the degree of graphitization of carbon structure increases significantly, consistent with that reported in the literature [30].

The specific surface area and pore size distribution of these samples were obtained using nitrogen adsorption desorption isotherm, as shown in Figure 8-2k, o and l, P. The specific surface areas are in the range of 659 to  $740\text{ m}^2\text{g}^{-1}$  for Co-N/C samples, higher than 405 to  $556\text{ m}^2\text{g}^{-1}$  obtained on metal-free N/C. High specific surface areas are benefit for exposing active sites and hierarchical pore structure is good for fast mass transfer process for ORR [31]. Nevertheless, both Co-N/C and N/C samples display similar hierarchical pore structure and pore size distribution with major part of mesopores concentrated in 20-50 nm and small portion of micropores of 2-10nm.

### 8.3.2. *Types of N species and coordination environment of catalysts*

The key contribution of this study is to control the types of n species by precursor modulation approach and this was verified by the X-ray photoelectron spectroscopy

(XPS) studies. Figure 8-3 shows the XPS results of Co-N/C+N<sub>G</sub>, Co-N/C+N<sub>P</sub>, Co-N/C+N<sub>PY</sub>, Co-N/C+N<sub>P</sub>+N<sub>G</sub> and for N/C+N<sub>G</sub>, N/C+N<sub>P</sub>, N/C+N<sub>PY</sub> and N/C+N<sub>P</sub>+N<sub>G</sub>. The XPS survey spectra of Co-N/C samples clearly show the presence of Co, N, C and O elements (Figure 8-3d), indicating the successful co-doping of Co and N in carbon matrix. The as-synthesized Co-N/C samples display the similar overall N and Co content with 4.14 - 4.68 at % for N and ~0.2 at% for Co, despite the fact that they were synthesized with different N-containing precursors. The high resolution of C1s spectra of the samples can be deconvoluted into four main peaks centered at 285.9 eV, 286.42 eV, 288.4 eV and 291 eV (Figure 8-3b), which are assignable to C-C, C-N, -COO and  $\pi$ - $\pi$ , respectively [32]. In addition, the weak peak of Co<sub>2p</sub> manifests the low content of Co dopant (at about 0.2 at%) in the samples (Figure 8-2c).

However, the characteristics of the N1s spectra in the samples is very different (see Fig.3d), implying the significant differences in the type and contents of the doped N species. The main peak of N1s in Co-N/C+N<sub>G</sub> is located at about 401.12 eV, which can be assigned to graphitic N. This indicates that the main type of N species in Co-N/C+N<sub>G</sub> synthesized from DPM precursor is graphitic N, N<sub>G</sub>. By contrast, the main peak of N1s in Co-N/C+N<sub>P</sub> and Co-N/C+N<sub>PY</sub> is located at 398.4 eV and 399.8 eV, corresponding to pyridinic N, N<sub>P</sub> and pyrrolic N, N<sub>PY</sub>, respectively. In the case of Co-N/C+N<sub>P</sub>+N<sub>G</sub> derived from the mixed precursors of DPM and MM, Co-N/C+N<sub>P</sub>+N<sub>G</sub> sample shows two main peaks located at 401 eV and 398.4 eV, characteristic peaks of N<sub>G</sub> and N<sub>P</sub>. Similar characteristics of the XPS spectra were also observed on Co-free N/C samples. The XPS results show evidently that the precursor modulation is very effective to

control the types of doped N species in the cobalt single atoms embedded carbon catalysts, consistent with previous results [33].

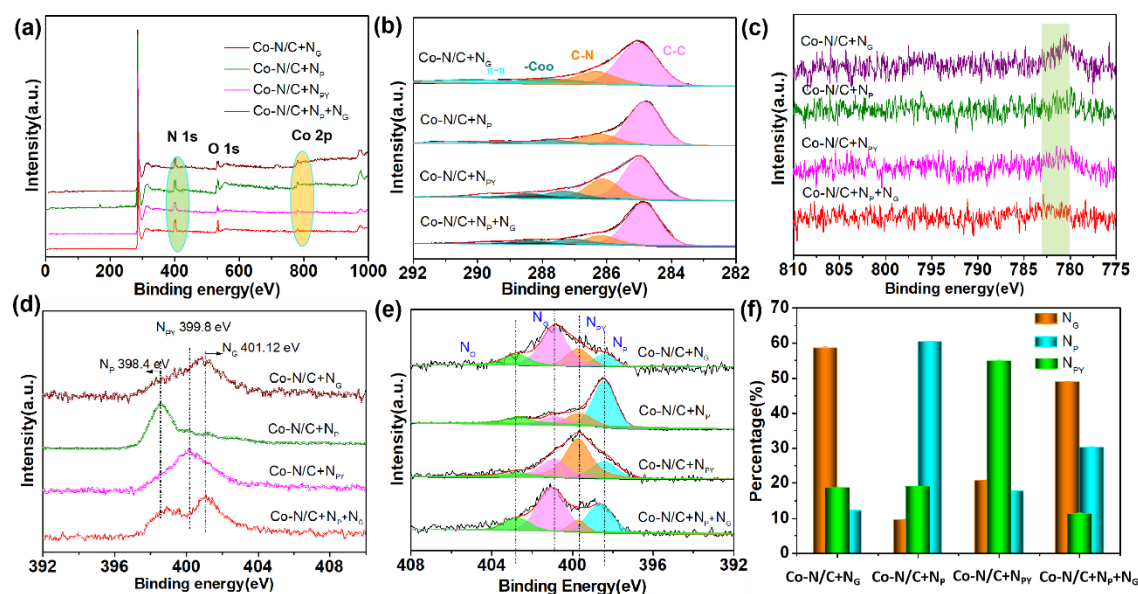


**Figure 8-3.** The XPS survey scans (a), high-resolution XPS spectra for C 1s (b), Co2p (c), the main peak of N1s (d) and high-resolution XPS spectra of N1s (e), the bar charts(f) of percentage of N species N in Co-N/C+N<sub>G</sub>, Co-N/C+N<sub>P</sub>, Co-N/C+N<sub>PY</sub>, Co-N/C+N<sub>P</sub>+N<sub>G</sub>.

The contents of specific N species of Co-N/C and N/C samples was obtained by deconvolution of the high resolution N1s spectra. The N1s spectra of the samples were fitted into four peaks located at 398.25, 399.79, 401.12 and 403.5 eV, corresponding to N<sub>P</sub>, N<sub>G</sub>, N<sub>PY</sub> and oxidized N (N<sub>O</sub>), respectively (Fig. 3e).<sup>34</sup> Although these samples possess the similar overall N content, the distribution of various N species is very much different, as shown in Fig. 3f. For Co-N/C+N<sub>G</sub> sample, the N<sub>G</sub> accounts for 58.65 %, followed by 12.41% N<sub>P</sub> and 18.26% N<sub>PY</sub>. By contrast, in the case of Co-N/C+N<sub>P</sub> sample, N<sub>P</sub> content is 60.4 %, followed by 9.57 % N<sub>G</sub> and 19% N<sub>PY</sub>. For Co-N/C+N<sub>PY</sub>, the highest content of N species is N<sub>PY</sub> (54.89 %), followed by 20.26 % N<sub>G</sub> and 17.54% N<sub>P</sub>. In addition, Co-N/C+N<sub>P</sub>+N<sub>G</sub> derived from mixed precursors of DPM and MM shows high content of N<sub>P</sub> (30.28 %) and N<sub>G</sub> (48.9%), followed by relatively low content of

$N_{PY}$  (11.25 %). Similar distribution of types of N species as a function of N-containing precursors also exists in Co-free N/C samples (Fig.S3). Table 1 gives the contents of elements of the catalyst samples studied in this work. The preferential formation of specific N species via the precursor modulation strategy provides an excellent platform for the tuning of the synergistic effect between Co atom and its coordinated N species and fundamental study of the coordination environment on the catalytic activity of Co- $N_4$  active centers.

X-ray absorption spectroscopy (XAS) test was conducted to further examine the specific coordination environment of Co-N center and surrounding N species in selected Co-N/C+ $N_G$  and Co-N/C+ $N_P$  samples and the results are shown in Fig. 4. Fourier transform (FT) profiles of Co K-edge  $k^2$ -weighted extended X-ray absorption fine structure (EXAFS) data identify the coordination environment of Co atoms in Co-N/C+ $N_G$  and Co-N/C+ $N_P$  samples. The XANES data at the Co K-edge of Co-N/C+ $N_G$  and Co-N/C+ $N_P$  clearly indicate that the peak position situates at lower energy than those of Co foil (Fig.4a), indicating that the average valence state of Co in Co-N/C+ $N_G$  and Co-N/C+ $N_P$  is higher than metallic Co (0). Furthermore, the peak position at the Co K-edge of Co-N/C+ $N_G$  is located at 7726.5 eV, slightly different from 7727.1 eV observed on Co-N/C+ $N_P$ , which indicates the different electronic states of Co in these two samples. The difference in the coordination environment in the samples was further analyzed by the Wavelet-transform (WT) EXAFS analysis. WT analysis is a powerful method for separating backscattering atoms, especially for the information of the  $k^2$ -weighted  $w(k)$  signals [35]. As shown in Fig. 4b and 4e, the corresponding Fourier

transforms of the Co-N/C+N<sub>G</sub> and Co-N/C+N<sub>P</sub> samples show different profiles, again indicating the different coordination environments of the Co atoms most likely due to the different types of N species in the samples [36]. The differences in the coordination environment have been verified by the WT contour plots of Co-N/C+N<sub>G</sub> and Co-N/C+N<sub>P</sub> based on Morlet wavelets ( $k \approx 3$ ,  $s \approx 1$ ) with optimum resolution at the first shell. Meanwhile, the maximum  $\text{\AA}$  location can be associated with the Co-N path, and the shift of the WT maximum  $\text{\AA}$  is usually closely linked with surrounding chemical environment [37]. For the Co-N/C+N<sub>G</sub> and Co-N/C+N<sub>P</sub> the maximum well-resolved  $\text{\AA}$  location is  $3.6 \text{\AA}^{-1}$  and  $3.8 \text{\AA}^{-1}$ , respectively. The shift of  $0.2 \text{\AA}^{-1}$  in the WT maximum  $\text{\AA}$  locations in Co-N/C+N<sub>G</sub> and Co-N/C+N<sub>P</sub> provides further evidences that the coordination environment at Co-N center is significantly affected by the type of the surrounding N species, i.e., N<sub>G</sub> and N<sub>P</sub> in this case. Since the locations of the WT maxima are highly predictable, they allow qualitative interpretation of the scattering path origins. The WT maximum is known to be affected by the path length R, Debye-Waller factors  $s_2$ , and energy shift DE and atomic number Z. For an isolated Co-N path ( $R \approx 2 \text{\AA}$ ), the WT maximum at  $3.5 \text{\AA}^{-1}$  in the q-space magnitude showed little dependence on R,  $s_2$  and DE, but it is largely affected by different Z (e.g.,  $3.5 \text{\AA}^{-1}$  for Co-N path,  $4.3 \text{\AA}^{-1}$  for Co-O path, and  $6.8 \text{\AA}^{-1}$  for Co-Co path). A small of  $0.2 \text{\AA}^{-1}$  between the maxima  $\text{\AA}$  for the Co-N/C+N<sub>G</sub> ( $3.6 \text{\AA}^{-1}$ ) and Co-N/C+N<sub>P</sub> ( $3.8 \text{\AA}^{-1}$ ) and the calculated Co-N path ( $3.5 \text{\AA}^{-1}$ ) might arise from the difference on the actual length of the Co-N path in Co-N/C+N<sub>G</sub> and Co-N/C+N<sub>P</sub> affected by coordinated N species [38].



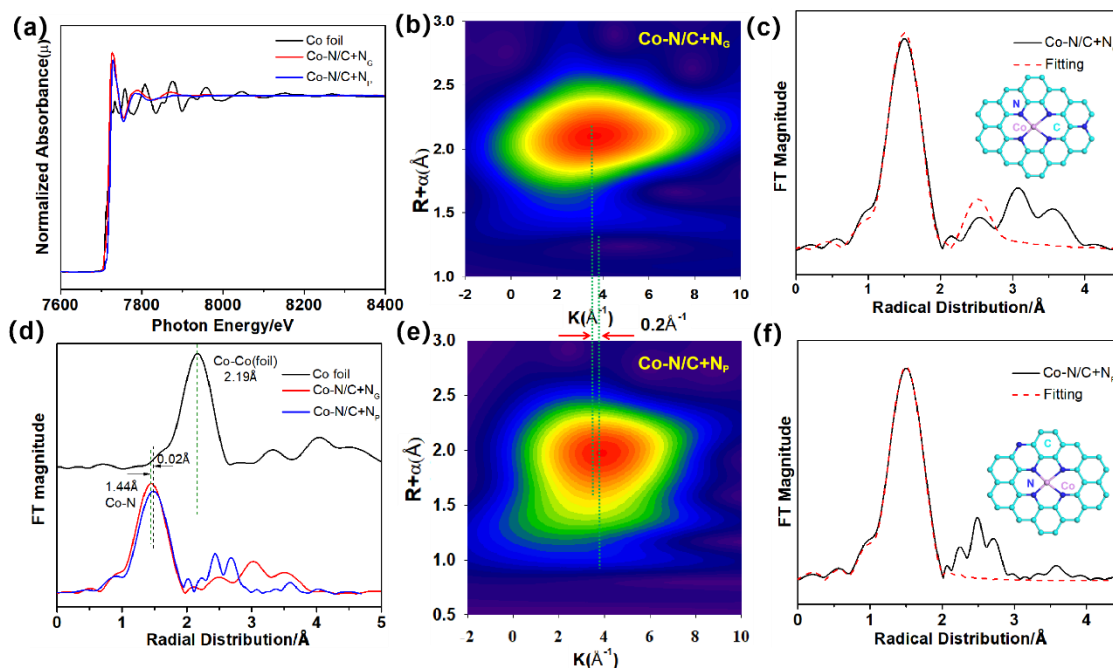


**Figure 8-4.** Normalized Co K-edge XANES spectra of Co foil, Co-N/C+N<sub>G</sub> and Co-N/C+N<sub>P</sub> (a), Wavelet transforms (WT) for EXAFS signals of Co-N/C+N<sub>G</sub> (b), experimental and fitted EXAFS spectra of the Co K-edge in Co-N/C+N<sub>G</sub> (c), FT EXAFS spectra of the Co K-edge in Co foil, Co-N/C+N<sub>G</sub> and Co-N/C+N<sub>P</sub> (d), Wavelet transforms (WT) for EXAFS signals of Co-N/C+N<sub>P</sub> (e), experimental and fitted EXAFS spectra of the Co K-edge in Co-N/C+N<sub>P</sub> (f). The inset shows the fitted structure. Pink, blue and green spheres refer to Co, N and C atoms, respectively.

The validity of the above WT-EXAFS analysis was further confirmed by a least-square curve fitting analysis carried out for the first coordination shell of Co, see Fig. 4d. The main peaks of Co-N/C+N<sub>G</sub> and Co-N/C+N<sub>P</sub> in R space located at about 1.44 Å and 1.46 Å that can be ascribed to the scattering path of dominant Co-N [39]. In the case of cobalt foil, the main peak is located at 2.19 Å, a characteristics of the Co-Co bond. The very weak peak located at 2.19 Å for Co-N/C+N<sub>G</sub> and Co-N/C+N<sub>P</sub> again indicates that Co mainly exists in the form of single atom and not in the form of metallic Co particles in Co-N/C+N<sub>G</sub> and Co-N/C+N<sub>P</sub>. On the other hand, a small shift of 0.02 Å in the main peak in Co-N/C+N<sub>G</sub> as compared to that of Co-N/C+N<sub>P</sub> implies the changes of Co coordination environments in the samples, induced by the dominant surrounding

N species,  $N_G$  for Co-N/C+N<sub>G</sub> and  $N_P$  for Co-N/C+N<sub>P</sub>. The  $k^2$ -weighted  $w(k)$  signals and the corresponding Fourier transforms (Fig. 4d) of the Co-N/C+N<sub>G</sub> and Co-N/C+N<sub>P</sub> samples show quite well fitting with the used model of Co-N<sub>4</sub>+N<sub>G</sub> and Co-N<sub>4</sub>+N<sub>P</sub> (see Fig 4 c, f insert) respectively, suggesting the coordination environments of the Co atoms in Co-N/C+N<sub>G</sub> and Co-N/C+N<sub>P</sub> samples are in agreement with the theoretical data.

Based on the structural characteristics of single Co atoms in the N doped carbon based materials, the tetrahedral geometry (Co-N<sub>4</sub>) structure model was thus adopted to perform the least-squares EXAFS fitting for the Fourier-transformed EXAFS curve of Co-N/C+N<sub>G</sub> and Co-N/C+N<sub>P</sub>, see Fig.4c and f. The fitted coordination number of Co is  $3.8 \pm 0.2$ , which is in a good agreement with the tetrahedral geometry (Co-N<sub>4</sub>). In addition, in combination with XPS results, the structure model of Co-N<sub>4</sub>+N<sub>G</sub> and Co-N<sub>4</sub>+N<sub>P</sub> were adopted to perform the least-squares EXAFS fitting for the EXAFS curve of Co-N/C+N<sub>G</sub> and Co-N/C+N<sub>P</sub> and good fitting was obtained (see Fig. 4c, f). The results indicate that a single Co site of Co-N<sub>4</sub> with four Co-N bonds coordinated with N<sub>G</sub> or N<sub>P</sub> is the dominant structure in Co-N/C+N<sub>G</sub> and Co-N/C+N<sub>P</sub>, respectively

### 8.3.3. Electrochemical activity for ORR

ORR performances of Co-N/C and N/C catalysts were evaluated by linear sweep voltammetry (LSV) using rotating ring disk electrode (RRDE) in 0.5M H<sub>2</sub>SO<sub>4</sub> acid, 0.1M KOH alkaline and 50 mM phosphate buffer (PB) neutral solutions. Without specification, the potential values given in this paper are all referred to RHE. Figure 8-5 shows the electrochemical activity of Co-N/C for ORR in acid, alkaline and neutral solution. The electrocatalytic activity of Co-free N/C samples is given in Fig.S5.

Among the electrocatalysts synthesized in this study, Co-N/C+N<sub>G</sub> exhibits the best

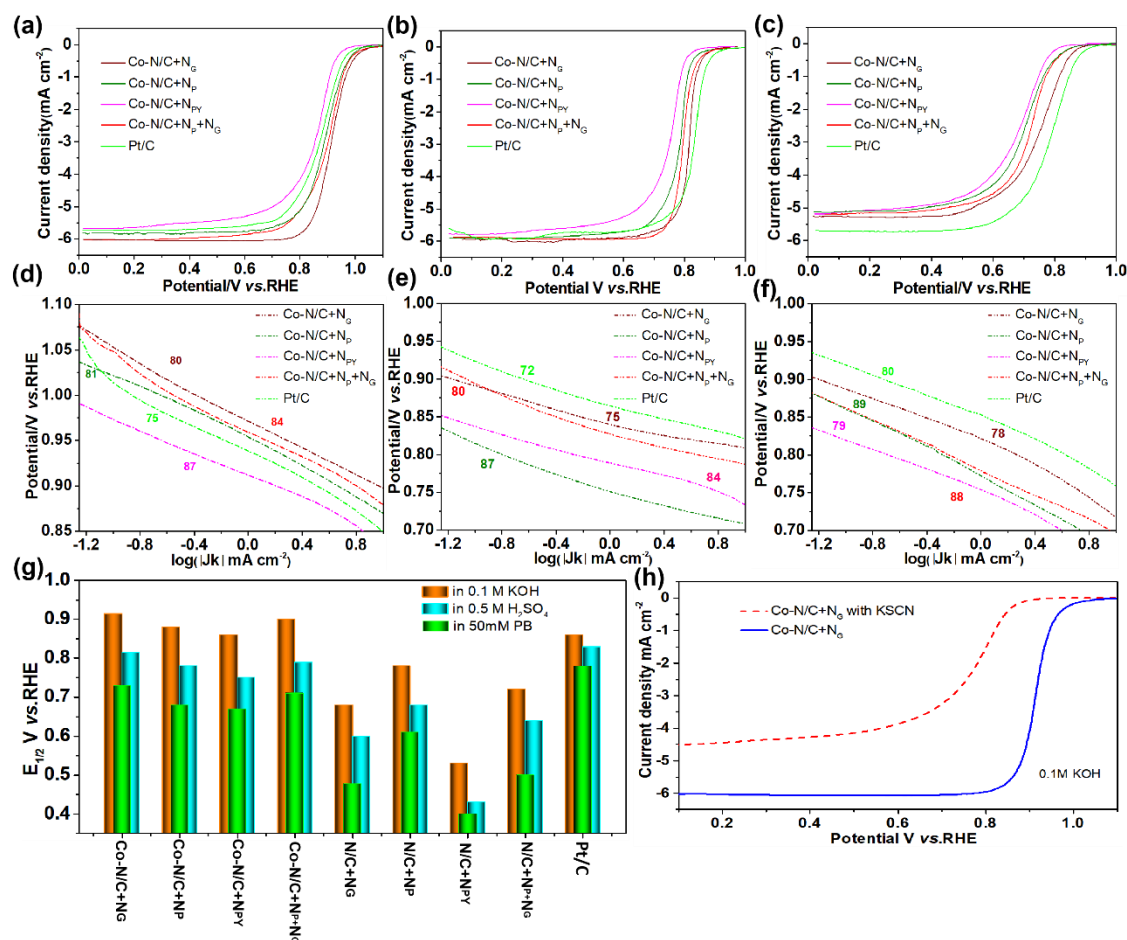


**Figure 8-5.** LSV curves of ORR and corresponding Tafel plots for ORR on Co-N/C and Pt/C in 0.1M KOH (a, d), 0.5M H<sub>2</sub>SO<sub>4</sub> (b, e), 50mM PB solutions (c, f), and the E<sub>1/2</sub> values of ORR on the catalysts measured in 0.1M KOH, 0.5M H<sub>2</sub>SO<sub>4</sub> and 50mM PB solutions are given in (g) and LSV curves of ORR on Co-N/C+N<sub>G</sub> before and after adding 5mM KSCN in 0.1M KOH solution are given in (h). Catalyst loading: 600ug cm<sup>-2</sup>; rotation rate: 1600rpm ; scan rate: 5 mV S<sup>-1</sup>. Numbers in the figure are Tafel slopes in mV/dec.

performance for ORR with the onset potential (E<sub>onset</sub>) and half-wave potential (E<sub>1/2</sub>, which is measured at a current density of 3.0 mA cm<sup>-2</sup> in this study) of 0.96 V and 0.815 V in 0.5M H<sub>2</sub>SO<sub>4</sub>, 1.04 V and 0.915 V in 0.1M KOH and 0.93 V and 0.73 V in 50 mM phosphate buffer (PB) solution, respectively. This is comparable to and better than the state-of-the-art Pt/C electrocatalysts in 0.1M KOH alkaline solution (E<sub>onset</sub>=1.01 V and E<sub>1/2</sub>= 0.86 V), 0.5M H<sub>2</sub>SO<sub>4</sub> acid solution (E<sub>onset</sub>=1.0 V and E<sub>1/2</sub>= 0.83 V) and in 50 mM

PB neutral solution ( $E_{\text{onset}}=0.96$  V and  $E_{1/2}= 0.78$  V). Tafel slopes for ORR on Co-N/C+N<sub>G</sub> is 75, 80 and 78 mV/dec in 0.1M KOH, 0.5M H<sub>2</sub>SO<sub>4</sub> and 50 mM PB solutions, almost identical to 72, 75 and 80 mV/dec obtained for the reaction on Pt/C catalysts in the same solutions (Fig.5d,e and f). The cyclic voltammograms of Co-N/C+N<sub>G</sub> for ORR conducted at the potential range of 0-1.3 V with a scan rate of 50 mV s<sup>-1</sup> in 0.1M KOH, 0.5M H<sub>2</sub>SO<sub>4</sub> and 50 mM PB solutions, it is found that well-defined cathodic ORR peaks potential at 0.81 V, 0.91 V and 0.69 V occurred in O<sub>2</sub> saturated CV curves in acid, alkaline and neutral solutions, respectively, demonstrating its superior catalytic performance for ORR in wide PH range. Furthermore, it is show that average electron-transfer number of ORR on Co-N/C+N<sub>G</sub> is in the range of 3.951 to 3.987 in the alkaline, acid and neutral solutions, very close to the electron-transfer number of 3.972 to 3.994 for ORR on Pt/C electrocatalysts under the identical conditions. The results demonstrate that ORR proceeds with 4-electron transfer process on Co-N/C+N<sub>G</sub> NPGM catalysts, similar to that occurred on Pt/C, demonstrating the highly efficient catalytic performance of Co-N/C+N<sub>G</sub> for ORR in the full pH range. The electrocatalytic activity of Co-N/C catalysts depends strongly on the coordination environment of the type of N species. When the type of coordinated N changes to N<sub>P</sub>, Co-N/C+N<sub>P</sub>, the activity for ORR is reduced, achieving  $E_{\text{onset}}$  and  $E_{1/2}$  of 1.03 V and 0.89 V in 0.1M KOH, 0.91 V and 0.79 V in 0.5M H<sub>2</sub>SO<sub>4</sub> and 0.91 V and 0.71 V in 50 mM PB solutions. On the other hand, Co-N/C+N<sub>P</sub>+N<sub>G</sub> sample displays good activity for ORR with  $E_{\text{onset}}$  and  $E_{1/2}$  of 1.02 V and 0.88 V in 0.1M KOH, 0.94 V and 0.78 V in 0.5M H<sub>2</sub>SO<sub>4</sub> and 0.91 V and 0.68 V in 50 mM PB solutions, which is lower than that of Co-N/C+N<sub>G</sub>, but slightly

higher than that of Co-N/C+N<sub>P</sub>. For Co-N/C+N<sub>PY</sub> with high content of pyrrolic N, electrocatalytic activity for ORR is relatively low with E<sub>on-set</sub> and E<sub>1/2</sub> of 0.99 V and 0.84 V in 0.1M KOH, 0.90 V and 0.75 V in 0.5M H<sub>2</sub>SO<sub>4</sub> and 0.88 V and 0.67 V in 50 mM PB solutions. In acid, alkaline and neutral solutions, the electrocatalytic activity of Co-N/C catalysts follows the order of

$$\text{Co-N/C+N}_G \sim \text{Pt/C} > \text{Co-N/C+N}_P+\text{N}_G > \text{Co-N/C+N}_P > \text{Co-N/C+N}_{PY} \quad (1)$$

Co-N/C catalysts are also stable. Accelerated cycle stability test conducted for Co-N/C+N<sub>G</sub> catalyst showed that the E<sub>1/2</sub> potential decay after 10000 cycles measured between potential range of 0.6 to 1.4 V is very small, 9, 2 and 5 mV in 0.1M KOH, 0.5M H<sub>2</sub>SO<sub>4</sub> and 50 mM PB solutions, respectively. This is lower than reduction of 22, 41, 11 mV of E<sub>1/2</sub> obtained for the reaction on Pt/C electrocatalyst under the same cyclic test conditions. Similar results were also obtained on other Co-N/C samples. The results indicate the excellent stability of Co-N/C with coordinated N species in a full pH range.

On the other hand, this study shows that the metal free N-doped carbon catalysts (N/C) not only exhibits lower catalytic performance for ORR but also show a different order as a function of the types of coordinated N species. Among the N/C catalysts, N/C+N<sub>P</sub> exhibits the best performance for ORR with the E<sub>onset</sub> and E<sub>1/2</sub> of 0.97 V and 0.78 V in 0.1M KOH, 0.84 V and 0.68V in 0.5M H<sub>2</sub>SO<sub>4</sub> and 0.87 V and 0.61 V in 50 mM PB solution, respectively. This is in consistent with previous reports that pyridinic N plays a crucial role on boosting catalytic performance for ORR.<sup>40</sup> Similar to that observed for the reaction on Co-N/C+N<sub>P</sub>+N<sub>G</sub>, the electrocatalytic activity of

$N/C+N_P+N_G$  is lower than that of  $N/C+N_P$ , but higher than that of  $N/C+N_G$ . The performance order of the  $N/C$  catalysts as the function of coordinated N species is

$$N/C+N_P > N/C+N_P+N_G > N/C+N_G > N/C+N_{PY} \quad (2)$$

This is different from that of Co- $N/C$  catalysts. In addition, the Tafel slope of the Co-free  $N/C$  catalysts is in the range of 90 to 115 mV/dec, higher than 78-88 mV/dec obtained on Co- $N/C$  catalysts. This demonstrates that the addition of Co single atoms contributes greatly for enhancing catalytic performance for ORR.

The active role of Co- $N_4$  clusters in catalytic activity for ORR was further verified by catalyst blocking tests using 5mM potassium thiocyanate (KSCN) as a probe to block the Co- $N_4$  centers. KSCN is known to strongly adsorb and poison the electrocatalytic activity of transition metals such as Co, Fe and Ni for ORR [41]. The results indicate that after adding 5 mM or mL KSCN, there is a significant decline on both  $E_{onset}$  and  $E_{1/2}$  values of Co- $N/C+N_G$  from 1.04 V and 0.91 V to 0.91 V and 0.75 V in 0.1M KOH solution, accompanying with sharply decreased limiting current density from 6 mA  $cm^{-2}$  to 4.5 mA  $cm^{-2}$  (see Fig.5h). Similarly, the  $E_{onset}$  and  $E_{1/2}$  for ORR is 0.80 V and 0.61 V in 0.5M  $H_2SO_4$  + 5 mM KSCN and 0.78 V and 0.52 V in 50 mM PB + 5 mM KSCN solution, much lower than that in pristine  $H_2SO_4$  and PB solutions. The substantial reduced activity of Co- $N/C+N_G$  in the KSCN-contained solutions is evidently due to the blocking and poisoning effect of KSCN on the single Co atoms of the Co- $N_4$  clusters, similar to the blocking effect of potassium cyanide on the transition metal impurities on carbon nanotubes [41b]. The results provide a clear evidence that the active center for ORR on Co- $N/C$  is the Co- $N_4$  clusters, which in turn is affected by

the types of the coordinated N species.

This study shows that Co single atom embedded in N-doped carbon materials with controlled  $N_G$  species, Co-N/C+ $N_G$  is one of the best electrocatalysts for ORR in full pH range with high activity and stability. Co-N/C+ $N_G$  shows not only comparable and better activity than Pt/C electrocatalysts, but also significantly better than those reported in the literature.

#### 8.3.4. Application for Zn-Air battery and fuel cells

The Co-N/C catalysts show excellent electrochemical activity and durability, comparable and even better than the state-of-the-art Pt/C electrocatalysts based on the conventional RRDE studies. Thus, it is essential to evaluate the practical application potential of Co-N/C electrocatalysts in electrochemical energy conversion devices. Here the best performed Co-N/C+ $N_G$  materials was evaluated as NPGM air electrode in a Zn-air battery (under alkaline test condition) and as NPGM cathode in a polymer electrolyte membrane fuel cell (under acid test condition). The evaluation results are shown in Fig. 6. The result indicates that the Zn-air battery with Co-N/C+ $N_G$  as cathode electrocatalyst exhibits a peak power density of  $248 \text{ mW cm}^{-2}$  at  $0.31 \text{ mA cm}^{-2}$ , much higher than  $141 \text{ mW cm}^{-2}$  obtained on the Zn-air batter with Pt/C cathode (Fig. 6b). As shown in Figure 8-6c, the specific capacities of the Co-N/C+ $N_G$  based batteries is  $789.3 \text{ mAh g}^{-1}$  at  $10 \text{ mA cm}^{-2}$ , which is higher than  $669.4 \text{ mAh g}^{-1}$  at  $10 \text{ mA cm}^{-2}$  obtained on the battery with Pt/C electrocatalysts. Furthermore, Co-N/C+ $N_G$  catalyst also shows excellent bifunctional electrocatalytic activity for ORR and oxygen evolution reaction (OER) and this is evidenced by the outstanding cycling stability of a rechargeable Zn-

Air batteries with Co-N/C+N<sub>G</sub> oxygen electrode (see Fig. 6d). After 300 cycles, the variation of discharging and charging potential of the Co-N/C+N<sub>G</sub> cell is decreased by 5.94 %, which is significantly smaller than 26.56 % decrease of the cell with the state-of-the-art Pt/C+IrO<sub>2</sub> oxygen electrode. The high discharging voltage, high specific capacity and much better recharge ability of Co-N/C+N<sub>G</sub> demonstrates excellent promising potential of Co-N/C materials as NPGM catalysts in Zn-air batteries. The feasibility of Co-N/C-N<sub>G</sub> catalyst as NPGM cathode was also evaluated in a polymer electrolyte membrane (PEM) fuel cell using 0.2 MPa H<sub>2</sub> and O<sub>2</sub> at 80 °C (Fig.6e). The results show that the PEM cell with Co-N/C+N<sub>G</sub> cathode and Pt/C anode achieved a good performance with maximum output power density of 0.43 W cm<sup>-2</sup>, indicating the promising potential of Co single atoms in N-doped carbon materials with engineering controlled N species as effective NPGM catalysts for fuel cells.

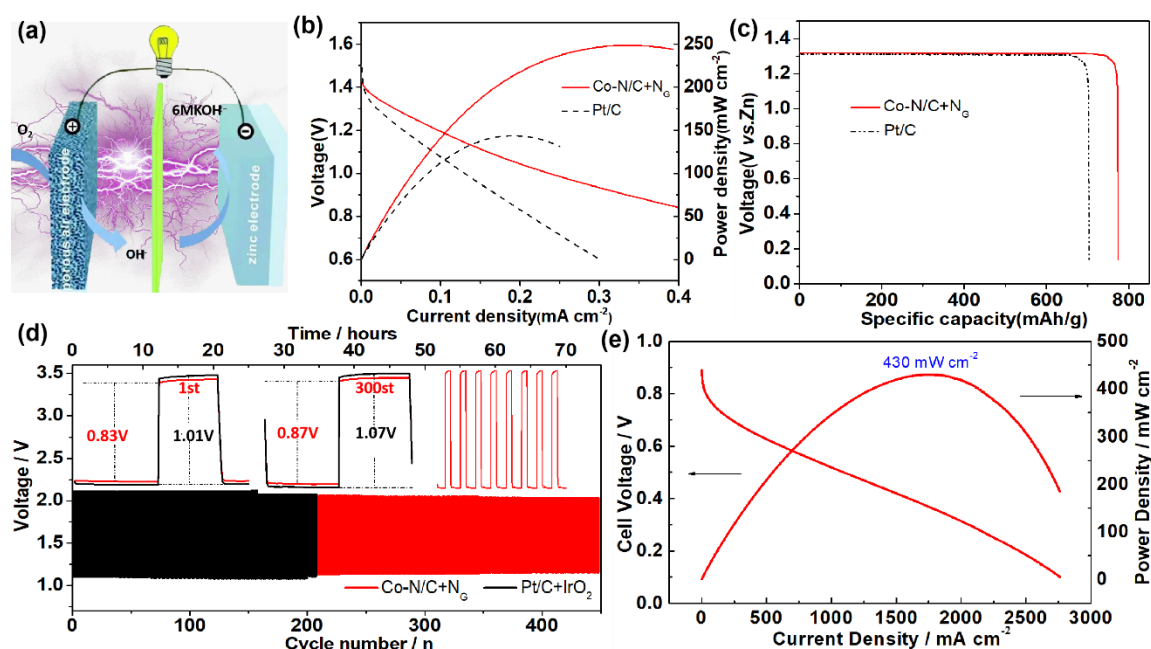


**Figure 8-6.** Illustration of the primary Zn-Air batteries (a); the discharge polarization curves and the corresponding power density plots of Zn-Air batteries with Co-N/C+N<sub>G</sub> and Pt/C air electrodes (b); specific capacities normalized to the mass of the consumed zinc of the Zn-Air batteries at a current density of 50 mAcm<sup>-2</sup> (c); galvanostatic discharge-charge cycling curves

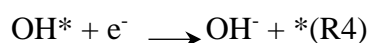
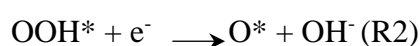


at 5 mA cm<sup>-2</sup> of rechargeable Zn-Air batteries with Co-N/C+N<sub>G</sub> and Pt/C air electrodes (d); and polarization curve and power density of a PEM fuel cell with Co-N/C+N<sub>G</sub> NPGM cathode at 80°C under 0.2 MPa H<sub>2</sub>/O<sub>2</sub>. The cathode Co-N/C+N<sub>G</sub> catalyst loading was 4.0 mg cm<sup>-2</sup> and the anode Pt/C loading was 0.5 mg cm<sup>-2</sup> (e).

### 8.3.5 Computational calculation

The fundamental reason for the significant effect of the N coordination environment in particular the types of N species on the catalytic performance of single atom cobalt for ORR was investigated by density functional theory (DFT) calculations. In this study, a C<sub>63</sub>H<sub>18</sub> cluster as the initial model and its derived models with single doping site of Co-N<sub>4</sub>, Co-N<sub>4</sub>+N<sub>G1</sub>, Co-N<sub>4</sub>+N<sub>G2</sub>, Co-N<sub>4</sub>+N<sub>P1</sub>, Co-N<sub>4</sub>+N<sub>P2</sub> and Co-N<sub>4</sub>+N<sub>PY</sub> were constructed as shown in Figure 8-7a. Here, the subscript 1 or 2 indicates the Meta- or para-position of specific N species of the Co-N<sub>4</sub> site. Based on the calculated free-energy diagram for ORR, Co single atom in the model of Co-N<sub>4</sub>+N<sub>G1</sub> (i.e., N<sub>G</sub> is located at meta-position of Co-N<sub>4</sub> site) has the lowest overpotential for ORR, i.e., 0.51 eV, followed by the Co single atom in the model of Co-N<sub>4</sub>+N<sub>G2</sub> (i.e., N<sub>G</sub> is located at para-position of Co-N<sub>4</sub> site) with overpotential of 0.56 eV (Fig.7b). On the other hand, single Co atom in the model of Co-N<sub>4</sub>+N<sub>P1</sub> and Co-N<sub>4</sub>+N<sub>P2</sub> displays relatively higher value of 0.62 eV and 0.68 eV as compared with the Co-N<sub>4</sub>+N<sub>G</sub> model. Among the models studied, single Co atom in the Co-N<sub>4</sub>+N<sub>PY</sub> model possess the highest overpotential for ORR, 0.73 eV. The result is consistent with the electrochemical performance of Co-N/C catalysts discussed above. Co-N/C-N<sub>G</sub> with the dominant N<sub>G</sub> content of 58.65 % shows the highest catalytic performance for ORR, while Co-N/C-N<sub>PY</sub> with the 54% N<sub>PY</sub> displays the lowest catalytic activity for ORR. The result validate that the synergistic effect between graphitic N (with location of meta-position of Co-N<sub>4</sub> site) and Co-N<sub>4</sub>

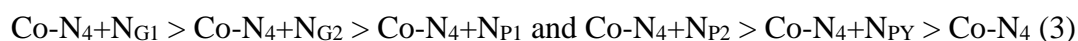
center contributes greatly for enhancing catalytic performance for ORR. This in turn indicates that the best catalytic activity of Co-N/C+N<sub>G</sub> for ORR is fundamentally related to the high content of N<sub>G</sub> located in the vicinities of highly dispersed Co-N<sub>4</sub> active centers. The diagrammatic sketch of optimized structure models of Co-N<sub>4</sub>+N<sub>G1</sub> during process for ORR are list in Figure 8-7c. The widely accepted 4-electron pathway for ORR in alkaline environment was adopted for DFT investigation:



Where \* represents the adsorption sites. In general, the ORR properties are intently correlated to the intermediates, such as OOH\*, O\*, and OH\*. Figure 8-7c showed the geometric structures of the intermediates and plausible catalysis mechanism.

partial density of state (PDOS) and *d*-band center of Co single atom were conducted to analyze the intermediates and catalytic process for ORR with emphasis on the adsorption energy of intermediates in the derived models and the results are given in Figure 8-7d. The *d*-band center of Co single atom is a crucial parameter that closely linked with Fermi level and its electron occupation state reflects the binding strength between intermediates and catalytic surface [42]. According to the projected density of states (PDOS) for *d* orbitals, the *d*-band center of Co in these models were calculated. The values of *d*-band in the model of Co-N<sub>4</sub>+N<sub>G1</sub> displays the most negative value of -1.91 eV compared to -1.699 eV obtained on pristine single atom Co-N<sub>4</sub> with no specific N species, followed by -1.8 eV obtained in Co-N<sub>4</sub>+N<sub>G2</sub> configuration. By contrast, the *d*-band centers in the Co-N<sub>4</sub>+N<sub>P1</sub> and Co-N<sub>4</sub>+N<sub>P2</sub> models exhibit the smaller negative

values of -1.772 eV and -1.769 eV, respectively. For Co-N<sub>4</sub>+N<sub>PY</sub>, the *d*-band center is -1.764 eV. The variation in the *d*-band center relative to the Fermi level is most likely due to the synergistic effect between the Co-N<sub>4</sub> and the coordinated N species (N<sub>G</sub>, N<sub>P</sub>, N<sub>PY</sub>). The shift in the *d*-band center is related to the change of the electron density of the metal core [43]. This indicates that the coordinated specific N species, N<sub>G</sub>, N<sub>P</sub> or N<sub>PY</sub> functions as electron donors, reflected by the downshift of the *d*-band center of Co-N<sub>4</sub>+N<sub>x</sub> (where *x* = G, P and PY). Nevertheless, the ability of donating electrons depends on the types and location of coordinated N species and follows the orders:



This is in excellent agreement with the electrocatalytic activities of Co-N/C catalysts for ORR as shown above. Therefore, the interaction strength between the specific N species and metal Co-N<sub>4</sub> center induce the downshift of *d*-band center, resulting in the negative change of binding energy and endowing it with an optimized free energy [42b,43]. A plot of *d*-band center energy as Y-axis, the specific models with N species and position as X-axis is shown in Figure 8-7e.

Therefore, the interaction strength between Co-N<sub>4</sub> site and graphitic N located at meta-position of Co-N<sub>4</sub> site with the downshift *d*-band center endows it with an optimized free energy and low overpotential for ORR. To validate the result, the Gibbs free energy diagram of these models were compared (see Figure 8-7b), for the reaction on Co-N<sub>4</sub>+N<sub>G1</sub> configuration, the rate-determining step is the excessive adsorption energy for intermediate products, as indicated by the large energy uphill (HO\* + e<sup>-</sup> → OH\* + \*). However, N<sub>G</sub> located at meta-position donates electrons to the Co-N<sub>4</sub> active center,

leading to the downshift in the d-band center and weakening the binding energies of the ORR intermediates on Co-N sites, displays a thermodynamic overpotential lower than

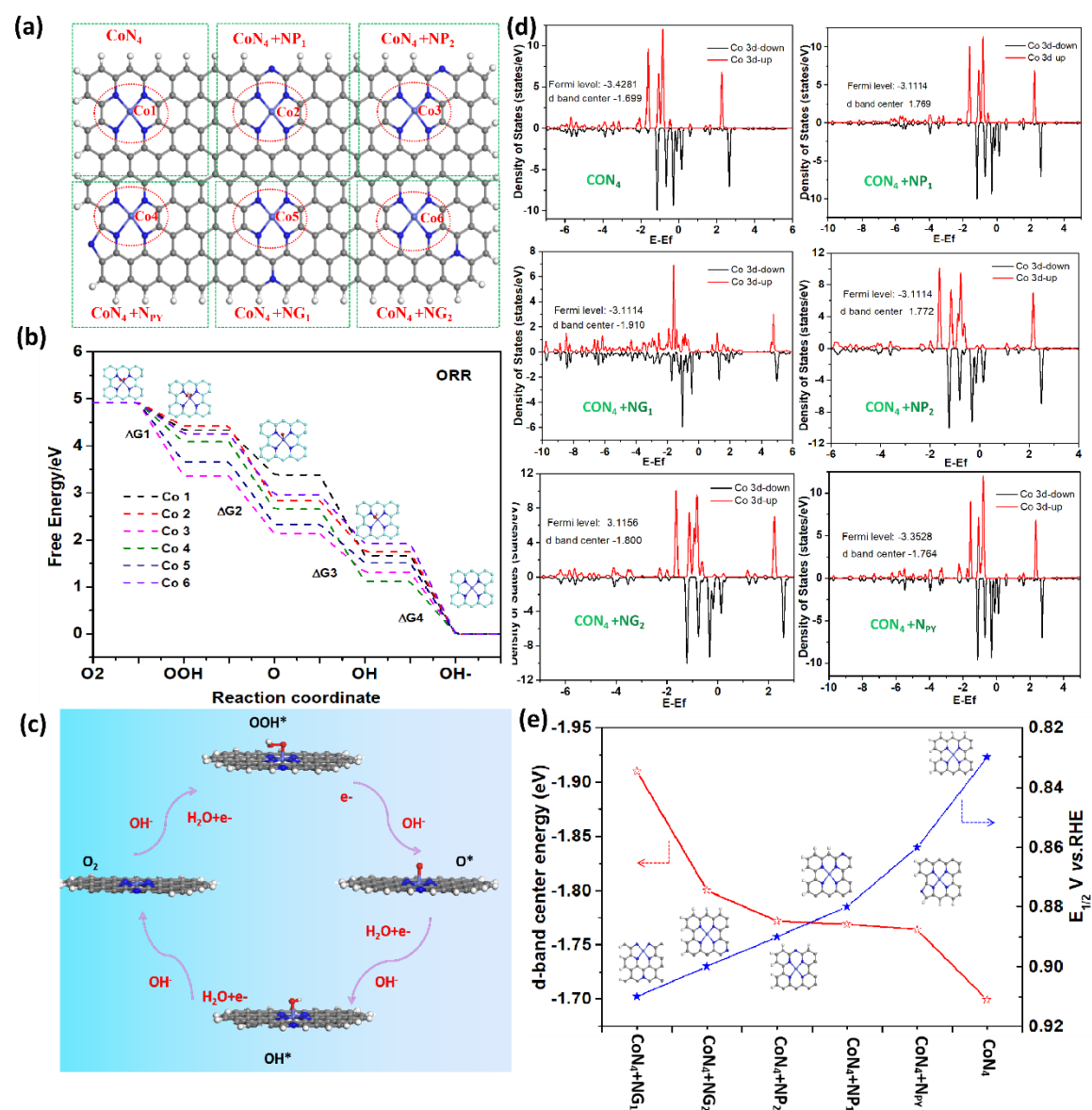


**Figure 8-7.** The constructed models (a) the Gibbs free energy diagram of ORR (b), the diagrammatic sketch of optimized structure models of Co-N<sub>4</sub>+NG<sub>1</sub> during process for ORR. (c) Calculated projected density of states (PDOS) (d) of these models. A plot of d-band center energy,  $E_{1/2}$  for ORR in 0.1MKOH, as Y-axis, the specific models with N species and position as X-axis (e).

that of Co-N<sub>4</sub> and other configuration of Co-N<sub>4</sub> and N species (N<sub>P</sub>, N<sub>PY</sub>). This contributes to the enhanced catalytic kinetics as well as thermodynamics for ORR, leading to a lower energy barrier and a faster ORR kinetics, giving theoretical evidence

for the highly efficient ORR catalytic activity. This is supported by the observed excellent electrocatalytic activity and stability of Co-N/C+N<sub>G</sub> catalysts for ORR in full pH range and as oxygen electrode catalyst in zinc-air batteries and in fuel cells as compared to state-of-the-art Pt based electrocatalysts.

**Table 1.** List of content of each element of the catalyst samples.

Samples	Co	C	O	N				
	(at %)	(at %)	(at %)	Total	N <sub>PY</sub>	N <sub>P</sub>	N <sub>G</sub>	N <sub>O</sub>
				at%	at% (100%)			
N/C+N <sub>G</sub>	0	92.21	3.27	4.49	0.552 (12)	0.546(12)	2.472(55)	0.920 (21)
N/C+N <sub>P</sub>	0	91.41	3.91	4.68	0.655(14)	2.434(52)	1.029(22)	0.562(12)
N/C+N <sub>PY</sub>	0	91.67	3.87	4.46	2.21(50)	0.69(15)	0.86(19)	0.70(16)
N/C+N <sub>P</sub> +N <sub>G</sub>	0	91.89	3.56	4.55	0.591(13)	1.410(31)	2.093(45)	0.500(11)
Co-N/C+N <sub>G</sub>	0.21	89.98	3.87	4.14	0.514(12)	0.508(12)	2.30(56)	0.818(20)
Co-N/C+N <sub>P</sub>	0.2	91.83	3.65	4.32	0.605(14)	2.246(52)	0.950(22)	0.518(12)
Co-N/C+N <sub>PY</sub>	0.23	92.12	3.49	4.39	2.41(55)	0.78(18)	0.91(21)	0.29(6)
Co-N/C+N <sub>P</sub> +N <sub>G</sub>	0.22	91.84	3.75	4.41	0.496(11)	0.838(19)	2.156(49)	0.92(21)

## 8.4 Conclusion

In this work, cobalt single atoms embedded in N-doped carbon matrix coordinated with controlled types of specific N species, Co-N/C+N<sub>G</sub>, Co-N/C+N<sub>P</sub> and Co-N/C+N<sub>PY</sub>, through the precursor modulation strategy were successfully synthesized. The formation of single Co atoms embedded in carbon matrix and the engineering and control of the types of coordinated doped N species have been verified extensively by XPS, XAS, and Wavelet-transform (WT) EXAFS analysis. The formation of tetrahedral geometry structure, Co-N<sub>4</sub>, was confirmed by the least-squares EXAFS fitting for the Fourier-transformed EXAFS curve. The electrochemical activities of Co-

N/C and metal-free N/C catalysts for ORR were carried out in a full pH range solutions, i.e., 0.1 M KOH alkaline, 0.5M H<sub>2</sub>SO<sub>4</sub> acid and 50mM PB neutral solutions.

Among them, Co-N/C+N<sub>G</sub> synthesized by using DPM (2,4-diaminopyrimidine with six membered ring with two N atoms) displays the highest electrocatalytic activity for ORR in full pH range, achieving E<sub>onset</sub> and E<sub>1/2</sub> of 0.96 V and 0.815 V in 0.5M H<sub>2</sub>SO<sub>4</sub>, 1.04 V and 0.915 V in 0.1M KOH and 0.93 V and 0.73 V in 50 mM phosphate buffer (PB) solution, respectively, compatible and better than that of the state-of-the-art Pt/C electrocatalysts, placing it the best NPGM catalysts reported in the literature. Co-N/C+N<sub>G</sub> catalyst also demonstrates the excellent performance as oxygen electrode in a zinc-air battery with a high power density (248 mW cm<sup>-2</sup>) and excellent cyclic stability in a rechargeable Zn-air battery, significantly better than the cell with Pt/C-IrO<sub>2</sub> oxygen electrode. The results show demonstrate the promising potential of Co-N/C+N<sub>G</sub> as NPGM cathodes in a PEM fuel cell. Most interesting, this study shows the Co-N/C materials depends strongly on the coordination environment of doped N species and types and the reaction activity follows the order as a function of the coordinated N species in the full pH range:



The single Co atoms play a critical role to enhancing the electrocatalytic activity of Co-N<sub>4</sub> cluster, which has been confirmed by the KSCN blocking studies. DFT calculation shows that the coordinated N species in the vicinities of the Co-N<sub>4</sub> clusters functions as electron donors to the center, reflected by the downshifting *d*-band center of Co atoms. The increased electron density of cobalt atom core reduces the adsorption

energy of intermediate species of ORR on the Co-N<sub>4</sub> cluster, leading to the significantly reduced energy barrier and enhanced reaction rates of ORR on Co single atom catalysts. The results indicate that N<sub>G</sub> located at the Meta position at the Co-N<sub>4</sub> center has the highest ability to donate electrons to the Co-N<sub>4</sub> active center, downshifting d-band center by 0.211 eV as compared to Co atoms in pristine Co-N<sub>4</sub> with no specific N species coordination. The changes in the *d*-band center of Co single atoms in Co-N<sub>4</sub> cluster as a function of coordinated N species are in excellent agreement with the electrocatalytic activities of Co-N/C catalysts reported in this work. This study provides insights into the optimal active centers in single Co atomic catalytic systems as well as a synthetic guidance for design of Co-based ORR catalyst in molecular level.

## References

- (1) a) X. Ge, A. Sumboja, D. Wu, T. An, B. Li, F. W. T. Goh, T. S. A. Hor, Y. Zong, Z. Liu, Oxygen Reduction in Alkaline Media: From Mechanisms to Recent Advances of Catalysts. *ACS Catal.* **2015**, *5*, 4643-4667; b) Y. Jiao, Y. Zheng, M. Jaroniec, S. Z. Qiao, Design of electrocatalysts for oxygen- and hydrogen-involving energy conversion reactions. *Chem. Soc. Rev.* **2015**, *44*, 2060-2086.
- (2) a) A. Rabis, P. Rodriguez, T. J. Schmidt, Electrocatalysis for Polymer Electrolyte Fuel Cells: Recent Achievements and Future Challenges. *ACS Catal.* **2012**, *2*, 864-890.  
b) J. Wang, W. Cui, Q. Liu, Z. Xing, A. M. Asiri, X. Sun, Recent Progress in Cobalt-Based Heterogeneous Catalysts for Electrochemical Water Splitting. *Adv. Mater.* **2016**, *28*, 215-230.
- (3) a) G. Wu, A. Santandreu, W. Kellogg, S. Gupta, O. Ogoke, H. Zhang, H. L. Wang,

L. Dai, Carbon nanocomposite catalysts for oxygen reduction and evolution reactions: From nitrogen doping to transition-metal addition. *Nano Energy* **2016**, *29*, 83-110. b) C. Y. He, J. J. Zhang, P. K. Shen, Nitrogen-self-doped graphene-based non-precious metal catalyst with superior performance to Pt/C catalyst toward oxygen reduction reaction. *J. Mater. Chem. A* **2014**, *2*, 3231-3236; c) Z. Q. Tian, S. H. Lim, C. K. Poh, Z. Tang, Z. Xia, Z. Luo, P. K. Shen, D. Chua, Y. P. Feng, Z. Shen, J. A. Lin, Highly Order-Structured Membrane Electrode Assembly with Vertically Aligned Carbon Nanotubes for Ultra-Low Pt Loading PEM Fuel Cells. *Adv. Energy Mater.* **2011**, *1*, 1205-1214.

(4) Y. X. Wang, H. Y. Su, Y. H. He, L. G. Li, S. Q. Zhu, D. K. Zhao, F. X. J. Xiao, Y. C. Zeng, M. H. Shao, S. W. Chen, G. Wu, J. Zeng, C. Wang, Advanced Electrocatalysts with Single-Metal-Atom Active Sites. *Chem. Rev.* **2020**, *120*, 12217–12314.

(5) C. Xie, Z. Niu, D. Kim, M. Li, P. Yang, Surface and Interface Control in Nanoparticle Catalysis. *Chem. Rev.* **2020**, *120*, 1184–1249.

(6) A. Kulkarni, S. Siahrostami, A. Patel, J. K. Nørskov, Understanding Catalytic Activity Trends in the Oxygen Reduction Reaction. *Chem. Rev.* **2018**, *118*, 2302–2312.

(7) Y. He, S. Liu, C. Priest, Q. Shi, G. Wu, Atomically dispersed metal-nitrogen-carbon catalysts for fuel cells: advances in catalyst design, electrode performance, and durability improvement. *Chem. Soc. Rev.* **2020**, *49*, 3484-3524.

(8) K. Yuan, D. Luetzenkirchen-Hecht, L. Li, L. Shuai, Y. Li, R. Cao, M. Qiu, X. Zhuang, ; M. K. H. Leung, Y. Chen, U. Scherf, Boosting Oxygen Reduction of Single Iron Active Sites via Geometric and Electronic Engineering: Nitrogen and Phosphorus



Dual Coordination. *J. Am. Chem. Soc.* **2020**, *142*, 2404-2412; b) Y. Tan, C. Xu, G. Chen, X. Fang, N. Zheng, Q. Xie, Facile Synthesis of Manganese-Oxide-Containing Mesoporous Nitrogen-Doped Carbon for Efficient Oxygen Reduction. *Adv. Funct. Mater.* **2012**, *22*, 4584-4591.

(9) R. Jasinski, A New Fuel Cell Cathode Catalyst. *Nature* **1964**, *201*, 1212-1213; b) G. Faubert, G. Lalande, R. Cote, D. Guay, J. P. Dodelet, L. T. Weng, P. Bertrand, G. Denes, Heat-treated iron and cobalt tetraphenylporphyrins adsorbed on carbon black: Physical characterization and catalytic properties of these materials for the reduction of oxygen in polymer electrolyte fuel cells. *Electrochim. Acta.* **1996**, *41*, 1689-1701.

(10) E. Jung, H. Shin, B.-H. Lee, V. Efremov, S. Lee, H. S. Lee, J. Kim, W. Hooch Antink, S. Park, Atomic-level tuning of Co-N-C catalyst for high-performance electrochemical H<sub>2</sub>O<sub>2</sub> production. *Nat. Mater.* **2020**, *19*, 436.

(11) M. Chen, Y. He, J. S. Spendlow, G. Wu, Atomically Dispersed Metal Catalysts for Oxygen Reduction. *ACS Energy Lett.* **2019**, *4*, 1619-1633.

(12) a) G. Wu, K. L. More, C. M. Johnston, P. Zelenay, High-Performance Electrocatalysts for Oxygen Reduction Derived from Polyaniline, Iron, and Cobalt. *Science* **2011**, *332*, 443-447. b) Y. Shao, J.-P. Dodelet, G. Wu, P. Zelenay, PGM-Free Cathode Catalysts for PEM Fuel Cells: A Mini-Review on Stability Challenges. *Adv. Mater.* **2019**, *31*, 1807615.

(13) a) H. T. Chung, D. A. Cullen, D. Higgins, B. T. Sneed, E. F. Holby, K. L. More, P. Zelenay, Direct atomic-level insight into the active sites of a high-performance PGM-free ORR catalyst. *Science* **2017**, *357*, 479-483. b) C. X. Zhao, B. Q. Li, J. N. Liu,

Q. Zhang, Intrinsic Electrocatalytic Activity Regulation of M-N-C Single-Atom Catalysts for the Oxygen Reduction Reaction. *Angew. Chem. Int. Ed.* **2021**, *60*, 4448-4463.

(14) a) H. J. Shen, G. E. Eduardo, J. Y. Ma, K. T. Zang, J. Luo, L. Wang, S. S. Gao, Xamxikamar Mamat, G. Z. Hu, S. J. Thomas Wagberg, Guo, Synergistic Effects between Atomically Dispersed Fe-N-C and C-S-C for the Oxygen Reduction Reaction in Acidic Media. *Angew. Chem. Int. Ed.* **2017**, *56*, 13800. b) J. Masa, W. Xia, M. Muhler, W. Schuhmann, On the Role of Metals in Nitrogen-Doped Carbon Electrocatalysts for Oxygen Reduction. *Angew. Chem. Int. Ed.* **2015**, *54*, 10102-10120.

(15) K. Yuan, L. H. Dirk, L. B. Li, M. Qiu, X. D. Zhuang, K. H. Michael, Y. W. Chen, Ullrich Scherf., Boosting Oxygen Reduction of Single Iron Active Sites via Geometric and Electronic Engineering: Nitrogen and Phosphorus Dual Coordination. *J. Am. Chem. Soc.* **2020**, *142*, 5, 2404-2412.

(16) H. Sun, M. F. Wang, X. C. Du, Y. Jiao, S. S. Liu, T. Qian, J. Xiong, C. L. Yan, Modulating the d-band center of boron doped single-atom sites to boost the oxygen reduction reaction. *J. Mater. Chem. A*, **2019**, *7*, 20952.

(17) a) H. Yang, L. Shang, Q. Zhang, R. Shi, G. I. Waterhouse, L. Gu, T. Zhang, A universal ligand mediated method for large scale synthesis of transition metal single atom catalysts. *Nat. Commun.* **2019**, *10*, 4585. b) C. Zhang, S. Yang, J. Wu, M. Liu, S. Yazdi, M. Ren, J. Sha, J. Zhong, K. Nie, A. S. Jalilov, Electrochemical CO<sub>2</sub> Reduction with Atomic Iron-Dispersed on Nitrogen-Doped Graphene. *Adv. Energy Mater.* **2018**, *8*, 1703487.

- (18) a) X. Cui, S. Yang, X. Yan, J. Leng, S. Shuang, P. Ajayan, Z. Zhang, Pyridinic-Nitrogen-Dominated Graphene Aerogels with Fe-N-C Coordination for Highly Efficient Oxygen Reduction Reaction. *Adv. Funct. Mater.* **2016**, *26*, 5708. b) Q. Wang, Y. Ji, Y. Lei, Y. Wang, Y. Wang, Y. Li, S. Wang, Pyridinic-N-Dominated Doped Defective Graphene as a Superior Oxygen Electrocatalyst for Ultrahigh-Energy-Density Zn-Air Batteries. *ACS Energy Lett.* **2018**, *3*, 1183.
- (19) X. Q. Wei, X. Luo, H. J. Wang, W. L. Gu, W. W. Cai, Y. H. Lin, C. Z. Zhu, Highly-defective Fe-N-C catalysts towards pH-Universal oxygen reduction reaction. *Applied Catalysis B: Environmenta.* **2020**, *l 263*, 118347.
- (20) J. Wang, L. Q. Li, X. Chen, Y. L. Lu, W. S. Yang, X. Duan, A Co-N/C hollow-sphere electrocatalyst derived from a metanilic CoAl layered double hydroxide for the oxygen reduction reaction, and its active sites in various pH media. *Nano Res.* **2017**, *10*, 2508-2518.
- (21) X. R. Zhang, Y. Q. Wang, K. Wang, Y. L. Huang, D. D. Lyu, F. Yu, S. B. Wang, Z. Q. Tian. P. K. Shen, S. P. Jiang, Active sites engineering via tuning configuration between graphitic-N and thiophenic-S dopants in one-step synthesized graphene nanosheets for efficient water-cycled electrocatalysis. *Chem. Eng. J.* **2021**, *416*, 129096.
- (22) X. R. Zhang, X. Zhang, S. Y. Zhao, Y. Q. Wang, Z. Q. Tian. P. K. Shen, S. P. Jiang, Precursor modulated active sites of nitrogen doped graphene-based carbon catalysts via one-step pyrolysis method for the enhanced oxygen reduction reaction. *Electrochimi. Acta* **2020**, *370*, 137712.
- (23) X. R. Zhang, X. Zhang, X. Xiang, C. Pan, Q. H. Meng, C. Hao, Z. Q. Tian. P. K.

Shen, S. P. Jiang, Nitrogen and Phosphate Co-doped Graphene as Efficient Bifunctional Electrocatalysts by Precursor Modulation Strategy for Oxygen Reduction and Evolution Reactions. *ChemElectroChem*. DOI10.1002/celec.202100599.

(24) J. Wang, W. Liu, G. Luo, Z. Li, C. Zhao, H. Zhang, M. Zhu, Q. Xu, X. Wang, C. Zhao, Y. Qu, Z. Yang, T. Yao, Y. Li, Y. Lin, Y. Wu, Y. Li, Synergistic effect of well-defined dual sites boosting the oxygen reduction reaction. *Energy Environ. Sci.* **2018**, *11*, 3375-3379.

(25) a) X. X. Wang, D. A. Cullen, Y.-T. Pan, S. Hwang, M. Wang, Z. Feng, J. Wang, M. H. Engelhard, H. Zhang, Y. He, Y. Shao, D. Su, K. L. More, J. S. Spendelow, G. Wu, Nitrogen-Coordinated Single Cobalt Atom Catalysts for Oxygen Reduction in Proton Exchange Membrane Fuel Cells. *Adv. Mater.* **2018**, *30*, 1706758; b) V. Gibson, C. Redshaw, G. A. Solan, Bis(imino)pyridines: Surprisingly Reactive Ligands and a Gateway to New Families of Catalysts. *Chem. Rev.* **2007**, *107*, 1745-1776.

(26). Q. Cheng, L. Yang, L. Zou, Z. Zou, C. Chen, Z. Hu, H. Yang, Single Cobalt Atom and N Codoped Carbon Nanofibers as Highly Durable Electrocatalyst for Oxygen Reduction Reaction. *ACS Catal.* **2017**, *7*, 6864-6871.

(27). Y. Tong, P. Chen, T. Zhou, K. Xu, W. Chu, C. Wu, Y. Xie, A Bifunctional Hybrid Electrocatalyst for Oxygen Reduction and Evolution: Cobalt Oxide Nanoparticles Strongly Coupled to B, N-Decorated Graphene. *Angew. Chem. Int. Ed.* **2017**, *56*, 7121-7125.

(28). J. Yang, X. Wang, B. Li, L. Ma, L. Shi, Y. Xiong, H. Xu, Novel Iron/Cobalt-Containing Polypyrrole Hydrogel-Derived Trifunctional Electrocatalyst for Self-

Powered Overall Water Splitting. *Adv. Funct. Mater.* **2017**, *27*, 1606497.

(29). Y. Su, Y. Zhu, H. Jiang, J. Shen, X. Yang, W. Zou, J. Chen, C. Li, Cobalt nanoparticles embedded in N-doped carbon as an efficient bifunctional electrocatalyst for oxygen reduction and evolution reactions. *Nanoscale* **2014**, *6*, 15080-15089.

(30). G. Wu, P. Zelenay, Nanostructured Nonprecious Metal Catalysts for Oxygen Reduction Reaction. *Acc Chem Res* **2013**, *46*, 1878-1889.

(31). Y. Zhu, B. Zhang, X. Liu, D.-W. Wang, D. S. Su, Unravelling the Structure of Electrocatalytically Active Fe-N Complexes in Carbon for the Oxygen Reduction Reaction. *Angew. Chem. Int. Ed.* **2014**, *53*, 10673-10677.

(32). L. Cheng, H. Huang, Z. Lin, Y. Yang, Q. Yuan, L. Hu, C. Wang, Q. Chen, N and O multi-coordinated vanadium single atom with enhanced oxygen reduction activity. *J. Colloid Interface Sci.* **2021**, *594*, 466-473.

(33). a) Z. Sheng, L. Shao, J. Chen, W. Bao, F. Wang, X. Xia, Catalyst-Free Synthesis of Nitrogen-Doped Graphene via Thermal Annealing Graphite Oxide with Melamine and Its Excellent Electrocatalysis. *ACS Nano* **2011**, *5*, 4350. b) J. Zhang, Y. Sun, J. Zhu, Z. Kou, P. Hu, L. Liu, S. Li, S. Mu, Y. Huang, Defect and pyridinic nitrogen engineering of carbon-based metal-free nanomaterial toward oxygen reduction. *Nano Energy* **2018**, *52*, 307.

(34) G. Wu, C. Johnston, N. Mack, K. Artyushkova, M. Ferrandon, M. Nelson, J. Lezamapacheco, S. Conradson, K. More, D. Myers, P. Zelenay, Synthesis-structure-performance correlation for polyaniline-Me-C non-precious metal cathode catalysts for oxygen reduction in fuel cells. *J. Mater. Chem.* **2011**, *21*, 11392.

- (35) Y. Han, Y.Wang, W.Chen, R.Xu, L.Zheng, J.Zhang, J.Luo, R.Shen, Y.Zhu, W.Cheong, C.Chen, Q.Peng, D.Wang, Y.Li, Hollow N-Doped Carbon Spheres with Isolated Cobalt Single Atomic Sites: Superior Electrocatalysts for Oxygen Reduction. *J. Am. Chem. Soc.* **2017**, 139, 17269.
- (36) J. Han, Y. Sa, Y. Shim, M. Choi, N. Park, S. Joo, S. Park, Coordination Chemistry of [Co(acac)<sub>2</sub>] with N-Doped Graphene: Implications for Oxygen Reduction Reaction Reactivity of Organometallic Co-O<sub>4</sub>-N Species. *Angew. Chem., Int. Ed.* **2015**, 54, 12622.
- (37) J.Wang, Z.Huang, W.Liu, C.Chang, H.Tang, Z.Li, W.Chen, C.Jia, T.Yao, S.We, Y.Wu, Y.Li, Design of N-Coordinated Dual-Metal Sites: A Stable and Active Pt-Free Catalyst for Acidic Oxygen Reduction Reaction. *J. Am. Chem. Soc.* **2017**, 139, 17281.
- (38) Fei, H. L, Dong, J. C, M. Josefina Arellano-Jime´nez, Ye, Gonglan, Kim, Nam Dong, Samue, L.G, Peng, Z. W, Zhu, Z; Qin, F, Bao, J. M, Yacaman, Miguel Jose, Ajayan, Pulickel M, Chen, D. L, Tour, James M. Atomic cobalt on nitrogen-doped graphene for hydrogen generation. *Nat. Commun.* **2015**, 6, 8668.
- (39). Y. He, Q. Shi, W. Shan, X. Li, A. J. Kropf, E. C. Wegener, J. Wright, S. Karakalos, D. Su, D. A. Cullen, G. Wang, D. J. Myers, G. Wu, Dynamically Unveiling Metal-Nitrogen Coordination during Thermal Activation to Design High-Efficient Atomically Dispersed CoN<sub>4</sub> Active Sites. *Angew. Chem. Int. Ed.* **2021**, 60, 9516-9526.
- (40) D. H. Guo, Riku. Shibuya, Chisato. Akiba, Shunsuke. Saji, Takahiro. Kondo, Junji. Nakamura, Active sites of nitrogen-doped carbon materials for oxygen reduction reaction clarified using model catalysts. *Science*, **2016**, 351, 6271.

(41) a) M. S. Thorum, J. M. Hankett, A. A. Gewirth, Poisoning the Oxygen Reduction Reaction on Carbon-Supported Fe and Cu Electrocatalysts: Evidence for Metal-Centered Activity. *J. Phys. Chem. Lett.*, **2011**, *2*, 295-298. b) Y. Cheng, J. Zhang, S. P. Jiang, Are metal-free pristine carbon nanotubes electrocatalytically active? *Chem. Comm.*, **2015**, *51*, 13764-13767.

(42). a) W. Zhang, Y. Zhang, Y. Li, S. Yang, L.-H. Zhang, F. Yu, Enhanced oxygen reduction performance of nitrogen and sulfur Co-doped graphene oxide by immobilized ionic liquid. *Chem. Eng. Sci.* **2021**, *236*, 116544. b) W. Qi, W. Huang, J. Niu, B. Zhang, Z. Zhang, W. Li, The role of S in the Co-N-S-C catalysis system towards the ORR for proton exchange membrane fuel cells. *Appl. Surf. Sci.* **2021**, *540*, 148325.

(43). a) H. Tsunoyama, N. Ichikuni, H. Sakurai, T. Tsukuda, Effect of Electronic Structures of Au Clusters Stabilized by Poly(N-vinyl-2-pyrrolidone) on Aerobic Oxidation Catalysis. *J. Am. Chem. Soc.* **2009**, *131*, 7086-7093. b) S. Y. Wang, F. Yang, S. P. Jiang, S. L. Chen, X. Wang, Tuning the electrocatalytic activity of Pt nanoparticles on carbon nanotubes via surface functionalization. *Electrochem. Comm.* **2010**, *12*, 1646-1649.

**Table 2.** Comparison of the electrocatalytic activity of the best performed Co-N/C-N<sub>G</sub> in this study with that reported in the literature for ORR in acidic medium. Potential values are given as vs RHE.

Catalysts	Electrolyte	E <sub>onset</sub> V	E <sub>1/2</sub> V	Tafel slope mV/dec	Ref.
Co-N/C-N <sub>G</sub>	Catalyst loading=0.6 mg, RDE, 1600 rpm, scan rate 5 mVs <sup>-1</sup>				This study
	0.1M KOH	1.04	0.91	80	

	0.5M H <sub>2</sub> SO <sub>4</sub>	0.96	0.815	75	
	50mM PB	0.93	0.73	78	
Pt/C	Catalyst loading=40ug, RDE, 1600 rpm, scan rate 5 mVs <sup>-1</sup>				This study
	0.1M KOH	1.01	0.86	75	
	0.5M H <sub>2</sub> SO <sub>4</sub>	1.0	0.83	72	
	50mM PB	0.96	0.78	80	
Co-N/C	Catalyst loading=0.6 mg, RDE, 1600 rpm, scan rate 5 mVs <sup>-1</sup>				Nano Res. 2017, 10(7): 2508-2518
	0.1M KOH	0.95	0.84		
	0.1M HClO <sub>4</sub>	0.75	0.52		
	50mM PB	0.87	0.7		
β-FeOOH/PNGNs	Catalyst loading=0.637 mg, RDE, 1600 rpm, scan rate 5 mVs <sup>-1</sup>				Adv. Funct. Mater. 2018, 28, 1803330
	0.1M KOH	1.017	0.883	83.65	
	0.5M H <sub>2</sub> SO <sub>4</sub>	0.84	0.68	149	
	0.1M PB	0.862	0.693	134	
GEF-900	Catalyst loading=0.1 mg, RDE, 1600 rpm, scan rate 5 mVs <sup>-1</sup>				ACS Appl. Mater. Interfaces 2018, 10, 28509–28516
	0.1M KOH	1.01	0.9		
	0.1M HClO <sub>4</sub>	0.85	0.69		
	0.1M PB	0.97	0.68		
Co-N-C	Catalyst loading=0.2 mg, RDE, 1600 rpm, scan rate 5 mVs <sup>-1</sup>				ACS Appl. Mater. Interfaces 2015, 7, 4048-4055.
	0.1M KOH	0.9	0.84		
	0.1M HClO <sub>4</sub>	0.83	0.71		
	0.1M PB	0.75	0.67		



Fe-N-C/H <sub>2</sub> O <sub>2</sub>	Catalyst loading=0.2 mg, RDE, 1600 rpm, scan rate 5 mVs <sup>-1</sup>	Applied Catalysis B: Environmental Science, 2020, 1263, 118347
	0.1M KOH	0.99    0.92    37.84
	0.1M HClO <sub>4</sub>	0.93    0.79    85.3
	0.1M PB	0.92    0.8    26.7
Fe <sub>50</sub> -N-C-900	Catalyst loading=0.1 mg, RDE, 1600 rpm, scan rate 10 mVs <sup>-1</sup>	Small 2018, 14, 1703118
	0.1M KOH	1.00    0.92
	0.1M HClO <sub>4</sub>	0.847    0.72
	0.1M PB	0.92    0.78
PT-MnN <sub>4</sub>	Catalyst loading=0.2 mg, RDE, 1600 rpm, scan rate 5 mVs <sup>-1</sup>	Carbon Energy, 2021,1-10.
	0.1M KOH	0.95    0.88    96
	0.1M HClO <sub>4</sub>	0.89    0.73    186
	0.1M PB	0.84    0.63    195
NPC-1000	Catalyst loading=0.4 mg, RDE, 1600 rpm, scan rate 10 mVs <sup>-1</sup>	Adv. Funct. Mater. 2017, 27, 1606190
	0.1M KOH	1.02    0.902
	0.1M HClO <sub>4</sub>	1.0    0.801
	0.1M PB	1.03    0.818

Note:  $E_{\text{onset}}$  in this study is defined as the current density at  $1.0 \mu\text{A cm}^{-2}$ ;  $E_{1/2}$  is defined as the potential of current density at  $3.0 \text{ mA cm}^{-2}$  when compared with reported performance to eliminate influence of different limited current density.

***Every reasonable effort has been made to acknowledge the owners of copyright material. I would be pleased to hear from any copyright owner who has been omitted or incorrectly acknowledged.***

## 9. Summary

The objective of this PhD project is the development of highly efficient heteroatoms doped carbon based materials with active sites engineering based on N-containing precursors platform as active electrocatalysts for oxygen reduction reaction (ORR), oxygen evolution reaction (OER) and hydrogen evolution reaction (HER). The correlation between active sites and polymer precursors as well as synergistic effect between various dopants and their application in electrochemical energy conversion and storage applications were explored. This work shed light on the optimal active centers as well as providing new concept for designing heteroatoms doped carbon materials in molecular level in general based on tuning N-containing precursor platform contributes to their preference for formation of high content of certain N species. The achievements of the PhD project are summarized as below:

- Precursor modulated active sites of nitrogen doped graphene-based carbon catalysts via one-step pyrolysis method for ORR. In this study, three kinds of nitrogen doped carbon materials with different N species configurations were obtained with 5-aminouracil as the same nitrogen-containing precursor platform. 2,6-diaminopyridine and 1,3-diaminobenzene were selected as another two precursors respectively to modulate N types such as pyridine nitrogen (NP), graphitic nitrogen (NG) and pyrrole nitrogen (NPY) respectively. These three nitrogen doped carbon materials with different active sites configurations such as N/C-NP+NG, N/C-NP+NP, and N/C-NP+NPY were successfully synthesized and a series of physical characterization were carried out. Electrochemical test results

display that nitrogen doped carbon materials with NP and NG as main component exhibits the highest catalytic activity for ORR which is even better than that of commercial Pt/C. By contrast, catalyst with high content of NP+NPY shows the lowest catalytic performance for ORR among all these nitrogen doped carbon materials. Combining with the Density functional theory (DFT) simulations results, it is found that the combination of NP and NG is benefit for producing a strong electron redistribution on carbon matrix that leads to high charge and high spin density on the surrounding carbon atoms. This work provides a facile strategy for designing graphene based nitrogen doped carbon materials with effective N configurations as active sites for ORR.

- Precursor modulated synergy of N, P co-doped graphene materials via a bottom-up doping strategy for electrocatalytic selectivity for oxygen redox reaction. We propose an effective active sites engineering strategy for obtaining N, P co-doped graphene (NPG) nanosheets with certain N species and graphitic P configurations based on 5-Aminouracil, 2,6-Diaminopyridine and 1,3-Diaminobenzene as adjustable N-containing precursor platform contributes to their preference for high content of certain N species, phytic acid was selected as P source. These graphene (NPG) nanosheets were developed via a facile pyrolysis of the mixed solid power of N-containing precursors as N source and phytic acid (PA) as S source. It is found that the configuration of Pyridinic N +Graphitic N+P prefer to producing enhanced catalytic activity for ORR. Meanwhile, Pyridinic N +Graphitic N+P contributes to promoting OER performance greatly.


- Correlating active site configuration of N doped and N, S-co doped carbon nanospheres with six-membered heterocyclic compounds as precursors for enhancing oxygen reduction reaction. In this work, two series of N doped and N, S co-doped carbon nanospheres were synthesized via pyrolysis of self-polymerized compounds of three typical analogous precursors of 2,6-Diaminopyridine, 1,3-Diaminobenzene and 4,6-Diaminopyrimidine using  $H_2O_2$  and ammonium persulfate as initiators respectively. Through the comprehensive characterization with the combination of morphology observation, chemical composition and states analysis, basicity measurements, electrochemical performance evaluation for ORR and density functional theory calculation as well, the results demonstrate that nitrogen atoms in the six-membered rings of three precursors exactly play a critical role on the formation of N-doping types and synergistic effects of N and S dopants in their derived carbon nanospheres, which directly induce the change of electronic structure of doped carbon and thus lead to a significant difference for ORR performance.
- S Precursors Modulated active sites of One-step Synthesized N, S co-doped Graphene Nanosheets for tuning the activity and selectivity for Oxygen redox reactions. Two N, S co-doped graphene nanosheets with different N, S dopant species were synthesized with 2, 6-Diaminopyridine as the same N-containing precursor platform, but 2, 5-Dithiobiurea and Ammonium persulfate were selected as S-containing precursors respectively. Interestingly, it is found that the different S-containing precursors play significant effect on formation of N dopant species in


graphene matrix. The results demonstrate that the NSG catalyst derived from Ammonium persulfate as S-containing precursors featured with the high content of graphitic N and S displays superior catalytic activity for ORR with the half-wave potential of 0.87V vs. RHE. By contrast, NSG catalyst derived from 2, 5-Dithiobiurea as S-containing precursor featured with relatively low content of graphitic N but high content of pyrrolic N and pyridinic N that induces bifunctional catalytic activity for both ORR and OER (with a metric potential difference of 0.76 V in 0.1 M KOH).

- Active site engineering is achieved by tuning the configuration between the Graphitic-N and Thiophenic-S dopants in N, S co-doped graphene for efficient electrocatalysis of water and oxygen. We present an efficient active site engineering of bottom-up synthesis of N,S co-doped graphene (NSG) nanosheets based on 2,6-diaminopyridine (DAP) as a tunable nitrogen-containing precursor platform strategy, the nanosheets have certain graphitic N and thiophene S configurations due to their preference to form a high percentage of graphitic N. These graphene (NSG) nanosheets were developed by simple pyrolysis of mixed solid powders with 2, 6-diaminopyridine (DAP) as N source and ammonium persulfate (AP) as S source. DAP with different mass ratios Both the NSG nanosheets prepared from 1000 m<sup>2</sup> g<sup>-1</sup> and AP have high specific surface area and high crystallinity, but show significant differences in electrocatalytic selectivity. It is found that the ratio of graphitic N and thiophene S has a great influence on the catalytic selectivity of ORR, OER and HER, respectively, and the lower the ratio

of graphitic N and thiophene S in N, S co-doped graphene nanosheets, the stronger the performance for HER, a moderate ratio of graphitic N and thiophene S contributes to the better performance of ORR, conversely, a higher ratio of graphitic N and thiophene S is beneficial to improve the performance of OER.

# Appendix: Permission of Reproduction from the Copyright Owner

? Help ▾



### Elemental superdoping of graphene and carbon nanotubes


**Author:** Yuan Liu et al  
**Publication:** Nature Communications  
**Publisher:** Springer Nature  
**Date:** Mar 4, 2016


*Copyright © 2016, The Author(s)*

#### Creative Commons

This is an open access article distributed under the terms of the [Creative Commons CC BY](#) license, which permits unrestricted use, distribution, and reproduction in any medium, provided the original work is properly cited.

You are not required to obtain permission to reuse this article.  
To request permission for a type of use not listed, please contact [Springer Nature](#)

Home ? Live Chat Xiao Zhang ▾



### Graphitic Carbon Nitride (g-C<sub>3</sub>N<sub>4</sub>)-Based Photocatalysts for Artificial Photosynthesis and Environmental Remediation: Are We a Step Closer To Achieving Sustainability?

**Author:** Wee-Jun Ong, Ling-Ling Tan, Yun Hau Ng, et al  
**Publication:** Chemical Reviews  
**Publisher:** American Chemical Society  
**Date:** Jun 1, 2016

*Copyright © 2016, American Chemical Society*

**PERMISSION/LICENSE IS GRANTED FOR YOUR ORDER AT NO CHARGE**

This type of permission/license, instead of the standard Terms & Conditions, is sent to you because no fee is being charged for your order. Please note the following:

- Permission is granted for your request in both print and electronic formats, and translations.
- If figures and/or tables were requested, they may be adapted or used in part.
- Please print this page for your records and send a copy of it to your publisher/graduate school.
- Appropriate credit for the requested material should be given as follows: "Reprinted (adapted) with permission from (COMPLETE REFERENCE CITATION). Copyright (YEAR) American Chemical Society." Insert appropriate information in place of the capitalized words.
- One-time permission is granted only for the use specified in your request. No additional uses are granted (such as derivative works or other editions). For any other uses, please submit a new request.

If credit is given to another source for the material you requested, permission must be obtained from that source.

BACK

CLOSE WINDOW

**Facile Gel-Based Morphological Control of Ag/g-C<sub>3</sub>N<sub>4</sub> Porous Nanofibers for Photocatalytic Hydrogen Generation**

**Author:** Jiangpeng Wang, Jingkun Cong, Hui Xu, et al  
**Publication:** ACS Sustainable Chemistry & Engineering  
**Publisher:** American Chemical Society  
**Date:** Nov 1, 2017

*Copyright © 2017, American Chemical Society*

**PERMISSION/LICENSE IS GRANTED FOR YOUR ORDER AT NO CHARGE**

This type of permission/license, instead of the standard Terms & Conditions, is sent to you because no fee is being charged for your order. Please note the following:

- Permission is granted for your request in both print and electronic formats, and translations.
  - If figures and/or tables were requested, they may be adapted or used in part.
  - Please print this page for your records and send a copy of it to your publisher/graduate school.
  - Appropriate credit for the requested material should be given as follows: "Reprinted (adapted) with permission from (COMPLETE REFERENCE CITATION). Copyright (YEAR) American Chemical Society." Insert appropriate information in place of the capitalized words.
  - One-time permission is granted only for the use specified in your request. No additional uses are granted (such as derivative works or other editions). For any other uses, please submit a new request.
- If credit is given to another source for the material you requested, permission must be obtained from that source.

[BACK](#)[CLOSE WINDOW](#)**Ammonia Electrosynthesis with High Selectivity under Ambient Conditions via a Li Incorporation Strategy**

**Author:** Gao-Feng Chen, Xinrui Cao, Shunqing Wu, et al  
**Publication:** Journal of the American Chemical Society  
**Publisher:** American Chemical Society  
**Date:** Jul 1, 2017

*Copyright © 2017, American Chemical Society*

**PERMISSION/LICENSE IS GRANTED FOR YOUR ORDER AT NO CHARGE**

This type of permission/license, instead of the standard Terms and Conditions, is sent to you because no fee is being charged for your order. Please note the following:

- Permission is granted for your request in both print and electronic formats, and translations.
- If figures and/or tables were requested, they may be adapted or used in part.
- Please print this page for your records and send a copy of it to your publisher/graduate school.
- Appropriate credit for the requested material should be given as follows: "Reprinted (adapted) with permission from (COMPLETE REFERENCE CITATION). Copyright (YEAR) American Chemical Society." Insert appropriate information in place of the capitalized words.
- One-time permission is granted only for the use specified in your RightsLink request. No additional uses are granted (such as derivative works or other editions). For any uses, please submit a new request.



**Insight into the Crucial Factors for Photochemical Deposition of Cobalt Cocatalysts on g-C3N4 Photocatalysts**



Author: Na Zhao, Linggang Kong, Yuming Dong, et al

Publication: Applied Materials

Publisher: American Chemical Society

Date: Mar 1, 2018

Copyright © 2018, American Chemical Society

**PERMISSION/LICENSE IS GRANTED FOR YOUR ORDER AT NO CHARGE**

This type of permission/license, instead of the standard Terms & Conditions, is sent to you because no fee is being charged for your order. Please note the following:

- Permission is granted for your request in both print and electronic formats, and translations.
- If figures and/or tables were requested, they may be adapted or used in part.
- Please print this page for your records and send a copy of it to your publisher/graduate school.
- Appropriate credit for the requested material should be given as follows: "Reprinted (adapted) with permission from (COMPLETE REFERENCE CITATION). Copyright (YEAR) American Chemical Society." Insert appropriate information in place of the capitalized words.
- One-time permission is granted only for the use specified in your request. No additional uses are granted (such as derivative works or other editions). For any other uses, please submit a new request.
- If credit is given to another source for the material you requested, permission must be obtained from that source.

BACK

CLOSE WINDOW

**License Details**

This Agreement between Xiao Zhang ("You") and Elsevier ("Elsevier") consists of your license details and the terms and conditions provided by Elsevier and Copyright Clearance Center.

Print Copy

License Number	5006900367531
License date	Feb 13, 2021
Licensed Content Publisher	Elsevier
Licensed Content Publication	Applied Catalysis B: Environmental
Licensed Content Title	Enhanced photocatalytic hydrogen evolution by partially replaced corner-site C atom with P in g-C3N4
Licensed Content Author	Bin Wang,Hairui Cai,Daming Zhao,Miao Song,Penghui Guo,Shaohua Shen,Dongsheng Li,Shengchun Yang
Licensed Content Date	5 May 2019
Licensed Content Volume	244
Licensed Content Issue	n/a
Licensed Content Pages	8
Type of Use	reuse in a thesis/dissertation
Portion	figures/tables/illustrations
Number of figures/tables/illustrations	1
Format	both print and electronic
Are you the author of this Elsevier article?	No
Will you be translating?	No
Title	Synthesis and properties of layered g-C3N4 and their applications
Institution name	Curtin University
Expected presentation date	Mar 2021
Portions	Figure 1
Requestor Location	Xiao Zhang B614 Curtin University  Perth, Bentley 6102 Australia Attn: Xiao Zhang GB 494 6272 12
Publisher Tax ID	000000000

**Molecule Self-Assembly Synthesis of Porous Few-Layer Carbon Nitride for Highly Efficient Photoredox Catalysis**

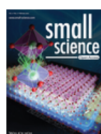
**Author:** Yuting Xiao, Guohui Tian, Wei Li, et al  
**Publication:** Journal of the American Chemical Society  
**Publisher:** American Chemical Society  
**Date:** Feb 1, 2019

*Copyright © 2019, American Chemical Society*

**PERMISSION/LICENSE IS GRANTED FOR YOUR ORDER AT NO CHARGE**

This type of permission/license, instead of the standard Terms & Conditions, is sent to you because no fee is being charged for your order. Please note the following:

- Permission is granted for your request in both print and electronic formats, and translations.
  - If figures and/or tables were requested, they may be adapted or used in part.
  - Please print this page for your records and send a copy of it to your publisher/graduate school.
  - Appropriate credit for the requested material should be given as follows: "Reprinted (adapted) with permission from (COMPLETE REFERENCE CITATION). Copyright (YEAR) American Chemical Society." Insert appropriate information in place of the capitalized words.
  - One-time permission is granted only for the use specified in your request. No additional uses are granted (such as derivative works or other editions). For any other uses, please submit a new request.
- If credit is given to another source for the material you requested, permission must be obtained from that source.

[BACK](#)[CLOSE WINDOW](#)**Electrocatalytic C–N Coupling for Urea Synthesis**

**Author:** Shuangyin Wang, Nihan He, Chen Chen  
**Publication:** SMALL SCIENCE  
**Publisher:** John Wiley and Sons  
**Date:** Oct 15, 2021

*© 2021 The Authors. Small Science published by Wiley-VCH GmbH*

**Open Access Article**

This is an open access article distributed under the terms of the [Creative Commons CC BY](#) license, which permits unrestricted use, distribution, and reproduction in any medium, provided the original work is properly cited.

You are not required to obtain permission to reuse this article.

For an understanding of what is meant by the terms of the Creative Commons License, please refer to [Wiley's Open Access Terms and Conditions](#).

Permission is not required for this type of reuse.

Wiley offers a professional reprint service for high quality reproduction of articles from over 1400 scientific and medical journals. Wiley's reprint service offers:

### Understanding the Electrocatalytic Interface for Ambient Ammonia Synthesis



**Author:** Lin Hu, Zhuo Xing, Xiaofeng Feng  
**Publication:** ACS Energy Letters  
**Publisher:** American Chemical Society  
**Date:** Feb 1, 2020

Copyright © 2020, American Chemical Society

#### PERMISSION/LICENSE IS GRANTED FOR YOUR ORDER AT NO CHARGE

This type of permission/license, instead of the standard Terms and Conditions, is sent to you because no fee is being charged for your order. Please note the following:

- Permission is granted for your request in both print and electronic formats, and translations.
- If figures and/or tables were requested, they may be adapted or used in part.
- Please print this page for your records and send a copy of it to your publisher/graduate school.
- Appropriate credit for the requested material should be given as follows: "Reprinted (adapted) with permission from {COMPLETE REFERENCE CITATION}. Copyright {YEAR} American Chemical Society." Insert appropriate information in place of the capitalized words.
- One-time permission is granted only for the use specified in your RightsLink request. No additional uses are granted (such as derivative works or other editions). For any uses, please submit a new request.

If credit is given to another source for the material you requested from RightsLink, permission must be obtained from that source.

### Te-Doped Pd Nanocrystal for Electrochemical Urea Production by Efficiently Coupling Carbon Dioxide Reduction with Nitrite Reduction



**Author:** Yonggang Feng, Hao Yang, Ying Zhang, et al  
**Publication:** Nano Letters  
**Publisher:** American Chemical Society  
**Date:** Nov 1, 2020

Copyright © 2020, American Chemical Society

#### PERMISSION/LICENSE IS GRANTED FOR YOUR ORDER AT NO CHARGE

This type of permission/license, instead of the standard Terms and Conditions, is sent to you because no fee is being charged for your order. Please note the following:

- Permission is granted for your request in both print and electronic formats, and translations.
- If figures and/or tables were requested, they may be adapted or used in part.
- Please print this page for your records and send a copy of it to your publisher/graduate school.
- Appropriate credit for the requested material should be given as follows: "Reprinted (adapted) with permission from {COMPLETE REFERENCE CITATION}. Copyright {YEAR} American Chemical Society." Insert appropriate information in place of the capitalized words.
- One-time permission is granted only for the use specified in your RightsLink request. No additional uses are granted (such as derivative works or other editions). For any uses, please submit a new request.